Thermodynamic Measurements on Frustrated Triangular and Honeycomb Lattices in the Millikelvin Range

Dissertation

zur Erlangung des akademischen Grades

Dr. rer. nat.

eingereicht an der
Mathematisch-Naturwissenschaftlich-Technischen Fakultät
der Universität Augsburg

von

Sebastian Bachus

Augsburg, November 2021

Erstprüfer: Prof. Dr. Philipp Gegenwart
Zweitprüfer: Prof. Dr. Alois Loidl

Tag der mündlichen Prüfung: 17. März 2022

Contents

List of Figures

List of Tables

1. Introduction

The adjective *frustrated* has usually purely negative connotations, but this is not always true. Sometimes, frustration is the origin of innovation because it strongly motivates to identify and solve problems. One famous example is the well-known coffee filter. Melitta Bentz desperately wanted to avoid frustrating particles in her coffee and invented an efficient, but easy-to-use filter in 1908. Nowadays, the Melitta group offers a wide range of household products. It comprises more than 50 subsidiaries on five continents, employs nearly 6,000 workers, and achieved annual sales of about 1.7 billion Euro in 2020 [1]. Consequently, frustration can initiate astonishing success stories.

In the context of magnetism, frustration can lead to fascinating new phenomena, too, which attracted strong interest due to, for example, the potential in the field of quantum computers. But how can a magnet be frustrated? Magnetic materials consist of interacting magnetic moments (or spins), and the strength of the interaction can be parameterized in the exchange coupling J. In an antiferromagnet, for instance, neighboring moments try to align antiparallel. If this is not possible with all neighbors at the same time, the moments are *frustrated*. The most direct realization is *geometrical* frustration. Imagine a triangle with three spins on each corner that either point up or down. They shall be coupled antiferromagnetically with exchange couplings of equal strength. The antiparallel alignment of all three spins cannot be fulfilled simultaneously, and there exist six energetically equivalent arrangements (or ground states), between which the moments can fluctuate (up-up-down, up-down-up, etc). Such frustration effects can prevent a magnetically ordered ground state, that usually sets in as soon as thermal fluctuations become small compared to the magnetic interaction, $T \lesssim J$. Instead of a symmetry breaking transition, a liquid-like state emerges, which is called spin liquid. In the case of small spins, quantum fluctuations are strong and survive even at zero temperature. Thus, the so-called quantum spin liquid (QSL) evades long-range magnetic order down to 0 K.

Such peculiar state has been proposed for the first time by Anderson in 1973 with the resonating valence bond (RVB) state on the triangular lattice [2]. Its elementary excitations are fractionalized (spinons), in sharp contrast to those in conventional magnets (magnons). Furthermore, the RVB state was suggested to be relevant for high-temperature superconductors [3, 4]. While it turned out that Anderson's original scenario with isotropic nearest-neighbor Heisenberg interactions does not host a QSL ground state [5, 6], many QSL have been identified theoretically on various lattices, including the triangular arrangement. For example, taking next-nearest neighbors into account (J_1-J_2 model) can be sufficient to stabilize a QSL, depending on the ratio J_2/J_1 [7]. Another famous example is the so-called Kitaev quantum spin liquid (KSL), found by Kitaev in 2006 on the honeycomb lattice with special anisotropic interactions [8] leading to frustrated neighboring spins. Therefore, this type of spin liquid is an example for *exchange* frustration. The KSL attracted enormous attention because of its potential for fault-tolerant quantum computing [9].

On the experimental side, however, progress could not keep pace with these discoveries because of several reasons. Real materials are usually more complex due to additional interactions, which leads to deviations from theoretical models. Moreover, a fundamental question

is how to evidence a QSL experimentally, which is rather challenging. A key feature is the absence of long-range magnetic order in combination with fluctuating spins even at 0 K [7]. Consequently, a bunch of different techniques have to be combined at temperatures as low as possible. Spin dynamics can be probed by muon spin relaxation (μSR) or nuclear magnetic resonance (NMR). Neutron scattering is an extremely powerful tool because it is sensitive to magnetically ordered structures, but can also provide information on the excitation spectrum of the material. On the other hand, it requires beam time at a large scale facility, where a well-justified proposal is mandatory several months in advance. Therefore, other methods are essential for the first characterization of QSL candidates. Thermodynamic measurements are ideally suitable for this purpose. The specific heat, for example, detects phase transitions and gives insight into the low-energy excitations. The technical challenge is to perform such experiments as close as possible to 0 K, which requires more advanced setups than standard cryostats on ^{4}He basis. In this work, a ^{3}He/^{4}He dilution refrigerator is employed to investigate potential QSL candidates down to far below 100 mK in fields up to 15 T.

The thesis is structured as follows. Chapter 2 introduces basic concepts in the field of magnetism, including crystal electric field (CEF), magnetization and magnetic ordering. Two different mechanisms of frustration are presented, namely the triangular and the honeycomb lattice, that are relevant for all investigated materials. Thermodynamic relations are crucial for connecting various variables and revisited before discussing principles of the thermodynamic properties specific heat, magnetic Grüneisen parameter, and entropy.

The technical aspects of the utilized devices and measurements methods are an essential part of this experimental thesis, and chapter 3 is addressed to that issue. The working principle of a ^{3}He/^{4}He dilution refrigerator is introduced. Reliable thermometry in the millikelvin range is challenging, and considerable efforts have been undertaken to prepare and calibrate small size thermometers down to below 30 mK in fields up to 17.5 T. The specific heat cells are equipped with one of these customized thermometers, respectively, and the measurement methods for specific heat and magnetic Grüneisen parameter are presented in detail. Furthermore, the working principle of the Faraday magnetometer is explained, which is utilized for determining the magnetization in the millikelvin range.

Chapter 4 comprises measurements on four different samples that all belong to the class of Yb^{3+} based triangular lattices. $YbMgGaO_4$ was the first rare-earth based QSL candidate and is still subject to vivid discussions. Its ground state is apparently disordered with fluctuating spins down to 50 mK, the key ingredients of a QSL [7]. On the other hand, the site-mixing of the non-magnetic ions Mg^{2+}/Ga^{3+} complicates the microscopic scenario due to locally differently charged environments of the Yb^{3+} ions. This could lead to a mimicry of a spin liquid [10, 11]. Additionally, spin-glass freezing has been suggested around 100 mK [12]. In order to address these issues, temperature- and field-dependent magnetization measurements down to 40 mK in fields up to 10 T are combined with a procedure to include the structural randomness into Monte Carlo simulations in Sec. 4.1.

To evade the concerns on the effects of site-mixing, disorder-free Yb^{3+} materials are highly desirable. The search was successful in the family of $AYbX_2$, where A and X stand for alkali metals (K, Na, Cs) and chalcogens (O, S, Se), respectively. The potential QSL candidates $KYbS_2$ and $NaYbO_2$ are investigated in this thesis by means of specific heat and magnetic Grüneisen parameter down to 50 mK in fields up to 15 T in Secs. 4.2.1 and 4.2.2. The zero-field specific heat characterization is discussed in detail, including the subtraction of the nuclear contribution that arises below about 100 mK. The field-dependent measurements are used to probe the non-trivial field evolution, which is compared to other triangular lattice materials. Finally, the phase diagram is established for both materials.

The chapter on triangular magnets is concluded by measurements on $KBaYb(BO_3)_2$ in Sec. 4.3. It turns out that its entropy evolution in magnetic fields is ideally suitable for adiabatic demagnetization refrigeration (ADR) down to temperatures below 20 mK, starting at 2 K and moderate fields. This material has great potential to replace established cooling materials due to its chemical stability under vacuum conditions and heating up to 600 °C. In this thesis, several cooling tests are presented, including a realistic application in the commercial Physical Property Measurement System (PPMS). Finally, possibilities for further optimization are discussed.

In chapter 5, the focus is changed towards the Kitaev material α-$RuCl_3$, where Ru^{3+} ions are arranged on a honeycomb lattice. Despite of sizeable Kitaev interaction, this system is not a KSL in zero field because of additional interactions. α-$RuCl_3$ undergoes a phase transition to a magnetically ordered phase in a zigzag pattern at around 7 K. If α-$RuCl_3$, however, is close to a KSL, suppressing the magnetic order by magnetic field potentially could uncover underlying spin liquid physics. Excitingly, a half-quantized plateau in thermal Hall conductivity was found, as soon as the order is suppressed at around 7-8 T [13]. This is in general considered to be a strong evidence for a field-induced KSL and, thus, for Majorana fermions in α-$RuCl_3$. On the other hand, this distinct spin liquid phase eventually has to enter the partially polarized state, when the magnetic field is further increased. It can be expected that this should be accompanied by another signature in thermodynamic measurements, but only very weak anomalies have been detected so far [14, 15]. In order to further investigate this, extensive field-dependent measurements are presented between 0 T and 14 T with the field applied along various in-plane orientations. This takes the in-plane anisotropy of α-$RuCl_3$ into account. The focus is on the magnetic Grüneisen parameter because of its high sensitivity to field-induced phase transitions. Moreover, the combination with specific heat gives direct access to the field-dependent entropy. Altogether, these thermodynamic measurements provide a powerful arsenal to explore the phase diagram of α-$RuCl_3$. Chapter 5 is closed by the comparison of several samples synthesized in different laboratories, which sheds light on unexpected in-gap states in the ordered state.

In the end, all results of this thesis are briefly summarized in chapter 6, together with an outlook on possible further measurements and developments.

2. Basic Concepts

Classical models exclude any magnetization in materials in thermal equilibrium and zero field, which is known as the Bohr-van Leeuwen theorem [16]. This is in clear contradiction to, for example, the probably most prominent permanent magnet, Fe_3O_4, also called magnetite. It is already known for more than two thousand years and was used to fabricate compass needles [16]. Consequently, a quantum mechanical description is essential for explaining magnetic phenomena. In Sec. 2.1, the concepts of magnetism in solids are presented mainly following Ref. [16]. Subsequently, the competing phenomena of magnetic ordering and frustration are introduced, including the lattice geometries relevant to this work [Sec. 2.2]. Additionally, an overview of thermodynamic basics and relations is presented in Sec. 2.3-2.6.

2.1. Magnetic Moments in Solid Materials

In the following sections, the magnetic moment of a single atom is introduced and environment effects in solids like the crystal electric field are discussed. Furthermore, the response of many non-interacting moments on magnetic fields is established.

2.1.1. On the Atomic Level: Hund's Rules and Spin-Orbit Coupling

For explaining magnetic phenomena, quantum mechanics are essential. In the following, the relevant basic concepts on an atomic level are introduced. An atom consists of a nucleus and surrounding electrons in the atomic shell. Each electron carries an orbital angular momentum $\widehat{\mathbf{l}}_\mathrm{i}$ as well as a spin angular momentum $\widehat{\mathbf{s}}_\mathrm{i}$. In the case of weak spin-orbit coupling (SOC), they both sum up to the total orbital and spin angular momentum $\widehat{\mathbf{L}} = \sum \widehat{\mathbf{l}}_\mathrm{i}$ and $\widehat{\mathbf{S}} = \sum \widehat{\mathbf{s}}_\mathrm{i}$, respectively. The resulting momenta couple to the total angular momentum $\widehat{\mathbf{J}}$,

$$\widehat{\mathbf{J}} = \widehat{\mathbf{L}} + \widehat{\mathbf{S}}, \tag{2.1}$$

generally known as Russel-Saunders or LS coupling. The commuting operators $\widehat{\mathbf{J}}^2$ and $\widehat{J}_\mathrm{z}$ with the eigenvalues $\hbar^2 J(J+1)$ and $m_\mathrm{J}\hbar$ represent the atom well [16, 17] with values between $J = |L-S|, ..., |L+S|$ in integer steps. J is the quantum number of the total angular momentum with the magnetic quantum number m_J. As a consequence, the SOC splits the atomic levels according to J, which results in the fine structure [17]. The atomic ground state can be determined by Hund's rules. According to the first and second rule, the total spin S and, subsequently, the total orbital moment L is maximized. Due to SOC, $J = |L-S|$ is energetically favored for less than half-filled orbitals, whereas $J = L+S$ is prefered for more than half-filling minimizing the spin-orbit energy given by $\mathcal{H}_\mathrm{SO} = \lambda \hat{\mathbf{L}}\hat{\mathbf{S}}$ [16–18]. The SOC constant λ increases towards heavier elements and will later become important for comparison with other energy scales [Sec. 2.1.2].

As an example for applying Hund's rules, the term scheme of the element Yb is illustrated in Fig. 2.1(a) where $S = L = 0$ because of fully filled orbitals and, thus, $J = 0$. In principle, the same rules can be applied to ions exemplarily shown in Fig. 2.1(b,c) for Yb^{3+} and Ru^{3+}

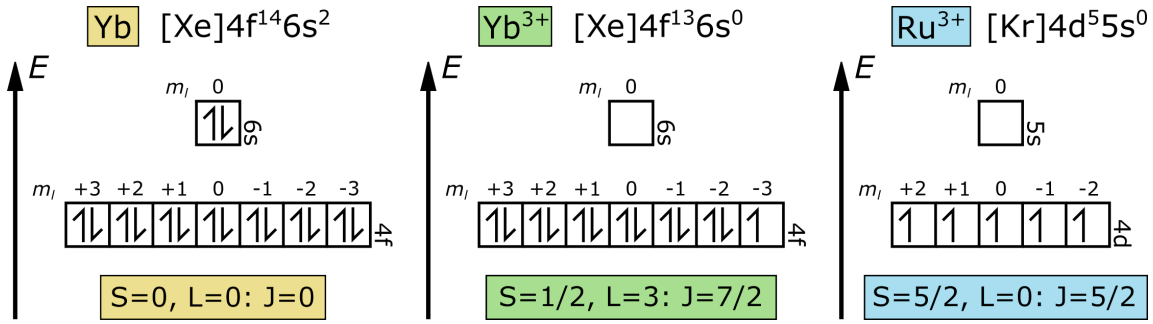

Figure 2.1. Application of Hund's rules on isolated atoms or ions without considering environment effects in solids: (a) Yb, (b) Yb^{3+}, and (c) Ru^{3+}.

with $J = 7/2$ and $J = 5/2$. Strictly speaking, this only holds true for free ions, where effects of the environment are neglected, see also Sec. 2.1.2. The total angular momentum $\widehat{\mathbf{J}}$ is linked to a magnetic moment,

$$\widehat{\boldsymbol{\mu}} = -g_\mathrm{J}\frac{\mu_\mathrm{B}}{\hbar}\widehat{\mathbf{J}}, \quad \mu_\mathrm{eff} = -g_\mathrm{J}\mu_\mathrm{B}\sqrt{J(J+1)}, \quad g_\mathrm{J} = 1+\frac{J(J+1)+S(S+1)-L(L+1)}{2J(J+1)}, \tag{2.2}$$

with the g-factor g_J, the Bohr magneton μ_B, and the Planck constant $\hbar$ [19]. The effective magnetic moment μ_eff is linked to the square root of the eigenvalue of $\widehat{\mathbf{J}}^2$ and, therefore, also to the quantum number J of the total angular momentum. As a result, no magnetic moment is expected for elementary Yb with $J = 0$ [16]. For ions, however, the situation becomes more complicated. Hund's rules predict the effective magnetic moment for 4f insulators extremely well, for example for Yb^{3+} with $J = 7/2$, but only at high temperatures. Moreover, transition metal compounds with partially filled $d-$shells significantly deviate from Hund's predictions [16, 19]. Consequently, further effects despite of SOC have to be considered such as the local environment of the magnetic ions. Implications on the energy level scheme will be discussed in the next section.

As a closing remark, it should be mentioned that the nucleus may also carry a magnetic moment due to its nuclear spin $\mathbf{I}$ from the protons and neutrons. Compared to the electronic magnetic moment, it scales by the mass ratio between electron and proton, $m_\mathrm{e}/m_\mathrm{p}$. Thus, its magnetism can usually be neglected [16].

2.1.2. Crystal Electric Field and Effective Total Angular Momentum J_eff

In solid materials, the ions naturally can not be considered as isolated, and environment effects are usually crucially important. The stability of ionic solids results from the attractive force between oppositely charged ions, e. g. between the central atom Ru^{3+} and the surrounding ligands Cl^- in the case of α-$RuCl_3$. The ligands are very often arranged in an octahedral configuration around the central atom. In α-$RuCl_3$, edge-sharing $RuCl_6$ octahedra are formed with six chlorine ions arranged around Ru^{3+} [Fig. 2.2(a)]. This octahedral configuration holds true for all investigated materials in this work. In general, the ligands may have an impact on orbitals of the central atom and, consequently, lift the orbital degeneracy. Here, the Crystal Electric Field (CEF) theory can provide further insights. It describes the ligands as negative point charge and can, in principle, be expanded to the ligand field theory by including molecular orbital theory [16].
In the following, a 3d transition metal ion is discussed in detail as a standard example. The 3d atomic orbitals with $l = 2$ are five-fold degenerate due to the possible magnetic quantum

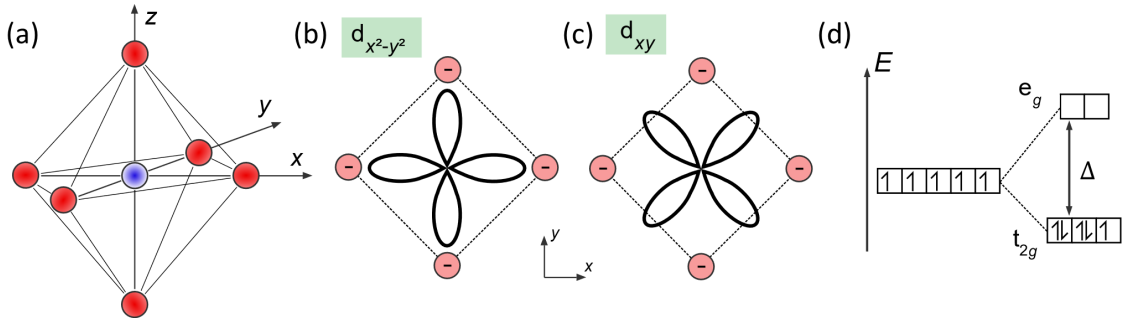

Figure 2.2. (a) 3d transition metal (blue) in octahedral ligand (red) configuration. (b) Electrons in $3d_{x^2-y^2}$ orbital experience electrostatic repulsion from the negative charge representing the ligands in the $xy-$plane. Consequently, this orbital is lifted in energy. (c) In contrast, the $3d_{xy}$ orbital is favorable for the electron due to the minimized repulsion. (d) As a result, the 3d levels split into t_{2g} and e_g. In the Low Spin configuration, as indicated here for $3d^5$, the electrons first occupy the lower orbitals. Figures partially adapted from Ref. [16].

numbers $m_l = \pm 2, \pm 1, 0$. In a crystal with the three spatial axes x, y, z, however, the real orbitals are linear combinations of the original atomic wave functions $d_{\pm 2}$, $d_{\pm 1}$, d_0 which again results in five degenerate orbitals. These are well-known as d_{xy}, d_{xz}, d_{yz}, $d_{x^2-y^2}$, and d_{z^2} orbitals. Please note that the quantum number m_l is not well defined anymore for these orbitals [20]. Consequently, calculating J by simply applying Hund's rules is no longer possible. Now, let us return to the influence of the ligands on the central atoms' $d-$orbitals. In Fig. 2.2(b), $d_{x^2-y^2}$ is illustrated. The neighbouring ligands in the xy-plane can be, for example, Cl^- or O^{2-} and are treated as negative point charges. In general, d-orbitals are fairly extended and not shielded by surrounding fully filled shells. As a consequence, an electron in $d_{x^2-y^2}$ experiences strong electrostatic repulsion from the ligands. Therefore, it is lifted in energy. In contrast, d_{xy} reveals maximal distance to the ligands being energetically favorable for an electron [Fig. 2.2(c)]. This way, the surrounding crystal field splits the d-orbitals into two groups, the so-called e_g and t_{2g} levels, with an energy difference Δ [Fig. 2.2(d)]. This holds true for the octahedral ligand configuration while other arrangements result in different splitting [16]. The filling of the t_{2g} and e_g levels with 4, 5, 6, or 7 electrons depends on the pairing energy of electrons in the same orbital. In general, pairing two spins in the same orbital is energetically unfavorable because it requires a finite energy due to Coulomb repulsion. If Δ is comparatively large, however, minimizing the total spin by first filling t_{2g} becomes preferable (Low Spin configuration, Fig. 2.2(d)). This is in contrast to Hund's first rule, where the spin would be maximized by occupying e_g before double-filling t_{2g} (High Spin configuration) [16].

This discussion emphasizes that determining the ground state of magnetic systems is more complex than merely applying Hund's rules and strongly depends on the strength of the CEF compared to SOC. In 3d transition metals, CEF is the dominating energy scale resulting in the t_{2g} and e_g levels for octahedral ligand environment as discussed above. For heavier elements, especially in the 5d metals, SOC becomes stronger and often comparable to the CEF. This can lead to further splitting of the t_{2g} manifold. In the case of d^5, the five electrons fill the lowest states leaving a hole in the J_{eff} level. This yields an effective magnetic degree of freedom of $J_{\text{eff}} = \frac{1}{2}$ [21, 22], dictating the low temperature magnetism of Ru^{3+} in α-$RuCl_3$ [23]. In rare earth ions, however, the 4f subshell is fairly localized and shielded by more expanded orbitals. This drastically suppresses effects of the CEF rendering SOC as dominating energy

scale, which results in $J = 7/2$ for Yb^{3+} following Hund's rules. That 8-fold degenerate multiplet, however, is split by the CEF into four doublets according to the Kramers theorem. At high temperatures, all levels are equally populated, and the theoretically predicted value $\mu_{\text{eff}} = 4.54\,\mu_{\text{B}}$ is confirmed experimentally with high accuracy [16]. The low-temperature physics, on the other hand, is dominated by the lowest Kramers doublet. For $YbMgGaO_4$ and the other investigated Yb^{3+} samples, their ground state is again expressed by an effective spin-$\frac{1}{2}$ [7]. Therefore, both ground states should carry the same entropy $R\ln 2$ [Sec. 2.6]. Nevertheless, the underlying principles are not the same for α-$RuCl_3$ and the Yb^{3+} materials leading to fundamentally different physics [Ch. 4 and 5].

2.1.3. Dia- and Paramagnetism

After establishing magnetic moments due to partially filled subshells, the response of a material on magnetic fields is discussed. For this purpose, the term of magnetic susceptibility χ is used, which is often defined as $\mathbf{M} = \chi\mathbf{H}$. It connects the volume magnetization $\mathbf{M}$ of a material with the external magnetic field $\mathbf{H} = \mathbf{B}/\mu_0$. In general, the magnetization does not depend linearly on the magnetic field and can also be anisotropic. Therefore, a more suitable definition of the magnetic susceptibility is $\chi_{ij} = \partial M_i/\partial H_j$. The volume magnetization is the total magnetic moment $\mathbf{m}$ normalized by the volume V, $\mathbf{M}_{\text{vol}} = \mathbf{m}/V$, and independent of the sample volume. In many experiments, on the other hand, the molar magnetization $\mathbf{M}_{\text{mol}} = \mathbf{m}/n$ with the unit $\text{J}\,\text{T}^{-1}\,\text{mol}^{-1}$ or $\mu_{\text{B}}\,\text{T}^{-1}$ is more common. These definitions must not be confused. In this section, interactions between the material's ions are neglected.

First, ions without unpaired spins are considered. From a classical point of view[1], the electrons of each ion move around their respective nucleus. Applying a magnetic field causes a current, which induces a magnetic moment in opposite direction compared to the external magnetic field. Consequently, χ takes a negative value. This effect is present in all materials and called diamagnetism [24]. Usually, diamagnetism is fairly weak and can be neglected in many materials [16].

As soon as permanent non-interacting magnetic moments are present due to non-zero J, the situation changes fundamentally. An external field aligns those moments and, thus, the magnetization $\mathbf{M}$ increases. For simplicity, the magnetization is treated as a scalar from now on because, in most cases, it is measured for the same direction like the magnetic field without any other components. At a certain field strength, the saturation magnetization $M_{\text{S}} = g_J\mu_{\text{B}}J$ is attained when all moments have become parallel. Note that M_{S} is here defined as molar magnetization. This behavior can be captured by

$$M_{\text{mol}} = M_{\text{S}}\text{B}_J(y), \tag{2.3}$$

with the Brillouin function[2] $\text{B}_J(y)$ and $y = g_{\text{J}}J(\mu_{\text{B}}B/k_{\text{B}}T)$ [16]. For $y \ll 1$, i.e. high temperatures $k_{\text{B}}T$ compared to the magnetic field $\mu_B B$, the Brillouin function can be expanded for calculating the molar magnetic susceptibility,

$$\chi_{\text{para}} = \frac{\mu_0\mu_{\text{eff}}^2}{3k_{\text{B}}T} = \frac{C_{\text{Curie}}}{T}, \tag{2.4}$$

which is the famous Curie Law [16]. This contribution is called paramagnetism. Its susceptibility diverges towards zero temperature, whereas diamagnetic contributions remain temperature independent [16, 24].

[1] The quantum mechanical solution yields the same expressions for Diamagnetism [24, 25].
[2] $\text{B}_J(y) = \frac{2J+1}{2J}\coth\left(\frac{2J+1}{2J}y\right) - \frac{1}{2J}\coth\left(\frac{y}{2J}\right)$, and for $J = 1/2$: $\text{B}_{1/2}(y) = \tanh(y)$.

A second paramagnetic contribution should be mentioned as well. Let us consider an atom obtaining a $J = 0$ ground state. In this case, a magnetic field is not expected to change the ground state energy. Nevertheless, a contribution to the susceptibility is possible when the ground state mixes with excited states exhibiting $J \neq 0$. Such an effect is known as Van-Vleck paramagnetism and, like diamagnetism, turns out to be temperature independent [16]. The susceptibility can then be expressed as $\chi_{\text{para}}(T) = C/T + \chi_0$ [26]. The Van-Vleck contribution χ_0 leads to an additional linear slope in the field-dependent magnetization $M(B)$ that may become dominant as soon as the magnetic saturation is reached. As an example, the Brillouin function for a paramagnetic spin-1/2 system together with a Van-Vleck contribution is shown in Fig. 2.3(a) with the magnetization normalized to the saturation magnetization. The linear increase at high fields results from the Van-Vleck term that can be precisely determined by a linear fit function (red-dotted line). After subtracting the Van-Vleck contribution, the Brillouin function is recovered (green curve), which saturates to M_{S} as soon as all magnetic moments are aligned parallel to the magnetic field. In other words, the paramagnet has entered the *fully polarized* state. The same behavior in the high-field limit can be observed in more complex magnets that will be introduced in the following sections. In some anisotropic magnets, however, extremely high magnetic fields are required to realize this phase. An example relevant to this work is α-$RuCl_3$. Here, the magnetization $M(B)$ for in-plane fields is reduced below the expected value because the strong anisotropic interactions prevent the parallel alignment of the spins. $M(B)$ still increases even at 60 T, and full saturation will only be approached in the limit of extremely high fields [27, 28]. This rather peculiar state is denoted as the *partially-polarized* state.

As a closing remark on paramagnets, the magnetic susceptibility $\chi(B)$ as field-derivative of the magnetization is shown in the inset of Fig. 2.3(a). $\chi(B)$ decreases monotonically and reaches the constant value χ_0 if a Van-Vleck contribution is present.

2.1.4. Magnetic Interaction

Hund's rules basically stem from interactions between electrons on the same atom [18]. Naturally, these electrons may also interact with neighbouring atoms which has been neglected so far. This is crucial for explaining cooperative magnetic phenomena because the classical dipole-dipole interaction clearly lacks any reasonable description. For typical parameters in solids, the dipole energy is in the order of 1 K and, as a consequence, is not capable to explain e. g. magnetic order at room temperature [16]. In the following, the very basics of magnetic interactions are briefly introduced following Ref. [18]. In insulating materials, they mainly can be ascribed to two distinct types, namely the potential and the kinetic exchange.

Let us consider two electrons located on two different atoms. In this configuration, the electron spins can form a singlet or a triplet state. By calculating the energy difference between those states, $E_{\text{s}} - E_{\text{t}}$, the nature of the ground state can be determined. For atoms being close enough to each other, like in the hydrogen molecule, a chemical bond is developed resulting in singlet state. Without overlap of the atomic wave functions, however, the ground state turns out to be a triplet. That corresponds to ferromagnetic interaction between the electrons. Since it originates from electron-electron repulsion and, therefore, influences the potential energy, that interaction is called **potential exchange**.

Furthermore, hopping processes between the two atoms are possible with a hopping probability t resulting in two electrons located on the same atom and orbital. Thus, the strong on-site Coulomb repulsion becomes important, which is often denoted as Hubbard U due to its cen-

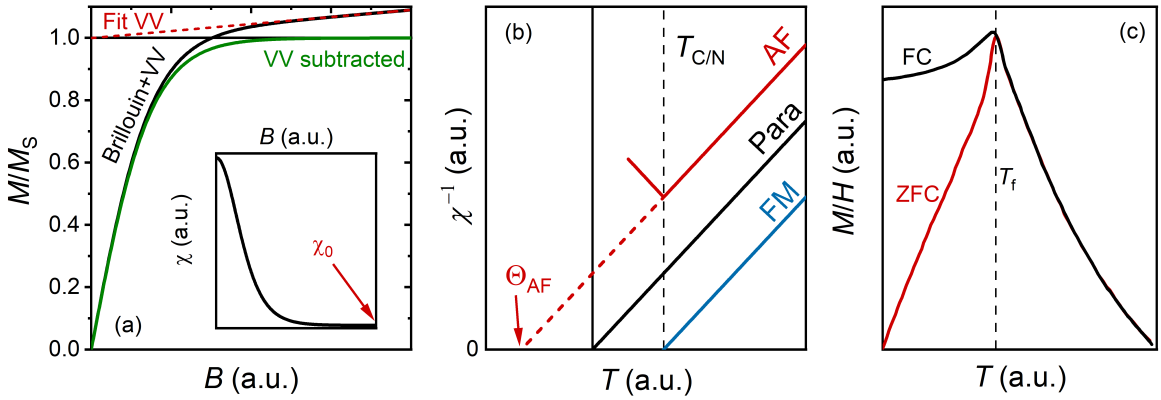

Figure 2.3. (a) Magnetization of an ideal $J = 1/2$ paramagnet using the Brillouin function together with a Van-Vleck contribution yielding a linear slope at high fields (black). Fitting this part with $M_{\mathrm{HF}} = \chi_0 B + M_{\mathrm{S}}$ (red) allows to subtract of the Van-Vleck term and to recover of the original Brillouin function (green). (b) Sketch of typical $\chi^{-1}(T)$ curves for a ferromagnet (blue) and an antiferromagnet (red) with an ordering temperatures of $T_{\mathrm{C/N}}$. In the high temperature limit, the Curie-Weiss law is valid and can be used to fit the linear regime with $\chi^{-1} \sim T - \Theta$. A negative Curie-Weiss temperature Θ indicates AF interactions, whereas FM interactions result in positive values. For a paramagnet (black), $\Theta = 0$ recovers the Curie law from Eq. 2.4. Graph adapted from Ref. [25]. (c) Magnetic susceptibility M/H of a typical spin glass system adapted from Ref. [29]. Below the freezing temperature T_{f}, the susceptibility depends on the measurement history. DC-susceptibility measurements require a small but finite magnetic field. Cooling the system in this field (FC) results in nearly constant susceptibility below T_{f} (black). If the system is cooled in zero-field (ZFC), however, it strongly decreases below T_{f} (red). This way, the freezing temperature can be determined.

tral role in the Hubbard model. In the regime of Mott insulators, the Coulomb repulsion is dominating, $U \gg t$. Returning to the hopping process, it is obviously only allowed for the singlet state due to the Pauli principle. Calculating again the energy difference $E_{\mathrm{s}} - E_{\mathrm{t}}$ reveals the singlet state as energetically favorable. Consequently, possible hopping processes reduce the energy and favor the antiferromagnetic configuration. Due to the imaginary movement of the electron, that effect is called **kinetic exchange**.

In insulating materials, these two exchanges determine if a material exhibit ferro- or antiferromagnetic interactions. In the Heisenberg model introduced in Sec. 2.2.1, both exchanges are summarized in the coupling constant J_{ij} and are not distinguished explicitly anymore.

2.1.5. Magnetic Ordering

As soon as magnetic interactions come into play, an abundance of magnetic structures can evolve. The most elementary arrangements are **ferromagnets** (FM) and **antiferromagnets** (AFM), where the magnetic moments reveal a well-defined and stable orientation below the ordering temperature. Such phenomena are called long-range order. In the FM case, all moments are aligned parallel leading to a non-zero magnetization. For AFM, the magnetic interaction forces neighboring moments to point into opposite directions. This way, two sublattices are created that add up to zero magnetization. Strictly speaking, the latter only holds true as long as both sublattices carry the same magnetic moments. Otherwise, a structure with nonzero net magnetization is obtained called **ferrimagnet**. For all these configurations, increasing the temperature results in thermal fluctuations competing with magnetic interac-

tions. Eventually, the magnetic order is destroyed at the characteristic ordering temperature T_C. For AFM, it is usually denoted as Néel temperature T_N. At temperatures far above the ordering temperature, the magnetic moments are dominated by thermal fluctuations reminiscent of the previously discussed paramagnet. For this regime, approximating magnetic interactions by a mean-field approach for FM (or AFM) yields the Curie-Weiss Law,

$$\chi = \frac{\mu_0 \mu_{\text{eff}}^2}{3k_B} \frac{1}{T - \Theta}, \tag{2.5}$$

with the Curie-Weiss temperature Θ [16, 18]. This quantity is standardly used to categorize magnetic materials by fitting experimental magnetic susceptibility measurements in the high temperature limit $T \gg \Theta$. As a technical remark, the temperature-dependent magnetic susceptibility is usually measured at a small but finite magnetic field to induce a detectable magnetic moment. This method is called DC-susceptibility measurement. In Fig. 2.3(b), typical inverse susceptibility curves $\chi^{-1}(T)$ of a FM (blue), an AFM (red), and a paramagnet (black) are presented. Both the FM and the AFM order at $T_{C/N}$, where deviations from the Curie-Weiss law are expected. A positive Curie-Weiss temperature evidences dominating ferromagnetic interactions. For AFMs, however, a negative value is observed. In the case of $\Theta = 0$, Eq. 2.4 for the pure paramagnet is recovered. Note that, in general, the Curie-Weiss temperature Θ does not predict the ordering temperature correctly because the mean-field approximation has limitations. Nevertheless, Θ and $T_{C/N}$ are usually assumed to be in the same order of magnitude.

Susceptibility measurements $\chi(T)$ can also serve as a direct probe for evidencing magnetic order. At $T_{C/N}$, an anomaly is commonly present as indicated in Fig. 2.3(b) for the AFM. The shape of the transition depends on the system under investigation. Additonally to magnetization measurements, there are many further complementary experimental methods such as specific heat or elastic neutron scattering as the most direct probe, where magnetic Bragg peaks appear in the ordered state [16, 30]. It is noted in passing that susceptibility measurements are useful, too, to detect the freezing temperature T_f in spin glasses, where the magnetic moments become frozen and point randomly into different directions [19]. Here, the magnetic susceptibility $\chi = M/H$ depends on the history before the measurement. If the sample is cooled below T_f in a magnetic field, M/H turns out to be nearly constant [Fig. 2.3(c)]. If the sample is cooled in zero field, however, the susceptibility becomes clearly distinct and shows a steep decrease below T_f. The freezing temperature is defined as the point where the field cooled (FC) and the zero field cooled (ZFC) curves start to deviate from each other [19, 29].

So far, only the ground state of FMs (AFMs) has been discussed. However, excitations are crucial to fully understand a material. In conventional magnets, the most elementary excitation in the ordered state is the magnon with its bosonic character. It evolves due to the symmetry breaking at the ordering temperature (Goldstone theorem) [18]. In a very basic picture, a magnon can be regarded as flipping a spin. In a FM, this is equivalent to reducing the total magnetization by $\Delta S = 1$. A more exotic excitation is the so-called spinon. It carries a spin of $1/2$ and, consequently, has fermionic character. Usually, spinons are discussed in the context of one-dimensional spin chains, where they appear as domain walls [16, 31], but they also attracted a lot of attention as possible excitations in frustrated two-dimensional magnets. This will be discussed in the following section.

2.2. Magnetic Frustration

Sometimes, a little frustration can make life interesting. - L. Balents [31]

Especially for magnetic systems, this certainly holds true. Magnetic frustration appears when competing magnetic interactions can not be fully satisfied simultaneously. In a simple picture, three Ising spins with antiferromagnetic (AF) interactions on a triangle illustrate the concept of frustration well [Fig. 2.4(a)]. Spin 1 and 2 point in opposite directions. For the third spin, however, concurrently meeting the AF configuration compared to 1 and 2 is not possible anymore. Hence, the system is frustrated. Since the effect originates from a special spin arrangement, it is termed **geometrical frustration**. Many geometries potentially show frustration, for example the Kagomé, triangular, square, or the Pyrochlore lattice [31]. Besides the geometrical configuration, **exchange frustration** offers another route for intriguing new physics. In this case, bond-dependent interactions between nearest neighbors (NN) may result in frustrated spins, too [8, 32]. Such highly anisotropic behavior requires special preconditions for realization in materials and will be discussed in more detail in Sec. 2.2.2.

But what is the effect of magnetic frustration? Usually, each magnetic system undergoes a symmetry-breaking transition as soon as magnetic interactions prevail over thermal fluctuations at the ordering temperature [Sec. 2.1.5]. If frustration becomes dominant, however, long-range order becomes increasingly suppressed, and the transition temperature shifts towards lower temperatures. For comparing different materials, the frustration parameter $f = |\Theta_{\mathrm{CW}}|/T_{\mathrm{N}}$ has been introduced [31, 33] as the ratio between Curie-Weiss and ordering temperature. A large f indicates a strongly frustrated magnet. In some cases, the magnetic order completely vanishes resulting in a liquid-like state with disordered spins, which is called spin liquid [31].

In the classical limit of large spins, models exhibiting spin liquids often have a large degeneracy of spin configurations. As standard example, AF coupled Ising spins on a two-dimensional (2D) triangular lattice obtain residual entropy reminiscent of that degeneracy [34]. A similar situation occurs in Pyrochlores with spins arranged on corner-sharing octahedra (3D). These spins are Ising-like and point either into or out of the octahedra. Satisfying the ferromagnetic NN interaction is not possible evoking frustration. The ground state for a single octahedron are two spins "in" and two "out", which is already sixfold degenerate. Consequently, Pyrochlores obtain a huge (classical) ground state degeneracy as well [31]. The ground states are separated by a sizable energy barrier since several spins need to be flipped requiring finite thermal fluctuations. If temperature is reduced to 0 K, however, the spins freeze in their randomly distributed two-in-two-out configurations forming a spin ice. As a consequence, magnetic moments become static in classical spin liquids at very low temperatures [31].

This aspect distinctly distinguishes quantum spin liquids (QSL) from their classical counterparts. Quantum fluctuations are strongest for spin-1/2 systems and survive at zero temperature. Therefore, magnetic moments remain dynamic and fluctuating in a QSL. The ground state is not degenerated anymore but rather consists of a superposition of different configurations. In this context, a widely used description is the resonating valence bond (RVB), which originally has been postulated for the triangular lattice by Anderson [2]. Here, all spins pairwise form a valence bond (spin singlet). That naturally accounts for the obviously zero net magnetization of a QSL. Due to quantum fluctuations of the spins, the valence bonds fluctuate between all possible configurations. Thus, the RVB state is the superposition of all possible local singlet configurations [Fig. 2.4(b)]. The valence bonds do

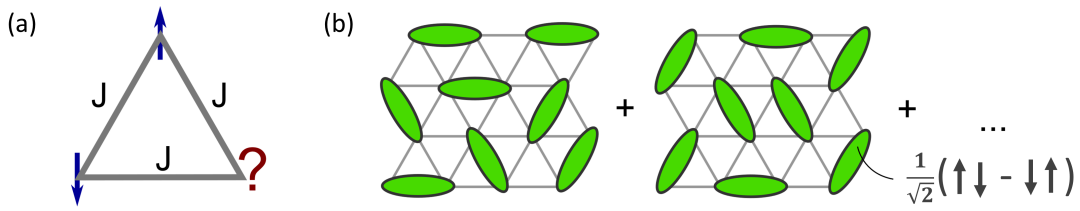

Figure 2.4. (a) Three AF Ising spins ($J > 0$) on a triangle as simplest example for magnetic frustration, because not all interactions can be satisfied simultaneously. In total, six equivalent ground states are possible. Consequently, the classical ground state is sixfold degenerated. (b) The superposition of all possible spin singlet configurations (green ellipses) forms the highly entangled QSL ground state. Following Anderson's description it is called RVB state, and the singlets fluctuate between different configurations even at 0 K [2, 31].

not necessarily only comprise neighboring spins and can have long-range character [31]. The lowest possible excitation in the RVB state is the breaking of a valence bond equivalent to flipping one single spin. This way, two unpaired spins are created, which can be separated without further energy costs and, therefore, be treated as independent quasiparticles. They both carry spin-1/2 since a single spin flip corresponds to $\Delta S = 1$. This fractionalization is a remarkable feature of those exotic quasiparticles called spinons. They are distinct from the conventional magnetic exitations (the bosonic magnons), and a key characteristic of certain QSL [31]. Besides their fascination in fundamental research, QSL might be a key for understanding high temperature superconductivity [3, 4]. Furthermore, the so-called Kitaev QSL is ideally suitable for fault-tolerant quantum computing [8]. As a result, huge efforts have been undertaken both from theoretical and experimental side for unveiling the mysteries of QSL.

In the remaining two subsections, a brief overview is presented over the spin models relevant to this work, namely the triangular and the honeycomb lattice. Both can host a QSL depending on the considered interactions.

2.2.1. Triangular Lattice

From the residual entropy of Ising spins [34] over Anderson's proposal of the RVB state [2] to unexpected magnetization plateaus or other unusual phases [35] - for many years, the triangular lattice has been subject to intriguing novel phenomena. New interest has been aroused by the discovery of $YbMgGaO_4$ six years ago. This material obtains magnetic ions on a perfect triangular lattice and does not show any magnetic order down to at least 50 mK despite a Curie-Weiss temperature of -4 K indicating strong frustration [36]. It triggered huge theoretical efforts to investigate the phase diagram of triangular lattices. Similar to many other magnetic systems, it can be described with the Heisenberg model [18]

$$\mathcal{H} = \sum_{\langle ij \rangle} J_{ij} \hat{\mathbf{S}}_i \hat{\mathbf{S}}_j \tag{2.6}$$

with the coupling constant J_{ij} between magnetic moments i and j, which are expressed by the spin operators $\hat{\mathbf{S}}_i$ and $\hat{\mathbf{S}}_j$. The summation is done over bonds $\langle ij \rangle$, and $J_{ij} > 0$ is defined as antiferromagnetic interaction[3]. Two aspects are important not to confuse here. First,

[3] Sometimes, the summation is done for each site i, j, resulting in a factor 2 for J_{ij}. Furthermore, the convention $J_{ij} < 0$ for antiferromagnetic interactions is also common.

the coupling constant J_{ij} must not be mixed up with the previously defined total angular momentum $\hat{\mathbf{J}}$ and its quantum number J. Second, the spin operators $\hat{\mathbf{S}}$ represent any angular momentum operator independent from the exact origin. Thus, it can also represent the total angular momentum $\hat{\mathbf{J}}$. In order to avoid confusion, however, the notation $\hat{\mathbf{S}}$ is preferable in this context [18]. So far, the exchange couplings are assumed to be isotropic. In a more generalized picture, Eq. 2.6 can be expressed as

$$\mathcal{H} = \sum_{\langle ij \rangle} \hat{\mathbf{S}}_i \mathbb{J}_{ij} \hat{\mathbf{S}}_j, \tag{2.7}$$

using the exchange matrix $\mathbb{J}_{ij}$, which can be split into a symmetric and an antisymmetric part, $\Gamma_{ij} = \Gamma_{ji}$ and $D_{ij} = -D_{ji}$, respectively. The latter stands for the Dzyaloshinsky-Moriya (DM) interaction, which changes sign depending on the bond direction.

$$\mathbb{J}_{ij} = \Gamma_{ij} + D_{ij} = \begin{pmatrix} J^x & \Gamma^{xy} & \Gamma^{xz} \\ \Gamma^{xy} & J^y & \Gamma^{yz} \\ \Gamma^{xz} & \Gamma^{yz} & J^z \end{pmatrix} + \begin{pmatrix} 0 & -D^z & D^y \\ D^z & 0 & -D^x \\ -D^y & D^x & 0 \end{pmatrix} \tag{2.8}$$

Due to inversion symmetry, the DM interaction is forbidden in triangular lattices [37] leaving the Hamiltonian

$$\mathcal{H} = \sum_{\langle ij \rangle} \hat{\mathbf{S}}_i \Gamma_{ij} \hat{\mathbf{S}}_j. \tag{2.9}$$

Naturally, the components of Γ_{ij} depend on the distance between spin i and j. Strictly speaking, J^x as well as all other components should have an index ij in Eq. 2.8, which is omitted for the sake of clarity. This opens an infinitively large parameter space rendering Eq. 2.9 impossible to solve in general. In many systems, however, it may be sufficient to restrict to (next) nearest neighbor interactions that strongly reduces the complexity. But even the pure nearest-neighbor Heisenberg model on the triangular lattice following from Eq. 2.6, where only one free parameter is needed, is not exactly solvable. Thus, numerical methods are required.

Up to here, lattice symmetry has been mainly ignored. For the specific case of a triangular lattice, Eq. 2.9 can be transformed by symmetry considerations explained in detail in Ref. [38] and takes the following form [7, 39],

$$\mathcal{H} = \sum_m \left[\mathcal{H}_m^{\mathrm{XXZ}} + \mathcal{H}_m^{\pm\pm} + \mathcal{H}_m^{\mathrm{z}\pm} \right]. \tag{2.10}$$

The summation index m represents interactions between nearest neighbors for $m = 1$, between next nearest neighbors for $m = 2$, etc. The first term stands for the XXZ-Hamiltonian, which is directly derived from Eq. 2.9 for $J_m^x = J_m^y \equiv J_m$ and $J_m^z = \Delta J_m$ when off-diagonal terms are neglected,

$$\mathcal{H}_m^{\mathrm{XXZ}} = J_m \sum_{\langle ij \rangle} \left(\hat{S}_i^x \hat{S}_j^x + \hat{S}_i^y \hat{S}_j^y + \Delta \hat{S}_i^z \hat{S}_j^z \right). \tag{2.11}$$

It reflects the anisotropy for the $z-$direction compared to the isotropic plane containing the triangles. The extend of that XXZ anisotropy is encoded in the parameter Δ [7]. The remaining two Hamiltonians reflect bond-dependent terms resulting from strong SOC creating highly anisotropic interactions [38],

$$\mathcal{H}_m^{\pm\pm} = \sum_{\langle ij \rangle} 2J_m^{\pm\pm} \left[\left(\hat{S}_i^x \hat{S}_j^x - \hat{S}_i^y \hat{S}_j^y \right) \cos\phi_\alpha - \left(\hat{S}_i^x \hat{S}_j^y + \hat{S}_i^y \hat{S}_j^x \right) \sin\phi_\alpha \right], \tag{2.12}$$

$$\mathcal{H}_m^{z\pm} = \sum_{\langle ij \rangle} 2J_m^{z\pm} \left[\left(\hat{S}_i^y \hat{S}_j^z - \hat{S}_i^z \hat{S}_j^y \right) \cos\phi_\alpha - \left(\hat{S}_i^x \hat{S}_j^z + \hat{S}_i^z \hat{S}_j^x \right) \sin\phi_\alpha \right]. \tag{2.13}$$

The former term represents diagonal anisotropic interactions additional to the XXZ model, while the latter describes the off-diagonal anisotropy. The bond-dependency is taken into account by the prefactor $\phi_\alpha = 0, \pm 2\pi/3$ [7, 39]. Eq. 2.10 is the most general Hamiltonian for the triangular lattice and has been extensively investigated, especially in the last years. In the isotropic case ($\Delta = 1$, $J^{\pm\pm} = J^{z\pm} = 0$) for nearest neighbors, the 120° ordered ground state is obtained [5, 6] and not the RVB state as originally proposed by Anderson. Frustration can be introduced, however, by extending this simplest model exploiting the large parameter space. QSL phases can be identified theoretically for several combinations. Including second nearest neighbors in the $J_1 - J_2$ Heisenberg model is one possibility, although the exact QSL nature is not resolved yet [40–47]. Alternatively, the anisotropic interactions $J^{\pm\pm}$ and $J^{z\pm}$ can stabilize a QSL phase as well [38, 39, 48]. It should be noted, though, that all these QSL are distinct from Anderson's originally proposed RVB scenario [7]. Nonetheless, the triangular lattice offers a fertile playground for the search of QSL. Understanding the interplay between all possible interactions is essential, and exploring the phase diagram on the triangular lattice still remains a highly active research field.

In Ch. 4, several materials with Yb^{3+} on a triangular lattice are investigated by temperature- and field-dependent thermodynamic measurements. All these examples obtain sizeable frustration, sometimes even the absence of magnetic order down to the lowest accessible temperatures. The possibility of hosting a QSL ground state is discussed in detail. For $YbMgGaO_4$, Eq. 2.10 is used for numerical calculations in order to reproduce the field-dependent magnetization.

2.2.2. Kitaev Model: Honeycomb Lattice

In the previous section, anisotropic spin interaction have already been introduced [Eq. 2.13], including the possibility of stabilizing a QSL phase. In the class of the so-called compass models, such anisotropy is pushed to the extreme limit without any isotropic part. In order to define a compass model, quantum degrees of freedom have to be arranged on a special lattice. In the following, this degree of freedom will be denoted as spin (or pseudospin) $\widehat{\mathbf{S}}$. Most importantly, only certain spin components are interacting depending on the specific bond. For the Kitaev model on the honeycomb lattice, each site obtains three bonds denoted as $\gamma = \{x, y, z\}$ in Fig. 2.5(a). The bond-dependent interactions can be summarized in the Kitaev Hamiltonian [8, 22, 49, 50]

$$\mathcal{H}_\mathrm{K} = \sum_{\langle ij \rangle_\gamma} K_\gamma \widehat{\mathbf{S}}_i^\gamma \widehat{\mathbf{S}}_j^\gamma = K \sum_{\langle ij \rangle_\gamma} \widehat{\mathbf{S}}_i^\gamma \widehat{\mathbf{S}}_j^\gamma, \tag{2.14}$$

with the summation over all bonds $\langle ij \rangle$ and the exchange coupling K. The latter may depend on the bond γ, but it is often considered as a constant. The convention without minus sign is chosen here, and $K < 0$ implies FM interaction [22]. In the notation of Eq. 2.7 and Eq. 2.8, this corresponds to the absence of DM interaction, $D_{ij} = 0$, and non-zero elements for Γ_{ij} only on the diagonal with $\Gamma_{ij} = \mathrm{diag}(K_x, 0, 0)$ on an X-bond, $\Gamma_{ij} = \mathrm{diag}(0, K_y, 0)$ on a Y-bond, and $\Gamma_{ij} = \mathrm{diag}(0, 0, K_z)$ on a Z-bond. Eq. 2.14 reveals that nearest-neighbor spins experience Ising interactions. The easy axis, however, depends on the bond. For minimizing the energy for X-bonds, the spins require an alignment perpendicular to that bond. At the same time, Y- and Z-bonds have the same condition, which cannot be satisfied simultaneously

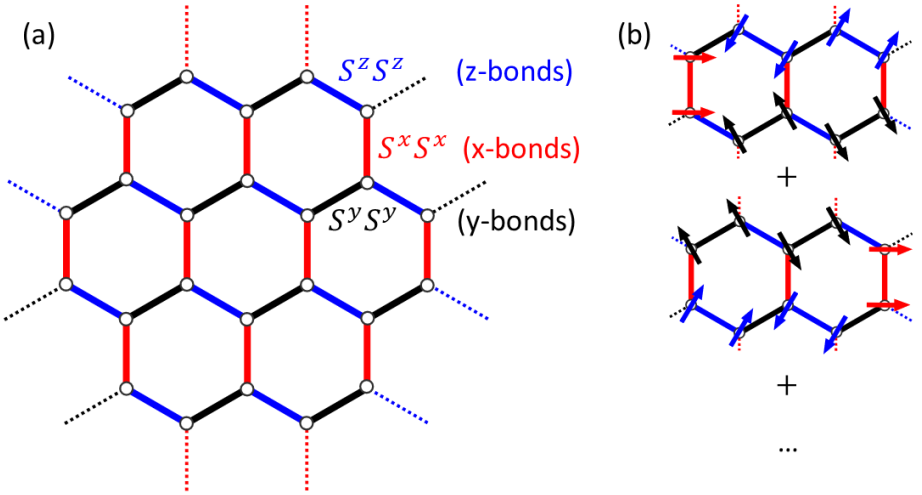

Figure 2.5. (a) Definition of Kitaev interactions on a honeycomb lattice from Ref. [22]. Each (x,y,z)-bond reveals an orthogonal Ising easy axis, respectively. As a consequence, only 1/3 of all bond interactions can be satisfied simultaneously. (b) Possible ground state configurations following Ref. [50], underlining the strong frustration. For quantum systems, in a simple picture, the ground state can be understood as a superposition of all spin configurations, forming an entangled QSL state.

and is illustrated in Fig. 2.5(b) [50]. Consequently, strong frustration arises, and Kitaev could show that the ground state of Eq. 2.14 is indeed a QSL, which is often referred to as Kitaev Spin Liquid (KSL) [8]. A peculiarity of the Kitaev model is that it is a rare example of an exactly solvable spin model [51]. Kitaev found further evidence that this specific QSL is potentially ideally suitable for fault-tolerant quantum computing due to the emergence of Majorana fermions with special topologocial properties [8, 52]. As a result, huge efforts have been undertaken to design materials hosting such QSL.

In 2009, Jackeli and Khalliulin [21] suggested a possible realization of Kitaev's model in transition metal (TM) oxides. They investigated TM in an octahedral environment resulting in a level splitting by the CEF [Sec. 2.1.2]. For heavy TM like the 4d and 5d elements, SOC becomes crucially important,

$$\mathcal{H}_{\mathrm{SO}} = \lambda \hat{\mathbf{L}}\hat{\mathbf{S}}, \tag{2.15}$$

because the SOC constant λ strongly increases towards larger atomic numbers Z [16]. Accordingly, the t_{2g} levels further split into a lower $j_{\mathrm{eff}} = 3/2$ doublet and a higher $j_{\mathrm{eff}} = 1/2$ singlet [22]. For the d^5 configuration illustrated in Fig. 2.6(a), the $j_{\mathrm{eff}} = 1/2$ singlet carries a single hole. If the on-site repulsion is strong (limit of large Hubbard U), each d^5 ion has one localized hole in the $j_{\mathrm{eff}} = 1/2$ state [22]. That gives rise to local effective spin-1/2 magnetic moments denoted as pseudo- or isospins [Fig. 2.6(b)] [21].

In a solid, beyond the single ion physics, these isospins interact, which is expected to be highly anisotropic due to the influence of SOC [37]. As already mentioned above, the way to the pure Kitaev model is paved by setting all elements of the exchange matrix $\mathbb{J}_{ij}$ from Eq. 2.8 to zero except of bond-dependent diagonal elements. Such peculiar situation can be engineered by taking advantage of d^5 ions in edge-sharing octahedral environment. When restricting to NN interactions, the DM interaction is symmetrically forbidden. The TM ions are connected via Ligand (L) ions. In the ideal case of 90° between TM-L-TM,

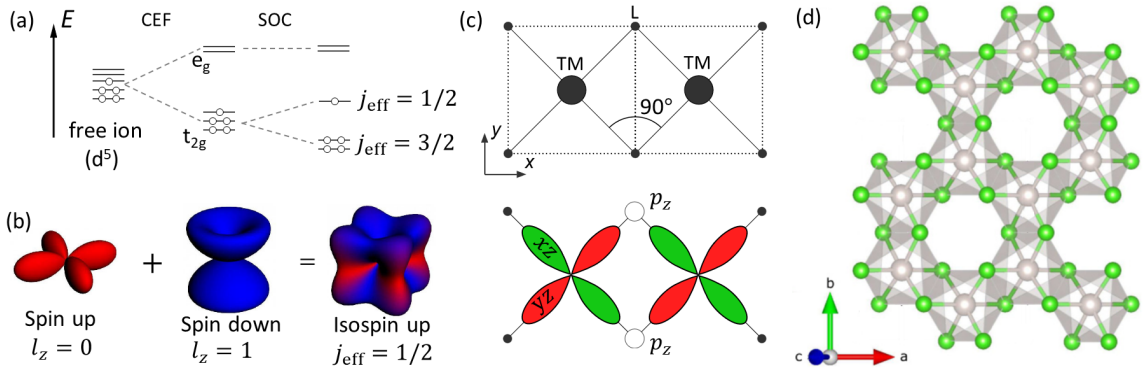

Figure 2.6. (a) Lifting of the five-fold degenerated d^5 state by an octahedral CEF combined with SOC. In the limit of large Hubbard U, a hole is localized in the $j_{\text{eff}} = 1/2$ state. This effective isospin (or pseudospin) determines the ground state properties [21, 22]. (b) Real space illustration of the $j_{\text{eff}} = 1/2$ isospin up state with its uncommon shape. The resulting interactions between such isospins are highly anisotropic. (c) Sketch of edge-sharing octahedra with the d^5 transition metal (TM) and surrounding ligands (L). Two possible hopping pathways TM-L-TM exist via the upper and lower p_z ligand orbitals. For ideal 90° angles, the isotropic part cancels out. The anisotropic part is exactly the Kitaev interaction. Panels (b,c) adapted from Ref. [21]. (d) Honeycomb structure in α-$RuCl_3$ with Ru (Cl) in grey (green), adapted from Ref. [27].

two dominant electron hopping paths are expected for a given bond. In Fig. 2.6(c), the only active orbitals together with the p_z-orbital are projected onto the xy-plane. In the ideal 90° configuration, the isotropic part of the Hamiltonian is completely suppressed, and only anisotropic interactions survive [21]. That part exhibit bond-dependent Ising axes, which is in exact analogy to the Kitaev model from Eq. 2.14. Jackeli's and Khalliulin's discovery triggered enormous interest into the synthesis of new heavy TM compounds with d^5 ions arranged on a honeycomb lattice like in Fig. 2.6(d) for α-$RuCl_3$. As first promising results, the 2D honeycomb iridates Na_2IrO_3 [53] and later α-Li_2IrO_3 [54] have been synthesized which show inherent Kitaev interactions [55, 56], as well as the up-to-date most promising Kitaev candidate material α-$RuCl_3$ [23, 57, 58]. The same holds true for the 3D honeycomb materials β-/γ-Li_2IrO_3 [59].

All these materials, however, show a magnetically ordered ground state due to interactions beyond the Kitaev model, which is inevitable in real materials. Several mechanisms may prevent the idealized Jackeli-Khalliulin configuration. Other hopping paths such as direct TM-TM hopping cannot be completely suppressed in general. Furthermore, the e_g-orbitals are ignored, and local distortions of the octahedral environment or deviations from the 90° angle in TM-L-TM bonds act against the assumptions of Jackeli and Khalliulin. Moreover, couplings between NNN and beyond cannot be avoided, which can symmetrically allow DM interactions. Altogether, the Hamiltonian in real materials has to be extended beyond the pure Kitaev model. As a result, the quest for a real-world KSL remains fairly challenging and has not been successful from the experimental side so far. Nevertheless, Kitaev interactions are present, and sometimes even dominating, in all of the above mentioned materials [22]. For each system, the complex ground state Hamiltonian has to be explored on its own by combining all results from both experimental and theoretical side. Both research fields often cross fertilize each other in this context. Progress will certainly be achieved in the next years, yet finding materials with pure Kitaev interactions probably remains an unfeasible task.

In Ch. 5, low-temperature thermodynamic measurements on the Kitaev candidate material α-$RuCl_3$ are presented. This material is vividly debated due to the discovery of a half-quantized thermal Hall conductivity [13, 60, 61]. Generally, this is considered to be a strong evidence for the celebrated KSL and, thus, of Majorana fermions in α-$RuCl_3$. In this work, the magnetic field dependence of α-$RuCl_3$ is explored inside the ordered state and beyond the phase transition through the putative QSL state. The experimental data are used to establish the phase diagram of α-$RuCl_3$ and discussed in the context of Refs. [13, 60–62].

2.3. Thermodynamic Relations

The focus of this work is on thermodynamic measurements in the millikelvin range. Consequently, it is important to repeat some thermodynamic basics. They are crucial to understand the definition of the heat capacity, its link to the entropy, as well as the derivation of some Maxwell relations for the Grüneisen parameter. In the following, only reversible processes are considered.

One of the fundamental aspects is the first law of thermodynamics. In a closed system (particle number N constant), the thermodynamical potential of the internal energy U can only be changed by the exchange of the heat δQ or the work δW with its surrounding [63],

$$\mathrm{d}U = \delta Q + \delta W. \tag{2.16}$$

The convention is chosen here that positive δQ (or δW) increases the internal energy, whereas negative δQ (or δW) results in a decreasing internal energy. In other words, $\delta Q > 0$ is equivalent to a heat transfer *into* the system, and $\delta W > 0$ means that the *surrounding does work on* the system. The heat δQ is directly connected to the entropy change $\mathrm{d}S$,

$$\delta Q = T\mathrm{d}S. \tag{2.17}$$

There are various expressions possible for the work δW. Volume work changes the pressure p and the volume V of the system. Magnetic work depends on the total magnetic moment m (unit: $\mathrm{A\,m^2} = \mathrm{J\,T^{-1}}$) and the magnetic field B. In analogy, electric work depends on the total electrical moment and the electrical field, but does not play a role here. First, the volume work is discussed. A system with a pressure p can perform work by changing its volume V. If it expands ($\mathrm{d}V > 0$), the system does work on its surrounding reducing the internal energy of the system ($\delta W_{\mathrm{Vol}} < 0$), and vice versa if the volume shrinks. Consequently, $\delta W = -p\mathrm{d}V$, and the first law of thermodynamics can be rewritten as

$$\mathrm{d}U = T\mathrm{d}S - p\mathrm{d}V. \tag{2.18}$$

The internal energy $U = U(S, V)$ is here a function of its natural variables entropy S and volume V. Via Legendre transformation, more thermodynamic potentials can be derived [63, 64]. Besides the Gibbs energy G and the enthalpy H, an important example is the Helmholtz free energy $F = F(T, V)$, which is transformed from the internal energy via $F = U - TS$ and that has the following differential form,

$$\mathrm{d}F = -S\mathrm{d}T - p\mathrm{d}V. \tag{2.19}$$

The definitions of $\mathrm{d}U$, $\mathrm{d}F$, $\mathrm{d}G$, and $\mathrm{d}H$ can be used to derive the so-called Maxwell relations [65]. A convenient mnemonic for these relations are shown in Fig. 2.7(a). Each

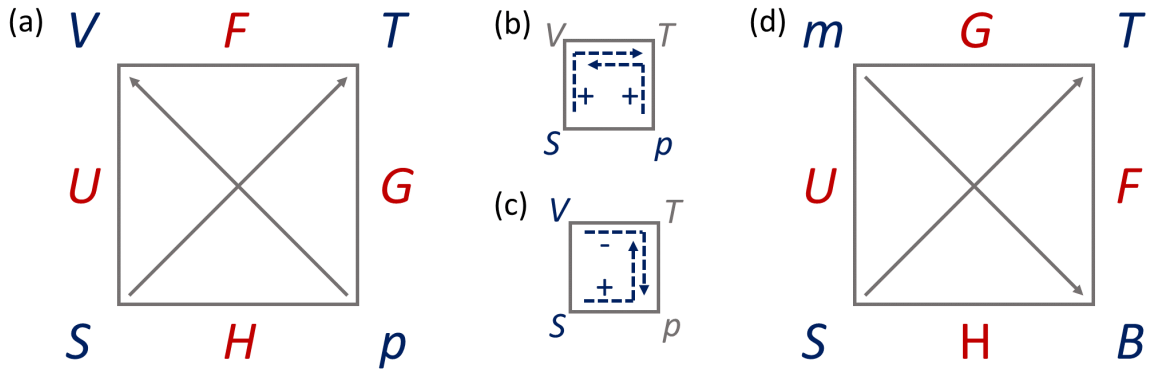

Figure 2.7. Thermodynamic square as a mnemonic for deriving the Maxwell relations adapted from Ref. [64]. (a) $\delta W = -p\mathrm{d}V$ neglecting magnetic field B and magnetic moment m. (b,c) Derivation of the Maxwell relations in Eqs. 2.20 and 2.21. (d) $\delta W = -m\mathrm{d}B$ keeping the volume V and pressure p constant.

thermodynamic potential (U, F, G, H) is shown in red, and the corners next to them show their natural variables (V, T, p, S), respectively. This "thermodynamic square" can also be used to derive the differential forms of the thermodynamical potentials such as Eq. 2.18 and Eq. 2.19 which will not be discussed here[4]. The Maxwell relations are formed in the following way. First, two neighboring natural variables have to be chosen, for example S and p in Fig. 2.7(b). Next, their derivative is formed following the dotted arrow, $\partial S/\partial V$ and $\partial p/\partial T$, and its ending denotes the constant variable. The sign of each expression, respectively, depends on the arrows in the square of Fig. 2.7(a). If it connects the starting and the ending point of the dotted arrow in Fig. 2.7(b), a positive sign has to be chosen. This way, the following relation is found,

$$+\left(\frac{\partial S}{\partial V}\right)_T = +\left(\frac{\partial p}{\partial T}\right)_V. \tag{2.20}$$

Another example is shown in Fig. 2.7(c) using the neighboring natural variables S and V. Following the dotted arrow results in

$$+\left(\frac{\partial S}{\partial p}\right)_T = -\left(\frac{\partial V}{\partial T}\right)_p. \tag{2.21}$$

The two other possible relations can be found elsewhere [65]. As soon as magnetic moments are allowed in the thermodynamic system, another possibility for doing work needs to be introduced, $\delta W_{\mathrm{mag}} = B\mathrm{d}m$ [63, 64]. Therefore, the first law of thermodynamics is expanded,

$$\mathrm{d}U = T\mathrm{d}S - p\mathrm{d}V + B\mathrm{d}m. \tag{2.22}$$

The Legendre transformation for the Helmholtz free energy takes the form $F = U - TS - mB$ resulting in

$$\mathrm{d}F = -S\mathrm{d}T - p\mathrm{d}V - m\mathrm{d}B. \tag{2.23}$$

As a consequence, more Maxwell relations become possible, and a new thermodynamic square has to be drawn [Fig. 2.7(d)]. Note that the potentials are rearranged and that the arrows

[4] For further information, please refer to Ref. [64].

point into a different direction. Moreover, pressure p and volume V need to be kept constant. Following the same procedure explained above, the relation

$$\left(\frac{\partial S}{\partial B}\right)_T = \left(\frac{\partial m}{\partial T}\right)_p \tag{2.24}$$

is found [64], which will be helpful in Sec. 2.5, where the magnetic Grüneisen parameter is discussed. Many other important connections between measured quantities, such as the heat capacity, and thermodynamic potentials and variables can be derived. Those relevant to this work will be discussed in the following sections.

2.4. Specific Heat

The specific heat C of a material is an important quantity in order to understand the underlying physics. It consists of several contributions from e. g. phonons or conduction electrons (see following chapters) and is very often used as a standard measurement to identify transitions like magnetic ordering or superconducting transitions. Furthermore, the temperature or field dependence $C(T)$ and $C(B)$, respectively, are very useful as input for new theoretical models as well as a benchmark of existing ones. In the following sections, a detailed description of the specific heat with its possible contributions are presented, following mainly Refs. [24, 66].

2.4.1. Definition of Heat Capacity and Specific Heat

The heat capacity of a system describes how much heat δQ is needed to increase the system temperature by dT. The heat capacity is defined as

$$C_x = \left(\frac{\delta Q}{\mathrm{d}T}\right)_x, \tag{2.25}$$

where x are state variables that are kept constant. Relevant variables are, for example, the volume V, the pressure p or the magnetic field B. Consequently, two different heat capacities can be defined in a non-magnetic system where the magnetization and the magnetic field can be ignored. In combination with the first law of thermodynamics Eq. 2.18, the following expressions can be derived [63],

$$C_V = \left(\frac{\delta Q}{\mathrm{d}T}\right)_V = \left(\frac{\partial U}{\partial T}\right)_V, \; C_p = \left(\frac{\delta Q}{\mathrm{d}T}\right)_p = \left(\frac{\partial U}{\partial T}\right)_V + \left[\left(\frac{\partial U}{\partial V}\right)_T + p\right]\left(\frac{\partial V}{\partial T}\right)_p. \tag{2.26}$$

Both expressions look similar except of the additional terms in C_p. It can be shown that C_p and C_V are linked by the volume expansion coefficient α at constant pressure and the isothermal compressibility κ_T [64–66],

$$C_\mathrm{p} - C_\mathrm{V} = \frac{\alpha^2}{\kappa_T} VT, \; \alpha = \frac{1}{V}\left(\frac{\partial V}{\partial T}\right)_p, \; \kappa_T = -\frac{1}{V}\left(\frac{\partial V}{\partial p}\right)_T. \tag{2.27}$$

In this work, the heat capacity measurement is performed at constant pressure, not at constant volume. While it is essential to distinguish C_p and C_V in gases, the difference becomes negligible in solids, especially at temperatures below 30 K. Therefore, C_p and C_V can be considered equal in this thesis [66, 67]. In analogy, the heat capacity in magnetic systems can

be expressed either at constant magnetization, C_M, or magnetic field, C_B, respectively [19, 64]. This will not be further discussed here. From experimental side, it is only possible to perform measurements at constant magnetic field B and pressure p. Due to the discussed assumptions above, C_B and C_p will not be explicitly distinguished anymore in the following,

$$C_B = C_p = \left(\frac{\delta Q}{\mathrm{d}T}\right)_{B,p} \approx T\left(\frac{\partial S}{\partial T}\right)_{B,p}. \tag{2.28}$$

To better compare the heat capacity of different samples, the absolute values are usually normalized and thereafter called specific heat. In this thesis, the normalization is in respect to the molar number n resulting in the unit $\mathrm{J\,K^{-1}\,mol^{-1}}$,

$$C_{\mathrm{p,mol}} = \frac{C_{\mathrm{p}}}{n} = \frac{C_{\mathrm{p}}}{m}M. \tag{2.29}$$

Here, m and M denote the mass and the molar mass, respectively. In the experimental part, most measured specific heat data have been normalized according to Eq. 2.29 unless explicitly stated differently, and the subscript *mol* is omitted in general.

The definition of the heat capacity in Eq. 2.25 is just phenomenological so far. It only quantifies the amount of energy that the system can absorb in a certain temperature window. This is defined by the possible *excitations* that contribute to the internal energy U of the system. The excitations may be completely different in their origin, like phonons, conduction electrons or magnons, but they sum up to the total heat capacity of the specific material. Therefore, the heat capacity is a powerful instrument to identify possible excitations, especially when the temperature dependence is known. An important contribution in metals, for example, are the conduction electrons which can be treated as Fermi gas with the heat capacity depending linearly on the temperature [24],

$$C_{V,\mathrm{el}} = \gamma T. \tag{2.30}$$

In this work, the electronic contribution does not play a role because all investigated materials are insulators. More important are the ubiquitous excitations of the lattice, better known as phonons, that will be shortly summarized in the following section.

2.4.2. Lattice Contribution (Phonons)

The specific heat of the lattice vibrations at low temperatures was already subject of intense discussions more than 100 years ago. In 1907, Einstein provided an explanation for its decrease upon cooling but failed regarding a correct low-temperature expansion [24]. Some years later, the Debye model significantly improved the understanding of the phononic contribution. Similar to Einstein, Debye considered the atoms of a solid as quantum mechanical oscillators. In his model, however, these oscillators are coupled, which results in a frequency dispersion that is not constant. The dispersion is approximated by $\omega(q) = vq$ with the sound velocity v and the wave vector q. To avoid infinite frequencies causing divergent density of states, the Debye frequency ω_{D} is introduced as cut-off, $\omega < \omega_{\mathrm{D}}$, which is determined by the number of atoms N in the solid [24]. These assumptions can be used to calculate the heat capacity of the phonons in solids with one atomic species,

$$C_{\mathrm{V}} = \left(\frac{\partial U}{\partial T}\right)_V = 9Nk_{\mathrm{B}}\left(\frac{T}{\Theta_{\mathrm{D}}}\right)^3 \int_0^{x_{\mathrm{D}}} \frac{x^4 \exp(x)}{(\exp(x)-1)^2}\mathrm{d}x, \tag{2.31}$$

with $x = \hbar\omega/k_\mathrm{B}T$ and $x_\mathrm{D} = \hbar\omega_\mathrm{D}/k_\mathrm{B}T$. Moreover, the famous Debye temperature Θ_D has been introduced, $k_\mathrm{B}\Theta_\mathrm{D} = \hbar\omega_\mathrm{D}$, with the Boltzmann constant k_B and the Planck constant $\hbar$. The Debye temperature depends on the material and defines relevant temperature scales. For high temperatures, $T \gg \Theta_\mathrm{D}$, Eq. 2.31 reduces to

$$C_\mathrm{V} = 3Nk_\mathrm{B},\ C_{V,\mathrm{mol}} = 3N_\mathrm{A}k_\mathrm{B} = 3R \tag{2.32}$$

with the gas constant R. This is equivalent to the Dulong-Petit law, the classical result for the specific heat of solids [24]. In the low-temperature limit $T \ll \Theta_\mathrm{D}$, the heat capacity can be determined as

$$C_\mathrm{V} \sim \left(\frac{T}{\Theta_\mathrm{D}}\right)^3. \tag{2.33}$$

Indeed, the experimental data of solids can be described extremely well by this cubic temperature dependence. Typical values for the Debye temperature are in the order of some $\sim 100\,\mathrm{K}$, strongly depending on the material [24]. According to Eq. 2.33, the phononic contribution vanishes rapidly towards lowest temperatures. Since the relevant temperature ranges are mainly below 2 K in this work, the phonons only play a minor role in most investigated materials.

2.4.3. Schottky Anomaly of the Two-Level System: Relevance to the Nuclear Contribution C_nuc

Another possibility to absorb energy is the two-level system indicated in the inset of Fig. 2.8(a). Here, the energy gap is given as $\Delta = E_\mathrm{gap}/k_\mathrm{B}$ in units of Kelvin. If N noninteracting and nondegenerate two-level systems are considered, the specific heat per mole can be calculated with the following formula [19],

$$C_\mathrm{V} = Nk_\mathrm{B}\left(\frac{\Delta}{T}\right)^2 \frac{\exp\left(\frac{\Delta}{T}\right)}{\left[\exp\left(\frac{\Delta}{T}\right)+1\right]^2}. \tag{2.34}$$

This contribution to the heat capacity is called Schottky anomaly and plotted normalized per mole in Fig. 2.8(a) for a gap of $\Delta = 1\,\mathrm{K}$ and a logarithmic temperature scale. At very low temperatures, $T \ll \Delta$, the thermal energy is too small to excite the system, and the specific heat vanishes towards zero exponentially[5]. As soon as the temperature becomes comparable to the energy gap, transitions to the excited state are possible increasing the internal energy. Therefore, the specific heat starts to grow quickly and, eventually, forms a broad peak at $T \sim 0.42\Delta$. In the limit of $T \gg \Delta$, the ground and the excited state become equally populated, and the system cannot absorb energy anymore. Consequently, the specific heat has to decrease and follows a power law behavior,

$$C_\mathrm{V} \sim \frac{1}{T^2}, \tag{2.35}$$

for temperature high enough above the enery gap Δ. The expression for multilevel systems becomes more complicated to calculate, but the resulting specific heat curve looks similar compared to the more simple two-level system [19]. Another important fact is the entropy related to the Schottky anomaly. For the two-level system, it approaches $R\ln(2)$ per mole

[5] To be more precise, there exists also a temperature-dependent prefactor $(\Delta/T)^2$ indicated in Fig. 2.8(a).

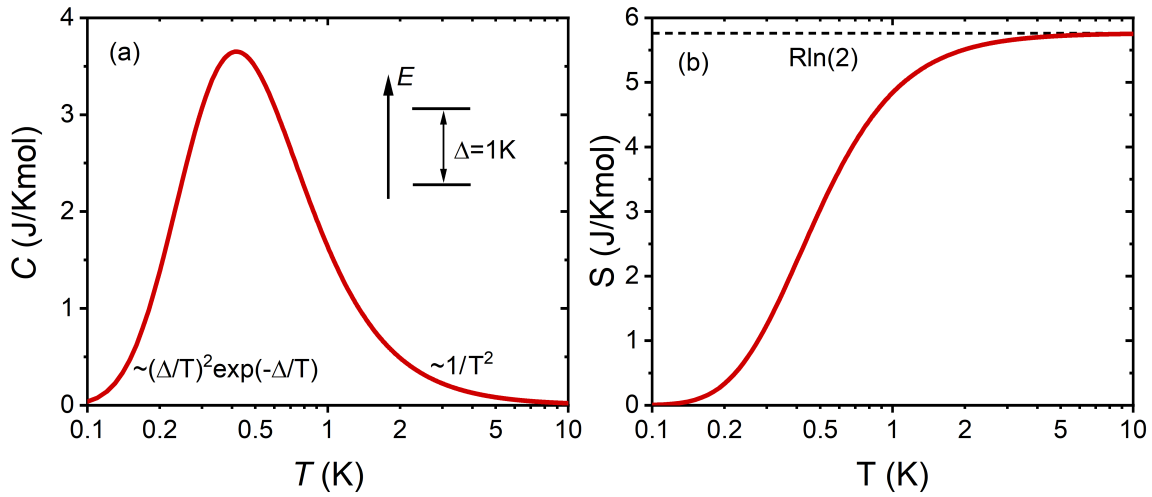

Figure 2.8. (a) Schottky anomaly in the specific heat of a two-level system with an energy gap of $\Delta = 1\,\mathrm{K}$. The maximum is located at $T \sim 0.42\Delta$. The high-temperature part shows a $1/T^2$ dependece, whereas the increase for $T \ll \Delta$ goes, in principle, exponentially. (b) Entropy related to the Schottky anomaly. At high temperatures, $T \gg \Delta$, the entropy approaches $R\ln(2)$.

in the high-temperature limit [Fig. 2.8(b)]. A more detailed interpretation of the expected entropy values is presented in Sec. 2.6.

Interestingly, the physical origin of the two- or multilevel system does not influence Eq. 2.34. The only relevant quantity is the level splitting encoded in Δ. One example are the energy levels resulting from CEF splitting, but they do not play a role in this work because, in general, $\Delta_{\mathrm{CEF}} \gg 10\,\mathrm{K}$. The energy gap to the first excited CEF level in $NaYbO_2$, for example, is as large as $\sim$400 K [68], and even larger in $YbMgGaO_4$ [69]. Nevertheless, the Schottky anomaly sometimes becomes important in the sub-Kelvin range. As already mentioned in Sec. 2.1.1, the atomic nuclei can carry a nuclear moment, which is much smaller than the moments of the electrons and, thus, usually neglectable. For the specific heat, however, the nuclei may become important because there are at least two degenerate levels if a nuclear magnetic moment exists. This degeneracy is lifted by internal or external magnetic fields, which results in a Schottky anomaly. Another possible level splitting without magnetic field can appear if a nuclear electric quadrupolar moment interacts with internal electric field-gradients. In most cases, the nuclear splitting Δ is fairly small, and the Schottky peak appears at very low temperature below 10 mK [19]. The high temperature tail with its $1/T^2$ behavior, however, can still be measurable up to several 100 mK. This work focuses on measurements in the millikelvin range, and evidence for a nuclear Schottky anomaly has been found, for example, in $KYbS_2$ and $NaYbO_2$ [Ch. 4]. Unless otherwise stated, it is not explicitly distinguished between quadrupolar and nuclear magnetic contribution because they show the same $1/T^2$ evolution. In the following, they are both referred to as *nuclear contribution* with the specific heat

$$C_{\mathrm{nuc}} = \frac{\alpha}{T^2}. \tag{2.36}$$

The parameter α is a measure of the overall nuclear level splitting. In principle, it can be used to obtain information about the internal magnetic field at the nucleus position, which is produced by the magnetization of the atom.

2.4.4. Magnetic Contribution C_m

As soon as the electrons of a material carry a magnetic moment, new excitations may arise. Naturally, they contribute to the specific heat as well, and their temperature dependence strongly depends on the specific scenario. Some standard examples are shortly introduced here together with several relevant examples in frustrated magnets.

The specific heat of insulating materials can be expressed by the sum of the following contributions,

$$C = C_\mathrm{lat} + C_\mathrm{nuc} + C_\mathrm{m}. \tag{2.37}$$

In materials with magnetic ordering, the spin waves are the elementary excitations with its already mentioned quasiparticle, the magnon [19]. In 3D ferromagnets, linear spin wave theory results in $C_m \sim T^{3/2}$ far below the ordering temperature [19]. Antiferromagnetically ordered magnets are expected to show $C_m \sim T^3$ in 3D [19] and $C_m \sim T^2$ in 2D [70, 71], respectively. So far, these are **gapless** excitations with a characteristic power law behavior. There are also **gapped** exitations possible when an excitation gap Δ appears in the energy spectrum. In this case, the specific heat follows an exponential behavior, $C_m \sim e^{-\Delta/T}$. In general, the exact form can be more complicated including a temperature dependent prefactor, as can be seen in Ref. [72] in the case of a 2D gapped AF. In the end, the exact formula depends on the specific magnon dispersion. It is noted in passing that the low-temperature evolution of the gapped two-level system described in Eq. 2.34 also shows the exponential form in the specific heat.

Additionally to the ordered states, there is an abundance of possible spin liquid ground states that has been theoretically discovered [31], which potentially show a different evolution of the specific heat. Here, magnons are not relevant anymore because of the lacking magnetic order. One prominent example are QSL with a spinon Fermi surface in analogy to the electronic Fermi surface in metals. Thus, spin liquids with spinon excitations should have a magnetic specific heat linear in temperature, $C_m \sim T$ [73, 74]. However, corrections to the spinon Fermi surface can lead to a sublinear behavior, $C_m \sim T^{2/3}$ [75]. Another type of spin liquid are the so-called Dirac QSL, where a quadratic evolution can be expected, $C_m \sim T^2$ [76]. On the other hand, this can be easily confused with conventional spin glasses with frozen spins, where a quadratic behavior can be found as well $C_m \sim T^2$ [77, 78].

In summary, there is no simple uniform expression for the magnetic contribution in the specific heat. It strongly depends on the system of interest, and the interpretation may easily lead to confusion. Nevertheless, the heat capacity is a powerful method to benchmark the expected physics in all materials, as long as it can be trustably separated from other emerging contributions. The latter will be a central aspect in Ch. 4 in the discussion of $KYbS_2$ and $NaYbO_2$.

2.5. Magnetic Grüneisen Parameter Γ_mag

The Grüneisen parameter, or Grüneisen ratio, Γ_λ has been widely used for the investigation of quantum critical points (QCP) [79–81], where the Grüneisen parameter is predicted to show universal divergent behavior [82]. At the QCP, an external control parameter λ suppresses the transition temperature of a system to zero [83]. This can be done, for example, by applying pressure or a magnetic field. Consequently, it is essential to distinguish between the structural and the magnetic Grüneisen parameter, Γ_struc and Γ_mag, respectively. The structural Grüneisen parameter is often simply denoted as Γ whereas the magnetic Grüneisen

parameter can be also found as Γ_B or Γ_H. They are defined in the following and very similar way [83],

$$\Gamma_{\mathrm{struc}} = -\frac{1}{VT}\frac{(\partial S/\partial p)_T}{(\partial S/\partial T)_p}, \tag{2.38}$$

$$\Gamma_{\mathrm{mag}} = -\frac{1}{T}\frac{(\partial S/\partial B)_T}{(\partial S/\partial T)_B}. \tag{2.39}$$

Both contain the derivative of the entropy in respect to the control parameter λ as well as its temperature derivative. In this work, several materials have been intensively investigated in magnetic fields. Consequently, the magnetic Grüneisen parameter can be a valuable tool to track the field-evolution of these systems and is discussed in the rest of this section.

The definition of the magnetic Grüneisen parameter in Eq. 2.39 can be transformed into a less abstract form using Eq. 2.28,

$$\Gamma_{\mathrm{mag}} = -\frac{(\partial S/\partial B)_T}{C_B}, \tag{2.40}$$

and the Maxwell relation in Eq. 2.24,

$$\Gamma_{\mathrm{mag}} = -\frac{(\partial m/\partial T)_B}{C_B} = -\frac{V(\partial M_{\mathrm{vol}}/\partial T)_B}{C_B} = -\frac{(\partial M_{\mathrm{mol}}/\partial T)_B}{C_{B,\mathrm{mol}}}. \tag{2.41}$$

This provides experimental access to the magnetic Grüneisen ratio by measuring the specific heat and the temperature-dependent magnetization to calculate its temperature derivative. On the other hand, this requires two measurements with different setups, which takes a lot of time. Additionally, magnetization measurements at very low temperature are fairly challenging. Thus, a more direct route to the magnetic Grüneisen parameter is highly required. Indeed, Eq. 2.39 can be rewritten using the following identity [64, 83],

$$\left(\frac{\partial X}{\partial Y}\right)_Z = -\frac{(\partial Z/\partial Y)_X}{(\partial Z/\partial X)_Y} \;\Rightarrow\; \Gamma_{\mathrm{mag}} = \frac{1}{T}\left(\frac{\partial T}{\partial B}\right)_S. \tag{2.42}$$

The temperature change induced by a magnetic field with constant entropy is the adiabatic magnetocaloric effect. Using an alternating-field method described in Sec. 3.5, this is the easiest and most accurate way to measure the magnetic Grüneisen parameter, which is even possible at very low temperatures far below 100 mK [83].

The field-dependence of the magnetic Grüneisen parameter is ideally suitable to detect field-induced 2$^{\mathrm{nd}}$ order phase transitions, where entropy is accumulated resulting in a maximum in $S(B)$. Consequently, the entropy derivative with respect to the field, $\partial S/\partial B$, becomes zero at the critical field. From Eq. 2.40, it becomes evident that the magnetic Grüneisen parameter $\Gamma_{\mathrm{mag}}(B)$ requires a sharp sign change from negative to positive at the transition field because $C_B > 0$ for all fields [84].

Furthermore, $\Gamma_{\mathrm{mag}}(B)$ might show a maximum at a 1$^{\mathrm{st}}$ order transition when the entropy shows a downwards step, equivalent to a large value of $\partial S/\partial B$. This interpretation, however, is much more complicated than a clear and abrupt sign change because the magnetic Grüneisen parameter includes two different quantities, the heat capacity C_B and the derivative of the magnetization, $\partial M/\partial T$. If there are, for example, several field-dependent contributions in the heat capacity, this might result in anomalies in the Grüneisen parameter that are difficult to interprete. Similar problems may arise in the magnetization because even small amounts of impurities can strongly influence the magnetization and, thus, its derivative. This is the same reason why the temperature-dependence of the magnetic Grüneisen ratio, $\Gamma_{\mathrm{mag}}(T)$, is sometimes difficult to analyse and understand. In this work, only field-dependent measurements of Γ_{mag} are presented to follow the field evolution of several QSL candidates.

2.6. Entropy

In the short part about thermodynamics, the entropy has already been mentioned several times due to its connection to a heat flux into (or out of) a macroscopic system. A different approach to determine the entropy comes from statistical physics using a microscopic picture such as the previously discussed two-level system [Sec. 2.4]. For this purpose, some terms have to be introduced first. A closed system, as discussed in Sec. 2.3, is called canonical ensemble. The system is in contact to a thermal bath and, thus, can exchange energy. The canonical partition function is defined in the following way [85],

$$Z_\mathrm{c} = \sum_n \exp\left(-\frac{E_\mathrm{n}}{k_\mathrm{B}T}\right). \tag{2.43}$$

The thermodynamical potential of the (Helmholtz) free energy F is directly connected to the canonical partition function [85],

$$F = -k_\mathrm{B}T\ln(Z_\mathrm{c}). \tag{2.44}$$

This allows to calculate the entropy in the canonical ensemble [85],

$$S = -\frac{\partial F}{\partial T} = k_\mathrm{B}\ln(Z_\mathrm{c}) + k_\mathrm{B}T\frac{\partial}{\partial T}\ln(Z_\mathrm{c}). \tag{2.45}$$

Now, the aforementioned two-level system is shortly revisited. It shall be defined that the ground state and the excited level have the energy of zero and E, respectively. In this case, the partition function takes the following form,

$$Z_\mathrm{c} = 1 + \exp\left(-\frac{E}{k_\mathrm{B}T}\right). \tag{2.46}$$

For N independendent two-level systems, the entropy after normalization by the molar number $n = N/N_\mathrm{A}$ turns out to be

$$S_\text{2-Lvl} = k_\mathrm{B}\left\{\ln\left[1+\exp\left(-\frac{E}{k_\mathrm{B}T}\right)\right] + \left(\frac{E}{T}\right)\frac{\exp\left(-E/k_\mathrm{B}T\right)}{1+\exp\left(-E/k_\mathrm{B}T\right)}\right\}. \tag{2.47}$$

This is equivalent to the curve in Fig. 2.8(b). The high temperature-limit of Eq. 2.47 can be easily calculated and results in

$$\lim_{T\to\infty} S_\text{2-Lvl} = R\ln(2), \tag{2.48}$$

as already shown graphically in Fig. 2.8(b). This observation can be generalized for multilevel systems. Each new level i contributes to the partition function with an additional term $\exp\left(-E_i/k_\mathrm{B}T\right)$. In the limit of $T\to\infty$, the only remaining part of the entropy of a n-level system is again the logarithmic term,

$$\lim_{T\to\infty} S_\text{n-Lvl} = R\ln(n). \tag{2.49}$$

From a physical point of view, this result can be used to draw conclusions on the ground state of a magnetic system. If its effective spin has the value of $J_\mathrm{eff} = \frac{1}{2}, 1, \frac{3}{2}, \ldots$ and the degeneracy in m_J is lifted, for example by a magnetic field, a two/three/four/...-level system

is created. Consequently, the expected molar entropy released at high temperatures can be easily calculated by

$$\lim_{T\to\infty} S = R\ln(2J_{\mathrm{eff}}+1), \tag{2.50}$$

which will become especially important in Sec. 4.3. Despite its importance, there is unfortunately no direct possibility to measure the entropy. On the other hand, it is connected to measurable parameters. One prominent example is the specific heat from the previous section directly using Eq. 2.25 with $\delta Q = T\mathrm{d}S$,

$$C_x = T\left(\frac{\partial S}{\partial T}\right)_x. \tag{2.51}$$

This provides direct access to the entropy $S(T)$ from the measurement of the specific heat by integrating $C_x(T)/T$,

$$S = \int_0^T \frac{C_x}{T'}\mathrm{d}T'. \tag{2.52}$$

It is advisable to collect heat capacity data at temperatures as low as possible to come close to the starting condition of the integral $T_0 = 0\,\mathrm{K}$. Moreover, it is important to distinguish between different contributions in the heat capacity. The nuclear contribution, for example, leads to an increase of the heat capacity towards lower temperature in the millikelvin range. Consequently, the entropy related to the magnetic moment from J_{eff} is overestimated if the nuclear contribution is not substracted carefully. Of course, the more contributions, the more complicated becomes the extraction of the magnetic entropy.

The field-dependent magnetic Grüneisen parameter combined with the heat capacity offers another route to gain information about the entropy. In this case, it provides insight into the evolution in a magnetic field. The following expression follows immediately from the definition of the magnetic Grüneisen parameter in Eq. 2.40,

$$\Delta S(B) = \int_{B_0}^{B} \Gamma_{\mathrm{mag}}(B')C(B')\mathrm{d}B'. \tag{2.53}$$

It should be noted that the measurements of $\Gamma_{\mathrm{mag}}(B)$ and $C(B)$ at a fixed temperature T do not contain enough information to determine the absolute value of the entropy. For this purpose, $S(T)$ has to be determined at a certain field in an additional measurement to shift $\Delta S(B)$ onto the correct absolute values. A natural option would be at zero-field. If this is not feasible, another possibility can be a measurement at higher fields [86]. In many cases, however, the exact absolute values are not the most important information. It allows to follow the entropy change over, for example, phase transitions, where pronounced anomalies are usually expectable. Therefore, the field-dependent entropy $\Delta S(B)$ in this work is always given in relative values.

3. Measurement Setup and Analysis

In this chapter, all measurement devices and techniques are presented that are used in this thesis. Reaching temperatures far below room temperature is nontrivial, espcially for the millikelvin range, and requires special equipment. For that purpose, the Physical Property Measurement System (PPMS) and the dilution refrigerator MK 4 are used. Customized RuO_2 thermometers were utilized for accurate temperature measurements in the millikelvin regime. The challenging calibration process in magnetic fields down to 22mK is described in detail. Furthermore, the setups are shown for measuring heat capacity, magnetic Grüneisen parameter, and magnetization in the MK 4. Additionally, the analysis methods are introduced.

3.1. Heat Capacity in the PPMS

The PPMS from Quantum Design covers an extensive temperature range from above room temperature down to 2 K. Using liquid helium, temperatures down to 4.2 K as the helium boiling temperature are directly accessible. For reaching lower temperatures, helium gas is pumped from the helium bath lowering the vapor pressure. As a consequence, liquid helium evaporates. Due to the latent heat, this process requires energy from the environment and, thus, reduces the temperature. This way, the lowest temperatures achievable are ∼1.8 K.

In this work, the PPMS has been used below 30 K for heat capacity measurements which are based on the relaxation method. For more details please refer to the PPMS manual [87]. The PPMS heat capacity puck consists of a platform with a thermometer and a heater mounted from below. The sample is attached onto the platform by Apiezon N-Grease. In order to account for the platform heat capacity including N-Grease, two subsequent measurements are required. First, the heat capacity of the puck together with some N-Grease is determined. Second, the sample is fixed by the already applied N-Grease and measured again. Subsequently, the sample heat capacity is obtained by subtraction.

3.2. Dilution Refrigerator MK4

For numerous materials, measurements in the millikelvin range are crucial to understand the underlying physics. However, reaching temperatures below 1 K is challenging. By pumping ^{4}He, the minimum temperature is 0.83 K requiring a multitude of pumps [88]. Using the lighter ^{3}He isotope can provide temperatures down to 0.3 K [88]. For covering temperatures even down to the microkelvin range [89], adiabatic demagnetization is often used in space applications [90] but is usually limited to one-shot measurements. Consequently, continuosly cooling ^{3}He-^{4}He dilution refrigerator are the method of choice in research laboratories for more than 50 years.

Those refrigerators take advantage of the special properties of mixtures containing both helium isotopes, ^{3}He and ^{4}He. At 2 K and below, such mixtures are in the (suprafluid) liquid state. Upon cooling, this liquid separates, and two different phases coexist with different ^{3}He concentrations. By reaching very low temperatures ($T \lesssim 0.1$ K), the ^{3}He rich phase eventually

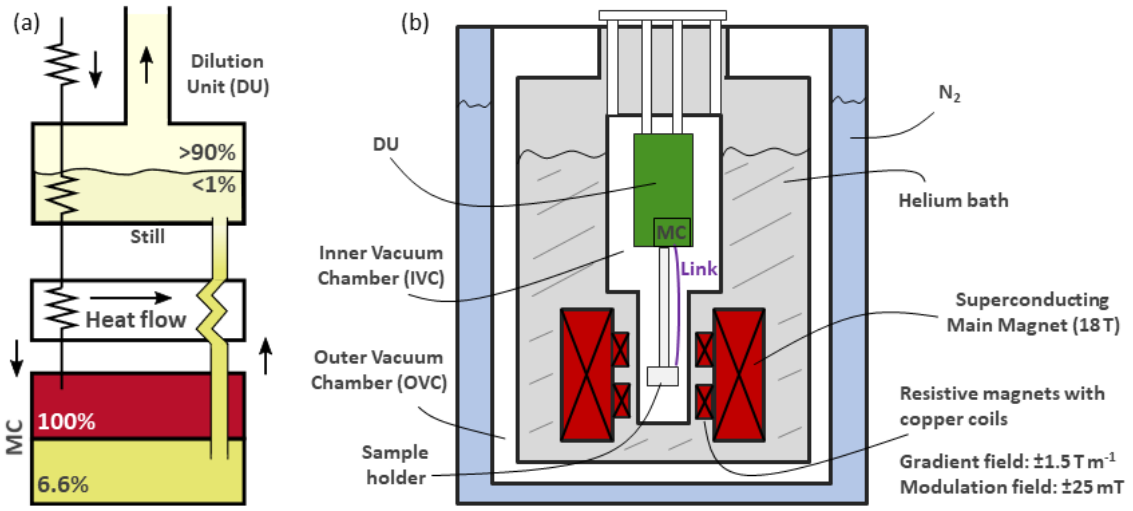

Figure 3.1. (a) Schematic circulation of the ^{3}He-^{4}He-mixture in the Dilution Unit (DU), following Ref. [88]. The phase separation between ^{3}He and ^{4}He necessary for the main cooling process takes place in the mixing chamber (MC). Consequently, the MC is the coldest part of the DU. (b) Sketch of the dilution refrigerator MK 4 with the helium and the nitrogen bath as well as the magnetic coils. The DU is shown in dark green, where the sample holder is attached. The sample is cooled by a thermal link from the MC and is located in the field center between the magnetic coils. More details can be found in the main text.

becomes pure ^{3}He. In the diluted phase, however, the ^{3}He concentration approaches 6.6 % as a constant concentration. This can be explained quantum mechanically and, in principle, stems from the binding energy between $^{3/4}$He atoms combined with the fermionic and bosonic character of ^{3}He and ^{4}He, respectively [19, 88]. Removing ^{3}He atoms from the diluted phase will be balanced by transferring ^{3}He from the pure to the diluted phase. This process requires a mixing enthalpy ΔH per atom which is prortional to the cooling power $\dot{Q}$,

$$\dot{Q} \sim x\Delta H. \tag{3.1}$$

Here, x denotes the ^{3}He concentration in the diluted phase. Since this stays constant and does not go to zero even for $T = 0\,\mathrm{K}$, dilution refrigerators maintain a high cooling power even at ultra low temperatures [88]. As a result, commercially fabricated devices like the MK 4 are nowadays able to typically approach $T \lesssim 10\,\mathrm{mK}$.

So far, no technical details have been mentioned, which are highly nontrivial compared to simple pumping of ^{4}He gas, where the cooling effect comes from the evaporation of liquid ^{4}He. In Fig. 3.1(a), a minimal example of a Dilution Unit (DU) is sketched. The phase boundary between the pure and the diluted phase is situated in the Mixing Chamber (MC) with the latter being located on the bottom (higher density). The diluted phase is connected to the Still which is held at elevated temperatures around 0.7 K. Due to their different vapor pressures, most of the ^{3}He evaporates, while ^{4}He remains as a (suprafluid) liquid. This drastically reduces the ^{3}He concentration in the Still below 1 %. This creates an osmotic pressure "pumping" ^{3}He atoms from the diluted phase to the Still. Accordingly, ^{3}He atoms cross the phase boundary from pure to diluted phase resulting in a cooling power dependent on the particle flow. To keep the osmotic pressure strong, the gas phase in the Still, containing mainly ^{3}He, is constantly removed by a conventional pump at room temperature (Still line in Fig. 3.2). The pumped gas mixture is cleaned in the N_2- and the He-trap at 77 K and 4.2 K,

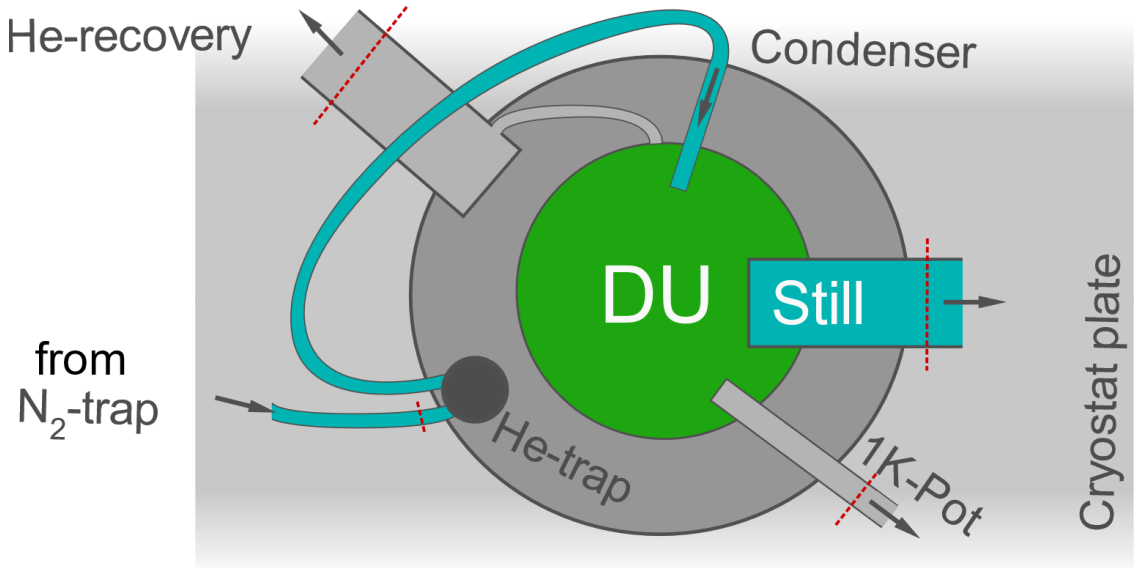

Figure 3.2. Pumping lines of the MK 4 including the DU. The direction of the gas flow is shown by the arrows. The red dotted lines indicate electrical insulation by plastic flanges and sealings to suppress disturbing electrical noise from the pumps and to prevent ground loops. The turquoise color is representative for the circulating ^{3}He-^{4}He-mixture. In the large Still line, the mixture is pumped away from the Still (see Fig. 3.1), and filtered in the N_2 and the He-trap, respectively. Subsequently, the mixture enters the DU again through the Condenser line, where it is precooled by pumping the 1 K-Pot and recondenses into the liquid state. The evaporating ^{4}He from the main bath is collected by the recovery system of the physics institute.

respectively, where impurities such as oxygen or nitrogen become frozen and stick to the wall. Thus, they are prevented to enter the DU to avoid blockages. The purified mixture enters the DU again through the Condenser line [Fig. 3.2]. After several precooling and liquefaction steps (1 K-Pot), it is transferred back to the MC as a liquid closing the ^{3}He-^{4}He circuit.

In this work, almost all measurements have been performed in the dilution refrigerator MK 4 in the low temperature laboratory of Experimental Physics VI (University of Augsburg)[1], schematically shown in Fig. 3.1(b). The DU is a Kelvinox from Oxford Instruments. Before starting the circulation of the ^{3}He-^{4}He-mixture, the DU is precooled to 4.2 K using the huge main bath (liquid ^{4}He). During the normal operation mode of the MK 4, however, the DU needs to be thermally decoupled from the main bath. Therefore, it is protected by the Inner Vacuum Chamber (IVC), which provides ultra high vacuum (UHV) conditions to minimize heat flow to the DU. The DU is fairly complex and contains many heat exchangers, precooling stages such as the 1 K Pot, and further equipment (heater, diagnostics). Furthermore, a Sorb pump is installed which adsorbs ^{4}He at lowest temperatures maintaining the UHV in the IVC. Otherwise, heat leaks to the "hot" ^{4}He bath will evaporate the ^{3}He-^{4}He mixture preventing the cooling process.

The MK 4 is equipped with a 18 T superconducting magnet cooled to 4.2 K by the ^{4}He main bath[2]. The measurement setup containing the sample is located in the field center and cooled by a thermal link to the MC in the DU[3] [Fig. 3.1(b)]. The MC is situated in a field-

[1] MK 4: Mischkühler 4. Located in the same lab is the MK 3, whereas MK 2 is in Göttingen.
[2] Above 16 T, the magnet requires further cooling down to 2 K by the so-called Lambda pump.
[3] Very often, the temperature regulation plate (TRP) is used for cooling the sample (heat capacity, Γ_{mag}) or the whole measurement cell (magnetization). The TRP is coupled to the MC by a copper cable

compensated zone taking advantage of the so-called cancellations coils attached to the main magnet. This way, devices mounted on the MC plate are not influenced by the magnetic field. Additionally to the main magnet, two smaller, equally winded copper coils can create an independent uniform magnetic field up to 25 mT if the current through the coils flows in the same direction. Here, the conversion factor for the coils is $1\,\mathrm{A} \equiv 3.277\,\mathrm{mT}$. If the current direction of one coil is reversed, a gradient field is created. Near the field center in between the coils, the field strength changes linearly along the axial axis of the coils with a maximum value of $\pm 1.5\,\mathrm{T\,m^{-1}}$ and a conversion factor of $1\,\mathrm{A} \equiv 0.202\,\mathrm{T\,m^{-1}}$ [Fig. 3.1(b)]. The former setting can be used to apply an oscillating current inducing an oscillating magnetic field superimposed to the main magnet. In this way, the magnetic Grüneisen parameter Γ_{mag} of the sample can be determined [Sec. 3.5]. The latter case with its gradient field is utilized for magnetization measurements [Sec. 3.6].

Dilution refrigerators including their customized measurement setups are highly optimized, and proper grounding is essential. For heat capacity or magnetic Grüneisen ratio measurements, the sample including platform, heater, and thermometer are thermally isolated from the environment. The customized thermal link to the bath of the MK 4 (MC or TRP) is rather weak. Thus, below 100 mK, even tiny amounts of heat generated by electrical noise may result in pronounced temperature increase because of the very small absolute sample heat capacity in the order of $\mu\mathrm{J\,K^{-1}}$. Connecting an arbitrarily grounded power supply to, for example, a heater can trigger undesired sample warming. This prevents to cool the sample down to the base temperature of the MK 4 and severely limits the accessible temperature range. In the magnetization setup, on the other hand, such heating effects are usually less severe due to its strong coupling to the thermal bath [Sec. 3.6], but the required capacitance measurement is extremely sensitive to electrical noise. Therefore, many wires have to be shielded in order to avoid catching noise, and shields must be grounded, too. In combination with the vast variety of measurement devices, diagnostics, and other equipment such as connecting pumping lines, a fairly complex grounding situation arises [Fig. 3.3].

In the following, a short overview on the MK 4 grounding is presented. Ideally, it should be kept in the current form. To a certain point, however, this setting was determined by trial and error and, consequently, there might be similar functioning configurations. The basic concept is the central copper grounding block placed on the stainless steel plate of the MK 4 cryostat. It is connected to the so-called lab ground which is installed in the low temperature laboratory. The lab ground is separated from the normal house ground, which is usually utilized as reference potential. By using the standard plug in the common power socket, each device in the physics building is automatically on the house ground. This potentially induces noise and may disturb the highly sensitive MK 4 measurements. Accordingly, considerable efforts have been undertaken (a) to separate the whole MK 4 setup from the house ground and (b) to optimize the grounding configuration.

First, we consider the former task (a). The most obvious potential contacts to the house ground are the pumping lines [Fig. 3.2]. Consequently, the Still, 1 K Pot, and both helium recovery lines have to be attached by plastic flanges. The Condenser line with its particular click-connecting system is permanently insulated at the He-trap input [Fig. 3.2]. Furthermore, three isolating transformers are used for the main magnet power supply Mercury iPS, the amplifier for the modulation/ gradient coils and the measurement rack containg devices such as LakeShore (LS) resistivity bridges or Keithley SourceMeters. In contrast, the Gas Handling

(⌀1 mm). Unlike the MC, the TRP can be heated above 1 K without breakdown of the ^{3}He-^{4}He circulation. Accordingly, the accessible temperature range is expanded.

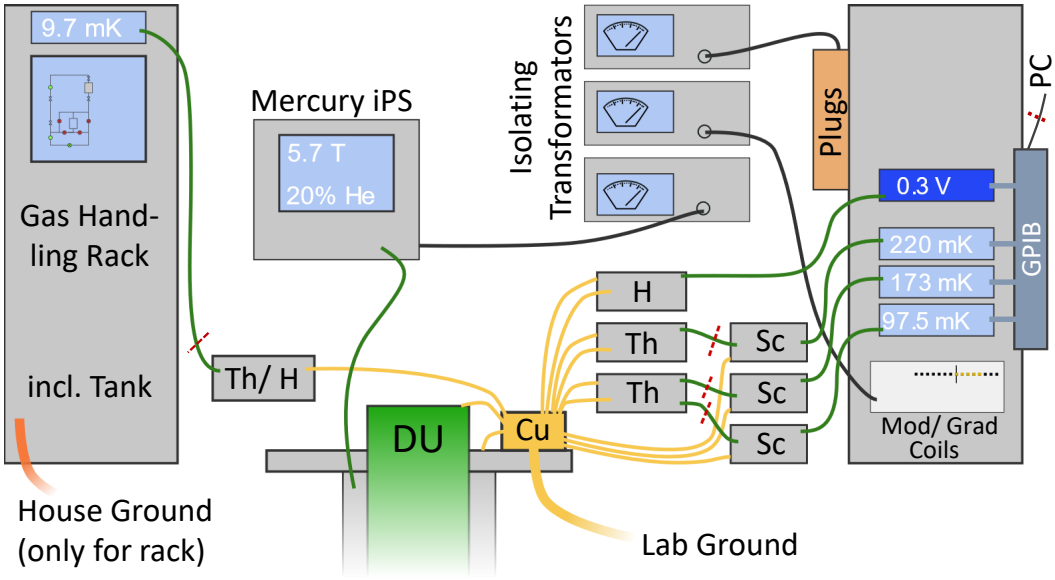

Figure 3.3. Grounding concept of the MK 4 with the central copper block (Cu), which is connected to the Lab Ground. Black lines represent power cords. The insulating transformators separate the house grounding from the measurement devices, the magnet power supply, and the amplifier used for the modulation/ gradient coils. Yellow lines are cables used for grounding of the thermometer (Th) and heater (H) filter boxes, the LakeShore scanner boxes (Sc) as well as the dilution unit (DU) and the cryostat plate. For the sake of clarity, all other connections to the DU (pumping lines, thermometer/ heater diagnostics) are omitted here. Green lines denote diagnostics cables to devices such as LakeShore bridges, Keithley SourceMeters, or between scanner and filter boxes. The red dotted lines indicate that the cable shielding is not connected. This avoids ground loops between the scanner and filter boxes or a connection to the house grounding of the measurement control PC via GPIB.

Rack is on the house ground. The only connection to the MK 4 is realized by its diagnostic cable (27 pin Fischer connector) to measure the temperature of the 1 K-Pot, MC, etc. Its shield is not connected through the diagnostics filter box (Th/H) preventing contact to the house ground [Fig. 3.3]. Last but not least, the GPIB to USB adapter has to be galvanically disconnected from the PC with the measurement programs.

The second assignment (b) is addressed by a copper block (Cu) directly linked to the specially installed lab ground in the low temperature lab. The copper block serves as the central point for all MK 4 grounding cables, which are fixed here for connecting the following parts depicted in Fig. 3.3.

- Both thermometer filter boxes (Th: 1x platine, 1x enclosure)
- Heater filter box (H: 1x platine, 1x enclosure)
- Filter box diagnostics (Th/H): DU thermometer and heater controlled by Gas Handling Rack
- Each LakeShore scanner box (Sc)
- Stainless steel plate of the MK 4 cryostat
- DU (for example at a screw)

Depending on the specific measurement setup[4], the connector strip for powering the measuring devices can be connected to the central copper block, too (not shown in Fig. 3.3). It is of crucial importance that the only electrical contact between those listed items is via the copper block. They must not be connected directly. Otherwise, ground loops are inevitable, which may cause heating or inaccurate measurements. For this purpose, the shielding between thermometer filter and scanner box are not connected in the plug indicated by the red dotted line. In general, those cable shieldings must be isolated against the DU as well which is fulfilled at the Fischer connectors at the DU which is not illustrated in Fig. 3.3 for the sake of clarity. The same holds true for the diagnostics filter box (Th/H). Furthermore, care has to be taken to avoid touches between filter and scanner box enclosures.

Several devices are not grounded on the copper block. The main magnet power supply Mercury iPS has several connections to the MK 4 setup. Besides the insulated main magnet power line and the Switch heater, two levelmeter exist for determining the current He and N_2 filling status. Their cable shielding is connected to the cryostat and, this way, the iPS becomes grounded. As previously pointed out, the Gas Handling Rack is set onto the house ground.

All in all, the MK 4 cryostat should be floating if the copper block is disconnected from the lab ground. This can be identified by measuring the resistance to the house ground which, in this case, should be at least in the MΩ range. Accordingly, that can be employed for checking the grounding configuration.

Potential problems are pumping lines touching the stainles steel plate, contact between helium recovery line and Mercury iPS, and connecting the Sub-D plug between Gas Handling Rack and Mercury iPS. The latter would be necessary if the main magnet shall be controlled by the rack, which is usually not required. Furthermore, it should be noted that the MK 3 is on the same lab ground like the MK 4, too. If a shortcut to the house ground exists here, it will affect the MK 4 as well. The same holds true for all other existing lab grounding blocks, e.g. in the PPMS laboratory (EP VI). As far as known, other chairs are not using the lab ground.

As a closing remark, the typical MK 4 measurement time is discussed. Unlike the PPMS with its routine 1-2 days duration, a dilution refrigerator measurement covers at least several days due to the time consuming sample preparation (up to 1-2 days), cool down (1 day), and warm up (1 day) procedure. Additionally, the measurement time drastically depends on the sample itself, the number of samples measured in one run, and the properties of interest. If only standard characterization $C(T)$ at zero field is involved, very few further days of measuring heat capacity may be sufficient. Frequently, extensive investigations are required including temperature and field dependent measurements. This way, measuring several weeks or even months in a single run is not unusual. Accordingly, the samples to be measured should be chosen with care, and, ideally, all have been already characterized as far as possible using the PPMS.

[4]The older Lake Shore Bridge LS 370 seems to be grounded by its Scanner box. Thereby, all other devices are grounded as well by the GPIB connections and, additionally, the connector strip over the LS370 plug. In general, the GPIB connections create an inescapable ground loop unless huge efforts are undertaken. However, this does not seem to affect the measurements.

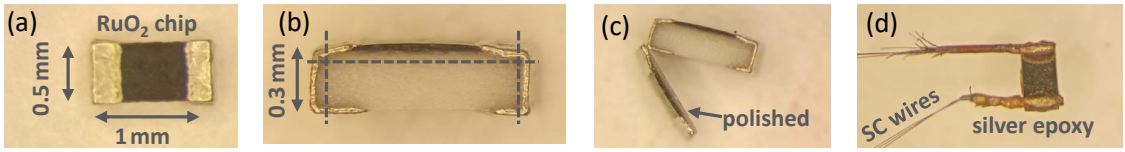

Figure 3.4. Overview of the RuO_2 thermometer production. (a,b) Top and side view of the pristine RuO_2 chips later used, for example, in the heat capacity cell. The dotted lines indicate the need of removing parts of the contacts as well as thinning of the insulating alumina layer by suitably fine sandpaper. (c) Comparison between pristine and polished chip. (d) RuO_2 thermometer after being contacted by the superconducting wires.

3.3. Thermometer Calibration

Thermometry plays a crucial role in entirely different disciplines. For mountain expeditions, the temperature is a crucial aspect deciding about success or fatal failure. Numerous industrial processes such as silicon wafer growth or chemical reagents production depend on precise temperature control. But also fundamental research requires accurate temperature determination in order to reveal underlying physical principles. Overall, relying on precise temperature measurements is important for abundant applications, and correct thermometer calibration is essential.

In this work, resistive RuO_2 thermometers have been prepared for determining temperatures far below 100 mK in magnetic fields up to nearly 18 T. This calls for a careful calibration to account for the temperature- and field-dependent thermometer resistance, which requires appropriate reference thermometers. The calibration procedure is described in detail in the following sections, including descriptions of the thermometer in use, and the calibration limits and errors are discussed.

3.3.1. RuO_2 Thermometer: Preparation and Calibration Setup

In the setup described in Sec. 3.4 and Sec. 3.5, a thermometer has to satisfy various conditions. First, its heat capacity needs to be small compared to the investigated samples. That guarantees fast thermalization and prevents disturbance of any measurement. Second, its dimensions are restricted by the sample as well. Ideally, the thermometer is not larger than the samples. Otherwise, problems with mounting the thermometer may occur. In this work, sample dimensions are typically in the order of several millimeter. Finally, heat flow to the thermal bath due to thermometer wires should be minimized. Commercially available thermometer do not meet all these criteria simultaneously, and, additionally, readily calibrated thermometers below 100 mK are precious, if available.

To this end, semiconducting RuO_2 chips (KOA Europe, Product Series: RK73B 1E 0402) are employed in this work as resistive sensors with a resistance of $\sim 2\,\mathrm{k\Omega}$ at room temperature. These chips have lateral sizes of $\sim 0.5\times1\,\mathrm{mm}^2$ (or $\sim 1\times1\,\mathrm{mm}^2$, depending on the batch), a thickness of 0.3 mm before polishing [Fig. 3.4(a,b)] and very tiny heat capacity at low temperatures. They are commonly used in an entirely different context, e.g. in the automotive industry, and inexpensive due to their mass production. Towards low temperatures, their resistivity exponentially increases providing excellent sensitivity for temperature changes below 1 K. They are contacted by superconducting wires strongly reducing heat flow from the thermal bath in the millikelvin range. Thus, the RuO_2 chips perfectly suit all above mentioned preconditions.

The preparation of the chips comprises several steps. First, the chips should be trained by at least 20 cooling-warming cycles from room temperature to 4.2 K. This is needed because the first cooling to such low temperature may cause microscopic cracks in the material and alter the chip resistance. After that procedure, the chip stays approximately unaffected upon further cycles. This could be further investigated by repeatedly measuring the temperature-dependent resistance of a selected RuO_2 chip in the PPMS. In a next step, the insulating alumina layer is thinned by grinding as far as possible. This reduces its heat capacity and optimizes the thermal coupling between RuO_2 layer and the sample, to which the thermometer is attached during a measurement [Fig. 3.4(b,c)]. Subsequently, the original multifilament superconducting wire (Supercon Inc) has to be customized as well. It consists of ∼30 NbTi filaments with copper cladding. The copper is removed by HNO_3 except of both ending parts that are protected by nail polish. They are needed for contacting the thermometer in the measurement setup. By cutting most filaments except of 2-3, the thermal conductance of the superconducting wire by phonons is greatly reduced. Finally, two wires are fixed to the RuO_2 chip by silver epoxy, an electrically conductive two-component glue from Epo-Tek. For ensuring good electrical contact to the sample, the whole chip is heated to ∼80 °C for at least several hours. The other sides of the wires are used for conducting a 4-point resistivity measurement, see Fig. 3.8(a). Note, that the superconducting filaments are extremely filigree, and the handling is delicate. Any tension on the filament has to be avoided in order to avert rupture. Unfortunately, repairing broken filaments is not feasible.

For the calibration, six RuO_2 chips (SB 1-6) were fixed on a massive silver block by GE Varnish. SB 3 could not be calibrated because the connection was lost at lowest temperatures. SB 6 was an old thermometer used in measurements before this thesis, but it turned out to be defect due to a strong kink in the last remaining superconducting wire. A very thin paper soaked by GE varnish was attached between silver and chip to prevent electrical shorts. The silver block was mounted to the MC plate by a silver rod to ensure optimal thermal contact. The rod length was chosen in a way that the chips were located in the magnetic field center of the MK 4. For reducing eddy current heating induced by magnetic fields, the silver block and rod were slitted, and the slits were filled by a plastic foil. The reference thermometer CMN and Cernox were attached to the MC plate, where they were unaffected by the magnetic field because of its suppression due to the cancellation coils [Sec. 3.2]. The functionality of both CMN and Cernox are explained in more detail in the following section. Two additional, differently constructed thermometers were mounted on the MC plate and calibrated, too (ICE 2, SB 7). They were used for measuring the MC or TRP temperature in subsequent experiments.

3.3.2. Reference Thermometer: CMN Device and Cernox

Independent of the individual setup, each calibration requires a reference. Here, the reference has to cover a wide range from ultra low temperatures far below 100 mK up to nearly 10 K. At the same time, the reference must be highly accurate. In order to fulfil these criteria, two independent thermometers are used in this work [Fig. 3.5]. Below about 200 mK, a device containing the paramagnetic salt cerium magnesium nitrate (CMN) was employed consisting of two coils [91]. The embedded water molecules in the crystal structure causes large distances between the magnetic cerium ions resulting in an extremely low Curie-Weiss temperature $\theta_{CW,CMN}$ in the order of several 0.1 mK [88]. Applying a sinus current of ∼5 µA by a Stanford Research lock-in amplifier (SR830) induces a 90° phase-shifted voltage U_{CMN} in the second coil being proportional to the magnetic susceptibility χ. In order to obtain

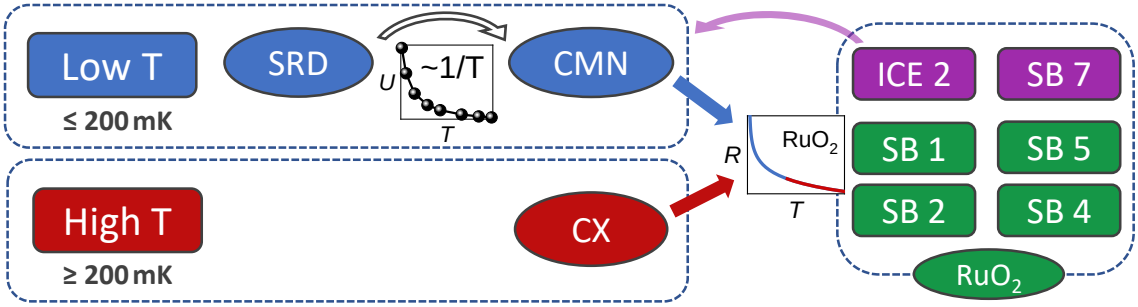

Figure 3.5. Thermometer calibration - schematic overview. Thermometer to be calibrated are depicted on the right. Subsequently, the RuO_2 thermometer (green) are used in the heat capacity and magnetic Grüneisen setup. The thermometer ICE 2 and SB 7 (purple) serve for temperature measurements of the TRP or MC. For the calibration procedure, two parts can be distinguished. At very low temperatures, the CMN thermometer obtains eminent precision due to its signal with paramagnetic 1/T behavior. Its calibration slightly varies after each warming-cooling cycle. Accordingly, the CMN first requires an in-situ calibration by the Fixed-Point Device SRD containing several superconducting materials with different, exactly known transition temperatures T_c (upper panel, blue). At temperatures beyond ∼300 mK, the CMN accuracy rapidly decreases, and the externally calibrated Cernox CX is utilized as reference thermometer (lower panel, red). Combining both CMN and Cernox, in principle, a temperature range from below 30 mK up to room temperature is covered. In this work, ICE 2, SB 7, and the RuO_2 thermometers are calibrated up to 8 K because, in general, more elevated temperatures are irrelevant in a dilution refrigerator. Note, that the ICE 2 thermometer was used for recalibrating the CMN after an unexpected, but inevitable warming-cooling cycle.

a reasonable signal-to-noise ratio, careful signal leads shielding is mandatory. Therefore, a BNO cable is used for transporting the secondary voltage signal from the low impedance filter box, which is usually used for heaters, to the Lock-In Amplifier. A BNO cable contains two shielded signal leads, and the difference between those two conductors is determined as U_{CMN}. This way, both conductors are shielded, respectively, all the way from the cryostat to the measurement device.

In general, the susceptibility of paramagnetic salts follows the Curie-Weiss Law, $\chi \sim U_{\mathrm{CMN}} \sim 1/(T - \theta_{\mathrm{CW}})$, resulting in diverging behavior for temperatures close to the Curie-Weiss temperature θ_{CW}. As a result, the CMN device is extremely sensitive in the lower millikelvin range. Unfortunately, the CMN calibration slightly changes after each warming and cooling cycle due to, e.g., tiny losses of crystal water in the unavoidable IVC vacuum at room temperature. Therefore, a prior in-situ calibration is necessary before being a valid reference. To this end, the Fixed Point Device SRD is utilized. It contains several superconducting materials, whose transition temperatures are exactly known. Note, that the ICE 2 was used to recalibrate the CMN after an unexpected, but inevitable warming up of the dilution fridge (detailed explanation in Sec. 3.3.3).

At high temperatures, however, the accuracy of the CMN thermometer becomes poor because the CMN signal is proportional to the Curie-Weiss susceptibility. For this purpose, a second reference was bought from Oxford Instruments including a calibration file. The resistive thermometer Cernox X112017 covers a range from nominally 100 mK to 325 K and was used as reference for $T \geq$ 150-200 mK. Its resistance was measured by a LS Bridge for calculating the corresponding temperature. This reference thermometer allows to extend the calibration range for the RuO_2 thermometers up to several Kelvin.

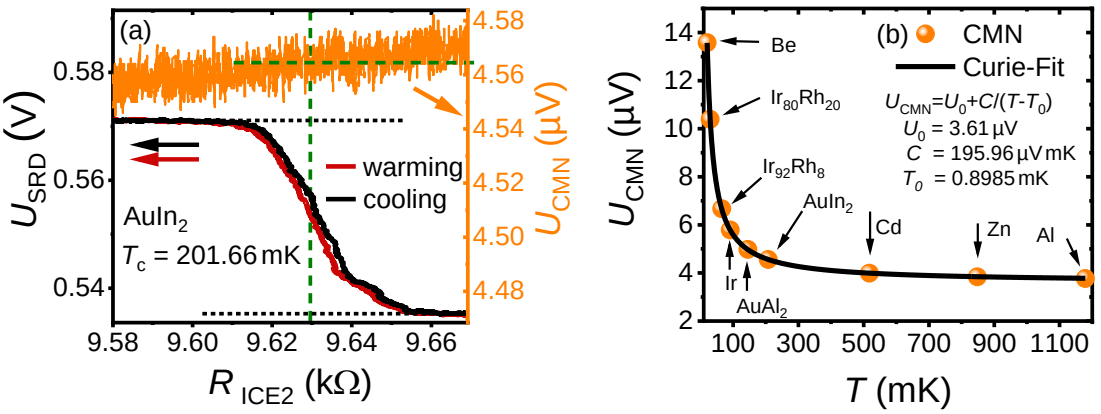

Figure 3.6. (a) Calibration of the CMN at the $AuIn_2$ transition. In the same way, the other superconducting transitions are analysed. (b) Fit through the nine calibrated CMN points. This way, the CMN becomes calibrated over the whole temperature range, and its signal U_{CMN} can be used to calculate the temperature.

3.3.3. Calibration of the CMN Thermometer by a Fixed Point Device

After each cooling from room temperature to lowest temperatures, the CMN has to be newly calibrated. With its signal $U_{CMN}(T) \sim 1/(T - \theta_{CW})$, several $U_{CMN}(T)$ points has to be measured at precisely known temperature values. Subsequently, a fit function is applied to these data,

$$U_{CMN}(T) = U_0 + C/(T - \theta_{CW}), \tag{3.2}$$

with the offset U_0, the constant C and the Curie-Weiss temperature θ_{CW} as free fitting parameter. In this work, the Fixed Point Device SRD1000 was used as reference for the CMN thermometer. It is a ready-to-use instrument fabricated by HDL (Hightech Development Leiden) including all measurement units and most connecting cables. It contains ten materials with superconducting transitions covering a wide temperature range from 15 mK to 1.2 K. The SRD signal measurement is very similar compared to the CMN device. A current through the primary coil induces a voltage in the secondary coil, in which all ten materials are located. At its transition temperature, each material causes a voltage drop when becoming superconducting, respectively. Accordingly, such a voltage drop in the secondary coil can be paralleled to the accurately known transition temperatures T_c. The simulteously measured signal U_{CMN} can be assigned to a temperature T_c, which is shown exemplarily in Fig. 3.6(a) for the $AuIn_2$ transition. Here, the horizontal axis shows the ICE 2 resistance because, at that moment, this thermometer was not calibrated yet. Note that smaller resistance is equivalent to higher temperature. This way, up to ten data points can be acquired for the fit from Eq. 3.2. In this work, the Wolfram (W) transition at 15 mK was not accessible leaving Beryllium (Be) as the lowest data point [Fig. 3.6(b)]. The Curie-Weiss temperature from the fit amounts to ∼0.9 mK being reasonably close to the expected value of several 0.1 mK [88].

For a highly accurate CMN calibration, it is essential to prevent shifts of the superconducting transition temperatures due to remanent magnetic fields from flux pinning in the superconducting magnet. To this end, the MK 4 main magnet was warmed up close to the nitrogen boiling temperature of 77 K before the calibration procedure. This way, it entered the normal conducting state, all pinned fluxes were removed, and the remanent field safely becomes zero. In addition, the SRD device is equipped with a cancellation coil, which can be

used for suppressing remaining fields such as the earth magnetic field or the remanent field of the MK 4 main magnet. It is shown in the Appendix that this is not needed for the calibration in this work [Fig. A.1]. It is noted in passing that the CMN is potentially affected by small magnetic fields, too, but the MK 4 cancellation coils were sufficient to guarantee valid temperature determination. This is evidenced by the thermometer ICE 2, which is located in the field-compensated zone, too. The calibration curve $R_{\mathrm{ICE\,2}}(T)$ determined by combining CMN and Cernox did not change between 0 T and 17.5 T [Fig. A.2]. Consequently, the CMN thermometer is not influenced by stray fields of the MK 4 main magnet.

After the successful CMN calibration, the SRD device unfortunately had to be sent back to the group in Dresden because it was only borrowed from them. The RuO_2 calibration was not started yet. For dismounting the SRD, the whole setup had to be warmed up, and, accordingly, the CMN calibration had to be checked after the subsequent cool down. For this purpose, the ICE 2 thermometer was calibrated by the SRD at the nine superconducting transitions T_c. These points were used to recalibrate and validate the CMN device after the unexpected warming-cooling cycle.

3.3.4. Calibration of the RuO_2 Thermometers

The RuO_2 chips used in this work are from two different batches. The most apparent difference concerns the lateral size with $1 \times 0.5\,\mathrm{mm}^2$ for SB 1/2 and $1 \times 1\,\mathrm{mm}^2$ for SB 4/5. More importantly, both batches obtain a non-negligible magnetoresistance, i.e., their resistance at a given temperature depends on the magnetic field. This requires several independent calibrations for each thermometer at a variety of fields. Here, the chips were calibrated from 0 to 16 T in 1 T steps. Beyond 16 T, the necessary additional cooling of the main magnet makes measurements cumbersome. As a result, only 17.5 T was calibrated here. A smaller increment was chosen at low fields (0.5 and 1.5 T) as well as at 15.5 T. The latter is in the field region where the superconductivity of the wires breaks down at low temperatures.

The calibration procedure for the RuO_2 thermometers is time-consuming but rather straightforward. All thermometers are very strongly thermally coupled to the MC plate in order to avoid any temperature gradients. As soon as all thermometers are in equilibrium, each RuO_2 thermometer resistance $R_{\mathrm{SB\,x}}$ ($R_{\mathrm{ICE\,2}}$) is determined and assigned to the simultaneously measured CMN and Cernox temperature T_{CMN} and T_{Cernox}, respectively. In order to obtain a dense number of data points, the MC was warmed up in small steps ($\Delta T/T \sim 3\%$), and the equilibrium was guaranteed by checking the slope of CMN, ICE 2 and SB 1. Following this procedure, each RuO_2 thermometer obtains its own $R_{\mathrm{SB\,x}}(T)$ curves, exemplarily shown for SB 1 in Fig. 3.7(a) at 0 T. Both references CMN and Cernox agree very well. Weak deviations appear only around $\sim 100\,\mathrm{mK}$ being the lower calibration limit of the Cernox (inset) and at higher temperatures, where the CMN becomes less accurate. For each calibration curve, a crossover temperature had to be defined where the overlap was best, which was usually between 150 and 200 mK (dotted line in the inset). The CMN was used for the lower temperature range, and the Cernox covered higher temperatures.

For obtaining a continuos calibration curve, each $R_{\mathrm{SB\,x}}(T)$ was plotted in the form $\ln(T)$ over $C - \ln(R - R_0)$ with R_0 being roughly comparable to the room temperature value and $C = 11.2$, which is an arbitrarily chosen, fixed constant for shifting the data [Fig. 3.7(b)]. This was fitted by a polynomial function,

$$\ln(T) = \sum_{k=0}^{n} a_k x^k, \tag{3.3}$$

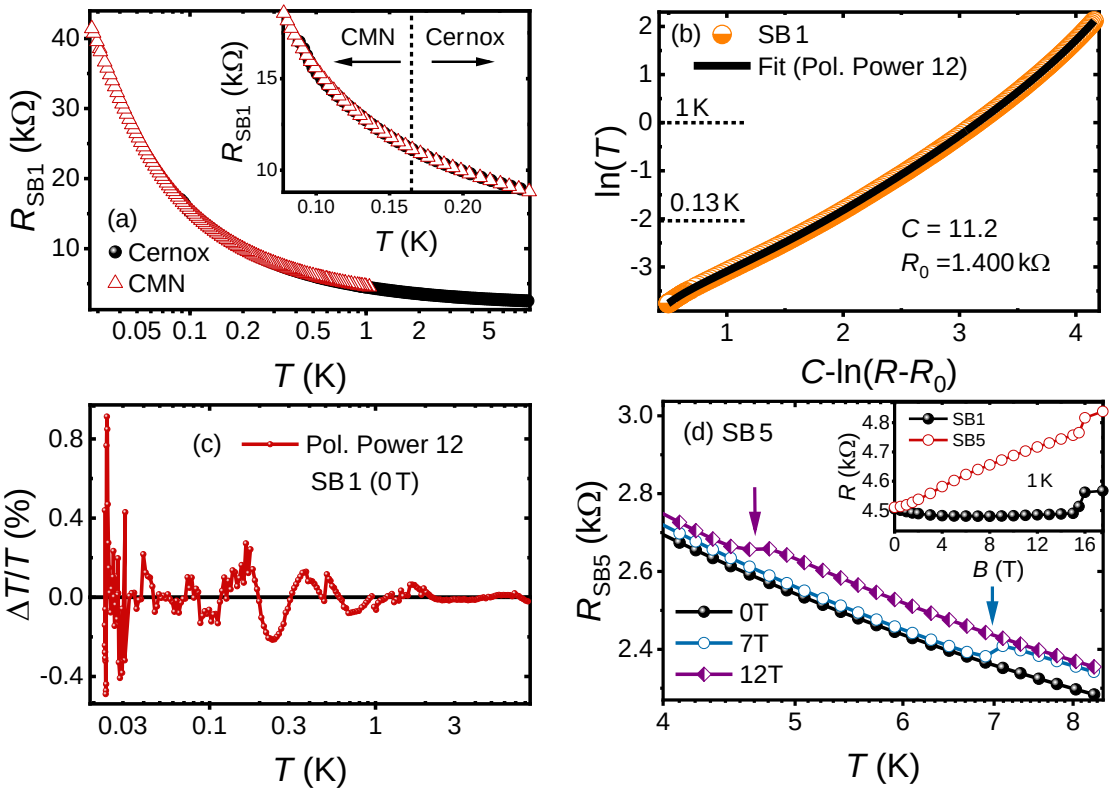

Figure 3.7. (a) Exemplarily for all other RuO_2 thermometers, the SB 1 resistance is plotted over CMN and Cernox temperature. The data points are acquired in 3 % steps. It is waited at each step until all thermometers are in thermal equilibrium. In this example, the crossover from CMN to Cernox as reference was defined at the dotted line (inset), where the overlap was best. (b) Fit of the data by polynomial function (details in the text). (c) Evaluation of the fit quality by calculating the difference between fit and data in percent. The deviation is less than 0.4 % over the whole field range except for the lowest temperatures. Even there, the discrepancy is below 1 %. (d) Jumps in the resistance over temperature shifting to lower temperatures for higher fields. This is due to the breakdown of superconductivity in the wires. The inset illustrates the sizeable magnetoresistance at 1 K in the batch SB 4/5, whereas it is less prominent in the batch SB 1/2. Furthermore, the breakdown of superconductivity can also be seen close to 16 T.

with a_k as free fitting parameter, $x = C - \ln(R - R_0)$ and $n = 12$ or 14, respectively. The parameter R_0 was adjusted until the fit following Eq. 3.3 was sufficiently precise. This was evaluated by calculating the difference between fit and measured data in percent as shown in Fig. 3.7(c). Here, the maximum fit deviation from the data amounts to 0.4 %. Naturally, the discrepancy becomes larger at ultra-low temperatures below ∼30 mK, but is still less than 1 %. In the program used for determining the sample temperature, the current temperature is calculated by using the parameter C, R_0, and a_k in combination with the measured thermometer resistance R,

$$T = \exp\left(\sum_{k=0}^{n} a_k x^k\right). \tag{3.4}$$

As already mentioned, $R_{SBx}(T)$ was measured at 22 different fields for all thermometers. This takes the magnetoresistance into account, which is different for each RuO_2 batch and

illustrated in the inset of Fig. 3.7(d) at 1 K. Here, SB 5 changes its resistance by more than 5 %, whereas SB 1 remains roughly constant. At lower temperatures, the magnetoresistance becomes even more pronounced, underlining the importance of the field calibration, which is shown in more detail in the Appendix [Fig. A.3].

Besides magnetoresistance, there is another peculiar observation which manifests in a jump at ~ 16 T. At this field, superconductivity is suppressed. The same behavior appears in the temperature dependence at higher fields marked by the arrows in Fig. 3.7(d). Consequently, a precise temperature determination is not feasible in the breakdown region, which is discussed in more detail in the following section.

3.3.5. Calibration Limits and Error Estimation

Knowing the valid RuO_2 calibration range is extremely important due to few shortcomings. In principle, the calibration holds between the lowest and highest measured temperatures $\sim$22 mK and $\sim$ 8 K, respectively. Yet, the fit formula of Eq. 3.4 is not capaple to account for jumps. For this reason, the previously mentioned superconducting breakdown can not be included and represents an upper limit for the RuO_2 calibration fit. As a consequence, using Eq. 3.4 might return erroneous values because of lacking implicit limits. Calculating a temperature by measuring R_{RuO_2} outside the calibrated range potentially arises in huge deviations to the actual temperature. In practice, however, crossing the superconducting transition results in peculiar temperature values, which makes it simple to detect that limit.

Furthermore, a central topic is the calibration accuracy being composed of several contributions. First, the two reference thermometers are potential error sources. The Cernox obtains an absolute error of 4 mK at 1.4 K, which is equivalent to less than 0.3 % relative error. For lower temperatures, no further information are available. Nevertheless, it is not expected that the relative error towards 100 mK increases strongly because the Cernox resistance grows rapidly upon cooling below 1 K ensuring precise temperature determination. As an upper limit, 1 % relative error at 100 mK can be assumed. For the CMN, the discrepancy between fit and calibration points at T_c from the SRD is below 1 %. Besides, the CMN fit was checked concerning slight variations in determining U_{CMN} at T_c as explained previously [Fig. 3.7(a)]. The relative error turned out to be robust. Second, the RuO_2 fit deviates from the data points by less than 1 % below 30 mK and less than 0.4 % above that temperature as shown in Fig. 3.7(c). This can be generalized for all thermometers by crosschecking several calibrations. Finally, the measurement of the RuO_2 resistance gives rise to a relative error being below 1 % [92]. This roughly results in similar deviations for the temperature calculation following Eq. 3.4. Overall, the RuO_2 thermometer error can be estimated to be around 2 % or below. In general, of course, a larger relative error can be expected at very low temperatures of e.g. $T = 50$ mK because a rather small absolute error of 1 mK is already equivalent to the above mentioned 2 %.

The RuO_2 calibration might change after several years with numerous cooling-warming cycles, which might stress the semiconducting layer, the wires or the contacts. However, ICE 2 was crosschecked by the SRD after 3.5 years. The temperature calculated by the former calibration resulted in $\Delta T/T < 1$ % underlining the thermometer stability. The thermometers in the heat capacity cells have not been crosschecked, but similar stability is expected if treated carefully.

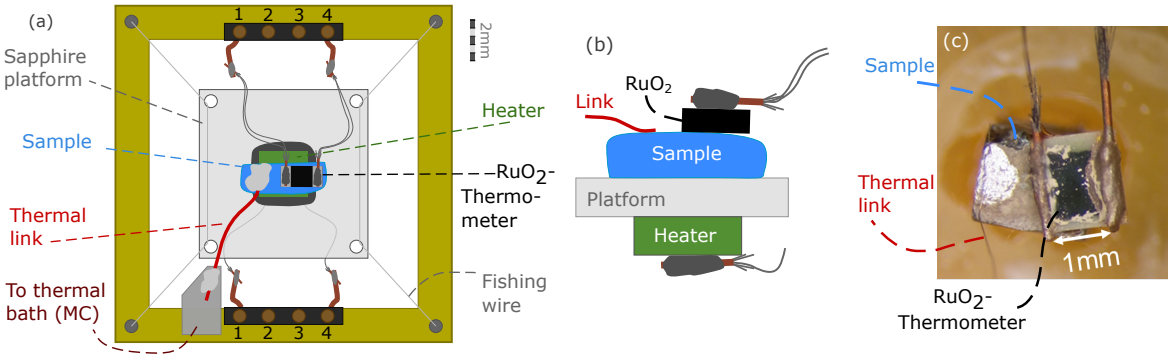

Figure 3.8. (a) Top view of a heat capacity cell. The sample (light blue) is mounted on a sapphire platform (grey) which is thermally insulated from the surrounding cell body by fishing wires. The RuO_2 thermometer (black) as well as the thermal link (red) are fixed onto the sample. The thermal link is a thin bronze or brass wire with different diameters, which is chosen in respect to the sample properties and is connected to the thermal bath (TRP or MC). The heater is located below the platform. (b) Side view of the setup. (c) Close-up view of a sample, where thermometer and thermal link are mounted.

3.4. Heat Capacity Setup

The possibilities for measuring heat capacity are numerous, but the appropriate choice depends on the sample. In this work, samples with small size ($\leq 5\,\mathrm{mm}$) and mass ($\leq 20\,\mathrm{mg}$) and, therefore, small absolute values of heat capacity ($\leq 20\,\mu\mathrm{J\,K^{-1}}$) are measured using a quasi-adiabatic heat pulse method and/ or a relaxation method. Both will be described in detail in the following sections as well as the used setup, which is specially designed for the above mentioned requirements. A schematic top view is shown in [Fig. 3.8(a)].

The sample holder is a thin sapphire plate with a thickness of less than 0.2 mm and a lateral size of $6 \times 6\,\mathrm{mm}^2$. To ensure good thermal insulation from the environment, it is fixed by fishing wires with a diameter of $\varnothing \leq 0.1\,\mathrm{mm}$. A resistive heater similar to the RuO_2 thermometer chips is glued below the platform with an epoxy (Stycast 1266), which is illustrated in the side view in Fig. 3.8(b). In comparison to the thermometers, the heaters have a lower room temperature resistance of several $100\,\Omega$. Ideally, the heater resistance shows only a small temperature dependence at low temperature[5]. The sample is centered above the heater and usually fixed with small amounts of GE varnish. Since this varnish contains some dissolvents that might dissolve very sensitive samples like α-$RuCl_3$, Apiezon N grease is used in rare cases. The next step is to mount the RuO_2 thermometer on top of the sample, again using GE varnish (or Apiezon N grease). Until now, the thermal coupling of the sample to the environment is very weak since the fishing wires as well as the superconducting wires of the thermometer and the heater, respectively, are poor thermal conductors at temperatures below 1 K. Compared to the PPMS, this gives the opportunity to choose a thermal link with an appropriate thermal conductivity κ. One (or more) bronze ($\varnothing = 22\,\mu\mathrm{m}$, $52\,\mu\mathrm{m}$) or brass wire ($\varnothing = 10\,\mu\mathrm{m}$) is used in the MK 4 and fixed on the sample using silver paste [Fig. 3.8(c)]. The other side of the wire is connected to a silver plate that acts as thermal bath since it is directly connected to the TRP (or MC) by thick silver wires. The appropriate choice of the thermal link is very important. It is always a compromise and varies from sample to sample.

[5]The heaters in cell 2, 3, and 4 fulfill this condition with a resistance change below 1 % between 4 K and 50 mK. In cell 1, however, the resistance changes by $\sim$ 10 % and needs to be measured once at the beginning of each new run.

For calculating the heat capacity, the sample's temperature response $T(t)$ is measured upon changing the heat flow (see Sec. 3.4.1 and Sec. 3.4.2). On the one hand, a stronger thermal link results in a faster temperature response. If this process is too quick, $T(t)$ does not contain enough data points to ensure adequate fitting, which is required to guarantee high-quality results. Consequently, the thermal link must not be too strong. On the other hand, very weakly coupled samples have long relaxation times, and approaching the desired base temperature takes a lot of time or might even become impossible. Furthermore, each heat capacity data point costs a lot of time. To realize a good compromise between these two undesired limits, the sample's heat capacity C guides the way. In first approximation, the heat capacity is linked to the thermal conductivity κ and the relaxation time τ, $C = \kappa\tau$ (see Sec. 3.4.1). Consequently, careful pre-characterization of the heat capacity in the PPMS down to 2 K or, even better, to 400 mK is extremely valuable. This can be used to estimate the expected heat capacity evolution in the millikelvin range and to choose a thermal link that provided adequate conditions for comparable samples measured in previous runs.

In the following, two different methods used in this work for the determination of the heat capacity are explained in detail.

3.4.1. Relaxation Method

Yet resembling the PPMS heat capacity option, the setup for the MK 4 has slight but important differences influencing the relaxation method analysis. In contrast to the PPMS setup, the thermal link to the bath and the thermometer are not directly attached to the platform, but on top of the sample. Additionally, temperatures below 1 K potentially give rise to nuclear heat capacity contribution(s) C_{nuc} of the sapphire platform (Al_2O_3) but also of the sample itself. If the spin-lattice relaxation time t_{n} is not neglectable, the nuclear spin temperature T_{n} is not in thermal equilibrium with the sample, $T_{\mathrm{n}}(t) \neq T_{\mathrm{Sa}}(t)$. On the other hand, it can be assumed that thermometer (Th), sample, platform and heater (H) are ideally thermally coupled, i.e., $T_{\mathrm{Sa}}(t) = T_{\mathrm{Pl/H/Th}}(t)$, which will be justified later. Again, this is distinct compared to the PPMS, where sample and platform temperature might differ due to poor thermal coupling. All in all, the heat flow scheme is fundamentally changed [Fig. 3.9(a)] and calls for a detailed discussion.

The thermal link between sample and bath has the thermal conductivity k_{SB} in units of $\mathrm{J\,K^{-1}\,s^{-1}}$. Analogously, the thermal coupling between nuclear contribution(s) C_{nuc} and platform (or sample) is denoted as k_{n}. Both thermometer and heater obtain negligible heat capacity and, thus, do not contribute to the total heat capacity $C_{\mathrm{tot}} = C_{\mathrm{Sa}} + C_{\mathrm{Pl}}$, which comprises sample and platform heat capacity. By applying a voltage U_{H} to the resistive heater, a current I_{H} is flowing through the heater generating the power $P_{\mathrm{H}} = R_{\mathrm{H}} I_{\mathrm{H}}^2$. This way, the sample temperature T_{Sa} can be adjusted. Using the heat flow scheme, two equations are derived for the temperature response of the sample $T_{\mathrm{Sa}}(t)$ and the nuclear contribution $T_{\mathrm{n}}(t)$,

$$\begin{aligned} &\text{(I)} \quad C_{\mathrm{tot}} \frac{dT_{\mathrm{Sa}}(t)}{dt} = P_{\mathrm{H}}(t) - k_{\mathrm{SB}} \left[T_{\mathrm{Sa}}(t) - T_{\mathrm{bath}}\right] - k_{\mathrm{n}} \left[T_{\mathrm{Sa}}(t) - T_{\mathrm{n}}(t)\right], \\ &\text{(II)} \quad C_{\mathrm{nuc}} \frac{dT_{\mathrm{n}}(t)}{dt} = -k_{\mathrm{n}} \left[T_{\mathrm{n}}(t) - T_{\mathrm{Sa}}(t)\right]. \end{aligned} \tag{3.5}$$

The left side denotes the temperature change due to the total incoming power derived from $P_{\mathrm{in}} = dQ_{\mathrm{in}}/dt$ with $C = dQ_{\mathrm{in}}/dT_{\mathrm{in}}$. The right side accounts for external power sources as well as heat flow because of temperature differences to directly coupled reservoirs. T_{bath} is

the constant bath temperature. For measuring the heat capacity, the system initially has to be in thermal equilibrium. To this end, a heater power P_i is applied and waited until $dT_\mathrm{Sa}(t)/dt = 0$ implying that $T_\mathrm{Sa} = T_\mathrm{n}$. Subsequently, a heater power P_f is set at $t = t_0$ causing a temperature increase. By analysing the measured temperature response $T_\mathrm{Sa}(t)$, information about the heat capacity C_Sa and C_nuc can be established.

If the spin-lattice relaxation time $t_\mathrm{n} = C_\mathrm{nuc}/k_\mathrm{n}$ is small, and, thus, the spin relaxation very fast, then nuclear spins and lattice are always in equilibrium, $T_\mathrm{Sa}(t) = T_\mathrm{n}(t)$. This holds true if the nuclear heat capacity is very small ($C_\mathrm{nuc} \ll C_\mathrm{tot}$) or if nuclear spins and lattice are ideally coupled ($k_\mathrm{n} \gg k_\mathrm{SB}$). In this case, Eq. 3.5 simplifies to

$$C'_\mathrm{tot}\frac{dT_\mathrm{Sa}}{dt} = P_\mathrm{H} - k_\mathrm{SB}\left[T_\mathrm{Sa} - T_\mathrm{bath}\right]. \tag{3.6}$$

This can be easily solved for $t \geq t_0$ resulting in a single exponential increase of the sample temperature,

$$T_\mathrm{Sa} = T_\mathrm{bath} + \frac{P_\mathrm{f}}{k_\mathrm{SB}} - \Delta T \exp\left[-\frac{t-t_0}{C'_\mathrm{tot}/k_\mathrm{SB}}\right] = T_\mathrm{f} - \Delta T \exp\left[-(t-t_0)/\tau\right]. \tag{3.7}$$

Here, T_f denotes the final sample temperature in equilibrium, $\Delta T = T_\mathrm{f} - T_\mathrm{i}$ with T_i as the starting temperature, and τ the relaxation time of the sample including platform and nuclear contribution. More importantly, the total heat capacity is calculated by $C'_\mathrm{tot} = k_\mathrm{SB} \cdot \tau$ with $k_\mathrm{SB} = \Delta P/\Delta T = (P_\mathrm{f} - P_\mathrm{i})/(T_\mathrm{f} - T_\mathrm{i})$. Note, that now the nuclear contribution is included in the total heat capacity analogous to the platform heat capacity, $C'_\mathrm{tot} = C_\mathrm{Sa} + C_\mathrm{Pl} + C_\mathrm{nuc}$. This way, a simple fit function following Eq. 3.7 can be used for extracting the heat capacity.

However, if the spin-lattice relaxation time t_n becomes comparable to the sample relaxation time, the solution of Eq. 3.5 becomes more complicated. The differential equation system has been solved in Python, and the solution now comprises two exponential functions,

$$\begin{aligned} T_\mathrm{Sa} &= T_\mathrm{f} - \Delta T_1 \exp\left[-(t-t_0)/\tau_1\right] - \Delta T_2 \exp\left[-(t-t_0)/\tau_2\right], \\ \Delta T_{1,2} &= A_{1,2}\frac{k_\mathrm{n}}{C_\mathrm{tot}}, \\ \tau_{1,2} &= \frac{2}{\alpha \mp \beta},\ \alpha = \frac{k_\mathrm{n}}{C_\mathrm{nuc}} + \frac{k_\mathrm{SB}+k_\mathrm{n}}{C_\mathrm{tot}},\ \beta = \sqrt{\left(\frac{k_\mathrm{n}}{C_\mathrm{nuc}} - \frac{k_\mathrm{SB}+k_\mathrm{n}}{C_\mathrm{tot}}\right)^2 + 4\frac{k_\mathrm{n}^2}{C_\mathrm{tot}C_\mathrm{nuc}}}. \end{aligned} \tag{3.8}$$

The prefactors $A_{1,2}$ depend on the starting conditions, and, again, T_f denotes the temperature in the final equilibrium state. The response of the sample temperature containing two exponential contributions is well-known in the literature as the 2τ-effect. It applies to different situations, e.g., in the PPMS, where it occurs in the case of insufficient thermal coupling between the sample and platform [87]. Furthermore, a similar situation containing nuclear contributions with a finite spin-lattice relaxation time has been reported as well [93]. Yet, the exact solution for the temperature response depends on the setup resulting in subtle differences in Eq. 3.8.

In Fig. 3.9(b,c), two different parameter sets are exemplarily used to calculate the sample temperature response due to the heater power step ΔP following Eq. 3.8. The first graph illustrates the case of $t_\mathrm{n} = C_\mathrm{nuc}/k_\mathrm{n} \ll C_\mathrm{Sa}/k_\mathrm{SB}$. The temperature $T_\mathrm{Sa}(t)$ follows a single exponential behavior, which is even more obvious in the inset with $\Delta T(t)$ in a logarithmic scale. A linear behavior is obtained, which is followed by the convergence to the end temperature T_f. This indicates the lack of a second exponential contribution. This further justifies the fit

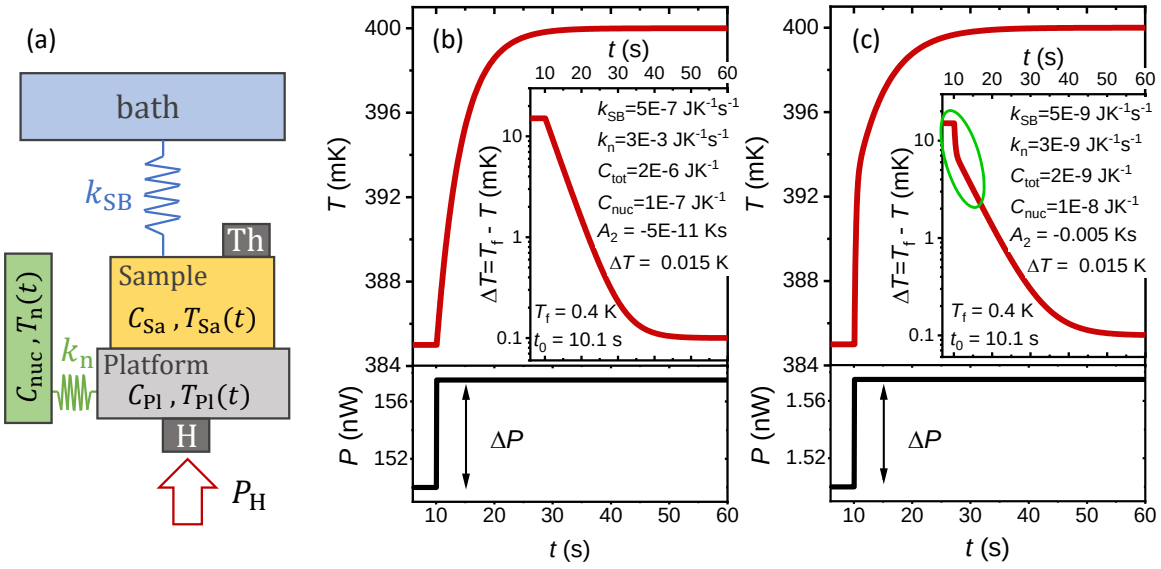

Figure 3.9. (a) Heat flow scheme of the relaxation method according to the setup in use [Fig. 3.8(a,b)]. Sample, platform, thermometer (Th) and Heater (H) are assumed to be ideally thermally coupled. The thermal link connects sample and thermal bath with the thermal conductivity k_{SB}. Nuclear spins may give rise to nuclear heat capacity contribution(s) C_{nuc}, which potentially are decoupled from the lattice. This is taken into account by the thermal conductivity k_n, which is directly linked to the spin lattice relaxation time $t_n = C_{nuc}/k_n$. (b) The case of small t_n, where the nuclear contribution is ideally coupled to the sample/ platform. The temperature response to a heater power step ΔP is calculated by Eq. 3.8 using the parameter given in the inset. The temperature relaxes to a final value T_f following a single exponential behavior, which can be easily fitted following Eq. 3.7. This way, the total heat capacity including the nuclear contribution is extracted. (c) In the case of large t_n, the temperature response now includes two exponential contributions easily identifiable in a logarithmic plot (inset). This can not be fitted by Eq. 3.7. Using Eq. 3.8 is highly challenging, if not impossible, because the number of possible solutions is abundant, and several starting parameter are unknown (k_n, C_{nuc}, C_{tot}, A_2). Even t_0 is challenging because of the slightly delayed temperature reaction. It is noting in passing that the plots of $\Delta T(t)$ in the inset of (b) and (c) are shifted by a constant offset of 0.1 mK to be able to illustrate the convergence of T_f for $t \to \infty$ in the logarithmic plot.

function Eq. 3.7 for such situations. In the second graph with $t_n \sim C_{Sa}/k_{SB}$, however, two different linear slopes are clearly visible in the inset certainly excluding the single exponential analysis.

There are two important outcomes from Eq. 3.8 and Fig. 3.9(b,c). On the one hand, a large sample heat capacity C_{Sa} naturally causes a single exponential temperature response making it possible to use Eq. 3.7. On the other hand, this is not fulfilled as soon as the sample heat capacity becomes small and comparable to the nuclear contribution. To be more precise, the spin-lattice compared to the sample relaxation time is decisive. In this case, C_{tot} can not be calculated straightforwardly by a double exponential fit with $\tau_{1,2}$ as free parameter using $C_{tot} = k_{SB} \cdot \tau_{1/2}$ or a similar simple expression. The sample temperature response $T_{Sa}(t)$ on the applied heater power P_H has to be fitted using the whole fit formula Eq. 3.8. This becomes fairly challenging, or even almost impossible with adequate accuracy, if several parameter besides C_{tot} are unknown.

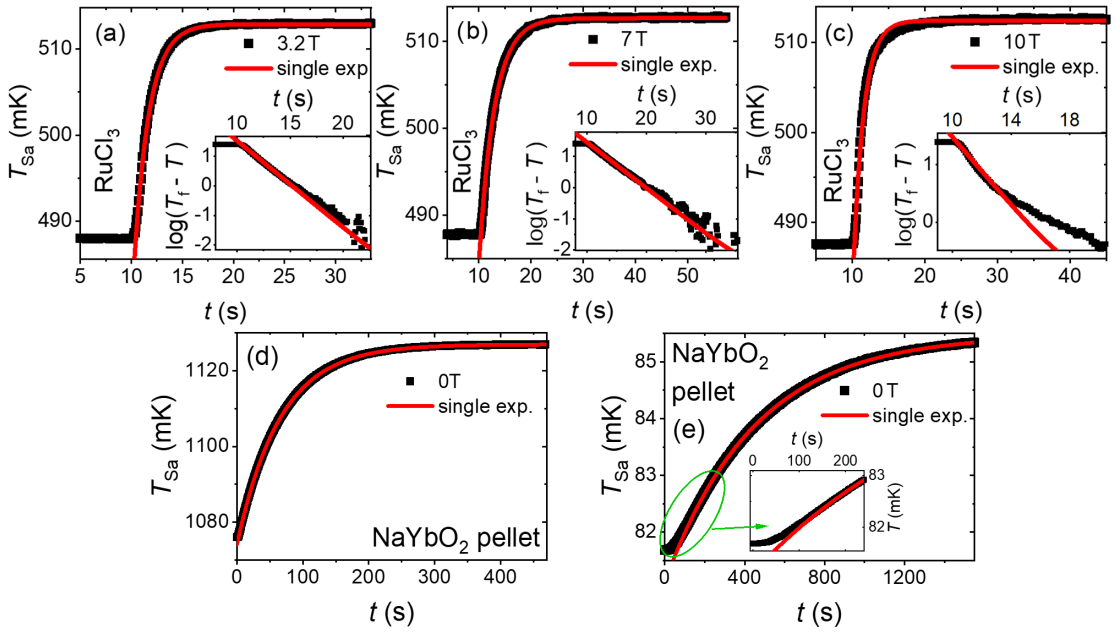

Figure 3.10. Potential problems of the relaxation method. (a)-(c) 2τ behavior in measurements of a sample with very tiny heat capacity below 1 K (α-$RuCl_3$), especially beyond 7 T. Published in Ref. [94], copyrighted by the American Physical Society. For moderate fields, a single exponential fit describes the data perfectly. At high fields, the 2τ effect is clearly observed in the inset of (c). This corroborates the influence of nuclear contribution here. The single exponential fit function can not be used for extracting the heat capacity. (d-e) Measurements of a $NaYbO_2$ powder pellet published in Ref. [68], copyrighted by the American Physical Society. In such powder samples, the grain boundaries decreases the internal thermal conductivity. At very low temperatures, this may result in thermal gradients along the sample height. Accordingly, the temperature measured by the thermometer increases delayed compared to the heater step. This is absent at high temperatures (d) but clearly present at low temperatures which is best visible in the inset of (e). As a result, the start of the fitting range has to be adapted. In order to avoid such issues, very thin pellets are advisable.

For α-$RuCl_3$ discussed in Ch. 5, the sample heat capacity at low temperatures becomes extremely small in the order of $0.01\,\mu J\,K^{-1}$ especially at fields beyond $B_c^{AF2} \sim 7 - 7.6\,T$. Fig. 3.10(a-c) shows the sample temperature responses $T_{Sa}(t)$ at 500 mK for three different fields pointing along the [110] direction (details in Ch. 5). At $B = 7\,T$ in (b), the sample heat capacity is relatively large and the single exponential behavior not surprising (inset). Both for (a) 3.2 T and (c) 10 T, the sample heat capacity is significantly smaller. Nevertheless, only (c) shows 2τ behavior prominently visible in the inset. This suggests that the 2τ origin is due to a decoupled nuclear contribution, which is enhanced in high magnetic fields. Furthermore, it excludes poor sample coupling because otherwise a 2τ effect should be observed in (a), too. This justifies the assumptions for the heat flow scheme in Fig. 3.9(a). Similar observations have been made in $KYbS_2$, where the heat capacity analysis at high fields showed pronounced 2τ behavior at very low temperatures.

Besides the 2τ effect, another peculiarity can complicate the analysis with the single exponential fit. Samples with weak internal thermal conductivity are prone to internal temperature gradients. As a consequence, the thermometer temperature increases delayed compared to the heater step. This is most prominent at very low temperatures because, in general, thermal conductivity decreases quickly in the millikelvin range [19]. Naturally, powder sam-

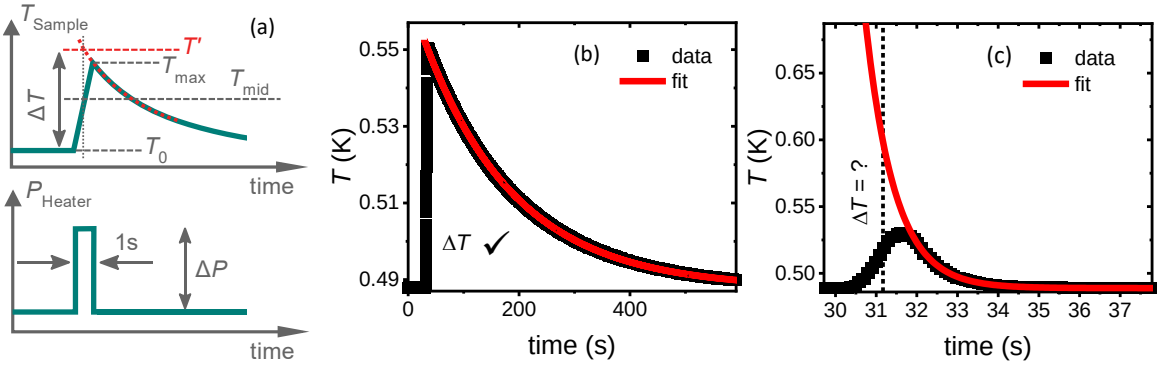

Figure 3.11. (a) Scheme of the quasiadiabatic pulse method, published in similar form in Ref. [95], copyrighted by the American Physical Society. A short heat pulse of 1 s is applied causing a heat input $\Delta Q = \Delta P \cdot 1\,\mathrm{s}$. Accordingly, the sample temperature steeply increases. In ideal adiabatic conditions, the increase would be ΔT, and the heat capacity can be calculated by $C = \Delta Q/\Delta T$. Due to the weak thermal link, however, heat flows to the thermal bath, which is responsible for the exponentially decreasing temperature after the heat pulse. This complicates an accurate ΔT determination, which has to be evaluated by an equal area construction using the extrapolated relaxation part. (b) Nearly perfect conditions for a precise ΔT determination with a rather weak thermal link compared to the sample heat capacity at the current temperature. The exponential fit and, thus, ΔT does not depend on the fitting range. On the other hand, this heat capacity data point takes roughly 10 min making the measurement time consuming. (c) Here, the thermal link is too strong in relation to the sample heat capacity preventing quasiadiabatic conditions. The exponential fit heavily depends on the fitting range making reasonable ΔT estimations impossible.

ples are predestined for this behavior due to abundant grain boundaries. In this work, a $NaYbO_2$ powder pellet was investigated [Ch.]4.2.2 showing this behavior. At elevated temperatures, $T_{\mathrm{Sa}}(t)$ immediately increases and can be described perfectly by a single exponential fit function over the whole time range [Fig. 3.10(d)]. Below 100 mK, however, the temperature reaction is clearly delayed which is better visible in the inset. After some time, $T_{\mathrm{Sa}}(t)$ follows again the single exponential behavior. Consequently, the lower fit limit is not set at $t = t_0 = 0\,\mathrm{s}$ but at $\sim$100 s. This has to be adapted manually for every relaxation curve.

As a closing remark, poor thermal coupling between sample and platform or sample and thermometer should result in similar delays in $T_{\mathrm{Sa}}(t)$.

3.4.2. Heat Pulse Method

As a second approach, the heat pulse method has been utilized for determining the sample heat capacity [96]. As starting condition, the sample is in thermal equilibrium at a constant temperature T_0. Next, a short heat pulse of 1 s is applied causing a heat input $\Delta Q = \Delta P \cdot 1\,\mathrm{s}$. This results in a steep temperature increase ΔT and a subsequent relaxation back to T_0 [Fig. 3.11(a)]. By assuming quasiadiabatic conditions, the heat capacity is calculated by $C = \Delta Q/\Delta T$ including sample and all other contributions.

There are two potential complications for this method. First, evaluating ΔT can be challenging. It is not simply defined as $\Delta T = T_{\mathrm{max}} - T_0$ using the peak temperature T_{max}. This would return too small ΔT values because the heat flow to the thermal bath reduces T_{max} compared to ideal adiabatic conditions. Consequently, the correct value has to be reconstructed. To this end, the relaxation part after the pulse is fitted by a single exponential

function and extrapolated. By an equal area construction, T' is identified and employed for calculating $\Delta T = T' - T_0$ [Fig. 3.11(a)]. For this method, nearly ideal conditions are fulfilled in Fig. 3.11(b). The fit function describes the data perfectly and is nearly independent on the fit range. The long relaxation time compared to the pulse corroborates the quasiadiabac conditions and, therefore, T' can be determined fairly accurately. It becomes problematic, however, when this is not fulfilled [Fig. 3.11(c)]. Here, the relaxation time is comparable to the pulse. The fit strongly depends on the fit range preventing a reasonable analysis. Accordingly, the thermal link [Fig. 3.8(a)] should always be chosen carefully in respect to the relaxation time, which is connected to the sample heat capacity, $\tau = C_{\mathrm{Sa}}/\kappa_{\mathrm{SB}}$. This guarantees a compromise between a slow enough relaxation process providing quasiadiabatic conditions ($\tau \gg 1\,\mathrm{s}$) and an acceptable waiting time to reach the desired lowest temperature.

The second potential problem has already been discussed in Sec. 3.4.1. As soon as there is a strongly decoupled heat capacity contribution resulting in 2τ behavior, the heat pulse analysis becomes fairly challenging. It often results in an overshoot of the temperature with a very steep temperature increase and decrease followed by the slower relaxation part. It is not obvious how to evaluate ΔT in this case. As a first approximation, it is sometimes possible to restrict to a single exponential function refering to the slower relaxation part. However, this should be crosschecked by the relaxation method.

In general, both relaxation and pulse method confirm each other with high accuracy [Fig. 3.12(a)]. The software written during this work offers different measurement options regarding pulse and relaxation method. For temperature dependent heat capacity measurements (T sweep), combining both methods is convenient because the relaxation method naturally sets a new starting temperature for a subsequent heat pulse. This way, two data points are acquired by two independent methods, respectively, at roughly identical temperatures. If it is preferable to save time, T sweeps can also be performed by relaxation steps alone. For field dependent measurements (B sweep), either pulse or relaxation method can be applied at a predefined temperature and subsequent fields.

As a closing remark, it should be mentioned that, in principle, several samples can be investigated at the same time because the heat capacity cells can be stacked. The new software is not restricted to a predefined number of samples measured in parallel. The limiting parameter, however, are currently the number of heat capacity cells (4) as well as the available LakeShore Bridges (3). Furthermore, it is problematic that the lower cells are not exactly located in the field center anymore. If measurements have to be performed in magnetic fields, the whole inset has to be lifted and suitable spacers used. Nevertheless, it is advisable to use as many cells as possible for each run if there are enough samples available. Especially for characterizing many samples in zero field, this can save a lot of time.

3.4.3. Background Subtraction

For samples with very tiny heat capacity, it is crucial to carefully subtract the background contribution, which is also called "addenda" in the following. It has to be determined by independent measurements using the setup described in Fig. 3.8(a,b) without the sample. Thereafter, the addenda is subtracted from the measurement including cell, adhesives, thermometer, and sample in order to obtain the sample's heat capacity [Fig. 3.12(b)],

$$C_{\mathrm{Sa}} = C_{\mathrm{tot}} - C_{\mathrm{add}}. \tag{3.9}$$

As already mentioned in Sec. 3.4.1, the 2τ effect can complicate the analysis. This behavior also emerges in the addenda measurement most likely due to the nuclear contribution of

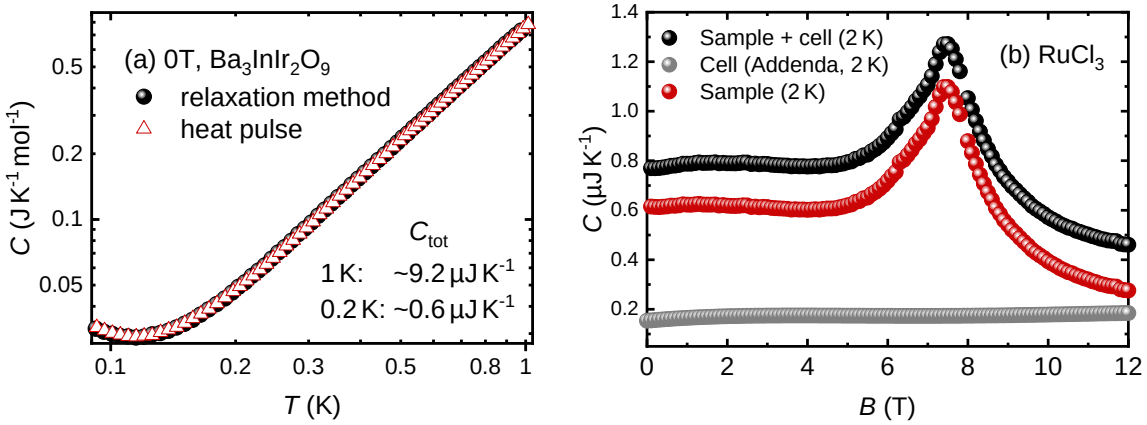

Figure 3.12. (a) Comparison between pulse and relaxation method for $Ba_3InIr_2O_9$ at 0 T. Both measurements match perfectly. (b) Background (Addenda) subtraction for α-$RuCl_3$ at 2 K. The addenda (grey) has been determined in an independent measurement using the setup from Fig. 3.8(a,b) without sample. The sample heat capacity (red) is obtained by the subtraction of the background from the total heat capacity (black). In this work, that procedure is usually only important above 1 K because of the rapidly diminishing background heat capacity towards low temperatures. Below 1 K, it is only mandatory for few samples with tiny heat capacity. For comparison, the absolute heat capacity of $Ba_3InIr_2O_9$ in (a) amounts to 0.5 µJ K^{-1} and 9.2 µJ K^{-1} at 0.2 K and 1 K, respectively.

aluminium in the sapphire platform (Al_2O_3). As a result, determining the background below 1 K is not possible at the moment. At first glance, this is highly problematic for measurements in the milikelvin range. Fortunately, the background becomes fairly tiny below 1 K in the order of 10 nJ K^{-1}. Consequently, this does not affect the low temperature behavior of the majority of samples measured in this work with typically $\geq$ 1 µJ K^{-1} around 1 K. Nevertheless, the background should be always kept in mind. Especially at temperatures far above 1 K, the background might become large enough to play a role. Additionally, samples like α-$RuCl_3$ with rapidly vanishing heat capacity below $T_N \sim 7$ K definitely require the background subtraction.

3.5. Magnetic Grüneisen Parameter Γ_{mag}

Measuring the magnetic Grüneisen parameter Γ_{mag} via the magnetocaloric effect (MCE) requires quasiadiabatic conditions such that Eq. 2.42 from Sec. 2.5 is fulfilled [83],

$$\Gamma_{mag} = \frac{1}{T}\left(\frac{\partial T}{\partial B}\right)_S .$$

In this case, Γ_{mag} can be determined by applying a weak oscillating magnetic field B_{AC} with an amplitude ΔB superimposed on the field from the main magnet B_{main}. Due to the MCE, this induces oscillations ΔT of the sample temperature. For this purpose, the heat capacity setup can directly be used and both heat capacity and Grüneisen parameter measured during the same run. In Fig. 3.13(a), very clear temperature oscillations are shown produced by the magnetic field oscillations with frequency f around an offset B_0, which is very close to zero. The field oscillations are determined indirectly by a measurement of the modulation coil current via the voltage drop at a resistance of 3.75 mΩ. A current of 7.63 A

through the coils produces a modulation field with $\Delta B = 25\,\mathrm{mT}$ [97]. Consequently, the ratio $25\,\mathrm{mT}/7.63\,\mathrm{A}$ can be used for calculating $B_{\mathrm{AC}}(t)$ from the $I_{\mathrm{Coil}}(t)$ measurement. The AC field is superimposed by the static field produced by the main magnet, here $B_{\mathrm{main}} = 2.7\,\mathrm{T}$. The static field, however, does not induce a MCE and is not included in Fig. 3.13(a) to only visualize the AC part of the magnetic field. Consequently, the main magnetic field does not need to be taken into account in the following fit functions. In order to extract ΔB and ΔT, the raw data are fitted by

$$\begin{aligned} B_{\mathrm{AC}}(t) &= \Delta B \sin\left[2\pi f(t-t_0)\right] + B_0, \\ T(t) &= \Delta T \sin\left[2\pi f(t-t_0)\right] + \Delta T_{2\mathrm{f}} \cos\left[4\pi f(t-t_0)\right] + b_0 + b_1 t + b_2 t^2. \end{aligned} \tag{3.10}$$

In general, a phase shift t_0 has to be considered. Ideally, both $B(t)$ and $T(t)$ obtain the same phase shift, but in reality they may slightly differ due to delayed temperature response. Furthermore, gradual temperature shifts are taken into account by a polynomial function $b_0 + b_1 t + b_2 t^2$ if, e.g., the sample is still relaxing towards a constant temperature. Most importantly, if eddy currents occur, $I_{\mathrm{eddy}} \sim \mathrm{d}B/\mathrm{d}t = 2\pi f \Delta B \cos(2\pi f t)$, a second oscillation arises. It shows a doubled frequency compared to the MCE because eddy current heating is proportional to the square of the eddy current, $I_{\mathrm{eddy}}^2 \sim f^2 \Delta B^2 [1 + \cos(2\pi 2 f t)]$ [83]. Consequently, a second oscillating part with doubled frequency is required capturing the so-called $2f$ oscillations. They occur in metallic samples and can seriously hinder an accurate analysis [83]. But also insulating materials with small absolute heat capacity may show $2f$ oscillations due to the background signal from, e.g., metallic wires in the cell. In Fig. 3.13(a), however, this problem is not present, and the fit function perfectly matches the raw data. By averaging all temperature data points, Γ_{mag} is calculated at B_{main} and T_{avg} using Eq. 2.42.

An example for $2f$ oscillations is presented in Fig. 3.13(b) for α-$RuCl_3$. At 7.6 T (upper panel), the sample heat capacity is comparably large, and no $2f$ behavior is visible. Beyond 8 T, the heat capacity rapidly decreases. Accordingly, the $2f$ signal increases (middle) and eventually dominates the whole temperature response (lowest panel). Nevertheless, the fit still describes the raw data well allowing evaluation of Γ_{mag}.

On the other hand, it is advisable to avoid $2f$ whenever possible to improve the accuracy. In general, eddy currents are efficiently suppressed by lowering the amplitude ΔB and/ or the frequency f. Yet, the latter is at the expense of fast measurements. Furthermore, a lower limit for the frequency is naturally given by the sample relaxation time τ (see Sec. 3.4.1). In order to maintain quasiadiabatic conditions, $1/f \ll \tau$ has to be fulfilled. This prevents strong heat flow to the thermal bath during an oscillation period, which would result in a decreased ΔT. For that reason, the frequency could not be reduced below $\sim 0.1\,\mathrm{Hz}$ in the case of α-$RuCl_3$ with its tiny heat capacity and, consequently, rather fast relaxation with small τ. At the same time, an upper frequency limit exists as well. If the oscillation is too fast, the internal thermalization can not keep up. In both cases of too high or too small frequency, ΔT and, accordingly, Γ_{mag}, is underestimated. Therefore, the frequency has to be chosen carefully [83]. To ensure an adequate frequency choice, constant values of Γ_{mag} has been checked for at least two different frequencies.

Compared to the heat capacity, the background subtraction is more subtle because the measured $\Gamma_{\mathrm{mag,tot}}$ comprises two contributions, $\partial M_{\mathrm{tot}}/\partial T$ and C_{tot} (Eq. 2.41 in Sec. 2.5), potentially both being influenced by the cell background [95]:

$$\Gamma_{\mathrm{mag,tot}} = -\frac{\partial M_{\mathrm{tot}}/\partial T}{C_{\mathrm{tot}}} = -\frac{\partial M_{\mathrm{Sa}}/\partial T + \partial M_{\mathrm{Cell}}/\partial T}{C_{\mathrm{Sa}} + C_{\mathrm{Pl}}} = \frac{\Gamma_{\mathrm{mag,Sa}} \cdot C_{\mathrm{Sa}} + \Gamma_{\mathrm{mag,Cell}} \cdot C_{\mathrm{Pl}}}{C_{\mathrm{Sa}} + C_{\mathrm{Pl}}}. \tag{3.11}$$

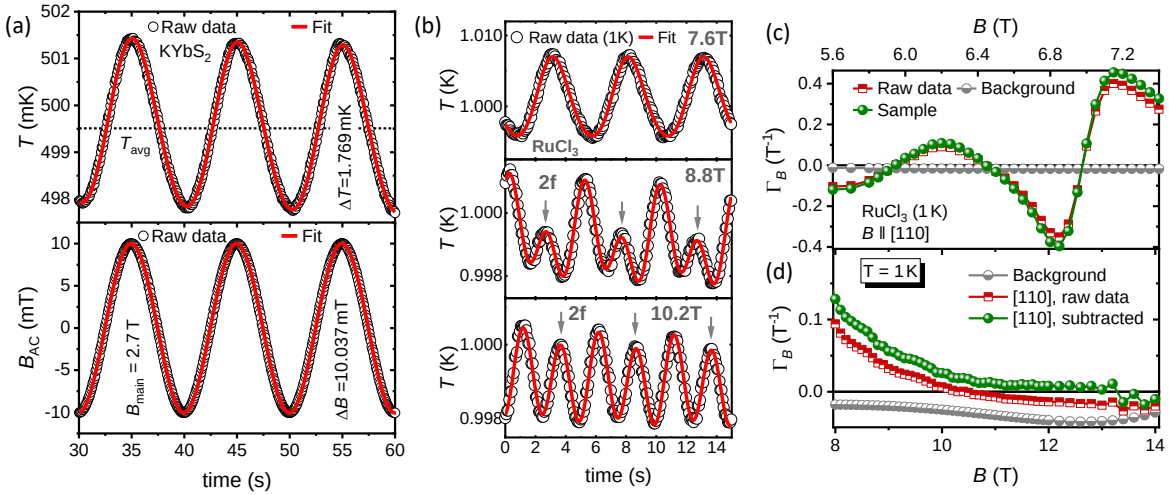

Figure 3.13. (a) Determination of Γ_{mag}. The oscillating magnetic field B_{AC} induces temperature oscillations because of the magnetocaloric effect (MCE) in the investigated material $KYbS_2$. The fit functions Eq. 3.10 perfectly match the raw data and are used to extract ΔB and ΔT for calculating Γ_{mag} at the main magnetic field B_{main} and T_{avg}. (b) Example for $2f$ contributions in the insulator α-$RuCl_3$ published in Ref. [95], copyrighted by the American Physical Society. Beyond 8 T, the sample heat capacity becomes small and background contributions from e.g. wires important. That results in additional oscillations with doubled frequency due to eddy current heating complicating accurate evaluation of Γ_{mag}. (c,d) Background subtraction following Eq. 3.12 for samples with small heat capacity (here α-$RuCl_3$, published in Ref. [94], copyrighted by the American Physical Society). The position of the characteristic features remain unchanged, and only the amplitude is slightly changed after subtraction (compare "Raw data" and "Sample", upper panel). Yet, this becomes important for very small signals like in α-$RuCl_3$ beyond 8 T, see panel (d). Here, the raw data become negative due to the background while the subtracted data stay positive and go to zero. In such cases, a subtraction is definitely required.

Here, $\Gamma_{\mathrm{mag,Cell}}$ and C_{Pl} denote the background contribution from the platform or, more general, the whole cell including e.g. wires. They both are measured in an independent run without the sample. From Eq. 3.11, the following expression can be derived for extracting the true Grüneisen parameter of the sample $\Gamma_{\mathrm{mag,Sa}}$,

$$\Gamma_{\mathrm{mag,Sa}} = \Gamma_{\mathrm{mag,tot}} + \frac{C_{\mathrm{Pl}}}{C_{\mathrm{Sa}}} \left(\Gamma_{\mathrm{mag,tot}} - \Gamma_{\mathrm{mag,Cell}} \right). \tag{3.12}$$

As soon as $C_{\mathrm{Sa}} \gg C_{\mathrm{Pl}}$, then $\Gamma_{\mathrm{mag,Sa}} = \Gamma_{\mathrm{mag,tot}}$ and, consequently, no background subtraction is required. For samples with small heat capacities, however, the background should be subtracted carefully. Fig. 3.13(c,d) shows exemplarily the subtraction for α-$RuCl_3$ at 1 K. The characteristic features like sign changes or maxima remain unchanged [Fig. 3.13(c)], and only the amplitude changes slightly. Nevertheless, the subtraction becomes crucial at high fields, where both heat capacity and Γ_{mag} rapidly decrease [Fig. 3.13(d)]. $\Gamma_{\mathrm{mag,tot}}$ (raw data) becomes negative above $\sim$ 10 T. Only upon subtracting the background following Eq. 3.12, it can be shown that $\Gamma_{\mathrm{mag,Sa}}$ goes to zero while staying positive. The data scattering above $\sim$ 13.5 T presumably originates from the strong $2f$ oscillations and the very tiny sample signal. In general, a paramagnetic material is expected to show positive Γ_{mag} because of $\partial M/\partial T < 0$, which converges towards zero upon approaching the field-polarized state.
As a closing remark to the section of the Grüneisen parameter, a potential problem in the

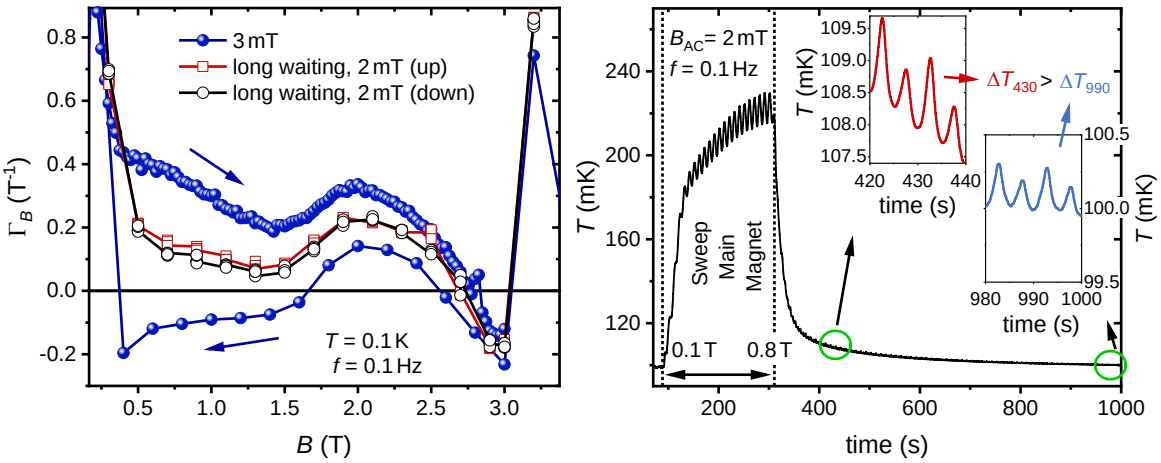

Figure 3.14. (a) Magnetic Grüneisen measurement $\Gamma_{\mathrm{mag}}(B)$ of $KYbS_2$ at low temperature, $T = 100\,\mathrm{mK}$, and an oscillation frequency of $f = 0.1\,\mathrm{Hz}$. The blue data points suggest a strong hysteresis between up and down sweep. This behavior is absent when long waiting times are applied before the measurement (black and red points). Consequently, the hysteresis is an artefact. Details can be found in the text. (b) Temperature of $KYbS_2$ over time showing a possible scenario of taking raw data for one Grüneisen ratio data point. Details again explained in the text. A modulation field of 2 mT and a frequency of 0.1 Hz is kept constant during the whole time. Between 100 s and 300 s, the main magnet is swept to 0.8 T increasing the temperature above 200 mK. Surprisingly, the temperature oscillations are not constant after the field sweep is finished. The inset shows the temperature over 20 s at t ∼400 s and t ∼1000 s, respectively. Clearly, the oscillations at t ∼1000 s have a smaller amplitude. It could also be shown that the sign of the oscillations can be reversed shortly after the field sweep, depending on the field sweep direction. Therefore, the measurement results depended on the waiting time after the sweep. This behavior was only found in the region of the hysteresis artefact.

measurement process is explained. It was observed in one of the last runs and neither could be solved nor addressed to a specific issue. Fig. 3.14(a) shows the field dependent magnetic Grüneisen parameter Γ_{mag} at 0.1 K. All curves were measured with the frequency $f = 0.1\,\mathrm{Hz}$ for $KYbS_2$ at very low temperatures, $T = 100\,\mathrm{mK}$. The blue data points suppose a hysteresis between up and down sweep in the field range of 0.3 and 3 T. The down sweep even shows a sign change at ∼ 1.7 T. This was fully reproducable in several measurements even though $2f$ oscillations complicated the analysis. If there was a long waiting time t_{wait} before the measurement, however, then this strange hysteresis was not observable anymore.

In order to explain that curiosity, the measurement procedure has to be explained in more detail. Each data point in Fig. 3.14(a) is determined in the following manner. First, the magnetic field is swept to the target value B_{i}. In general, this increases the sample temperature and, accordingly, the temperature has to relax to the desired value. In the measurement program, this is guaranteed by a fixed waiting time t_{wait}. The exact value has to be adjusted before starting the program and depends from the sample relaxation time τ. It is always the same for each data point. As a general rule of thumb, t_{wait} is usually set in the range between 30 s and 10 min. After that time, the temperature and field oscillations are measured for several periods and analysed in order to calculate Γ_{mag}. Subsequently, the measurement protocol is restarted by sweeping the field to $B_{\mathrm{i+1}}$.

Exemplarily, Fig. 3.14(b) depicts a possible scenario for measuring a Γ_{mag} point at 0.8T and ∼ 110 mK. The modulation coil parameter are fixed to 2 mT and 0.1 Hz. As described

above, the main magnet is swept to 0.8 T raising temperature up to 220 mK. Furthermore, the temperature oscillations are strongly enhanced because the total change of the field amplitude is magnified by the main magnet. Subsequently, the temperature rapidly decreases but the temperature does not stabilize even after more than 10 min. More importantly, the temperature oscillations are not constant, too. At $\sim$ 400 s, the peak-to-peak amplitude including the $2f$ oscillations are roughly 1 mK. In contrast, the peak-to-peak value at 1000 s is only 0.3 mK. The amplitude ΔT_1 is affected in the same way, which was confirmed by fitting the oscillations after different waiting times. As a consequence, the Γ_{mag} results depend on the chosen t_{wait} values, which is highly problematic. This behavior was only present in the $KYbS_2$ measurements at temperatures far below 250 mK and in the field range where the putative hysteresis appears. Most interestingly, it was dependent on the previous main magnetic field, which explains the hysteresis for short waiting times. Yet, waiting a long time before measuring the oscillations seems to guarantee reasonable Γ_{mag} evaluation as shown in Fig. 3.14(a).

It could be shown that the temperature oscillations show the very same behavior of "damped" $2f$ oscillations when the situation is vice versa, namely, the modulation coil is ramped up to e.g. 2 mT at a constant main magnetic field. Strangely enough, ramping the modulation coil to 0 and back again to 2 mT does not result in the same "damping" curve because the $2f$ appeared to be already weaker.

Unfortunately, for all observations, it can only be conjectured about the reason of this odd behavior. Maybe changing the field induces a current flow in a weakly damped resonant circuit, and its oscillations may influence the modulation coil. But, to be honest, this is purely speculative and not a satisfying explanation. As a guide for future measurements, however, it might be advisable to check the Γ_{mag} dependence on different waiting times at the lowest measured temperature, or to measure once in up and down steps. It is not clear at the moment if this is a general problem in the MK 4 or only specific to $KYbS_2$.

3.6. Faraday Magnetometer

Investigating the magnetization is crucial for understanding the underlying physics of magnetic materials but challenging at very low temperatures. Using the DC method or the vibrating sample magnetometry (VSM) option like in the Magnetic Property Measurement System (MPMS from Quantum Design) requires large in-situ movements of the sample. Therefore, this is not applicable in a dilution refrigerator because mechanical friction generates strong heating. As a consequence, a static method is required in such demanding environments. To this end, a Faraday magnetometer has been installed for this work.

The setup is sketched in Fig. 3.15(a) and mainly follows Sakakibara *et al.* [98]. The central part is the capacitor formed by a fixed brass plate and the Stycast 1266 stamp with its silver epoxy coated bottom side. Great care has to be taken to guarantee a parallel plate alignment. The sample is placed on top of the stamp, which is fixed by a pair of phosphorbronze wires with a diameter of 0.125 µm. This way, the sample platform and, consequently, the upper capacitor plate can slightly move up or down upon a force acting along the z-direction. It will later become clear that this force depends on the sample magnetization $\mathbf{M}$. In contrast to the MPMS methods, this movement is in the range of µm and does not heat the setup. The lower capacitor plate is carefully insulated against the remaining metallic cell body. Fig. 3.15(b) depicts a magnetometer in top view under the microscope. The upper plate from the Stycast stamp (not visible in this perspective) is electrically contacted by a thin gold wire

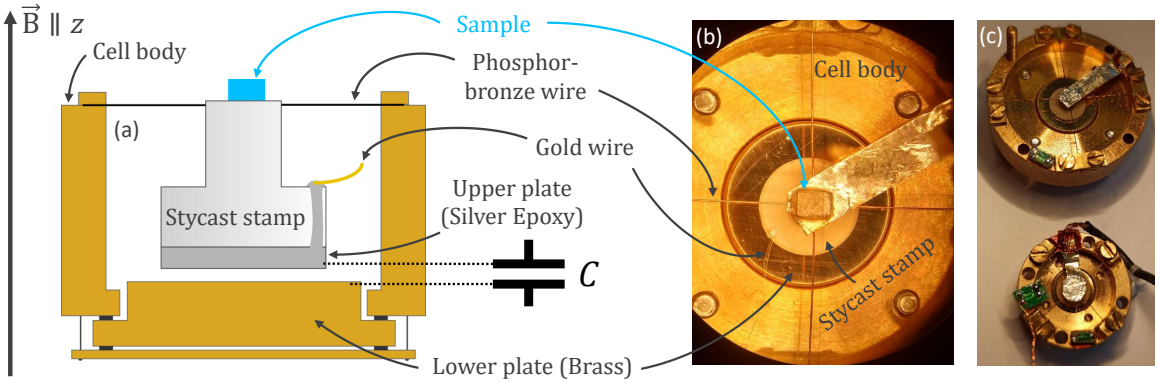

Figure 3.15. (a) Sketch of the Faraday Magnetometer. (b) Top view of a magnetometer under the microscope. (c) The upper magnetometer is shown in (b) and was used for the measurements presented in this work. The lower device was developed for measurements in combination with two Goniometer in order to minimize disturbing torque effects.

($\varnothing = 25\,\mu m$), which is barely viewable in the current magnification. The larger magnetometer shown in Fig. 3.15(c) was used for the magnetization measurements presented in this work. The smaller one was developed to be combined with two goniometers to minimize disturbing torque effects. The goniometers can be controlled in-situ, which limits the diameter of the magnetometer dimensions. Details are given in the end of this section.

In the following, the measuring principle is explained in detail. Additionally to the main magnetic field in z-direction, an inhomogenic field is applied by two identical coils with same absolute value of current but in opposite directions[6]. In good approximation, the magnetic field strength in the center between the coils changes linearly along z [97] generating a constant field gradient $\partial B_z/\partial z$ for this direction. The sample holder is directly located in that region, and, accordingly, a force $\mathbf{F}$ acts on the sample,

$$\mathbf{F} = \nabla(\mathbf{M} \cdot \mathbf{B}) = \nabla(M_x B_x + M_y B_y + M_z B_z). \tag{3.13}$$

Since $M_{x,y,z}$ does not depend on the direction, and the lateral field gradient can usually be assumed to be negligible compared to the vertical component [98], $\partial B_x/\partial x, \partial B_y/\partial y \ll \partial B_z/\partial z$, this can be simplified to

$$F_x = F_y = 0, F_z = M_z \frac{\partial B_z}{\partial z}. \tag{3.14}$$

The resulting force changes the distance between the capacitor plates by δ which can be detected by an Andeen-Hagerling AH 2500A/ AH 2550A capacitance bridge. The distance change δ is directly proportional to $\mathbf{F}_z$ under the assumption of parallel capacitance plates. Using $C = \epsilon_0 A/d$ for the capacity, this can be expressed as [98]

$$F_z \sim \delta = d_0 - d = \epsilon_0 A \left(\frac{1}{C_0} - \frac{1}{C} \right), \tag{3.15}$$

where C_0 and C denote the capacity value without and with applied gradient field and a distance of d_0 and d, respectively, while ϵ_0 stands for the dielectric constant and A for the

[6] The same coils are used like for the Grüneisen measurement but with a different connector. This way, the current direction can be switched for additionally applying either a small uniform magnetic field or a gradient field. Both are additional to and independent of the main magnetic field.

capacitor area. The sign of the force depends on the definition of the z-direction. In the choice of Fig. 3.15(a), a negative gradient field increases the capacity by a downwards force. By combining Eq. 3.14 and Eq. 3.15, the z component of the magnetization can be linked to the capacitance change,

$$M_\mathrm{z} = k_0 \left(\frac{1}{C_0} - \frac{1}{C} \right). \tag{3.16}$$

The proportionality constant k_0 includes the gradient field $\partial B_\mathrm{z}/\partial z$ as well as all other constant parameters related to the setup. For determining the field dependent magnetization, the measurement process comprises two parts. First, the gradient field is set to zero and the main magnetic field is slowly swept to the desired value. In parallel, the capacity $C_0(B)$ is measured. This measurement is advisable to eliminate disturbing torque effects in the analysis. Otherwise, that can lead to a capacity change even without gradient field, as explained later. Second, this procedure is repeated but now with a gradient field $\partial B_\mathrm{z}/\partial z \neq 0$ for evaluating $C(B)$. The magnetization $M(B)$ is calculated by using Eq. 3.16 with $C_0(B)$ and $C(B)$. Analogically, that protocol can be used for temperature dependent magnetization measurements. It is advisable to check at least once in a run, preferably at the lowest measured temperature, if there is a hysteresis between up and down sweep because of a too fast sweep rate.

In principal, the maximum gradient field values specified for the gradient coils in the MK 4 are $\pm 1.5\,\mathrm{T/m}$. Yet, the amplifier used in the setup limits this to $\sim \pm 1\,\mathrm{T/m}$, which is rather small compared to other laboratories with superconducting gradient coils and $\pm 10\,\mathrm{T/m}$ [98, 99]. It can be shown, however, that

$$M_\mathrm{z} = k_1 \left(\frac{1}{C_{-1\,\mathrm{T/m}}} - \frac{1}{C_{+1\,\mathrm{T/m}}} \right), \tag{3.17}$$

with $C_{\pm 1\,\mathrm{T/m}}$ being the capacity at the respective field gradient and $k_1 = k_0/2$. This way, the signal to noise ratio can be improved by a factor of 2 by measuring $C_{-1\,\mathrm{T/m}}(B)$ instead of $C_0(B)$.

In Fig. 3.16(a), an exemplary field dependent capacity measurement for $YbMgGaO_4$ along the c-direction at 2 K is presented. For better comparison, three different gradient fields are used. For $0\,\mathrm{T/m}$, up and down sweep are perfectly on top of each other confirming an adequate sweep rate. Both $\pm 1\,\mathrm{T/m}$ are symmetric around $0\,\mathrm{T/m}$ and used for calculating the magnetization $M(B)$ shown in the inset. For absolute units, it has to be compared with a MPMS measurement at the same temperature and scaled accordingly. Furthermore, the reliability of the measurement is confirmed by obtaining a good scaling of the two $M(B)$ data sets from the Faraday magnetometer and the MPMS, respectively.

In the following, the origin of the capacitance change at zero gradient field is explained. For zero gradient field, the force F_z should be also zero according to Eq. 3.14. Anisotropic materials, though, can experience another force due to the torque effect τ. In the example of the strongest possible anisotropy, the Ising model with $g_{\parallel z} \neq 0$ and $g_{\perp z} = 0$, a magnetic moment can only be induced along the z-direction (easy axis). Consequently, an Ising magnet with the magnetic moment $\mathbf{m}$ in a magnetic field $\mathbf{B}$ experiences a torque $\tau = \mathbf{m} \times \mathbf{B}$ to minimize its potential energy $U = -\mathbf{m} \cdot \mathbf{B}$. In real materials, a field oriented perpendicular to the easy axis magnetizes the sample as well because $g_{\perp z} = 0$ never strictly holds true. That direction is denoted as hard axis/ plane. Nevertheless, each material tends to align its easy axis parallel to the field for the same reason as the pure Ising magnet. Regarding the Faraday magnetometer, this leads to the tilting of the sample including the stamp with

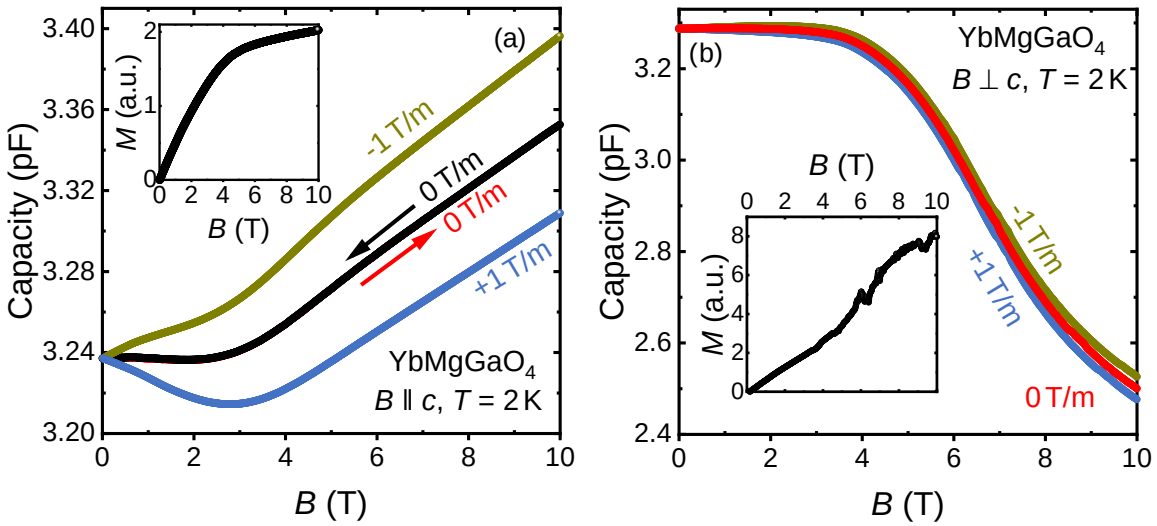

Figure 3.16. (a) $YbMgGaO_4$ at 2 K as an example measurement for determining the field dependent magnetization $M(B)$ along the easy direction (inset, alternative units). The gradient fields $\pm 1\,\mathrm{T/m}$ are symmetric around $0\,\mathrm{T/m}$ and comparable to the additional torque effect responsible for the capacity change at $0\,\mathrm{T/m}$. (b) Measurement at the same temperature but the field perpendicular to the easy axis. The torque effect dominates the whole field range making a reasonable analysis impossible (inset).

the capacitor plate. Therefore, the capacitance can change even for $\partial B_z/\partial z = 0\,\mathrm{T\,m^{-1}}$ due to the torque effect possibly disturbing the measurement, especially when the plates start to strongly deviate from being parallel. The torque effect is most pronounced for highly anisotropic samples ($g_\parallel \gg g_\perp$) and fields far away from being parallel to the easy axis.

In the example of $YbMgGaO_4$ in Fig. 3.16(a), a weak anisotropy is present with the easy axis along the crystallographic c-direction with $g_\parallel = 3.7$ and $g_\perp = 3.0$ [100]. The magnetic field is intended to be exactly along c, but a small misalignment gives rise to the torque effect in zero gradient field. The analysis, however, allows to obtain reliable results, as shown by the presented magnetization $M(B)$ in the inset. In general, this becomes more problematic if the field is applied perpendicular to the easy axis. If a sample misalignments exists, a pronounced torque effect can be expected. Accordingly, the analysis is severely affected. Such a questionable situation is presented in Fig. 3.16(b) for $YbMgGaO_4$ with the field close to the hard ab-plane perpendicular to the easy axis c. The torque dominates the whole field range being greatly enhanced compared to the difference between the $\pm 1\,\mathrm{T/m}$ curves. The resulting calculated magnetization curve reveals many jumps and can not be used.

In principle, such a problem can be circumvented if the magnetic field is applied exactly parallel to the hard axis. Due to the symmetric arrangement, no magnetization along the easy axis is induced and the torque effect suppressed. For realizing this scenario, an in-situ tilting of the magnetization cell is ideal, which is possible by using two goniometers (attocube, ANGt101res-B1-112, ANGp101-A7-045). Both cover angles roughly between $-3...3°$ along perpendicular directions spanning a range large enough for accounting typical sample misalignments of $\sim 1°$. Due to space limitations, a smaller magnetization cell was developed [Fig. 3.15(c)]. It was first tested at 4.2 K without goniometer using a sample of $YbMgGaO_4$ with the field applied parallel to the c-direction.

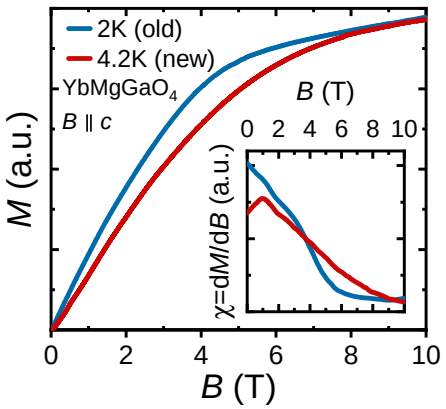

Figure 3.17. First test of the smaller Faraday magnetometer mounted without goniometer using $YbMgGaO_4$ at 4.2 K and $B \parallel c$. The magnetization curve measured in the larger magnetometer at 2 K [Fig. 3.16(a)] was used for scaling at 10 T. The comparison indicates reasonable results from the new magnetometer, except of some problems at lower fields (inset).

The resulting magnetization curve is shown in Fig. 3.17 in comparison to the magnetization at 2 K from Fig. 3.16(a) determined by the older and larger magnetometer. Both curves are scaled to overlap at 10 T, where the material saturates. This comparison indicates reasonable results of the new magnetometer, except of some problems at lower fields (inset of Fig. 3.17). In a next step, the goniometers have to be mounted as well to be able to align the sample. In-situ rotation in the millikelvin range strongly heats the setup, and all alignment steps to eliminate the torque effect should be performed at elevated temperatures of e.g. 4.2 K. The corresponding settings are then kept during the whole run allowing, in principle, measurements at millikelvin temperatures. During this work, the extremely time consuming tests for the goniometer setup could not be finished yet. Among other difficulties, the wiring is particularly challenging because the setup requires somewhat flexible cables due to the goniometer movements. Otherwise, the goniometer might be blocked with impending damages, or the electrical contact to the capacitor plates might be broken and lost. Clearly, this calls for further optimization in order to realize previously impossible measurements along the hard axis of anisotropic materials.

4. Yb^{3+} on a Triangular Lattice

Very often, theoretical breakthroughs inspire experimentalists to expand the frontier of the unkown – but sometimes, it is the other way round. The discovery of $YbMgGaO_4$ in 2015 opened a completely new field in the context of quantum spin liquids (QSL). It is a triangular lattice antiferromagnet (TLAF) based on the rare-earths ion Yb^{3+} and does not show long-range order down to at least 50 mK. It triggered enormous interest in exploring 4f ions in the triangular configuration and lead to the discovery of several possibilities to stabilize a QSL phase in the theoretical phase diagram. The microscopic origin of the unusual behavior in $YbMgGaO_4$, however, remains vividly debated because of its site-mixing of the non-magnetic ions Mg^{2+}/Ga^{3+}. Therefore, $YbMgGaO_4$ fuelled the search for rare-earth TLAF without structural disorder that was eventually successful in 2018 in the $AYbX_2$ family with $NaYbO_2$, $NaYbS_2$, or $KYbS_2$, to name just a few potential QSL candidates. Further compounds are already available or will certainly follow due to the abundant possible variations in this material class. Furthermore, beyond QSL physics, TLAF exhibit a plethora of field-induced phases that are still subject to active research. Consequently, the $AYbX_2$ compounds offer a rich playground for benchmarking recently developed theoretical concepts.

In this chapter, several Yb^{3+} TLAF materials are investigated. Each section starts with a summary of relevant information about the compound, respectively, followed by the thermodynamic measurements performed in this work. For $YbMgGaO_4$, the possible scenario of spin freezing is investigated as well as its unexpected field evolution. $KYbS_2$ and $NaYbO_2$ are thoroughly characterized using specific heat and magnetic Grüneisen parameter. The field-temperature phase diagram is established for both materials. Finally, $KBaYb(BO_3)_2$ is introduced as a potentially frustrated magnet with very weak interactions. This allows possible applications for adiabatic demagnetization refrigeration down to the millikelvin range.

4.1. Influence of Disorder in the QSL Candidate $YbMgGaO_4$

The report on the synthesis of $YbMgGaO_4$ attracted immediate attention. Many publications appeared in the last years, and excellent reviews are already available [7, 101]. The following summary of relevant results on $YbMgGaO_4$ are mainly based on Ref. [7]. Despite a Curie-Weiss temperature of $\Theta_{CW} \sim -4\,K$, heat capacity measurements did not show any long-range magnetic order in this material down to 60 mK. Its residual entropy becomes too small to expect a phase transition below 60 mK, and, thus, it most likely remains disordered even at 0 K [36]. $YbMgGaO_4$ was an extremely promising example of a real-world QSL candidate on a triangular lattice – especially intriguing since that geometrical arrangement has been the theoretical prototype to host a QSL [2]. However, the microscopic origin of this potential QSL in $YbMgGaO_4$ was not understood. Anderson's original proposal of a QSL in the isotropic nearest-neighbor (NN) Heisenberg model turned out to exhibit 120° long-range order as the true ground state [5, 6]. Consequently, the existing theories had to be expanded for explaining $YbMgGaO_4$. It was found that anisotropic NN interactions ($J^{\pm\pm}$, $J^{z\pm}$) as well as isotropic next-nearest neighbor (NNN) interactions (J_2) can act in favor of a QSL state [7]. Soon, the first single crystals became available allowing field-dependent measurements along

different crystallographic directions, and non-neglectable $J^{\pm\pm}$ and $J^{z\pm}$ have been proven by electron-spin resonance (ESR) [100]. Additionally, a next nearest neighbor coupling J_2 should be considered as well [102, 103]. Altogether, $YbMgGaO_4$ seems to potentially fulfill the preconditions for exhibiting a QSL.

Other measurements pushed the spin liquid interpretation, too. Inelastic neutron scattering revealed a broad continuum [102, 104] that has been interpreted as evidence for fractionalized excitations. A spinon Fermi surface in $YbMgGaO_4$ has been proposed [104, 105], yet another INS report convincingly interprets exactly that high-energy part of the spectrum as evidence of nearest neighbor RVBs [106]. The latter is particularly thrilling because of the analogy to Anderson's original proposal on the triangular lattice [2]. The low-energy part, however, cannot be explained by the gapped RVB state because the apparent power law in specific heat evidences gapless excitations of the ground state [36, 102]. That observation supported the interpretation of $YbMgGaO_4$ as a gapless U(1) QSL, where theoretical calculations predict a power-law exponent of 2/3 in specific heat [75, 104, 105, 107] coinciding well with experiment. Additionally, muon spin relaxation (μSR) excludes any spin freezig or static long-range order down to 50 mK further supporting the QSL scenario [108].

On the other hand, serious doubts on $YbMgGaO_4$ as clean and perfect QSL have arisen, too. The lack of magnetic thermal conductivity clearly contradicts expectations of free spinons that should be able to transport heat [109]. A possible interpretation are localized spinons with very short mean free path caused by the site disorder of Mg^{2+}/Ga^{3+} sharing the same crystallographic site. Though being non-magnetic, the arbitrary distribution of those two ions generates locally different environments for the Yb^{3+} ions. That directly affects the physical properties of $YbMgGaO_4$, which has been proven by thoroughly analysing the CEF excitations [69]. This randomness may influence the magnetic interactions and could be the key for understanding the suppression of magnetic order. Interestingly, the proposed ratio of $J_2/J_1 \sim 0.2$ [102, 103] suggests $YbMgGaO_4$ to be deep in the stripe phase region of the theoretical phase diagram [10], which is clearly not realized experimentally. The randomness, however, may "melt" the magnetic order, possibly leading to a mimicry of a QSL [10, 11]. In this vivid debate, another report challenged the QSL interpretation because ac-susceptibility measurements may indicate a spin glass freezing in $YbMgGaO_4$ at 100 mK similar to the related compound $YbZnGaO_4$ [12].

To investigate that scenario further, temperature-dependent dc-magnetization experiments as an excellent tool for detecting possible spin freezing have been performed in this thesis. A temperature range down to 40 mK in fields up to 1 T has been covered. The single crystals grown by Yuesheng Li (EP VI, University of Augsburg) have been used for all presented measurements, and the results including discussion have been published in Ref. [110].

Fig. 4.1(a,b) shows $M(T)$ scaled by $|\mathbf{H}| = |\mathbf{B}|/\mu_0$ in the low temperature regime $T <$ 400 mK for the in-plane and out-of-plane field direction $\mathbf{H} \perp \mathbf{c}$ and $\mathbf{H} \parallel \mathbf{c}$, respectively. Each curve has been measured from 40 mK up to 2 K either with previous field cooling (FC) or zero field cooling (ZFC). Obviously, a kink is observable around $\sim$ 100-200 mK comparable to the ac-susceptibility report. However, several aspects speak against a conventional spin glass freezing scenario. (i) For a spin glass, a splitting between FC and ZFC curves is expected around the freezing temperature, where the ZFC data should significantly decrease [111–113]. This behavior is clearly absent even at fields as small as 0.01 T, which is far below the exchange coupling $J_0/g\mu_B \sim 1$ T. (ii) If the kink in $M(T)$ signaled spin freezing, no direction dependence would occur in contradiction to the measurements with $T^{\parallel}_{\mathrm{kink}} \sim 100$ mK and $T^{\perp}_{\mathrm{kink}} \sim 200$ mK. The factor of 2 between those two temperatures most likely reflects the

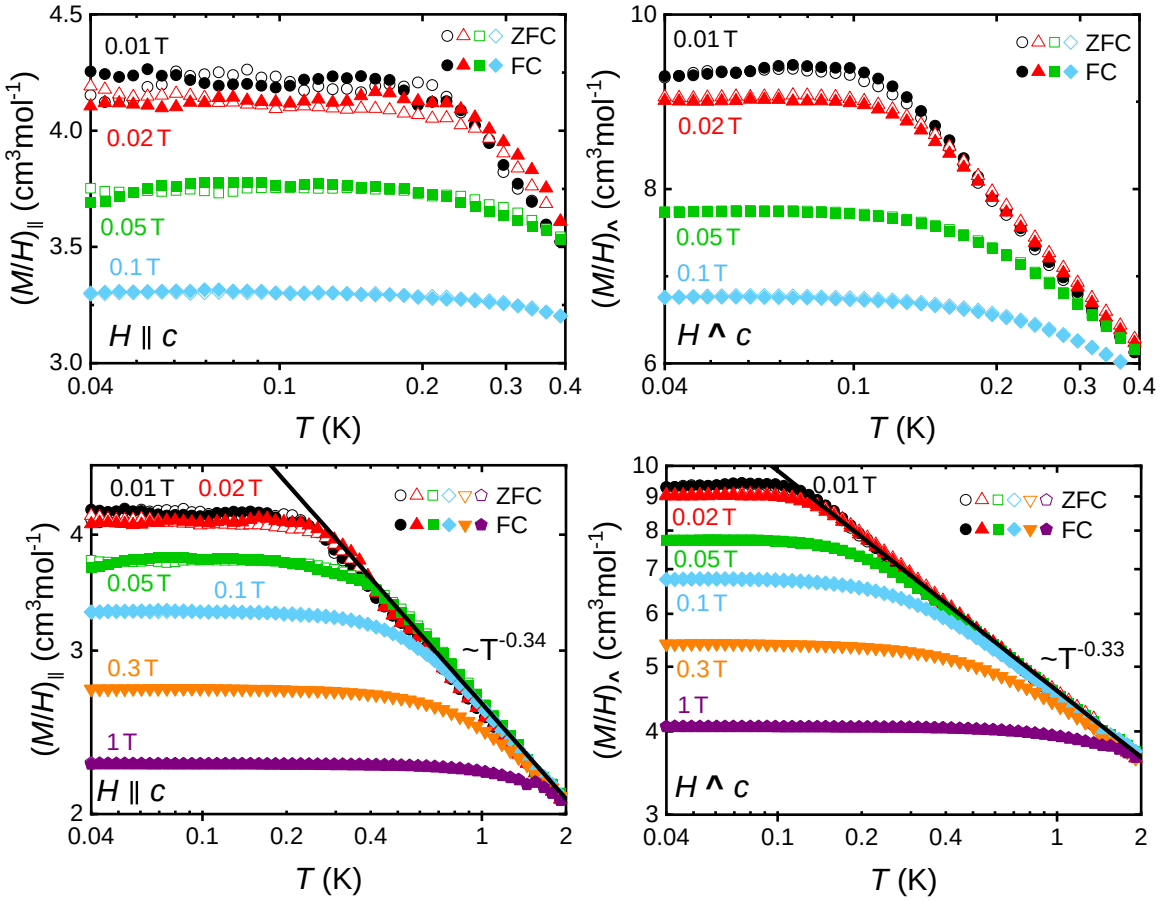

Figure 4.1. Temperature dependent magnetization of $YbMgGaO_4$ between 40 mK and 400 mK in small applied fields pointing (a) parallel and (b) perpendicular to the c-direction. A kink is visible around T_{kink}=100-200 mK. The directional dependence of T_{kink} cannot be explained by the formation of a conventional spin glass. No splitting between ZFC and FC measurements is present, another argument speaking against spin freezing at T_{kink}. (c), (d) Magnetization up to 2 K for both field directions, respectively. The power law behavior above T_{kink} does not fit to spin glass scaling with a freezing temperature of T_{kink}. Data published in Ref. [110], copyrighted by the American Physical Society. All graphs (a)-(d) have been scaled to absolute values by using the MPMS measurement of Yuesheng Li [110]. Data published in Ref. [110], copyrighted by the American Physical Society.

anisotropic magnetic couplings in $YbMgGaO_4$, $J^{zz} \sim 1$ K and $J^{xx} = 2J^{\pm} \sim 2$ K. (iii) The anomaly is shifted towards elevated temperatures by applying stronger magnetic fields. In a spin glass, a suppression of the freezing temperature is expected [114]. (iv) The spin dynamics in a spin glass slow down upon lowering the temperature until, eventually, the spins fall out of equilibrium and freeze at the characteristic temperature T_{f}. Above T_{f}, scaling behavior is expected with $\chi \sim (T - T_{\mathrm{f}})^{\gamma}$ [115]. $YbMgGaO_4$ at 0.01 T indeed reveals a power law above the anomaly with an exponent of $\gamma \sim 1/3$ [Fig. 4.1(c,d)], but the fitting also yields $T_{\mathrm{f}} \approx 0$ K instead of ∼100 mK. Consequently, spin glass scaling does not apply to $YbMgGaO_4$. Altogether, the temperature-dependent magnetization measurements confirm that the spins do not freeze in $YbMgGaO_4$, corroborating the results of μSR experiments [108]. Further insight into the ground state is provided by another INS measurements with very small

background allowing to probe the low-energy spin excitations in $YbMgGaO_4$ [110]. They are clearly distinct from the high-energy spectrum, strongly suggesting the coexistence of valence bonds and a significant amount of unpaired spins. The propagation of the latter by rearranging valence bonds requires a finite amount of energy, which would not be needed in the pure RVB picture [110]. These additional low-energy states are located in the RVB gap and present down to lowest energies resulting in the gapless ground state of $YbMgGaO_4$ [7]. The movement of orphan spins is restricted to few neighbors resembling the interpretations of confined spinons that cannot transport heat [109]. A plausible reason for the limited propagation is the already mentioned site-mixing between Mg^{2+}/Ga^{3+}.

While the influence of structural disorder on the presumed QSL ground state has been discussed to great extend, its implications on the field-evolution remained unclear for quite some time. In general, 2D triangular magnets feature a plethora of field-induced states [35]. A prominent example is the formation of the up-up-down (uud) phase accompanied by a magnetization plateau at 1/3 of the saturation magnetization M_{Sat}. It has been evidenced experimentally, for example, on the Co^{2+} triangular lattice compound $Ba_3CoSb_2O_9$ [116–118]. Similar behavior has been observed in the $AYbX_2$ family [119, 120] that will be discussed in Sec. 4.2. Interestingly, this pattern does not apply for $YbMgGaO_4$, which will be demonstrated in the rest of this section. The presented methods and results have been published in Ref. [121], and the following paragraphs are closely related to that publication.

The experimental magnetization $M(H)$ has been determined down to 40 mK and up to 10 T by a Faraday magnetometer in the dilution refrigerator MK 4. With this setup, measurements were only possible with the magnetic field applied along the c-direction because in-plane field directions ($\mathbf{H} \perp \mathbf{c}$) were not feasible due to strong torque effects at fields above 1 T. Thus, Fig. 4.2(a) shows only the out-of-plane direction ($\mathbf{H} \parallel \mathbf{c}$). For this configuration, the expected saturation magnetization M_{Sat} is $1.86\,\mu_{\mathrm{B}}/Yb^{3+}$ using the previously reported g-values of $g_{\parallel} = 3.72$ [100] and $M_{\mathrm{Sat}} = g\mu_{\mathrm{B}}J_{\mathrm{eff}}$ from Sec. 2.1.3 with the effective total angular momentum $J_{\mathrm{eff}} = 1/2$. The saturation is reached at $H^{\parallel}_{\mathrm{Sat}} \simeq 5\,\mathrm{T}$. The linear increase above $M^{\parallel}_{\mathrm{Sat}}$ stems from Van Vleck contributions due to the CEF levels. Even at the lowest temperature of 40 mK, a clear indication of the 1/3-magnetization plateau is absent, although a nonlinear behavior is present at approximately $M_{\mathrm{Sat}}/3$. In the magnetic susceptibility as the first derivative, $\chi = \mathrm{d}M/\mathrm{d}H$, that change of slope results in a plateau in $\chi(H)$ located around 1.8 T for $\mathbf{H} \parallel \mathbf{c}$ [Inset of Fig. 4.2(a)]. Notably, there is no apparent difference between 750 mK and 40 mK. Consequently, that anomaly cannot originate from broadening of a putative magnetization plateau by thermal fluctuations because they should become almost fully suppressed at such low temperatures. Thus, it must be intrinsic to $YbMgGaO_4$. These results are in accordance with MPMS measurements down to 500 mK [121]. The in-plane field direction has been measured there, too, that reveals very similar behavior. The susceptibility plateau, however, is located at ~ 3.5 T which is approximately twice the value compared to the out-of-plane direction. The magnetization data presented here and in Ref. [121] agree with Steinhardt *et al.* [122], where the magnetization has been measured indirectly down to 24 mK by the tunnel diode oscillator technique and torque magnetometry. They report similar values of saturation magnetization, $H^{\parallel}_{\mathrm{Sat}} \simeq 4-5\,\mathrm{T}$ and $H^{\perp}_{\mathrm{Sat}} \simeq 7-8\,\mathrm{T}$. Furthermore, their suggested field-induced crossover matches the plateaus in $\chi(H)$. All in all, the field evolution of $YbMgGaO_4$ turns out to be unusual compared to other TLAF [116–120].

The field evolution of $YbMgGaO_4$ can be probed by other measurement techniques, too. The field-dependent specific heat at very low temperatures of 200 mK is shown in Fig. 4.2(b). In general, several contributions have to be considered in the heat capacity, but the condi-

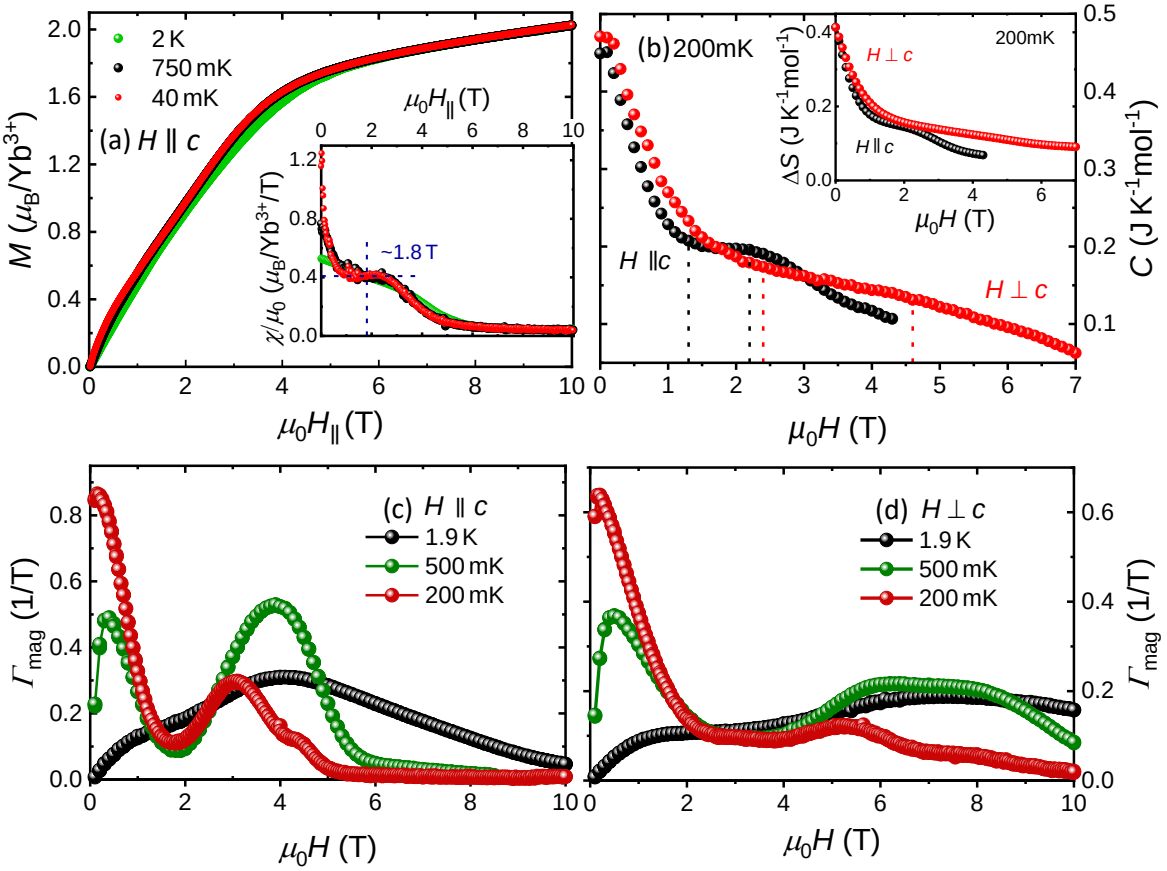

Figure 4.2. Field-dependent thermodynamic measurements on $YbMgGaO_4$ in the dilution refrigerator MK 4, published in Ref. [121], copyrighted by the American Physical Society. (a) Magnetization down to 40 mK and up to 10 T with field applied along the c-direction. In the inset, the susceptibility shows a nonmonotonic field-evolution with a plateau around 1.8 T. This in agreement with MPMS measurements down to 500 mK [121]. (b) Specific heat for both field directions at 200 mK. The position of the plateaus in $\chi(H)$ from Ref.[121] is marked by dotted lines. In the same field range, the slope of $C(H)$ changes, and $\mathbf{H} \parallel \mathbf{c}$ reveals a plateau, too. Inset: Evolution of entropy at 200 mK, reminiscent of the specific heat behavior. The entropy has been shifted by $0.07R\ln 2$ according to the zero-field entropy [36]. (c), (d) Magnetic Grüneisen parameter Γ_{mag} for both field directions and several temperatures. In summary, none of the presented measurements indicate a field-induced phase transition in $YbMgGaO_4$.

tion $T \ll 1\,\mathrm{K}$ safely allows to neglect the phonons. Furthermore, no conduction electrons are present because of the the insulating behavior of $YbMgGaO_4$. A nuclear contribution may appear at 200 mK but should increase at higher fields, which is clearly absent in the measured field range. Consequently, the presented specific heat is governed by the magnetic contribution. Applying a magnetic field results in a rapid suppression of the specific heat [36, 102, 109] due to the gradually growing gap in the low-lying excitations [123]. Intriguingly, the evolution is nonmonotonic since a plateau feature is clearly visible for $\mathbf{H} \parallel \mathbf{c}$. It appears exactly in the same field region like the plateau in $\chi(H)$ [Fig. 4.2(a)]. For $\mathbf{H} \perp \mathbf{c}$, such a plateau cannot be identified unequivocally, but the change of slope followed by the linear slope between ∼2.5 T and ∼4 T well matches the broad plateau region in $\chi(H)$ from Ref. [121], too.

The magnetic Grüneisen parameter $\Gamma_{\mathrm{mag}}(H)$ is highly sensitive to field-induced phase transitions. An abrupt sign change from negative to positive would indicate a sharp maximum in the field-dependent entropy, typical for a 2$^{\mathrm{nd}}$ order phase transition, due to the Maxwell relation $\mu_0 \partial S/\partial H = \partial M/\partial T = -\Gamma_{\mathrm{mag}} C$. Such characteristic behavior is absent in $YbMgGaO_4$ for both field directions [Fig. 4.2(c,d)]. On the other hand, a minimum in Γ_{mag} is observed near the plateau regions of $\chi(H)$, which is more pronounced for $\mathbf{H} \parallel \mathbf{c}$. This can be related to a change in the slope of the entropy directly obtained by integrating $-\Gamma_{\mathrm{mag}} C$. The field-dependent entropy is presented in the inset of Fig. 4.2(b). Indeed, the field direction $\mathbf{H} \parallel \mathbf{c}$ reveals a plateau in the same field range like specific heat and magnetic susceptibility. The other field direction, $\mathbf{H} \perp \mathbf{c}$, is reminiscent of the specific heat by only changing the slope, which explains the weaker response in the magnetic Grüneisen ratio [Fig. 4.2(d)]. Finally, at high fields, both magnetic Grüneisen parameter tend to become zero above the saturation field, respectively, because the polarized state with an increasing gap is approached and the field-dependent entropy becomes rapidly suppressed.

Altogether, the presented thermodynamic measurements exclude thermodynamic transitions in $YbMgGaO_4$, which is also corroborated by magnetostriction [121]. In a next step, the unusual plateau in the magnetic susceptibility is discussed in more detail. As a first interpretation, the nonlinearity in $M(H)$ might result from a smeared 1/3 plateau due to the structural disorder in $YbMgGaO_4$. This will be evaluated in the following paragraphs by numerical methods. All Monte Carlo magnetization curves have been calculated by Ilia Iakovlev (Theoretical Physics and Applied Mathematics Department, Ural Federal University, Ekaterinburg). Subsequently, his magnetization results have been used for the averaging procedure developed to mimic structural disorder, which has been implemented in Origin C by the author of this thesis.

The general Hamiltonian for interacting spins on a triangular lattice has been introduced in Eq. 2.10 in Sec. 2.2.1, $\mathcal{H}_{\mathrm{exch}} = \sum_m \left[\mathcal{H}_m^{\mathrm{XXZ}} + \mathcal{H}_m^{\pm\pm} + \mathcal{H}_m^{\mathrm{z}\pm}\right]$, with the summation over NN ($m = 1$), NNN ($n = 2$), etc. The first term reflects the XXZ anisotropy parametrized in Δ. All studies on $YbMgGaO_4$ coincide in the presence of easy-plane anisotropy with $\Delta < 1$, but the determined values vary between 0.54 and 0.88 depending on the chosen microscopic scenario [7]. The second and third term in the Hamiltonian represent diagonal and off-diagonal anisotropy condensed in the exchange couplings $J_m^{\pm\pm}$ and $J_m^{z\pm}$, respectively. A serious obstacle in numerically simulating this Hamiltonian is the quantum nature of $YbMgGaO_4$. Exact diagonalization naturally includes quantum effects, but is limited to very small lattice sizes. Therefore, a different approach is realized using the classical spin Hamiltonian

$$\mathcal{H} = \mathcal{H}_{\mathrm{exch}} - \sum_i \mathbf{H}\mathbf{S}_i - \sum_{i \neq j} b(H)_{ij} \left(\mathbf{S}_i \mathbf{S}_j\right)^2 , \tag{4.1}$$

where the exchange Hamiltonian from Eq. 2.10 is extended by the Zeeman term to account for magnetic fields and by the biquadratic exchange imitating quantum fluctuations [124]. The biquadratic coupling is optimized by the following formula, where the procedure from Ref. [124] has been slightly modified,

$$b(H^\alpha) = J_1^{zz} \left[0.0536(1 - 0.03 H^\alpha \sqrt{H_{\mathrm{Sat}}^\alpha - H^\alpha})\right] n. \tag{4.2}$$

H_{Sat}^α denotes the saturation field for a given field direction α, and n is an integer. The g-factor anisotropy in $YbMgGaO_4$ is taken into account by scaling the magnetic field after the numerical simulation, respectively.

Table 4.1. Overview of the exchange parameters for the spin Hamiltonian of Eq. 4.2. Refs. [100, 103] are the frameworks for the models A and B, respectively. For the latter model, the second-neighbor coupling J_2 is added using the same J_2/J_1 ratio. Table adapted from Ref. [121].

Model	Δ	$J_1^{\pm\pm}/J_1$	$J_1^{z\pm}/J_1$	J_2/J_1	$g_\parallel$	$g_\perp$
A	0.88	0.176	0.176	0.18	3.81	3.53
B	0.54	0.086	0.02	0.18	3.72	3.06

For calculating the magnetization from the Hamiltonian of Eq. 4.2, the classical Monte Carlo (MC) method with the Uppsala Atomistic Spin Dynamics (UPPASD) package is used. The temperature has been adjusted to $T = 0.15J^{zz}$ for the presented graphs with $J^{zz} = \Delta J_1$. As already mentioned, all Monte Carlo simulations have been performed by Ilia Iakovlev, and further technical details can be found in Ref. [121].

Quantitatively identifying the exchange couplings in $YbMgGaO_4$ has been subject of vivid debates [7]. In this work, two representative parameter sets are used based on different measurement techniques. They are summarized in Table 4.1. Model A is in close relation to the results of terahertz and neutron spectroscopy [103]. In that report, the influence of NNN interactions has been corroborated proposing a finite ratio $J_2/J_1 = 0.18$. This study, however, is far from unambiguously fixing all parameter, and the values of $J_1^{\pm\pm}/J_1 = 0.4(3)$ and $J_1^{z\pm}/J_1 = 0.6(6)$ obtain large uncertainties. For Model A, the parameter space has been explored in the limits of [103], and the values of Table 4.1 could describe the experimental data best. Model B stems from the first analysis of the microscopic spin model in $YbMgGaO_4$ using the Curie-Weiss temperature and ESR measurements. It is augmented by interactions beyond NN with the same ratio $J_2/J_1 = 0.18$ from Model A.

Calculating the magnetization for both models results in steplike features exemplarily shown in Fig. 4.3(a) for model B, $\mathbf{H} \perp \mathbf{c}$. Interestingly, the clearly visible plateaus formed around 1/2 of the saturation magnetization being distinct to the anticipated 1/3 plateau. Model A reveals comparable results for both field directions. In that sense, model B with $\mathbf{H} \parallel \mathbf{c}$ deviates slightly from the other cases because the step is present without plateau. In general, the formation of a 1/2 plateau is not uncommon on the triangular lattice. The so-called up-up-up-down (uuud) phase has been evidenced by quantum simulations in the case of sizable NNN couplings $J_2/J_1 > 0.125$ [125]. $YbMgGaO_4$ would naturally be located in that regime, yet the situation might be more complex due to the additional anisotropic couplings. Nevertheless, all curves do not represent the experimental data at all, compare Fig. 4.2(a) and [121], because the structural disorder has been neglected so far. That effect will be simulated by a procedure explained step by step in the next paragraph.

The random occupation of the Mg^{2+}/Ga^{3+} sites creates locally differently charged environments for the Yb^{3+} ions influencing their CEF levels [69]. Furthermore, the magnetic exchange couplings in $YbMgGaO_4$ change as well. It has been shown that the randomness changes the absolute value of J_1, while the other parameter Δ, $J_1^{\pm\pm}/J_1$, and $J_1^{z\pm}/J_1$ remain constant in good approximation [126]. Therefore, for simulating the randomness in the magnetization, the following assumptions are made: (i) The J_1 values in the crystal follow a Gaussian distribution. (ii) J_2 is Gaussian distributed as well with a constant J_2/J_1 ratio. (iii) Δ, $J_1^{\pm\pm}/J_1$, and $J_1^{z\pm}/J_1$ remain fixed, too. Altogether, these three assumptions can be taken into account by first calculating the pristine magnetization $M(H)_{\text{prist}}$ using an averaged value J_{avg} resulting, for example, in Fig. 4.3(a). Subsequently, the field of that curve is rescaled by a factor $f = J_1/J_{\text{avg}}$ reflecting different exchange couplings depending on

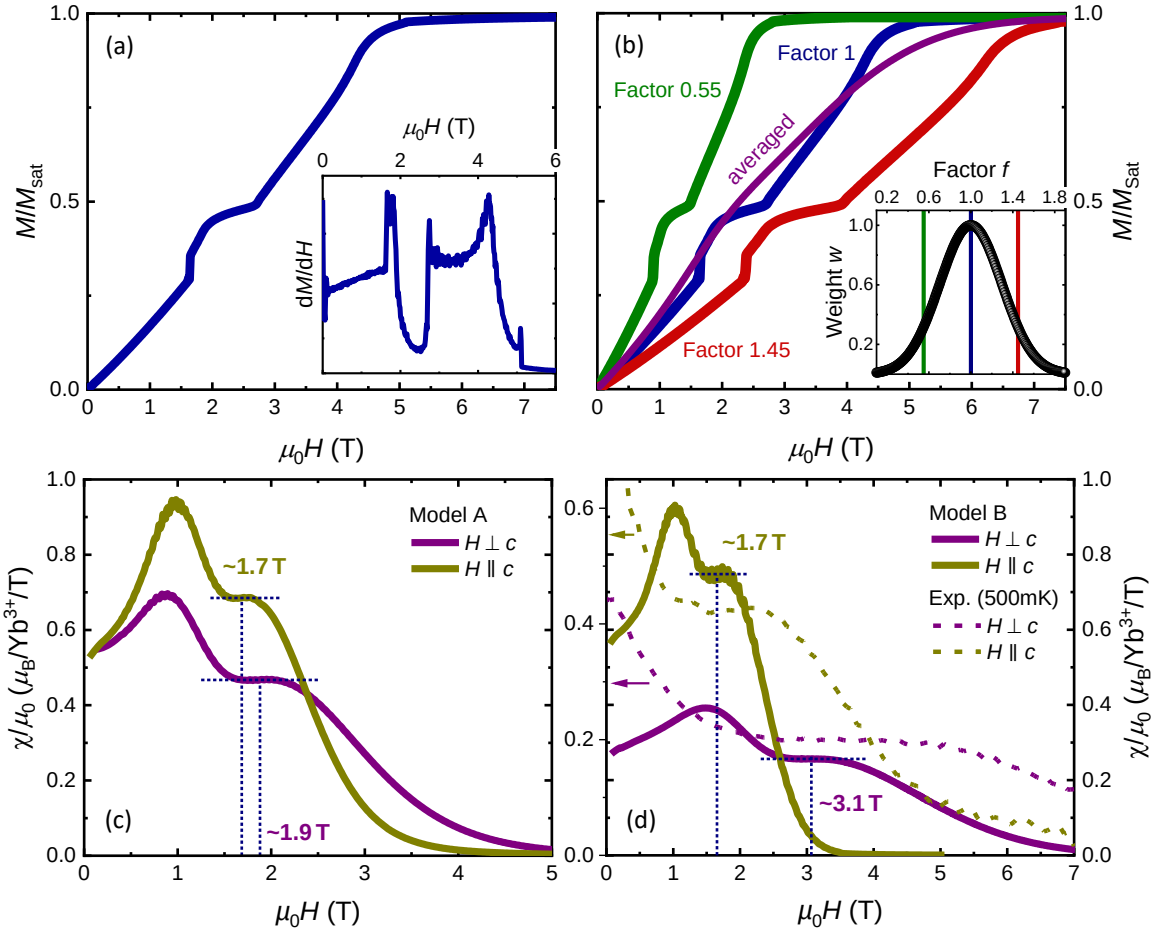

Figure 4.3. (a) Model B with $H \perp c$, $J_{\text{avg}} = 2.26\,\text{K}$, and $T = 0.15 J_1^{zz}$ results in the presented $M(H)$ and $\chi(H)$ curves. Here, no averaging procedure over different values of J_1 has been performed. Calculating $\chi(H)$ reveals that it does not match the experimental data. Monte Carlo simulation performed by Ilia Iakovlev. (b) Simulating random exchange couplings by averaging of the $M(H)$ curve. The original curve from (a) is equivalent to $f = 1$. The other factors, $f = 0.55$ and $f = 1.45$, represent two different values of J_1. They contribute with a smaller weight w to the averaged curve following Eq. (4.3). The factors' weight follows a Gaussian distribution $w(f)$, as shown in the inset. The obtained averaged $M(H)$ curve is presented in purple. (c) Calculated $\chi(H)$ for model A after averaging using $J_{\text{avg}} = 1.63\,\text{K}$ with $2\sigma = 0.53\,J_{\text{avg}}$, $n = 5$, $T = 0.15 J_1^{zz}$ for $H \parallel c$ and $2\sigma = 0.61\,J_{\text{avg}}$, $n = 2$, $T = 0.15 J_1^{zz}$ for $H \perp c$. (d) Calculated $\chi(H)$ for model B after averaging using $J_{\text{avg}} = 2.26\,\text{K}$ with $2\sigma = 0.46\,J_{\text{avg}}$, $n = 6$, $T = 0.05 J_1^{zz}$ for $H \parallel c$ and $2\sigma = 0.6\,J_{\text{avg}}$, $n = 5$, $T = 0.15 J_1^{zz}$ for $H \perp c$. This parameter set coincides best with the experimental behavior. For comparison, the dotted lines represent the experimental data measured at 500 mK [121]. Graphs published in Ref. [121], copyrighted by the American Physical Society.

the local environment. The form of the magnetization curve with step and plateau remains untouched, but these anomalies including saturation magnetization shift to lower or higher fields depending on the factor f [Fig. 4.3(b)]. Consequently, such scaled magnetization curves correspond to different exchange couplings J_1. The distribution of J_1 is implemented by the weighting factor w [Inset of Fig. 4.3(b)], and factors with a weight $w < 0.01$ are discarded. In the example of Fig. 4.3(b), this is equivalent to J_1/J_{avg} of 0.1 and 0.9, respectively, or

to a full width at half maximum (FWHM) of ~ 0.7 with the standard deviation $\sigma \sim 30\,\%$. Most of the weight is located in the interval of $J_{\mathrm{avg}} \pm \sigma$, where the total variation of J_1 is about $\sim 60\,\%$, which is comparable to the results of the simulations in Ref. [126]. In order to average over all factorized magnetization curves, the following sum is applied,

$$M(H)_{\mathrm{avg}} = \frac{\sum_{i=0}^{n} w_i f_i M(H)_{\mathrm{prist}}}{\sum_{i=0}^{n} w_i}, \tag{4.3}$$

resulting in the averaged magnetization curve in Fig. 4.3(b). For all curves presented in this work, 201 f_i values are used, and the parameters for the Gaussian distribution of w are summarized in Table 4.2 for each model and field direction.

The averaged curves for $\chi(H)$ in model A and B are presented in Fig. 4.3(c,d). The experimental data at 500 mK from Ref. [121] are indicated by dotted lines in Fig. 4.3(d). Both models can reproduce the experimental plateau features in the magnetic susceptibility, and the calculated order of magnitude matches well, too. The position of the plateau, however, is in much better agreement in model B using $J_{\mathrm{avg}} = 2.26\,\mathrm{K}$, where the factor of about 2 between $\mathbf{H} \perp \mathbf{c}$ and $\mathbf{H} \parallel \mathbf{c}$ is obtained. The previously reported values for the exchange coupling of $J = 1.8\,\mathrm{K}$ [100] and $J = 2\,\mathrm{K}$ [103], where structural disorder has been neglected, are slightly lower, but still comparable. On the other hand, the MC calculations do not agree with the experiment for fields below 1 T. A natural explanation might be quantum effects in the proximity to the disordered state that are not captured by the classical MC method. An example for strong quantum fluctuations in such a regime have been found in a frustrated square lattice [127]. Furthermore, the plateaus in the experimental data are broader than the simulated ones. Nevertheless, the qualitative evolution above 1 T can be captured very well. Another interesting aspect is the influence of the chosen parameter on the simulated magnetization. Model A and B are far from being the unambiguous choice due to the huge parameter space. Several trends can be identified by changing different parameter. The plateau in χ and its position is rather insensitive to weak variations of $J_1^{\pm\pm}$ and $J_1^{z\pm}$ up to a limit of $0.4\,J_1^{zz}$, where the uuud order with the 1/2 plateau might become suppressed by the strong off-diagonal couplings. The second important parameter is the extend of XXZ anisotropy Δ. A smaller value than suggested in Ref. [103] is required to reproduce the plateau positions indicating a pronounced XXZ anisotropy in $YbMgGaO_4$. At the same time, this appears to be a lower limit because a stronger anisotropy with $\Delta < 0.5$ does not produce a plateau in $\chi(H)$ in $\mathbf{H} \parallel \mathbf{c}$ anymore. Finally, the impact of the NNN exchange can be estimated from Fig. 4.4, where $J_2/J_1 = 0$ favors the 1/3-magnetization plateau. The averaging procedure does not result in the experimental anomalies. This strongly supports the presence of substantial J_2 in $YbMgGaO_4$.

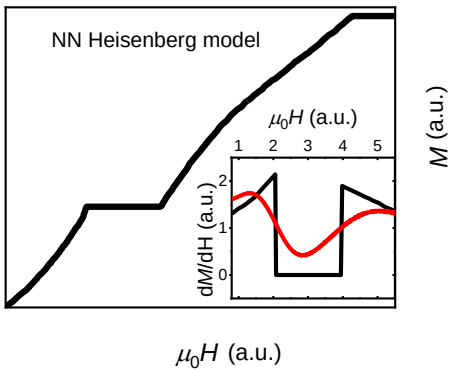

Figure 4.4. 1/3-magnetization plateau in NN Heisenberg model. Applying the averaging procedure cannot reproduce the plateau in the susceptibility observed in $YbMgGaO_4$ (inset, red line). Graph adapted from Ref. [121], copyrighted by the American Physical Society. Originally from Ref. [128].

Altogether, all presented measurements unambiguously exclude the existence of a plateau phase that is in contrast to other TLAF such as $Ba_3CoSb_2O_9$ [116–118] or several QSL candidates in the $AYbX_2$ family [119, 120]. The difference to these materials is the structural

Table 4.2. The chosen parameter for the averaging procedure are summarized here. They are used to obtain the averaged $\chi(H)$ curves in Fig. 4.3(c) and Fig. 4.3(d). The standard deviation is denoted as σ, and the interval $J_{\text{avg}} \pm \sigma$ carries most of the total weight. Table adapted from Ref. [121].

Model	FWHM (% of J_{avg})	$J_{1,min/max}$	2σ (% of J_{avg})
A, $\mathbf{H} \parallel \mathbf{c}$	62	$0.2/1.8\, J_{\text{avg}}$	53
A, $\mathbf{H} \perp \mathbf{c}$	71	$0.08/1.92\, J_{\text{avg}}$	61
B, $\mathbf{H} \parallel \mathbf{c}$	54	$0.3/1.7\, J_{\text{avg}}$	46
B, $\mathbf{H} \perp \mathbf{c}$	70	$0.1/1.9\, J_{\text{avg}}$	60

randomness in $YbMgGaO_4$ that, in turn, randomize exchange couplings. It is expectable that such a phenomenon intrinsically broadens all possible field-induced transitions. The simulation of the magnetization data in Fig. 4.3(c,d) indicate a strong distribution of J_{avg}. Consequently, the randomness in $YbMgGaO_4$ might smear out any anomaly related to a plateau phase, resulting in a smoothly evolving magnetization curve. The susceptibility and the specific heat as second derivatives of the free energy, however, reveal a nonmonotonic behavior in form of a plateau. Again, this is distinct to the usual behavior [Inset of Fig. 4.2(f)] and can be explained by simulating randomness effect using the averaging procedure explained above. The different plateau positions for in-plane and out-of-plane fields underline the presence of XXZ anisotropy in $YbMgGaO_4$. Interestingly, the MC calculations cannot describe the experimental $\chi(H)$ curves, when the common 1/3-magnetization plateau of the uud order is averaged [red curve in the inset of Fig. 4.2(f)]. The 1/2 plateau as a result of the uuud phase, however, can reproduce these features. Therefore, the anomalies in the susceptibility and specific heat of $YbMgGaO_4$ might be vestiges of the 1/2 plateau. The chosen value $J_2/J_1 = 0.18 > 0.125$ deduced from Ref. [103] lies in the range where uuud order is anticipated [125] corroborating the influence of second nearest neighbors. On the other hand, neutron scattering experiments of $YbMgGaO_4$ show a shift of spectral weight from the M-point towards the K-point by applying intermediate fields [122]. This has been associated with the uud order and the 1/3 plateau, and could not be reproduced with the parameter sets presented here. Further investigations are certainly needed to clarify that issue.

In place of simulating the magnetization by the presented microscopic spin model, the evolution of the magnetic susceptibility might be described in a different, more phenomenological manner. As illuminated by the temperature-dependent magnetization measurements [Fig. 4.1], the zero-field ground state of $YbMgGaO_4$ can be well understood as a combination of valence bonds and free unpaired spins. Those orphan spins may be polarized fairly quick, and the plateau in $\chi(H)$ as the change of slope in the magnetization refers to fully polarized orphan spins. Breaking the valence bonds requires a conversion from the singlet to the triplet state that likely needs higher energies and, thus, stronger magnetic fields resulting in the observed nonmonotonic field evolution.

4.2. Disorder-Free QSL Candidates in the Family of AYbX$_2$

$YbMgGaO_4$ was the pioneer material in exploring spin liquid physics on 2D triangular rare earth systems. The structural randomness, however, introduces an additional component that complicates its microscopic scenario. Consequently, similar material systems *without* disorder were highly desired. In 2018, several promising candidates have been identified in the family of AYbX$_2$ [129], where A and X stand for alkali metals (K, Na, Cs) and chalcogens (O, S, Se), respectively. Site-mixing between non-magnetic ions is absent here. $NaYbO_2$, $NaYbS_2$, $CsYbSe_2$ and $NaYbSe_2$, for example, do not show magnetic ordering but fluctuating spins down to lowest temperatures [7], reminiscent of spin liquid physics. Interestingly, the appearance of field-induced phases such as magnetization plateaus strongly resembles other triangular magnets such as $Ba_3CoSb_2O_9$. Therefore, the AYbX$_2$ materials offer a rich playground on exploring novel phases in triangular magnets. In this work, two members have been investigated, namely $KYbS_2$ and $NaYbO_2$. Extended thermodynamic measurements have been performed in temperatures down to far below 100 mK and fields up to 15 T. $KYbS_2$ is available as single crystals, and two different field directions have been examined. For $NaYbO_2$, however, single crystal growth has not been successful so far, and a powder pellet has been investigated. Both samples have been prepared by Franziska Grußler (EP VI, University of Augsburg).

4.2.1. Single Crystals of $KYbS_2$

The first report about $KYbS_2$ in 2020 [130] presented several thermodynamic measurements. Magnetic susceptibility does not indicate any long-range ordering down to 1.9 K, and zero-field heat capacity extends the temperature range without magnetic order down to 400 mK. The Curie-Weiss temperature has been determined to be -5 K and -12 K for fields oriented out-of-plane (perpendicular to the triangular planes, $\mathbf{B} \parallel \mathbf{c}$) and in-plane ($\mathbf{B} \perp \mathbf{c}$), respectively [130]. This estimation might be improved by using field-dependent magnetization measurements $M(B)$ beyond the saturation magnetization in order to fix the Van-Vleck contribution and to improve the susceptibility fit [7]. Nevertheless, the frustration parameter $f = \Theta_{CW}/T_N > 10$ indicates strong frustration in $KYbS_2$. Many aspects remain unclear due to the lack of data below 400 mK and especially in magnetic fields, where other AYbX$_2$ materials show interesting behavior [68, 119, 131, 132]. In this work, an extensive single crystal study has been performed to shed further light on this potential QSL candidate. The thermodynamical properties specific heat, magnetic Grüneisen parameter, and entropy change have been measured in a temperature range between 50 mK and 3 K in fields up to 15 T for $\mathbf{B} \parallel \mathbf{c}$ and $\mathbf{B} \perp \mathbf{c}$.

All heat capacity measurements in this chapter have been performed by using the relaxation method [Sec. 3.4.1]. The lattice contribution is considered to be around 10 mJ K^{-1} mol^{-1} at 3 K [130] and, thus, is negligible in the investigated temperature range. Furthermore, the cell background is subtracted in all presented data. $C_{cell}(T)$ has been estimated using a previous addenda measurement and becomes negligible below $\sim$2 K [Fig. 4.5(a)]. It should be noted that the background might be even overestimated here. In the original addenda measurement, N-Grease has been used, which was needed for the solvent-sensitive α-$RuCl_3$ sample (see Ch. 5). For the $KYbS_2$ crystal with its chemical stability, however, the usual approach was applied with a very small amount of GE Varnish due to the tiny sample size. Nevertheless, another highly time-consuming background measurement with GE varnish instead of N-Grease is not necessary due to the large sample signal.

Fig. 4.5(a) shows the sample heat capacity $C_{\mathrm{Sa}}(T)$ of the $KYbS_2$ single crystal at zero-field down to 50 mK. It reveals a very broad maximum between around 1 K and 3 K reproducing the results of Ref. [130], yet the two presumed distinct peaks are not resolved here. Such a broad feature is characteristic for several $AYbX_2$ materials [68, 119, 120, 129, 131, 133–137] as well as for $YbMgGaO_4$ [36]. It can be interpreted as a crossover to the spin liquid state, marking the onset of short-range correlations [36, 68]. Below 1 K, the specific heat decreases down to ∼100 mK. In zero field, the Yb^{3+} quadrupolar moments give rise to a Schottky anomaly at ultra low temperatures. Consequently, the increase towards below 100 mK stems from the high-temperature part of the nuclear contribution. Altogether, no lambda-type anomaly is detected in the whole accessible temperature range. This strongly indicates the absence of long-range ordering down to at least 50 mK resulting in a lower limit of the frustration parameter $f \geq 100$. It underlines the extremely high degree of frustration in $KYbS_2$ and provides first evidence of a possible QSL ground state. However, a subtle aspect deserves attention. At around 200 mK, marked by the dotted line in red, a weak kink is visible in $C(T)$, whose origin is not obvious. Ordinary bulk long-range magnetic order, though, can be excluded since it should be much more pronounced.

In order to further investigate the zero-field data, the nuclear contribution has to be subtracted. For this purpose, the low temperature specific heat is carefully fitted. The high-temperature part of the nuclear Schottky anomaly can be well approximated by $C_{\mathrm{nuc}} = \alpha/T^2$. As insulating material, the only further contribution for $KYbS_2$ results from the unknown magnetic excitations. Here, two possibilities are considered. First, gapless excitations would give rise to a power law, $C_{\mathrm{m,pow}} = bT^p$ [68, 138, 139]. Second, the specific heat of a 2D AF gapped magnet well below the gap ($T \ll \Delta$) can be expressed as exponential behavior with a temperature dependendent prefactor, $C_{\mathrm{m,exp}} = A(x^2 + 2x + 2)\mathrm{e}^{-x}$ with $x = \Delta/T$ and $A \sim 1/J$, assuming a quadratic gap dispersion, $\epsilon_{\mathrm{k}} \approx \Delta + J\mathbf{k}^2$ [68, 72]. It should be mentioned that the gap Δ must not be confused with the amount of XXZ anisotropy discussed in Sec. 4.1.

In Fig. 4.5(b), both fitting functions are used to describe the low temperature specific heat up to ∼150 mK as indicated by the gray dotted line. At first sight, both least square fits describe the data well in this small fitting range. First, the power law expression is discussed in more detail. The resulting power exponent turns out to be $p = 1.8$. This value is robust upon reducing the fitting range down to 110 mK. Increasing the interval to 250 mK, on the other hand, clearly worsens the fit quality and reduces p to 1.5 [Fig. 4.5(c)]. Therefore, the kink at around 200 mK limits the valid temperature range of the power law expression. Now, let us turn to the gapped scenario that returns a small gap of $\Delta = 0.24$ K. This fit function, however, has a slightly lower R value than the power law fit and might show small deviations from the data marked by the arrows in Fig. 4.5(b). A larger fitting range results in the same gap $\Delta = 0.25$ K [Fig. 4.5(c)], but then the assumption $T \ll \Delta$ does not hold anymore. The small possible fitting range makes it difficult to judge the validity of the concurrent functions in zero field, but, overall, a gapless behavior seems to describe the data better.

Applying magnetic fields rapidly suppresses the kink around 200 mK allowing an expansion of the fitting interval. Therefore, the same fit functions for $C(T)$ are compared at 1 T with $\mathbf{B} \perp \mathbf{c}$ and a fitting range up to 300 mK [Fig. 4.5(d)]. The fit quality of the gapped function is drastically reduced. The same yet weaker tendency is visible for the data at 0.125 T [Fig. 4.5(e)], where the kink is not fully suppressed yet, as discussed later. The results with a fitting interval comparable to Fig. 4.5(b) show again that the power law fit seems to be favorable. It is noted that a field of 0.125 T is already in the same order of magnitude like the putative zero-field gap $\Delta = 0.24$ K [Fig. 4.5(b)] using $B \sim k_{\mathrm{B}}\Delta/g_{\perp}\mu_{\mathrm{B}} \sim 0.1$ T. Thus,

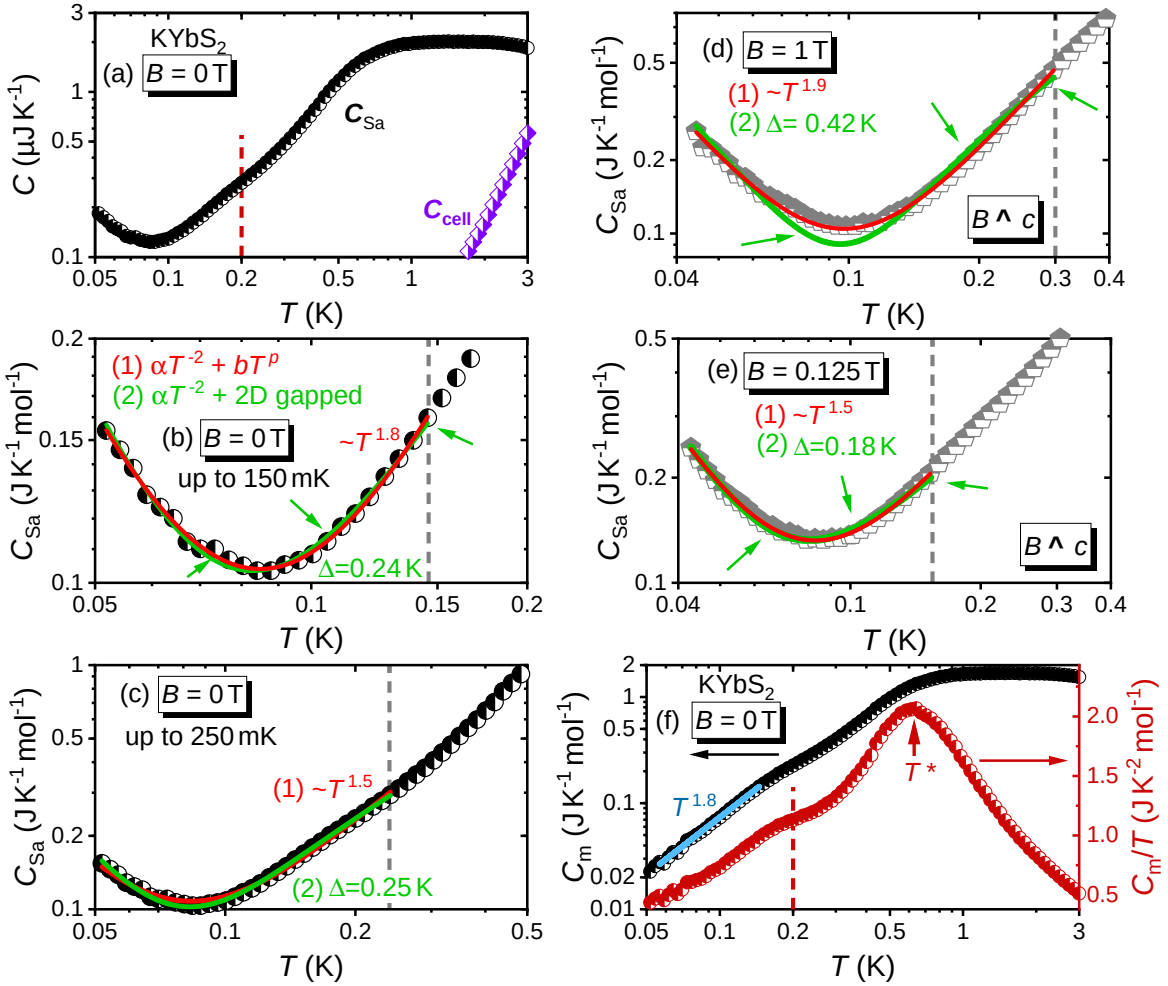

Figure 4.5. (a) $C(T)$ of $KYbS_2$ in zero field. Black data points represent $C(T)$ after subtraction of the cell background (purple, negligible below ∼2 K). No long-range magnetic order can be found down to 50 mK, yet a weak kink appears around 200 mK (red dotted line). Phononic contributions are neglectable below ∼3 K [130]. The increase below 100 mK is due to the nuclear contribution. (b) Determination of the nuclear contribution by fitting the low-temperature part up to 150 mK with $C_{\mathrm{Sa}} = \alpha/T^2 + C_{\mathrm{m}}$, here in zero field. Two different approaches are used for the magnetic contribution. For the red curve, a gapless ground state is assumed with a power law. A gapped 2D AF system shows a characteristic exponential behaviour. Both describe the data well, but the gapped function slightly deviates from the data, indicated by the arrows and a slightly lower R-value. (c) Larger fitting range up to 250 mK. The power law becomes problematic due to the above mentioned kink around 200 mK. The exponential fit seems to be better, but the required condition $T \ll \Delta$ is not fulfilled anymore. (d, e) Low temperature fits at small fields of 1 T and 0.125 T, respectively. The power law fit shows better agreement with the data. (f) Zero field magnetic heat capacity $C_{\mathrm{m}}(T)$ and $C_{\mathrm{m}}(T)/T$ of $KYbS_2$ after subtracting the nuclear contribution. The power law behavior is indicated by the blue line. The crossover to the presumable QSL state is indicated by the maximum in $C_{\mathrm{m}}(T)/T$ at T^*.

the putative gap from the zero-field fit could already be closed by such small fields. However, the deviations between fit and data points tend to be consistently at the same positions like at 0 T. Consequently, it is concluded that $KYbS_2$ at zero-field and below 200 mK most likely reveals gapless behavior. This certainly deserves closer attention, and probing the ground

state at ∼100 mK by, for example, inelastic neutron scattering (INS), muon spin relaxation (muSR) or nuclear magnetic resonance (NMR) would be interesting.

After subtracting the respective nuclear contribution with $\alpha = 4.22(3)\,\mathrm{J\,K\,mol^{-1}}$ using the gapless fit in Fig. 4.5(b), the magnetic specific heat is plotted in Fig. 4.5(f). In $C_\mathrm{m}(T)/T$ (right axis), the anomaly at 200 mK is even more clearly visible. Furthermore, a pronounced maximum is visible at T^*, which is interpreted as a crossover to a short-range correlated state [68, 130] and added to the phase diagram established later [Fig. 4.12]. The blue line represents the power law behavior with an exponent of $p = 1.8$ being close to 2. The exponent of a power law can in principle benchmark theoretical models because of its direct connection to the low-temperature excitations. Therefore, the presumed power law exponent of $p = 2$ is discussed in the next paragraphs.

In the case of a potential spinon Fermi surface, an exponent of $p = 1$ is expected [73], which has been experimentally observed in triangular QSL compounds such as the organic materials κ-(BEDT-TTF)$_2$Cu$_2$(CN)$_3$ [74] and EtMe$_3$Sb[Pd(dmit)$_2$]$_2$ [140], or in the 6H-B phase of $Ba_3NiSb_2O_9$ [141]. Corrections to the spinon Fermi surface can change the exponent to $p = 2/3$, as discussed for $YbMgGaO_4$ [Sec. 4.1]. The quadratic behavior in the specific heat of $KYbS_2$ seems to be clearly distinct.

An exponent of $p = 2$ can be found in many scenarios, though, for example for some spin glasses [77, 78] or 2D AF magnons [70, 71, 78]. It is also present in QSL candidates, but in a (hyper)kagomé lattice ($Na_4Ir_3O_8$, $ZnCu_3(OH)_6Cl_2$) [139, 142] or in a spin-1 system in the 3D phase 3C-$Ba3NiSb_2O_9$ [141]. Thus, they are probably not relevant for $KYbS_2$. Some triangular lattice materials with magnetically disordered ground state such as $NiGa_2S_4$ and $Ba_3CuSb_2O_9$ show $C(T) \sim T^2$ [11, 143], but the latter only in an intermediate temperature regime, while the former is a $S = 1$ system with quadrupolar order [141, 144, 145]. Last but not least, the quadratic specific heat could be related to a Dirac QSL, as suggested for the strongly frustrated 2D triangular S=1/2 material $Sr_3CuSb_2O_9$ [76]. While the possible connection to such a QSL scenario is thrilling, more evidence is certainly needed to support that conclusion, especially in the light of the small fitting interval in Fig. 4.5(b).

A natural next step is the direct comparison with other $AYbX_2$ compounds without apparent order. This turns out to be difficult in many cases because the zero-field specific heat has only been measured down to 400 mK [120, 131, 134, 136, 146], or with very few data points [129, 134], which seriously hinders clear interpretations. In $NaYbO_2$, on the one hand, $C_\mathrm{m} \sim T^2$ has first been anticipated down to 200 mK [133], but the analysis turned out to be more complex [68], see also Sec. 4.2.2. A quadratic specific heat evolution has been suggested for $NaYbS_2$, too, which was interpreted as a signature of a Dirac QSL [134]. Their fit, however, includes only five data points, and the specific heat has to be extended to much lower temperatures for more confident statements. In a study on $NaYbSe_2$ single crystals, the nuclear contribution subtraction remains unclear to some extend [119]. Furthermore, the data show several humps, which severely limits the conclusion of a potentially linear specific heat. The report on powder samples [135] did not analyse the low-temperature specific heat. Therefore, the underlying microscopic scenario in $KYbS_2$ remains unclear so far, and additional measurements in the 100 mK region are crucially important. Local probes such as μSR or NMR can evidence dynamically fluctuating spins even at lowest temperatures, which is a key feature of a QSL. Ac-susceptibility and FC/ZFC dc-magnetization are very sensitive to spin freezing as well and would be useful to exclude spin glass physics. Neutron scattering could confirm the absence of magnetic order and benchmark theoretical models by, for example, determining points of spectral weight accumulation in the Brillouin zone [68]. After discussing the properties in zero field, the focus is now shifted towards a different as-

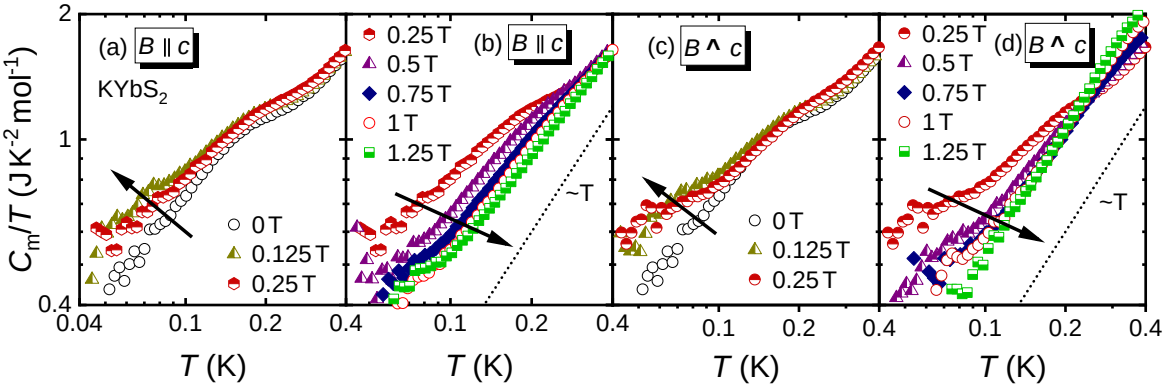

Figure 4.6. Magnetic specific heat $C_\mathrm{m}(T)/T$ after subtraction of the nuclear contribution to follow the evolution of the low-temperature kink around 200 mK discussed in the context of Fig. 4.5(f). Small magnetic fields up to 0.25 T result in slight enhancement but preserves the kink. Further increasing the field, however, suppresses the kink and recovers $C_\mathrm{m} \sim T^2$ (dotted line) independent from the applied field direction (a),(b) $\mathbf{B} \parallel \mathbf{c}$ and (c),(d) $\mathbf{B} \perp \mathbf{c}$, respectively.

pect. The triangular lattice in general hosts a plethora of field-induced states [35]. One prominent example is the up-up-down (uud) state, which manifests in a 1/3-magnetization plateau and has been initially proposed in the isotropic NN Heisenberg model [128]. This has been verified experimentally, for example in $Ba_3CoSb_2O_9$ [116–118]. Despite the potential QSL ground state, that is clearly distinct to the simple NN Heisenberg model, $KYbS_2$ might reveal similar non-trivial states in magnetic fields. Intriguingly, magnetization plateaus have already been observed in other AYbX$_2$ materials such as $NaYbO_2$ [68], $NaYbSe_2$ [119] and $CsYbSe_2$ [120]. A pronounced anisotropy is present in these materials – the plateau is only detected for applying the magnetic field in the ab–plane of the triangular lattice. Similar behavior is expected for $KYbS_2$.

Consequently, the effect of magnetic fields on $KYbS_2$ is investigated in detail for both in-plane ($\mathbf{B} \perp \mathbf{c}$) and out-of-plane ($\mathbf{B} \parallel \mathbf{c}$) field directions. As a first aspect, a closer look is taken on the evolution of the aforementioned kink around 200 mK. Fig. 4.6 depicts the magnetic specific heat divided by temperature, $C_\mathrm{m}(T)/T$, after the subtraction of the nuclear contribution as explained later. Both field directions reveal similar behavior. For fields up to 0.25 T, the specific heat becomes slightly enhanced at lowest temperatures, but the kink is still visible [Fig. 4.6(a,c)]. Further increasing the magnetic field has two effects. First, the specific heat at lowest temperatures is suppressed. Second, the kink broadens and finally vanishes above fields of 0.5 T leaving a robust power law behavior close to T^2, as indicated by the dotted lines in Fig. 4.6(b,d).

In a next step, the nuclear contribution is examined systematically by fitting the low-temperature part of the specific heat. The Schottky peak shifts towards higher temperatures upon increasing magnetic fields [Fig. 4.7(a,b)]. All curves are fitted by assuming gapless magnetic excitations, $C_\mathrm{Sa}(T) = C_\mathrm{nuc}(T) + C_\mathrm{m,pow}(T) = \alpha/T^2 + bT^p$, from lowest available temperatures up to around 300 mK for $\mathbf{B} \perp \mathbf{c}$, whenever reasonable. For $\mathbf{B} \parallel \mathbf{c}$, the fitting range can be expanded to 400 mK because no disturbing features are induced by the magnetic field. The chosen fit function perfectly describes the experimental data for both field directions. This way, the nuclear contribution $C_\mathrm{nuc}(T)$ can be subtracted to obtain the magnetic specific heat $C_\mathrm{m}(T)$ for each field, respectively. At high enough fields, $KYbS_2$ will eventually enter the polarized state by opening a gap, but even at 11 T applied in the easy-

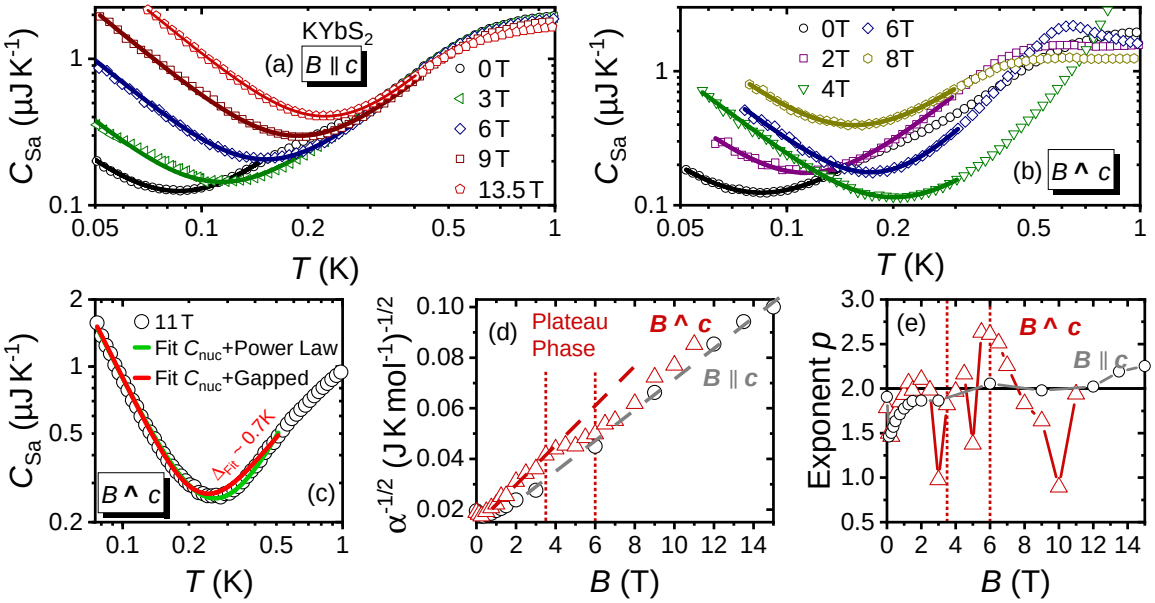

Figure 4.7. Fitting of the heat capacity of $KYbS_2$ at lowest temperatures assuming a power law for gapless magnetic excitations, $C = \alpha/T^2 + bT^p$ (details in the main text). (a),(b) The fit function perfectly describes each of the chosen representative data sets. The fitting range is from the lowest available temperatures up to 400 mK (300 mK) for $\mathbf{B} \parallel \mathbf{c}$ ($\mathbf{B} \perp \mathbf{c}$), whenever possible. More details are summarized in the Appendix (Fig. A.4 and Table A.3). The fit parameter α is used for subtracting the nuclear contribution from each curve, respectively. (c) Even for 11 T, the 2D gappped function cannot account correctly for the magnetic contribution excluding the opening of a gap. (d) Field dependence of the nuclear contribution parameter α. For the out-of plane field direction, $\sqrt{\alpha}$ grows nearly linearly. The in-plane direction, however, shows a distinct change of slope between 3 T and 6 T. This indicates the presence of a magnetization plateau in $KYbS_2$ (details in the main text). (e) Evolution of the power law exponent p. Starting from ~ 1.5 at lowest fields, it smoothly tends towards 2 for $B \parallel c$. The field direction $B \perp c$, however, scatters between 1 and nearly 3, especially in the range of the presumed plateau phase region. For both field directions, p at 0 T is taken from the smaller applied fitting range, see Fig. 4.5(b).

plane ($\mathbf{B} \parallel \mathbf{c}$), the 2D gapped function is significantly worse than the power law [Fig. 4.7(c)]. These results evidence gapless excitations in $KYbS_2$ in the whole measured field range yet the nature of the ground state and, thus, of the excitations changes upon applying in-plane magnetic fields. This can exemplarily be seen in Fig. 4.7(b) for an in-plane field of 6 T, where a magnetic ordering peak is induced.

Before further highlighting the field-induced order, the evolution of the nuclear fitting parameter α is discussed in detail [Fig. 4.7(d)]. While $\sqrt{\alpha}$ for out-of-plane fields increases roughly linearly, the in-plane direction is different. Starting from ~ 3.5 T, the slope becomes less steep and increases again around ~ 6 T. The exact $\sqrt{\alpha}$ values slightly depend on the selected fitting range, but the observed slope change in α is robust (see Appendix, Fig. A.4 and Table A.3). To further evaluate this anomaly, the meaning of α has to be revisited again. It is a measure of the nuclear level splitting Δ (including both quadrupolar and Zeeman contributions) with $\alpha \sim \Delta^2$ when expanding the Schottky formula in the limit of $T \gg \Delta$ [Sec. 2.4.3]. The splitting is directly linked to the local magnetization of the respective ion such as Yb^{3+} [147]. Consequently, in a first approximation, a nonmonotonic behavior in $\sqrt{\alpha}(B)$ indicates an anomaly in the magnetization $M(B)$. Fig. 4.7(d) for $\mathbf{B} \perp \mathbf{c}$ resembles a

magnetization plateau and, thus, gives a first hint on a nontrivial field evolution of $KYbS_2$. The highly anisotropic behavior in $KYbS_2$ is additionally witnessed by the power exponent p of the presumed gapless excitations. The values for the field direction of $\mathbf{B} \parallel \mathbf{c}$ show a smooth evolution, starting from $p \sim 1.5$ at lowest fields and converging towards $p \sim 2$. The field of 0 T stands as an exception if the smaller fitting region is chosen, as explained above. For $\mathbf{B} \perp \mathbf{c}$, however, the exponent starts to deviate from $p = 2$ when coming close to the presumed plateau. Especially the exponents at the fields of 3 T and 5 T are clearly distinct compared to neighboring fields, but the exponents also obviously deviate from $p = 2$ between 5.5 T and 6.5 T. It is noted that the field of 10 T results in a rather abrupt change of the exponent, too, despite being far above the plateau region. The p values are robust under different fitting ranges [Fig. A.4], and the fitting parameters α, p, and b are summarized for all fields in the Appendix [Table A.2].

Let us now return to the field-induced magnetic ordering. Fig. 4.8 shows the magnetic specific heat of $KYbS_2$ between 400 mK and 2 K for two different field directions. In the case of out-of-plane magnetic fields, the specific heat remains nearly unchanged up to fields of 13.5 T and is only slightly suppressed [Fig. 4.8(a)]. For in-plane fields, however, magnetic order is induced. A relatively broad maximum starts to appear in the specific heat, located around 600 mK at 2 T, which becomes increasingly sharp for higher magnetic fields. It is most prominent for the fields of 4 T and 4.5 T [Fig. 4.8(b)]. The lambda-type peak evidences field-induced magnetic order with a pronounced temperature dependence. The maximum first shifts towards higher temperatures, but it eventually reveals the opposite trend for fields above 4.5 T [Fig. 4.8(c)]. This non-monotonic behavior of the phase transition is typical for the uud state and very similar to, for example, $NaYbSe_2$ [119]. At even higher fields above 7 T, the ordering peak smears out until the specific heat becomes completely suppressed at 12 T due to the formation of the field-induced polarized state.

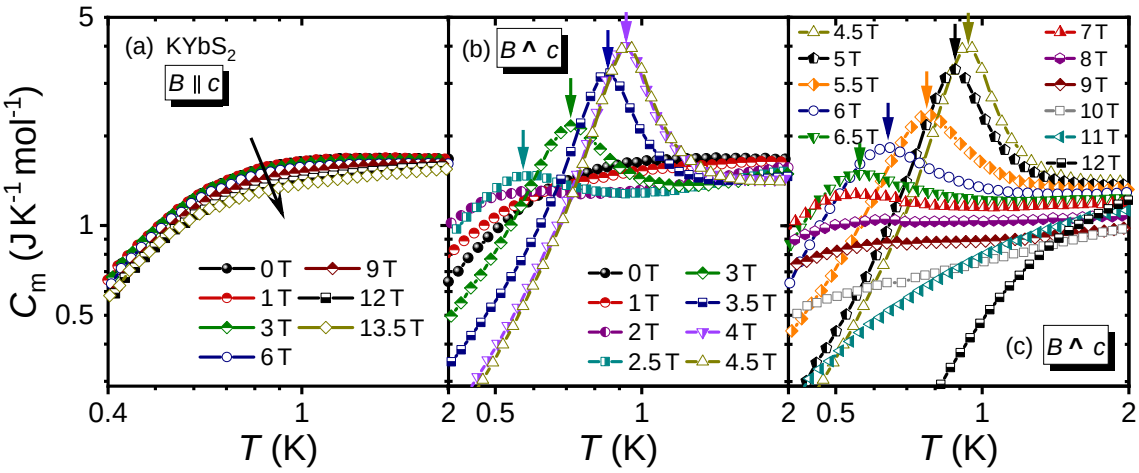

Figure 4.8. Magnetic specific heat $C_m(T)$ of $KYbS_2$ between 400 mK and 2 K after subtracting the nuclear contribution C_{nuc}. (a) Fields up to 13.5 T along the hard axis ($\mathbf{B} \parallel \mathbf{c}$) lead only to a weak suppression of the specific heat as indicated by the arrow. (b) Applying magnetic fields in the easy-plane ($\mathbf{B} \perp \mathbf{c}$) induces magnetic order visible as a peak, which is marked by the colored arrows for selected fields. The peak shifts towards higher temperatures upon increasing the field. (c) For fields above 4.5 T, the ordering peak moves to lower temperatures (colored arrows), becomes broad again and finally vanishes. At 12 T, $KYbS_2$ approaches the polarized state, and the specific heat is rapidly suppressed.

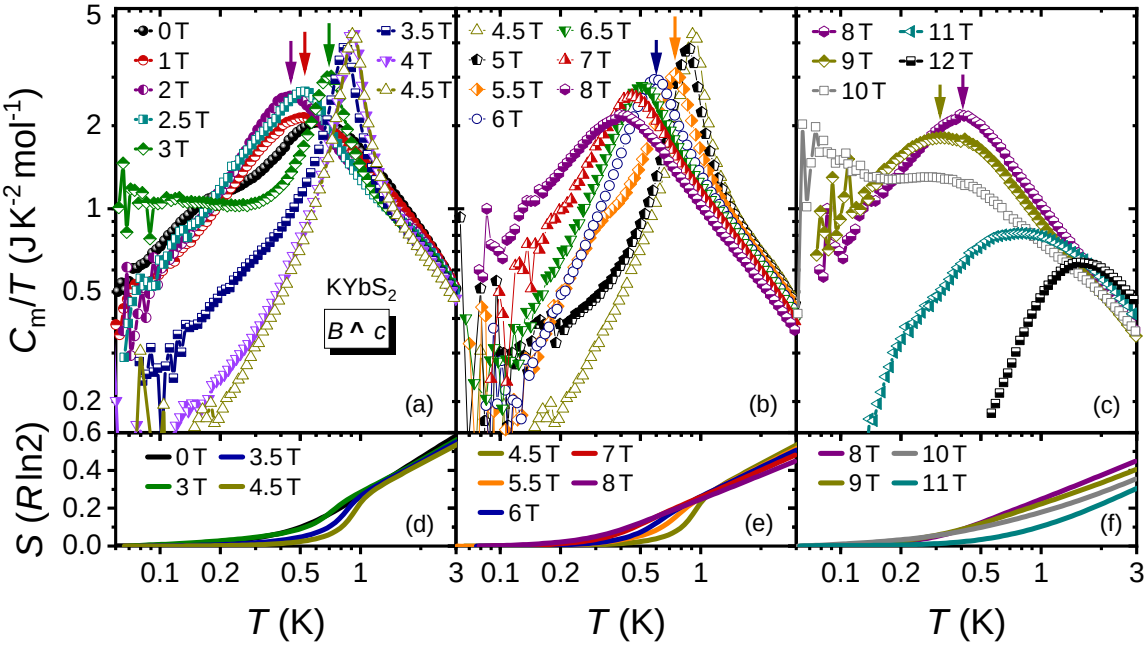

Figure 4.9. Magnetic specific heat of $KYbS_2$ divided by temperature, $C_m(T)/T$, for in-plane fields ($\mathbf{B} \perp \mathbf{c}$, nuclear contribution subtracted). For some representative fields, the arrows indicate the maximum position used for the phase diagram. (a) The temperature dependence of 3 T clearly deviates from comparable fields. (b) Here, 5 T and 5.5 T with their change of slope are distinct to neighboring fields, too. (c) The constant slope of 10 T might result from the suppression of specific heat upon approaching the polarized state. (d)-(f) Evolution of the magnetic entropy from integrating $C_m(T)/T$. At 3 K and 0 T, 60 % of the expected $R \ln 2$ for $J = 1/2$ systems is reached. The field-induced order is visible by the clear change of slope.

In order to establish a phase diagram, the phase boundaries have to be followed carefully. On the one hand, $C_m(T)$ gives first valuable insights. On the other hand, $C_m(T)/T$ provides the opportunity to additionally track the crossover T^* defined in Fig. 4.5(f). Therefore, the latter is presented in Fig. 4.9 between 60 mK and 3 K (nuclear contribution subtracted) where several aspects draw attention. First, the maximum in zero-field in Fig. 4.9(a) shifts towards lower temperatures until the above described magnetic order sets in. On the high-field side, the maximum remains visible up to 9 T yet becomes fairly broad [Fig. 4.9(c)]. For some representative fields, the colored arrows mark the position of transitions or crossovers. Second, the low temperature specific heat becomes rapidly suppressed by the field-induced magnetic order [Fig. 4.9(a)]. A remarkable exception is the field of 3 T, where the specific heat reveals a constant temperature dependence down to the lowest measured temperatures. Obviously, the excitations appear to be distinct compared to the data at similar fields of 2.5 T and 3.5 T, consistent with the results of the power law exponent [Fig. 4.7(e)]. Fig. 4.9(b) shows the opposite trend. Increasing the magnetic field enhances the specific heat at low temperatures again. Two curves, though, reveal anomalous behavior compared to the other fields. Both specific heat curves at 5 T and 5.5 T obtain a change of slope or even a kink around 400 mK. The huge scatter of the data below 100 mK is a result from the very low heat capacity. Finally, the 10 T curve also seems to become nearly constant towards lower temperatures [Fig. 4.9(c)]. However, this simply might be due to the complete suppression of the specific heat upon approaching the saturation magnetization. Altogether, the specific

heat of $KYbS_2$ shows a non-trivial evolution in magnetic fields, as already discussed in the context of Fig. 4.7(d,e).

The temperature-dependent measurements are completed by the calculation of the magnetic entropy $S(T)$ [Fig. 4.9(d-f)]. At 3 K and 0 T, it reaches ∼60 % of the expected value for a spin-1/2 system, $R \ln 2$. This is consistent with [130], where data down to only 400 mK are used. The rest of the ground state entropy is released at higher temperatures, comparable to other AYbX$_2$ materials [131, 132]. The magnetic order induced by magnetic field is accompanied by a sharp increase of the entropy, visible best for the data at 4.5 T [Fig. 4.9(d)]. Larger magnetic fields shift entropy towards lower temperatures in combination with a decrease at 3 K. Eventually, the entropy becomes suppressed in the strongest applied magnetic fields because entropy is shifted towards higher temperatures [Fig. 4.9(e,f)].

To further explore the phase diagram, field-dependent measurements at constant temperatures are highly advantageous. The magnetic Grüneisen parameter $\Gamma_{\mathrm{mag}}(B)$ is ideally suitable for detecting field-induced phase transitions. Consequently, it has been measured up to 14 T for the relevant direction $\mathbf{B} \perp \mathbf{c}$ for several temperatures between 2 K and 100 mK [Fig. 4.10]. The data at elevated temperatures of 2 K and 1.5 K do not show any anomalies except of a broad maximum at 10.8 T. It becomes increasingly sharp by lowering the temperatures down to 100 mK, yet the height becomes smaller again below 250 mK. The position is nearly unchanged over the whole temperature range indicated by the dotted grey line. Such a distinct maximum in the Grüneisen parameter indicates a strong decrease in the field-dependent entropy, which will be discussed later. Most likely, it is related to the closeness to the polarized state and may mark a crossover. Despite that high-field feature, decreasing the temperature down to 500 mK reveals further anomalies in the Grüneisen parameter [Fig. 4.10(a)]. Another maximum as well as a minimum appear around ∼ 3 T and ∼ 5 T indicative for decreasing and increasing entropy, respectively. These features, however, can not be interpreted as a phase transition. Typical for a 2$^{\mathrm{nd}}$ order phase transition is a sign change from negative to positive Γ_{mag} values exactly at the critical field in combination with divergent behavior [82, 84, 148, 149]. Indeed, several relevant sign changes can be detected for 250 mK marked by the purple arrows in Fig. 4.10(b). Those at 2.9 T and 5.3 T are clearly evidencing such a phase transition and can be confirmed down to 100 mK by the arrows in

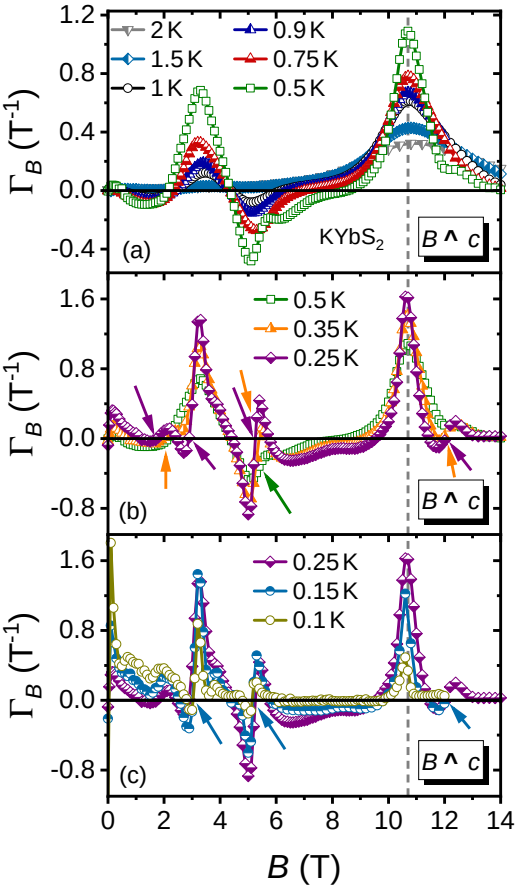

Figure 4.10. Field dependence of the Grüneisen parameter $\Gamma_{\mathrm{mag}}(B)$ of $KYbS_2$ for various temperatures down to 100 mK and fields up to 14 T. The arrows mark presumed phase transitions used for the phase diagram [Fig. 4.12]. At these positions, a (sharp) sign change from negative to positive is visible indicating a 2$^{\mathrm{nd}}$ order phase transition.

Fig. 4.10(c). That result coincides well with the above discussed fields in $C_m(T)/T$ revealing distinctly different low-temperature behavior. It should be noted that the 350 mK data show the sign change at ~ 5.3 T, too (orange arrow), but not at ~ 2.9 T, where only a very weak kink is visible. Furthermore, the 500 mK curve shows a signature (green arrow) yet without sign change. Nevertheless, this feature is interpreted as a phase transition because it resembles a sign change shifted by additional contributions.

Besides the two discussed sharp features, two further sign changes might be relevant at 250 mK. The arrow at ~ 12 T probably marks the transition to the fully polarized state. It is also observable at 350 mK and 150 mK (purple, orange, and blue arrows). At 100 mK, however, the signal becomes too weak to resolve that anomaly anymore. The last remaining sign change at ~ 1.7 T is far more speculative. It might indicate a change of the presumable QSL ground state to a different state. Yet, that sign change is only visible for the data at 350 mK (left orange arrow), and it seems to be shifted upwards for lower temperatures. Nevertheless, it may still be present, and the exact nature of this presumable phase transition remains unclear. An alternative scenario might be a first order transition at 2.2 T, where a maximum can be detected. A comparable signature in the Kitaev material α-$RuCl_3$ has been interpreted that way [94, 95]. Consequently, this field region certainly deserves further attention in the future. After discussing the field evolution of the Grüneisen parameter, the field-dependent specific heat is investigated for the same field direction up to 14 T [Fig. 4.11(a)]. The data at the highest temperatures of 2 K and 1.5 K show a monotonic decrease except of a broad maximum at highest fields, which is visible for all temperatures yet slightly shifted (grey arrow). Similar to the high-field features in $\Gamma_{mag}(B)$, it most likely results from the closeness to the polarized state. It should be noted here that the raw data analysis at high fields ($B \gtrsim 11$ T) and low temperatures ($T \leq 350$ mK) becomes problematic due to 2τ-behavior, which can not be fitted by a single exponential function. The 2τ fit, however, requires too many unknown starting parameter and can not be employed in a reasonable way yet, see Sec. 3.4.1. Therefore, the increase towards highest fields especially at 250 mK is probably not a transition, but an artefact of the problematic analysis.

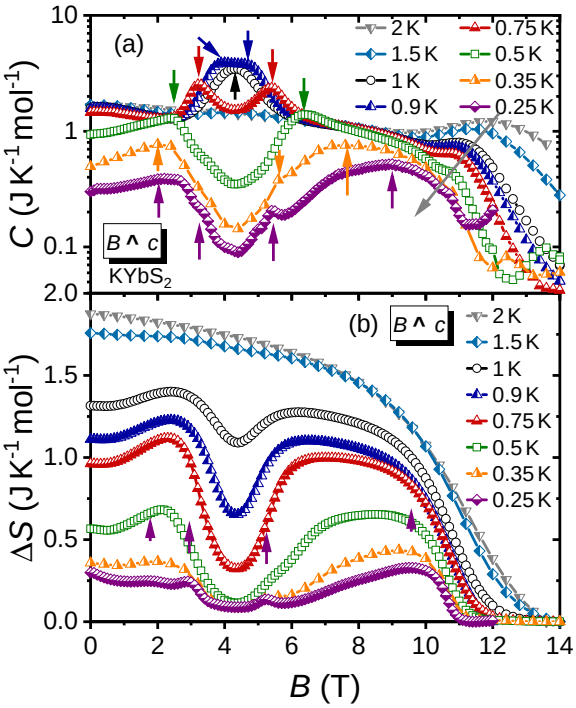

Figure 4.11. Field dependence of the (a) specific heat and (b) entropy change, $C(B)$ and $\Delta S(B)$, respectively. Arrows indicate anomalies taken for the phase diagram. The grey arrow in the specific heat marks the evolution of the presumed crossover at high fields. Colored arrows stand for transitions or crossovers at different temperatures, respectively.

At 1 K, a maximum appears in the specific heat around 4 T, which splits into two separate peaks upon lowering the temperature further. At the lowest temperature of 250 mK, the original two peaks become very broad (left and right arrow). More features appear at this temperature as a peak at 5.4 T and the more subtle kink at 3.3 T. In summary, Fig. 4.11(a) confirms the critical fields determined from $\Gamma_{mag}(B)$.

As a next step, the relative change of the field-dependent entropy is calculated using $\partial S/\partial B = -\Gamma_{\mathrm{mag}} C$ from Eq. 2.40. The results are shifted such that $\Delta S = 0\,\mathrm{J\,K^{-1}\,mol^{-1}}$ at the highest measured field, respectively. As expected, the entropy at high temperatures monotonically vanishes. The steep decrease at high fields is visible for all temperatures, and the inflection point of $\Delta S(B)$ is equivalent to the peak in the Grüneisen parameter $\Gamma_{\mathrm{mag}}(B)$ around 11 T. At 1 K, a prominent minimum evolves around 4 T that becomes steeper for lower temperatures. Eventually, it changes the form at 250 mK, where several maxima appear. They correspond to the previously discussed sign changes in $\Gamma_{\mathrm{mag}}(B)$.

Using all collected information, the field-temperature phase diagram can be drawn, which has not been reported yet. The phase boundaries have been tracked by specific heat, $C(T)/T$ and $C(B)$, as well as the magnetic Grüneisen parameter $\Gamma(B)$. The entropy change $\Delta S(B)$ is included as a color map after normalization to the maximum value ΔS_{max} for each temperature, respectively. This is needed to reasonably compare the entropy change between highest and lowest temperature. Fig. 4.12 reveals the phase diagram of $KYbS_2$. The determined phase transitions follow the entropy evolution very well corroborating the previous analysis. No magnetic order has been found in specific heat $C(T)$ in zero-field down to 50 mK. Therefore, $KYbS_2$ is extremely frustrated with $f \geq 100$ and a prime candidate for a potential QSL. The maximum in $C(T)/T$ at lower fields has been interpreted as a crossover towards the presumed QSL, indicated by the open rectangular symbols in Fig. 4.12. A central feature of the phase diagram is the dome-like structure with its maximum at 4 T and 1 K. Its non-monotonic behavior strongly resembles the formation of the uud state typical for triangular lattices [35] and is most likely responsible for the field-induced magnetic ordering in $KYbS_2$. The presumed uud phase seems to persist down to lowest measured temperatures in $KYbS_2$, which is distinct to classical theoretical calculations restricted to nearest-neighbors [124, 150]. This might be due to quantum effects or indicate an influence of the next-nearest neighbors exchange coupling J_2. On the experimental side, the uud phase in several triangular magnets is suggested to survive down to 0 K, for example, in $Ba_3CoSb_2O_9$ [118, 151] and, in particular, in the related compound $NaYbSe_2$ [119]. This coincides well with $KYbS_2$.

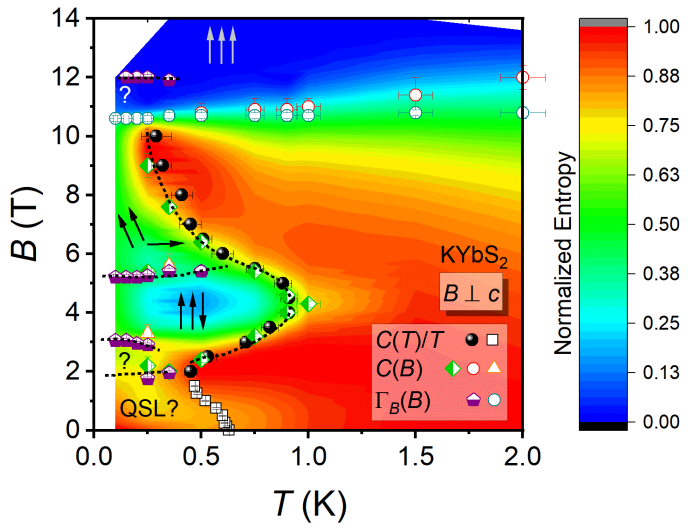

Figure 4.12. Phase diagram of $KYbS_2$ under in-plane magnetic fields ($\mathbf{B} \parallel \mathbf{c}$). Dotted lines are guides to the eye and indicate a phase transition. The open rectangular symbols mark a crossover to the presumed QSL phase. The open circular symbols at high fields probably indicate another crossover.

Increasing the magnetic field destroys the uud configuration, and the canted phase is formed at lowest temperatures, sometimes also called V-phase. At highest fields, the V-phase is left towards the fully polarized state around 12 T, where the Grüneisen parameter shows another sign change. Unfortunately, this is only visible for lowest temperatures. Before entering the fully polarized state, there might be a crossover marked by the open circles in Fig. 4.12. Its

origin is not clear at this point. Another peculiarity is the shape of V-phase boundary. It appears to have a concave form and does not converge to 0 K at a finite field. This is rather different compared to the experimental phase diagrams of other 2D triangular magnets such as $Ba_3CoSb_2O_9$ [118, 151] or $RbFe(MoO_4)_2$ [152] as well as to the classical theoretical phase diagram [124, 150]. It might be a result of the determination of the phase transition in $C(T)/T$, where the maximum becomes very broad above 8 T. Additional measurements to track this phase boundary would be very interesting.

The other possibility to leave the uud state is to lower the magnetic field towards the presumed QSL at lowest temperatures. Interestingly, another phase might evolve between the uud and the QSL phase, which is indicated by $C(B)$ and $\Gamma_{\mathrm{mag}}(B)$. A similar behavior has been suggested for $NaYbSe_2$, yet the lowest measured temperatures are not below 400 mK [119]. The additional phase could be related to the distorted 120° arrangement (Y-phase). In the classical phase diagram of TLAF, the Y-phase connects the 120° ordered ground state in zero-field with the field-induced uud state [35, 124, 150]. Apparently, $KYbS_2$ has a different zero-field ground state, but applying magnetic field may destroy the QSL phase already before the formation of the plateau phase, which could recover the Y-phase.

In summary, several phases have been identified in $KYbS_2$. The exact nature, however, can not be probed by the presented thermodynamic measurements. Further measurements are therefore highly required. Neutron scattering will provide detailed insights into the nature of the zero-field ground state. Despite most likely confirming the absence of long-range magnetic ordering, detecting fractionalized excitations would be a fingerprint of the QSL. Additionally, local probes such as μSR and NMR can exclude possible spin freezing and evidence dynamically fluctuating spins at lowest temperatures. The field-induced phases are interesting as well. The most direct way for evidencing the uud state is the 1/3-plateau in the field-dependent magnetization $M(B)$. Furthermore, neutron scattering in magnetic fields like in NaYbO2 [153] would be extremely valuable to benchmark the proposed phase diagram. Finally, these measurements provide crucial input for developing a microscopic model to shed light on the exact position of $KYbS_2$ in the theoretical phase diagram. QSL on the triangular lattice can be stabilized by considering nearest and next-nearest neighbors in the J_1-J_2 model, but the off-diagonal terms in the spin Hamiltonian can favor such state, too [7]. Which scenario holds for $KYbS_2$ will certainly be central key aspects of future studies.

4.2.2. Polycrystalline $NaYbO_2$

$NaYbO_2$ as a potential QSL candidate has been first reported by Liu *et al.* in 2018 [129]. They showed specific heat and ac-susceptibility of several $A\mathrm{Yb}X_2$ compounds down to temperatures below 100 mK with no sign of magnetic order. This triggered immediate interest and established $NaYbO_2$ as a disorder-free QSL with fluctuating spins even at lowest temperatures [68, 133]. Moreover, the field evolution has been investigated as well, suggesting a rich phase diagram [132, 153]. In this work, the specific heat of $NaYbO_2$ is presented in detail down to 70 mK and up to 14 T. Similar to the previous section about $KYbS_2$, the nuclear contribution is discussed and subtracted carefully. Parts of the presented specific heat measurements have already been published in Ding *et al.* [68]. $NaYbO_2$ crystallizes in the $R\bar{3}m$ space group like $YbMgGaO_4$ and $KYbS_2$ [Fig. 4.13(a)]. The Yb^{3+} ions form a perfect triangular lattice with a distance of 0.334 nm to nearest in-plane neighbors [Fig. 4.13(b)]. The triangular planes are well separated by layers of Na^+, and the larger interplane distance of 0.582 nm suggests strong quasi two-dimensional character of the material. In analogy to $KYbS_2$, no structural disorder is present in $NaYbO_2$ because site-mixing of non-magnetic ions is not possible [68]. This is in contrast to $YbMgGaO_4$ (see Sec. 4.1), rendering $NaYbO_2$ an ideal candidate to explore QSL physics without structural disorder.

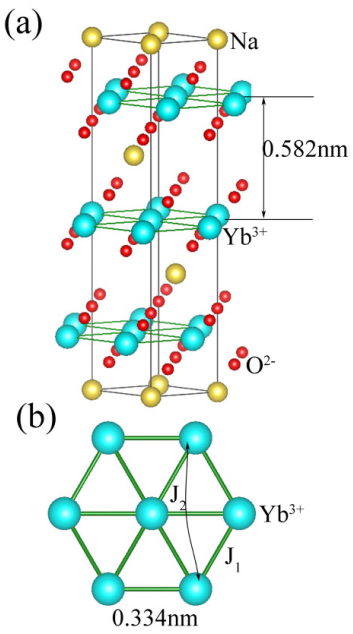

Figure 4.13. (a) Crystal structure of $NaYbO_2$. (b) Triangular arrangement of the Yb^{3+} ions. Graph adapted from Ref. [68], copyrighted by the American Physical Society.

Fig. 4.14(a) shows the specific heat of $NaYbO_2$ between 70 mK and 20 K in zero field. The dilution refrigerator MK 4 was used up to 4 K, and the PPMS measurements from Franziska Grußler extended the temperature range towards higher temperatures. The cell background has been subtracted for both measurements. The inset shows that it becomes negligible below 2 K. Furthermore, a PPMS measurement of the non-magnetic reference $NaLuO_2$ (F. Grußler) is used to subtract the lattice contribution that becomes neglectable at low temperatures as well. Consequently, the resulting magnetic specific heat $C_\mathrm{m}(T)$ of $NaYbO_2$ is dominating the depicted temperature range. It reveals a broad maximum around 2 K reproducing the results of [132] and [153]. The latter presumed a weakly visible double peak structure that, in turn, is not present here. Most importantly, the specific heat shows no sign of magnetic order down to 70 mK rendering $NaYbO_2$ a promising QSL candidate. In the light of a Curie-Weiss temperature of $\Theta_\mathrm{CW} \sim -6\,\mathrm{K}$ [68, 132], the empirical frustration parameter evidences strong frustration, $f \gtrsim 85$.

At low temperatures, the specific heat reveals an upturn [Fig. 4.14(b)]. Like in $KYbS_2$, the Yb^{3+} nuclei create a Schottky anomaly at ultra low temperatures. The quadrupolar splitting of the nuclei levels is responsible for that anomaly in zero field, and applying magnetic fields shifts the Schottky peak towards higher temperatures. This nuclear contribution C_nuc complicates the specific heat analysis. Thus, its subtraction is extremely desirable. In analogy to $KYbS_2$, the specific heat at lowest temperatures is fitted with $C(T) = C_\mathrm{nuc} + C_\mathrm{m} = \alpha/T^2 + bT^p$, assuming gapless excitations for the magnetic contribution. The exponential counterpart of a gapped system is excluded because it describes the data worse, see Fig. A.7 in

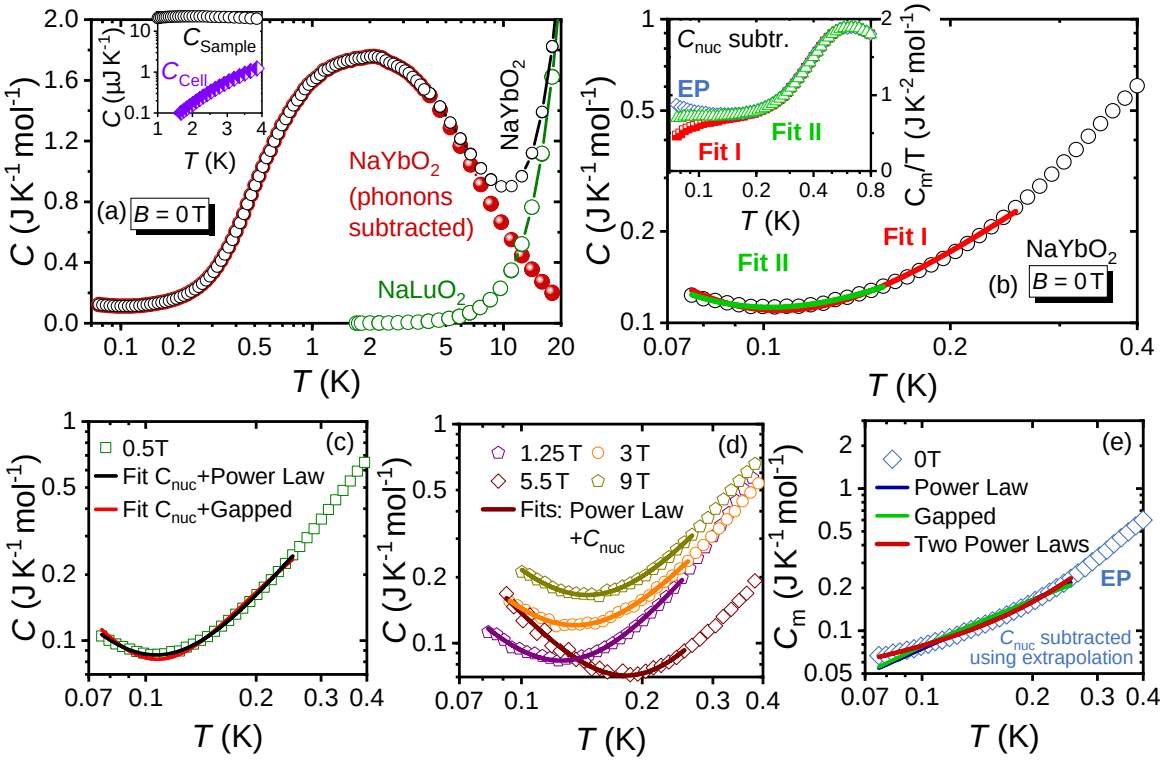

Figure 4.14. (a) Specific heat of $NaYbO_2$ in zero field. PPMS measurements at higher temperatures performed by Franziska Grußler. The phonon contribution C_{lat} is subtracted using the non-magnetic reference $NaLuO_2$, which vanishes rapidly below 5 K. The cell background in the MK 4 is subtracted as well and becomes negligible below 2 K (inset). No magnetic ordering is visible down to the lowest temperature of 70 mK. (b) The upturn below 100 mK stems from the nuclear contribution. Gapless behavior is assumed for the fitting function $C = \alpha/T^2 + bT^p$ (see main text). However, fitting the data turns out to be ambiguous. The results depend on the chosen fitting interval leading to different low temperature evolutions (inset). Another possibility to subtract the nuclear contribution in zero field is shown in blue. Here, the linear extrapolation (EP) of the results in low fields is used, described in detail in Fig. 4.15(a). Consequently, the exact low temperature behavior remains unsettled to some extent. (c,d) Specific heat in various magnetic fields. Assuming gapless magnetic excitations (power law) results in perfect agreement between fit and data, in contrast to a gapped fit function. (e) Attempt to fit magnetic specific heat $C_{\mathrm{m}}(T)$ in zero field up to 250 mK to stress the difference compared to the measurement at $B = 0.5$ T. The nuclear contribution was subtracted using the extrapolation explained in Fig. 4.15(a). A single power law or aingle gapped function is not satisfactory, but two power laws with the exponents of ∼0.5 and ∼2.9 are a possibility to describe the experimental data well. This fit, however, is ambitious to some extent because the fit results are rather sensitive to the fitting interval and the nuclear contribution subtraction. Data partially published in Ref. [68], copyrighted by the American Physical Society.

the Appendix, where also all fitting parameters (α, p, prefactor b) are summarized [Table A.4]. Unfortunately, the power law function in zero field remains problematic as well. Three different approaches to subtract the nuclear contribution are presented in the following. First, using a fit range up to 250 mK does not represent the data perfectly and, specifically, seems to overestimate the nuclear contribution (Fit I, red, in Fig. 4.14(b)). Second, reducing the temperature interval down to $\sim$ 150 mK allows, on the one hand, a much better fit (Fit II, green). On the other hand, such a small range might not have enough data points for

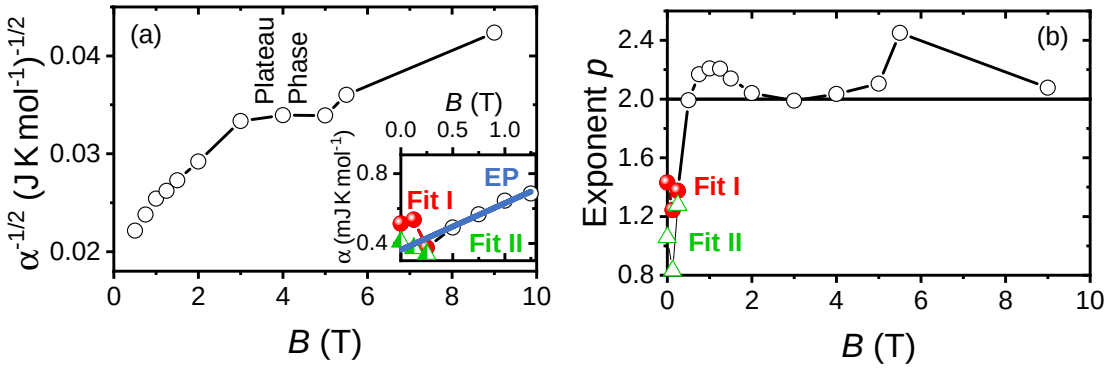

Figure 4.15. (a) Field-dependence between 0.5 T and 9 T of $\sqrt{\alpha}$ that parameterizes the strength of nuclear contribution. Lines are guide to the eye. The slope clearly changes between 3 T and 5 T giving rise to a plateaulike feature. This indicates the formation of a field-induced phase. The inset shows the dependence of $\alpha(0\,\mathrm{T})$ for Fit I (red) and Fit II (green). The linear extrapolation (EP) of $\alpha(B)$ is presented in blue using fields between 0.5 T and 1.25 T. (e) Evolution of the power exponent p. The exponents at $B \leq 0.25$ T depend on the chosen fit range. Except of these fields, p is close to 2. At 5.5 T, the exponent clearly exceeds $p = 2$, which is maybe related to the destruction of the plateau phase.

reliable results. The third approach determines the zero-field nuclear contribution indirectly. If small magnetic fields are applied, $C_\mathrm{m}(T)$ can be perfectly described by a simple power law, for example at 0.5 T and higher fields in Fig. 4.14(c,d). This way, the nuclear contribution parameter α can be determined at those fields. Subsequently, $\alpha(0\,\mathrm{T})$ is estimated by linearly extrapolating $\alpha(B)$ between 0.5 T and 1.25 T towards zero field as shown in Fig. 4.15(a). Subtracting the nuclear contribution with $\alpha = 5.1(2)\,\mathrm{J\,K\,mol^{-1}}$ (Fit I), $\alpha = 4.09(7)\,\mathrm{J\,K\,mol^{-1}}$ (Fit II), and $\alpha = 3.66(9)\,\mathrm{J\,K\,mol^{-1}}$ (from extrapolation: EP) yield different specific heat below 200 mK. This is visualized best by plotting $C_\mathrm{m}(T)/T$, which is shown in the inset of Fig. 4.14(b). The data might become constant indicating $C_\mathrm{m}(T) \sim T$ (Fit II), but $C_\mathrm{m}(T) \sim T^p$ with $p < 1$ or even a similar low temperature kink like in $KYbS_2$ (Fit I) could be reasonable as well. A linear specific heat might indicate spinons in $NaYbO_2$, but this interpretation remains speculative as long as the nuclear contribution subtraction is not unambiguously solved. Definitely, the magnetic specific heat in zero-field up to above 200 mK cannot be described by a single power law function. However, two power laws, $C_\mathrm{m}(T) = bT^p + dT^q$, are sufficient to fit the data reasonably well when the extrapolated nuclear contribution is used for the subtraction [Fig. 4.14(e)]. The resulting power law exponents of $q \sim 2.9$ and $p \sim 0.5$ vaguely resemble the T^3 behavior of 3D antiferromagnetic magnons and the magnetic contribution of $YbMgGaO_4$ in zero-field with $T^{0.7}$, respectively. On the other hand, this two power law fit is strongly sensitive to the chosen fitting interval and the subtraction of the nuclear contribution. Furthermore, four independent fitting parameter are used in the rather small fitting range between 70 mK and 250 mK. Other fit functions might account for the observed behavior as well. Thus, this approach should not be overestimated, and the exact behavior remains speculative to a certain point. For more confident statements and, in particular, to confirm the validity of fit range II, further data points at even lower temperatures would be crucial, yet technically challenging.

As a triangular lattice material, $NaYbO_2$ is expected to exhibit interesting field-induced behavior. Before focusing on higher temperatures, the nuclear contribution is examined systematically. Fig. 4.14(d) shows several specific heat curves for representative magnetic fields

up to 9 T. As already mentioned above, they can be perfectly fitted by $C(T) = \alpha/T^2 + bT^p$ up to 250 mK evidencing gapless excitations. Similar to $KYbS_2$, the field-evolution of the nuclear contribution parameter α does not evolve monotonically [Fig. 4.15(a)] and indicates the formation of a plateau phase between 3 T and 5 T. This coincides with magnetization data revealing a 1/2-plateau [68], which appears in the J_1-J_2-model for $J_2/J_1 > 0.125$ [125]. Inelastic neutron scattering suggests the onset of such a phase at 2.75 T, too, yet the phase was identifed as the 1/3-plateau [153]. While the exact origin might still remain under debate, the nuclear contribution parameter evidences the non-trivial field evolution of $NaYbO_2$, in close analogy to $KYbS_2$. Moreover, the power law exponent p vaguely resembles $KYbS_2$ as well [Fig. 4.15(b)]. The exponent is close to $p = 2$ except at very low fields ($B \leq 0.25$ T), where considerable lower values are obtained, depending on the chosen fit range. Furthermore, the exponent at the field of 5.5 T stands as an exception, too, because of its larger value. This might be related to the destruction of the presumed plateau phase. Nevertheless, the evolution of the power law exponent in $NaYbO_2$ seems to have fewer anomalous features than in $KYbS_2$, especially upon entering the plateau phase, compare $p \sim 1$ for $KYbS_2$ at 3 T [Fig. 4.7(e)]. One possible explanation is that a $NaYbO_2$ powder pellet has been measured. This naturally averages over all crystallographic directions, rendering all anomalies less pronounced. On the other hand, $NaYbO_2$ and $KYbS_2$ might simply reveal distinct plateau phases (1/2 vs. 1/3), where potentially different behavior could be expected. This would, in turn, indicate different J_2/J_1-ratios in those compounds.

The appearance of the plateau phase can be followed by heat capacity, too. Here, the focus is on temperatures below 2 K. Fig. 4.16(a-d) depicts the temperature-dependent magnetic specific heat $C_m(T)$ between 300 mK and 2 K after subtracting the nuclear contribution for each field, respectively. For the data at 2 T, a bump manifests at $\sim$ 500 mK. It evolves into a lambda-type peak shifting towards higher temperatures with increasing fields being sharpest and most pronounced at $\sim$ 1 K for the field of 5 T. By further increasing the field, this peak becomes suppressed roughly staying at the same temperature. At the same time, a second feature appears as a kink that is marked by an arrow in Fig. 4.16(c). For 9 T and higher fields, only a broad maximum remains in the magnetic specific heat, which becomes rapidly suppressed upon approaching the polarized state above 10 T.

In order to track these anomalies better, the specific heat divided by temperature, $C_m(T)/T$, is used in accordance with Ranjith *et al.* [132]. Fig. 4.16(e,f) show the measured data from 80 mK up to 2 K after subtracting the nuclear contribution. As a side note, all curves measured down to below 300 mK follow a power law as discussed above. In analogy to the analysis of $KYbS_2$, the maximum in zero-field is interpreted as the crossover to the presumed QSL state (black arrow). Applying a magnetic field first shifts this maximum to lower temperatures, but the opposite trend is observed after exceeding 2 T, as already discussed (colored arrows). Above 5 T, the double peak becomes better visible than in $C_m(T)$ and can already be identified at 5.5 T (orange arrows). The 9 T curve might still show a weak leftover of the right peak around 900 mK (brown arrow with question mark), but it is completely vanished for even higher fields. The left peak persists as a broad maximum probably even up to 12 T, which is very close to the saturation of $NaYbO_2$ [68, 132]. Remarkably, the two peaks neither seem to merge nor to be suppressed to zero temperature. The vanishing at finite temperature might indicate a first order transition. As a closing remark on the temperature-dependent measurements, the entropy $S(T)$ calculated from $C_m(T)/T$ seems to be very similar to $KYbS_2$. Roughly 65 % of the expected entropy of $R \ln 2$ is reached at a temperature roughly comparable to the exchange coupling in $NaYbO_2$, $T \sim 4$ K [68]. At 20 K, the magnetic entropy saturates at approximately 90 % of $R \ln 2$, see Appendix Fig. A.7.

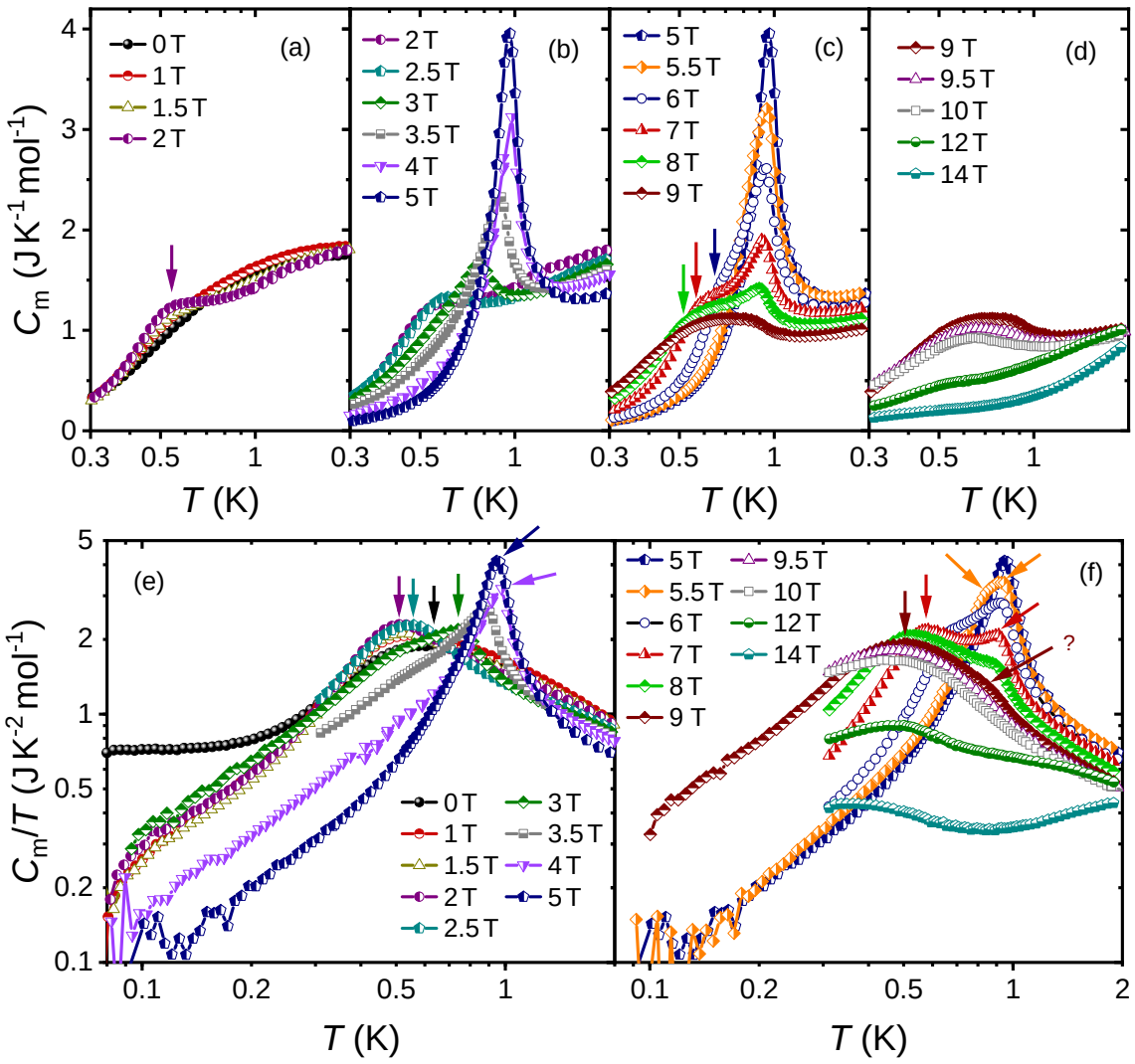

Figure 4.16. Tracking of field-induced phase transitions in $NaYbO_2$. (a)-(d) Magnetic specific heat $C_m(T)$ between 300 mK and 2 K. At 2 T, a broad bump appears that is transformed to a sharp lamda-type peak for higher fields up to 5 T. Further increasing the field suppresses the peak and induces a second anomaly [arrows in panel (c)]. Above 9 T, the remaining broad maximum smears out and vanishes when the polarized state is approached. (e)-(f) Magnetic specific heat divided by temperature $C_m(T)/T$ between 80 mK and 2 K. This allows to follow several anomalies easier. Especially the double peak structure is better visible, for example in the 5.5 T data [orange arrows].

In the following, the field-evolution up to 4 T of the Grüneisen parameter and specific heat are briefly discussed. Time limitations in the measurement plan thwarted more detailed measurements towards higher fields. Nevertheless, first insights can be gained even with the reduced field range.

The Grüneisen parameter $\Gamma_{mag}(B)$ is presented in Fig. 4.17(a) for temperatures between 150 mK and 2 K. It strongly resembles the behavior of $KYbS_2$. The data at high temperatures are featureless, but anomalies start to become visible upon lowering the temperaure. A first clear evidence of a 2nd order phase transitions appears at $\sim$ 3 T in the data at 200 mK(right

purple arrow). It confirms the onset of the plateau phase in the nuclear contribution parameter α [Fig. 4.15(a)]. At this temperature, a second sign change from negative to positive is visible around 2 T (left purple arrow), which may indicate another second order phase transition. The alternative scenario of a first order transition at 2.3 T at the position of the broad maximum has been discussed in $KYbS_2$. Apart from the nature of the putative phase transition, it might simply be explained as the suppression of the QSL favoring the more common Y-phase expected in TLAF [35, 124, 150] before transforming into the plateau phase. Nevertheless, the exact origin remains speculative at this point. Complementary to the magnetic Grüneisen parameter, the specific heat $C(B)$ has been measured, too. It does not show any anomaly in the measured field range at elevated temperatures of 2 K [Fig. 4.17(b)]. Nonetheless, the onset of the plateau phase around 3 T becomes visible in the data below 1 K, where the maximum looks very similar to the $KYbS_2$ specific heat data. Beyond 4 T, another maximum is expected, when the plateau phase is left. It is worth mentioning that the temperatures $T \leq 200$ mK exhibit a maximum around small fields of 0.2 T. That is again in analogy to $KYbS_2$ and can be seen in $C(T)$ at lowest temperatures and fields as well, see Appendix Fig. A.6. The entropy change $\Delta S(B)$ is presented in Fig. 4.17(c). It has been shifted such that $\Delta S(4\,\mathrm{T}) = 0\,\mathrm{J\,K^{-1}\,mol^{-1}}$. Having higher fields up to the polarized state would be extremely advantageous for a better direct comparison between the data at different temperatures, similar to the discussion in $KYbS_2$. The steep entropy reduction due to plateau phase can be clearly identified in the curves at temperatures below 1 K, though.

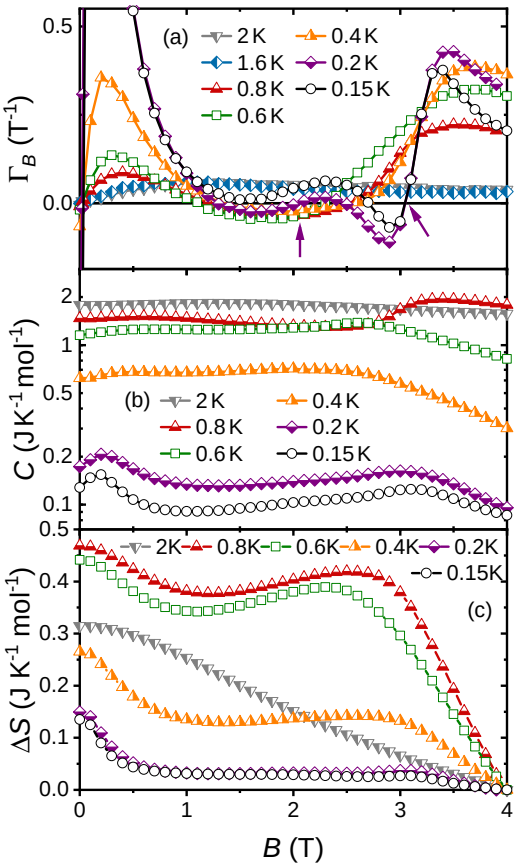

Figure 4.17. Field evolution of $NaYbO_2$ up to 4 T. (a) Magnetic Grüneisen parameter $\Gamma_{\mathrm{mag}}(B)$. The data at 200 mK and below show an abrupt sign change at 3 T indicating the formation of the plateau phase. The overall behavior is similar to $KYbS_2$, including the potential sign change marked by the arrow in purple around 2 T. (b) Specific heat $C(B)$ and (c) entropy change $\Delta S(B)$ indicate the onset of the plateau phase above 3 T as well.

With the thermodynamic measurement results, the phase diagram of $NaYbO_2$ can be drawn [Fig. 4.18]. There are several similarities compared to $KYbS_2$. The presumed QSL phase is located in the low-temperature and low-field limit. Several reasons support that interpretation. Zero-field specific heat data do not show any sign of long-range order down to $\sim$ 70 mK despite some ambiguities in the exact subtraction of the nuclear contribution. μSR measurements show fluctuating spins down to 100 mK [68]. Moreover, the spectral weight in neutron scattering accumulates at the K-point [68] as predicted from theory for a Dirac QSL [39]. Furthermore, ac-susceptibility excludes spin freezing as well [129, 133]. These results firmly establish $NaYbO_2$ as a promising QSL candidate. The QSL phase is destroyed by applying medium magnetic fields, which is evidenced by

at least one sign change in the Grüneisen parameter indicative of a 2$^{\text{nd}}$ order phase transition. Subsequently, the system enters another region associated with a plateau phase in the magnetization $M(B)$ at ∼500 mK [68, 132]. The plateau forms around half of the saturation magnetization $M_{\text{Sat}}/2$ suggesting the up-up-up-down (uuud) phase, indicating a sizeable next-nearest neighbor interaction, $J_2/J_1 > 0.125$ [125]. This is in contrast to the original proposal of the uud phase by analysis of neutron scattering data [133, 153]. Consequently, the exact nature of this phase remains unsettled so far. In sharp contrast to $KYbS_2$, $NaYbO_2$ reveals two phase transitions in $C(T)$ measurements above $T \geq 5.5$ K reproducing Ranjith *et al.* [132]. An additional phase seems to be stabilized as soon as the anticipated canted V-phase is destroyed by increasing the temperature. This is clearly different compared to the phase diagram of $KYbS_2$ in Fig. 4.12 or to other triangular magnets [118, 119, 151, 152]. The two transitions do not merge up to 9 T, and at higher fields, the second transition seems to be completely suppressed. This may indicate a 1$^{\text{st}}$ order phase transition. Indeed, neutron scattering data suggest a similar scenario by detecting a hysteresis behavior between up and down sweep of the magnetic field. Bordelon *et al.* find evidence for a different, non-collinear magnetic order when sweeping the field from 10 T down again [153]. However, this was shown for temperatures below 100 mK and, thus, can not be responsible for the phase appearing between ∼ 500 mK and 1 K. It would be interesting to repeat the neutron scattering experiment in that higher temperature range. Another possible explanation for the two phase transitions is the polycrystalline nature of the sample. If, for example, the V-phase can be stabilized for different field directions, but with different ordering temperatures, measuring a powder pellet might give rise to the presented phase diagram. Single crystalline samples would definitely help to clarify that issue, but the synthesis seems to be impossible so far.

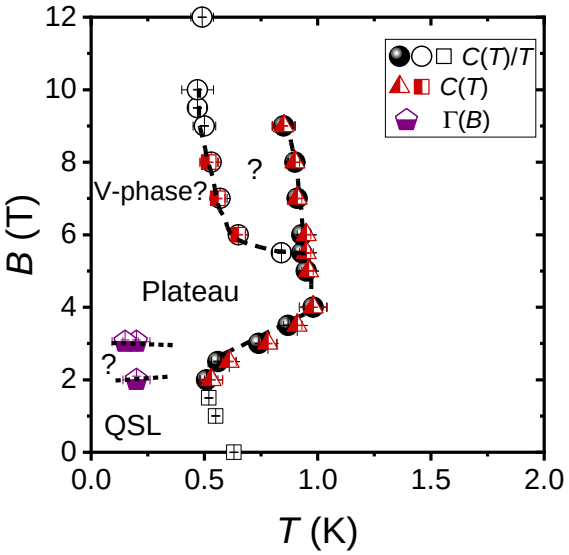

Figure 4.18. Phase diagram of $NaYbO_2$. At low fields, it strongly resembles the phase diagram of $KYbS_2$. The open rectangular symbols mark the crossover to the presumed QSL phase. The field-dependence of the magnetic Grüneisen parameter $\Gamma_{\text{mag}}(B)$ was only measured up to 4 T and could not be used to track the expected transition from the plateau to the canted phase (V phase). In contrast to $KYbS_2$, an additional phase seems to be stabilized at intermediate temperatures. Dotted lines indicate phase transitions.

Additionally, the presented temperature dependent experiments alone do not seem to be sensitive to the expected phase transition between the plateau and the putative V-phase. Consequently, additional field-dependent specific heat and Grüneisen parameter measurements up to 12 T are crucial to track this transition, as already seen in the case of $KYbS_2$. Moreover, they could be used to calculate the entropy change $\Delta S(B)$ over the whole phase diagram, like it is shown in the phase diagram of $KYbS_2$. This might help to follow the two phase transitions in more detail. Using the temperature-dependent entropy $S(T) = \int C(T)/T \mathrm{d}T$ only vaguely tracks the lower transition, as shown in the Appendix [Fig. A.8].

4.3. Adiabatic Demagnetization in $KBaYb(BO_3)_2$

Besides the $AYbX_2$ compounds, other rare-earth based 2D triangular lattices have been explored in order to discover more spin liquid candidates. The Ytterbium borates are one example with a huge variety of different chemical compounds [154–161]. Like in $YbMgGaO_4$, the Yb^{3+} ions form a Kramers doublet ground state with an effective spin $J_{\text{eff}} = 1/2$. Geometrical frustration combined with strong quantum effects due to the low spin potentially prevents magnetic ordering. The following section focuses on powder samples of $KBaYb(BO_3)_2$ grown by K. Kavita (EP VI, University of Augsburg). Several thermodynamic measurements are analysed and potential practical applications of this material presented. This section refers to a large extent to Ref. [162], where most of the results have been published. The PPMS measurements of $KBaYb(BO_3)_2$ and $KBaLu(BO_4)_2$ have been performed by K . Kavita together with Yoshifumi Tokiwa (both from EP VI, University of Augsburg). Interestingly, the PPMS measurement only worked if the internal thermal conductivity of the $KBaYb(BO_3)_2$ sample was increased by mixing with silver powder before pressing the pellet. The contribution of silver was subtracted after the measurement.

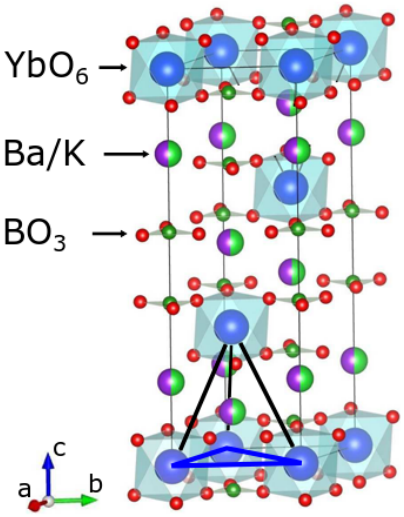

Figure 4.19. Crystal structure of $KBaYb(BO_3)_2$, adapted from Ref. [162] (Creative Commons Attribution 4.0 International License). The triangular arrangement of Yb^{3+} is indicated by the blue lines. The black lines show the relative displacement between neighboring triangular layers.

The crystal structure of $KBaYb(BO_3)_2$ is depicted in Fig. 4.19. The YbO_6 octahedra are arranged on a triangular lattice in the *ab*-plane, indicated by the blue lines that represent the shortest distance to neighbouring Yb^{3+} of 5.41 Å. That configuration potentially gives rise to frustration comparable to the previously discussed materials. The out-of-plane distance between Yb^{3+} is marginally larger (6.64 Å), which could cause additional frustration because the triangular layers are shifted in respect to each other. Furthermore, Ba^{2+} and K^+ occupy the same crystallographic site and, despite of separating the Yb^{3+} layers, introduce structural disorder. This leads to a locally differently charged environment of the Yb^{3+} ions that may result in random exchange couplings comparable to $YbMgGaO_4$, as described in Sec. 4.1 [10, 11, 69, 121]. All these effects potentially suppress magnetic order. In this sense, $KBaYb(BO_3)_2$ might reveal QSL behaviour comparable to $YbMgGaO_4$ and initiated its synthesis and characterization [154, 155, 163].

Due to the larger distance between the magnetic ions, $KBaYb(BO_3)_2$ is expected to show much weaker magnetic interactions compared to $YbMgGaO_4$, $KYbS_2$ and $NaYbO_2$. This is evidenced by the magnetization $M(H)$ at 500 mK, where thermal fluctuations are still dominating over magnetic interactions. It can be fully described by the Brillouin function characteristic of a paramagnet [162]. Fitting the temperature dependent magnetic susceptibility with a fixed van-Vleck term of $\chi_0/\mu_0 = 0.0111\,\mu_B T^{-1}$ yields an effective magnetic moment of $\mu_{\text{eff}} = 2.28\,\mu_B$ and a Curie-Weiss temperature of $\Theta_{CW} = -60(2)$ mK [162]. This can be used to estimate the NN exchange coupling on a triangular lattice [7, 68, 164], $J = (2/3)\Theta_{CW} \sim 40$ mK, being approximately two order of magnitudes smaller than in $NaYbO_2$ ($J \sim 4$ K [7, 68]) or $YbMgGaO_4$ ($J \sim 2$ K [7]). Consequently, ultra low temperatures $T \ll J$ would be required to explore cooperative magnetism

in $KBaYb(BO_3)_2$, which is extremely challenging, or even impossible, and clearly beyond the scope of this work.

The apparent paramagnetic behavior dictates the magnetic specific heat of $KBaYb(BO_3)_2$ down to the lowest measured temperatures [Fig. 4.20(a)]. Here, the non-magnetic reference $KBaLu(BO_3)_2$ has been subtracted as phonon reference. In zero field, no magnetic ordering is visible down to 50 mK except of a small anomaly near 400 mK. It only contributes $\sim 1\,\%$ of the expected entropy $R\ln(2)$ in an effective spin-1/2 system, and, thus, most likely stems from a small impurity phase [162]. A similar anomaly is present in the related compound $NaBaYb(BO_3)_2$, too [156]. Therefore, $KBaYb(BO_3)_2$ remains disordered down to at least 50 mK, which confirms the paramagnetic state. Integrating C_m/T gives direct access to the entropy change [Fig. 4.20(b)]. The zero-field entropy related to the Yb^{3+} Kramers doublet is mostly released below 50 mK that explains the upturn in the specific heat below 300 mK towards lowest temperatures. The doublet is split by magnetic field creating a two-level system ($m_j = \pm 1/2$), which gives rise to a Schottky anomaly in the specific heat, and higher magnetic fields increase the temperature of the peak position [Fig. 4.20(a)]. Consequently, the entropy curves are shifted to higher temperatures as well. At 5 T, only $\sim 10\,\%$ of $R\ln 2$ is released at 2 K. If the field is sweeped to 0 T under adiabatic conditions, then the temperature has to decrease to ensure constant entropy. The end temperature is expected to be well below 50 mK, as indicated by the black arrow in Fig. 4.20(b). This is the concept of cooling by adiabatic demagnetization, and the potential of $KBaYb(BO_3)_2$ will be examined in more detail later. First, the Schottky anomaly in the specific heat is analysed quantitatively.

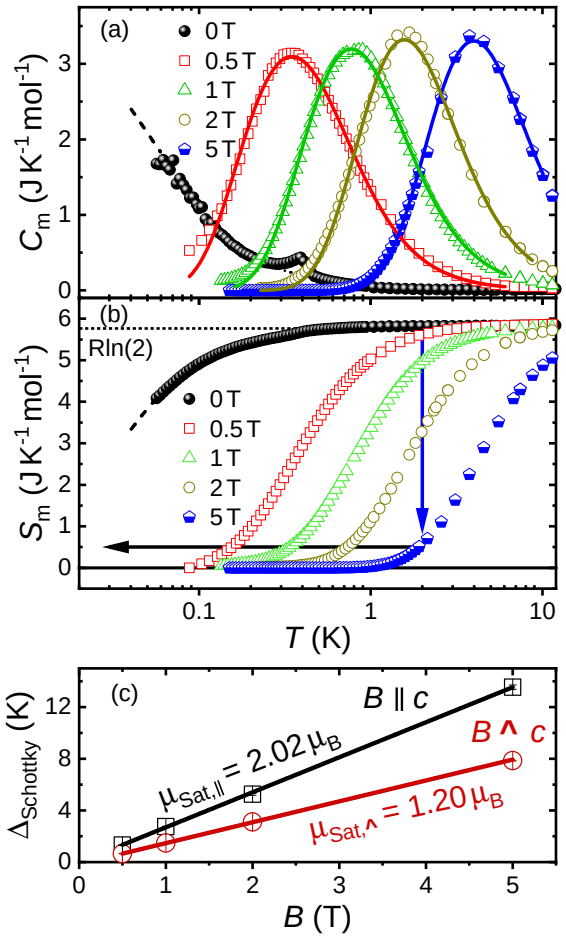

Figure 4.20. (a) Specific heat of $KBaYb(BO_3)_2$ in magnetic fields up to 5 T. Solid lines are fits to the Schottky peak. (b) Entropy of $KBaYb(BO_3)_2$. Magnetic fields shift the entropy of the ground state doublet towards higher temperatures. Adiabatic demagnetization from 5 T to 0 T at 2 K should reach temperatures below $\sim$ 50 mK, indicated by the black arrow. (c) Exctracted gap values from the Schottky fit of the specific heat. The slope corresponds to the saturation magnetization. Data partially published in Ref. [162] (Creative Commons Attribution 4.0 International License).

$KBaYb(BO_3)_2$ exhibits a pronounced easy-axis anisotropy evidenced by the g-factors, $g_\perp = 2.4$ and $g_\parallel = 4.2$, that have been determined in single crystalline samples [163]. The gap due to the Zeeman splitting of the ground state doublet depends on the field direction following $\Delta_{\perp(\parallel)} = 2\mu_{Sat}B = 2g_{\perp(\parallel)}J_{eff}\mu_B B$ [163] – an effect that has to be taken into account here because the specific heat has been measured on a powder pellet. In that case, the small polycrystals

have random orientations. In a first approximation, each direction in space contributes with an individual Schottky anomaly,

$$C_{\text{Schottky,powder}}(T) = \frac{C_{\text{a}}(T) + C_{\text{b}}(T) + C_{\text{c}}(T)}{3}. \tag{4.4}$$

$C_{\text{a/b/c}}(T)$ represents a two-level Schottky anomaly, respectively, in the form of Eq. 2.34 normalized per mole. In $KBaYb(BO_3)_2$ with no in-plane anisotropy, the a- and b-directions are equivalent resulting in

$$\begin{aligned} C_{\text{Schottky,powder}}(T) &= \frac{2 \cdot C_{\perp}(T) + C_{\parallel}(T)}{3} \\ &= \frac{nR}{3}\left\{2\left(\frac{\Delta_{\perp}}{T}\right)^2\left[\frac{\exp\left(\frac{\Delta_{\perp}}{T}\right)}{\left[\exp\left(\frac{\Delta_{\perp}}{T}\right)+1\right]^2}\right] + \left(\frac{\Delta_{\parallel}}{T}\right)^2\left[\frac{\exp\left(\frac{\Delta_{\parallel}}{T}\right)}{\left[\exp\left(\frac{\Delta_{\parallel}}{T}\right)+1\right]^2}\right]\right\}. \end{aligned} \tag{4.5}$$

This formula allows perfect fitting of the Schottky anomalies, and the gap evolution can be simultaneously determined for both field directions, $H \parallel c$ and $H \perp c$, respectively [Fig. 4.20(c)]. The saturation magnetization is exctracted by the slope yielding $\mu_{\text{Sat}\parallel} = 2.02(1)\,\mu_{\text{B}}$ and $\mu_{\text{Sat}\perp} = 1.20(1)\,\mu_{\text{B}}$. These results agree very well with the single crystal study of Pan *et al.* [163]. In order to explore possible frustration effects, however, temperatures far below $\Theta_{\text{CW}} \sim 60\,\text{mK}$ would be required. Consequently, statements on potential QSL physics in $KBaYb(BO_3)_2$ are not feasible with the presented studies, as already mentioned above.

While the ground state of $KBaYb(BO_3)_2$ remains elusive so far, its practical implications in the context of adiabatic demagnetization refrigeration (ADR) are highly promising. The entropy evolution in $KBaYb(BO_3)_2$ is a strong indicator that it can be used for efficient cooling to the millikelvin range. Thus, an actual cooling test has been performed in the quasiadiabatic environment of the MK 4. A ∼280 mg pellet has been prepared, where $KBaYb(BO_3)_2$ was mixed with fine silver powder (Ag, 10-50 µm) in equal weights and sintered at 600 °C to improve the internal thermal conductivity. It has been mounted onto the sapphire plate of the heat capacity setup by GE Varnish, and the RuO_2 thermometer on top allows tracking of the pellet temperature [Fig. 4.21(a)]. This setup is designed to minimize thermal contact with the surrounding, which guarantees a very weak thermal coupling to the thermal bath (TRP). The heat flow from and to the pellet, $\dot{Q} = \kappa\Delta T$, is furthermore drastically reduced by giving feedback control to the TRP to minimize $\Delta T = T_{\text{pellet}} - T_{\text{TRP}}$. After applying a magnetic field of 5 T, the sample is cooled down to 2 K to reach the starting point of the demagnetization cooling indicated in Fig. 4.20(b). Then, the magnetic field is sweeped to zero using a rate of 0.25 T/min [red curve in Fig. 4.21(b)]. Immediately, the pellet temperature starts to decrease [black curve] and finally reaches temperatures below the calibration limit of the thermometer (∼22 mK). The minimal temperature is estimated to be around 16 mK by extrapolating the thermometer calibration [162]. The spike around 80 mK is most likely an artefact from the flux pinning in the superconducting magnet. After reaching the lowest temperatures, the pellet slowly begins to warm up due to the weak but finite coupling to the surrounding. The TRP, for example, remains at elevated temperatures because it cannot follow the rapid pellet cooling anymore around 400 mK [dotted line in gray]. Furthermore, the metallic shielding in the MK 4 with temperatures in the order of ∼ 100 mK emits thermal radiation and provides additional heating.

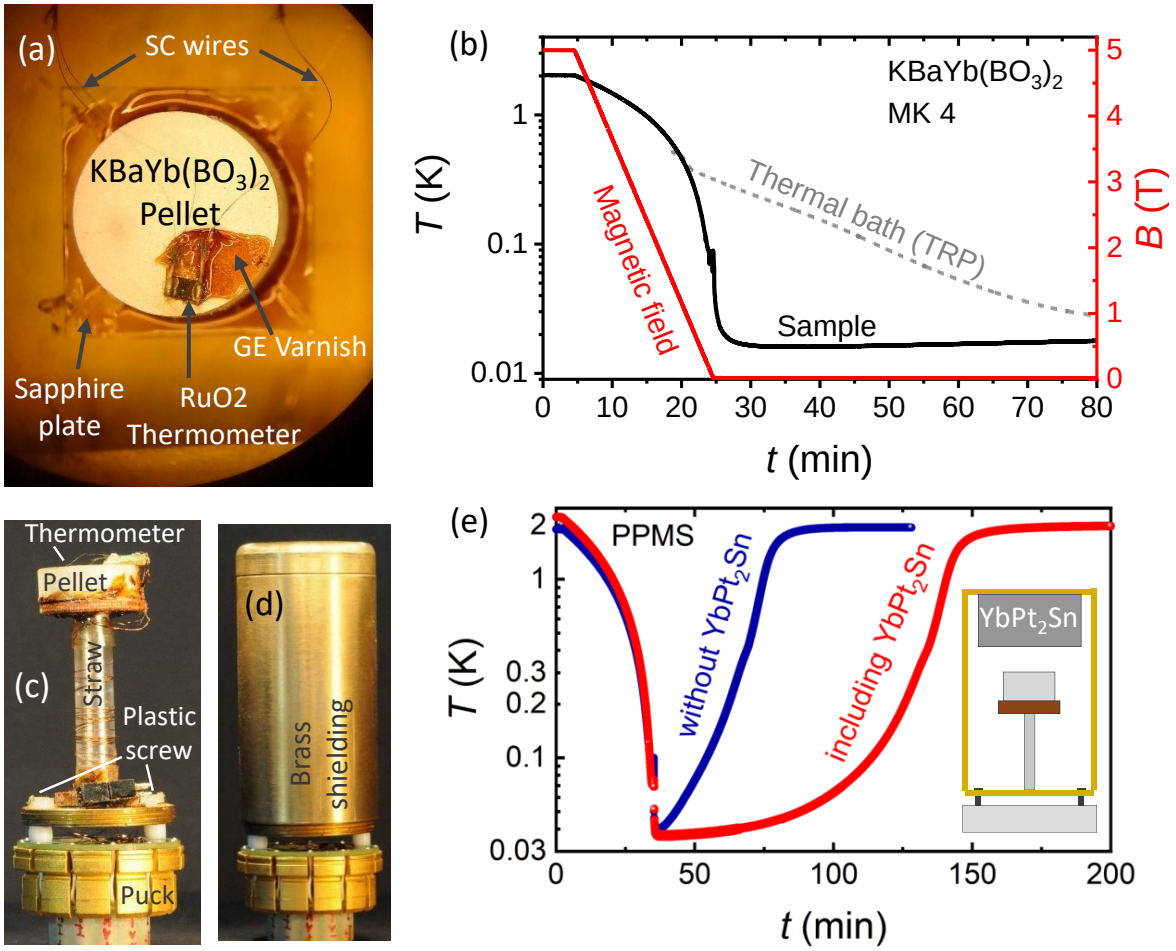

Figure 4.21. (a) Setup for adiabatic demagnetization of $KBaYb(BO_3)_2$ under optimized conditions in the MK 4. The $KBaYb(BO_3)_2$ pellet has been mixed with silver powder to increase the internal thermal conductivity . It is fixed in a heat capacity cell on a sapphire plate. (b) Example for a cooling process in the MK 4 starting at 2 K and 5 T. The measured sample temperature gives feedback control to the thermal bath (TRP). Sweeping the magnetic field to zero starts the cooling of the sample that becomes too fast for the TRP to follow. The sample base temperature is below the thermometer calibration of $\sim$ 22 mK. (c) Setup for adiabatic demagnetization of $KBaYb(BO_3)_2$ in a more realistic application in the 14 T PPMS. The pellet is insulated to the surrounding by several means (straw, plastic screws, Teflon spacer). (d) Brass cap for shielding the setup against external radiation. (e) Cooling curve in the PPMS starting at 2 K and 5 T. The base temperature at 0 T is approximately 40 mK. The warming time up to 2 K can be enlarged by actively cooling the brass stage using another ADR material ($YbPt_2Sn$, details in the text). Similar figures published in Ref. [162] (Creative Commons Attribution 4.0 International License).

The cooling curve of $KBaYb(BO_3)_2$ further strongly suggests the absence of magnetic ordering down to the lowest measured temperatures. A phase transition at the Néel temperature T_N would result in a kink or plateau-like anomaly due to an accumulation of entropy at the phase transition. Below T_N, the entropy rapidly goes to zero and, thus, the ordering temperature would constrain the minimal reachable temperature. Consequently, $KBaYb(BO_3)_2$ remains disordered down to at least $\sim$ 20 mK that, as a side note, results in a frustration parameter of $f \geq 3$.

Naturally, the cooling efficiency of $KBaYb(BO_3)_2$ strongly depends on the chosen setup. The dilution refrigerator offers an extremely cold thermal bath that is not realized in practical applications. In order to demonstrate a more realistic cooling performance, the 14 T PPMS of Quantum Design has been used, where the surrounding is not colder than ∼2 K. A $KBaYb(BO_3)_2$/Ag pellet of 4.02 g is mounted on an adapted resistivity puck [Fig. 4.21(c,d)]. The heat flow from the puck to the sample is reduced by mounting a second platform separated by two Teflon spacer and plastic screws in combination with a plastic straw. Like in the dilution refrigerator setup, a RuO_2 thermometer is glued on top of the pellet. External thermal radiation is suppressed by the brass shield shown in Fig. 4.21(d). The test has been performed in a 14 T PPMS in the HiVac mode. Starting from 2 K, sweeping the magnetic field from 5 T to zero reduces the temperatures down to at least 40 mK. As expected, the temperature increases much faster than in the MK 4 and approaches 2 K after ∼ 50 min. Nonetheless, this would provide enough time for transport measurements, for example the electrical resistivity of a sample attached to the cooling pellet.

The time at lowest temperatures can be easily expanded by actively cooling the brass shielding, too. For this purpose, another ADR compound ($YbPt_2Sn$) is inserted into the brass cap as indicated by the sketch in Fig. 4.21(e). That metallic material shows excellent cooling properties due to its high density of magnetic moments. Although the Yb^{3+} are packed very close to each other, they reveal unusually small magnetic interactions and develop short-range order only around 250 mK [165, 166]. Therefore, attaching an $YbPt_2Sn$ piece of ca. 21 g to the shielding should reduce thermal radiation. Indeed, the $KBaYb(BO_3)_2$ pellet reaches slightly lower temperatures and, most importantly, stays more than one hour below 100 mK [red curve in Fig. 4.21(e)]. The rapid increase towards 2 K is comparable to the blue curve. This indicates that the shielding returns to thermal equilibrium with the warm environment and cannot function as additional cooling stage anymore. Further improvements are certainly possible by enhancing the cooling performance of the second cooling stage. In summary, the presented setup is competitive compared to the commercial ADR stage of the PPMS. Those devices reach a base temperature of 100 mK using the paramagnetic salt chromium potassium alum (CPA) with typical time of 2 hours below 1.9 K [167].

After providing the proof of concept in a practical application, it is of great interest to unscramble the mechanism that renders $KBaYb(BO_3)_2$ a promising cooling material. This might pave the way to design even more optimized ADR compounds among the rare earth borates. First, some general aspects have to be considered. The concept of ADR is based on materials in the paramagnetic state, where the entropy strongly depends on the magnetic field. An ideal ADR compound to achieve ultra-low temperatures needs to fulfill several criteria. (i) Low ordering temperature. Typically, magnetic moments undergo a phase transition towards an ordered state at the ordering temperature T_N around their Curie-Weiss temperature. Then, entropy usually rapidly goes to zero, which effectively constrains the lowest final temperature to approximately $T_f \sim T_N$ [88, 90]. This is directly linked to the interaction strength, $T_f \sim J$ [162]. Therefore, cooling materials for the millikelvin range incorporate crystal water to expand the crystal structure and enlarge the distance between magnetic ions. This, in turn, reduces magnetic interactions and enables lower end temperatures. (ii) High density of magnetic ions. This guarantees adequate cooling power per volume, but it is in direct conflict with the first requirement when crystal water is used to artificially increases the volume of the unit cell. (iii) Maximal entropy change. The entropy related to the ground state multiplet depends on the paramagnet's effective spin, $S = R \ln(2J_{eff} + 1)$. A large spin, however, entails stronger interaction, which is again contrary to (i) [90]. Consequently, if very low end temperatures are required, it is usually at the expense of lower cooling power [90].

Table 4.3. Comparison of different adiabatic demagnetization refrigeration materials. T_{mo} denotes the magnetic order temperature, S_{GS} stands for the entropy of the ground state multiplet, and R is the gas constant. The following abbreviations are used: MAS: $Mn(NH_4)_2(SO_4)_2 \cdot 6H_2O$ (manganese ammonium sulfate [168]), FAA: $NH_4Fe(SO_4) \cdot 12H_2O$ (ferric ammonium alum [168]), CPA: $KCr(SO_4) \cdot 12H_2O$ (chromium potassium alum [169]), CMN: $Mg_3Ce_2(NO_3)_{12} \cdot 24H_2O$ (cerium magnesium nitrate [170]). Table adapted from Ref. [162] (Creative Commons Attribution 4.0 International License).

Material	T_{mo} (mK)	mag. ion/Vol. (nm^{-3})	S_{GS}	S_{GS}/Vol. ($mJ\,K^{-1}\,cm^{-1}$)
MAS [168]	170	2.8	$R\ln(6)$	70
FAA [168]	30	2.1	$R\ln(6)$	53
CPA [169]	10	2.2	$R\ln(4)$	42
CMN [170]	2	1.7	$R\ln(2)$	16
$KBaYb(BO_3)_2$	<22	6.7	$R\ln(2)$	64
$YbPt_2Sn$ [165]	250	12.9	$R\ln(2)$	124
$Yb_3Ga_5O_{12}$ [171]	54	13.2	$R\ln(2)$	124

Frustration and structural disorder, both present in $KBaYb(BO_3)_2$, provide an ideal compromise to combine these requirements. They suppress the magnetic ordering far below Θ_{CW} and allow to achieve much lower temperatures. Furthermore, an amplification of the magnetocaloric effect is possible in frustrated magnet if soft modes are present [172]. Table 4.3 lists several state-of-the-art materials with cooling ability in the millikelvin range. $KBaYb(BO_3)_2$ shows a much higher density of magnetic ions per volume than the paramagnetic salts MAS, FAA, CPA, and CMN that contain crystal water. The ground state entropy used for the cooling process is estimated as $S_{GS} = R\ln(2J_{eff} + 1)$ because all materials approximately use the full entropy of their ground state multiplet in moderate fields [162]. MAS and FAA have a larger value than $KBaYb(BO_3)_2$ due to the higher spin compensating the lower ion density. That makes their entropy to volume ratio S_{GS}/V comparable. However, those two salts magnetically order at 170 mK and 30 mK, respectively, whereas $KBaYb(BO_3)_2$ potentially reaches temperatures below 20 mK. Even lower temperatures can be achieved by CPA and CMN, yet at the cost of reduced S_{GS}/V. Due to its magnetic frustration and structural randomness, $KBaYb(BO_3)_2$ combines dense magnetic ions with an ultra low end temperature, which allows fabrication of more compact ADR devices. It should be noted that there are even higher densities possible in other Yb-based compounds such as $YbPt_2Sn$ or $Yb_3Ga_5O_{12}$. However, the lowest achievable temperature is limited by magnetic ordering at around 250 mK and 54 mK, respectively [165, 171]. All in all, $KBaYb(BO_3)_2$ can compete with the performance of standard materials for ADR in the millikelvin range.

Most importantly, paramagnetic salts as established ADR compounds for $T \leq 100$ mK have two enormous drawbacks compared to $KBaYb(BO_3)_2$. First, thermally contacting the insulating salts requires advanced production methods because the crystals have to incorporate a metallic framework. Second, these cooling materials must not be heated or exposed to vacuum because the huge amount of crystal water destabilizes the crystal. Evaporation of the crystal water is irreversible, thus, the materials easily degrade requiring air-tight sealings. The water-free $KBaYb(BO_3)_2$ overcomes these problems. For the pellet on the adapted PPMS setup, Yb-borate powder has been ground, mixed with silver powder, and pressed into the desired form. Subsequently, it has been sintered at several 100 °C. The chemical stability

under vacuum condition is proved by the experiment in the MK 4 with typical pressures of 1×10^{-6} mbar in the IVC at room temperature. Therefore, $KBaYb(BO_3)_2$ can be used under extreme conditions without further sealing, for example in ultra-high vacuum applications such as millikelvin scanning tunneling microscopes (STM), where baking out the sample chamber including the ADR pill is highly desired [173].

Despite the already highly promising perfomance of $KBaYb(BO_3)_2$, there still might be potential for improvement. Replacing Yb^{3+} by another rare-earth ion with higher spin would drastically increase the amount of available entropy. The Gd^{3+} compound probably has a spin degree of freedom of 7/2 at lowest temperatures [154, 155] resulting in $S = R\ln(8)$, a factor of 3 larger compared to $KBaYb(BO_3)_2$. High spin values have been proposed for Dy^{3+} or Ho^{3+}, too. On the other hand, higher spin values render magnetic interactions stronger. Indeed, the Curie-Weiss constant in $KBaGd(BO_3)_2$ is around 1 K [154, 155]. Thus, it is very unlikely that cooling down to 20 mK is possible. Nevertheless, there is potential to suppress this order by introducing more structural disorder in a doping series such as $KBaGd_{1-x}Yb_x(BO_3)_2$ to combine low end temperature and high entropy. It might be even promising to add more rare-earth ions for maximizing the disorder and the entropy at the same time. Another interesting approach is the replacement of non-magnetic ions, for example K by Na or Ba by Sr to vary the distance between the rare-earth ions. This could be used to adjust the strength of magnetic interaction J. Additionally, it might be worth a try to maximize the site-disorder between the non-magnetic ions using elements with comparable radii, for example by going from K to Rb and from Ba to Sr. Altogether, this could allow to fine-tune the entropy curves and to tailor the compound exactly to the required starting temperature and magnetic field of the specific ADR application. Furthermore, other rare-earth borates could be suitable for ADR as well. Recently, $Ba_3YbB_9O_{18}$ has been reported to obtain a Curie-Weiss temperature of 77 mK [161], which is comparable to $KBaYb(BO_3)_2$. The temperature evolution below 300 mK as well as the field-evolution of the entropy are unknown, though, but further investigations might be auspicious. In summary, exploring the rare-earth borates in detail may reveal further highly competitive and water-free ADR materials.

5. Field Evolution of the Kitaev Material α-$RuCl_3$ for Various In-Plane Field Directions

After Jackeli's and Khalliulin's proposal to realize Kitaev's model, several honeycomb materials such as Na_2IrO_3, α-Li_2IrO_3 ($5d^5$), and α-$RuCl_3$ ($4d^5$) have been intensively investigated. Despite sizeable Kitaev interactions, they do not host a zero-field KSL because a magnetically ordered ground state is formed at low temperatures [22]. The same holds true for the recently proposed Kitaev materials based on the $3d^7$ ion Co^{2+}, for example in $Na_3Co_2SbO_6$, $Na_2Co_2TeO_6$, and $BaCo_2(AsO_4)_2$ [174, 175]. In the specific case of α-$RuCl_3$, zigzag magnetic order evolves below $T_N \sim$ 7–8 K [176–178]. It is a Mott insulator with $j_{\text{eff}} = 1/2$ [23, 57, 179] and sizeable spin orbit coupling (SOC), $\lambda \sim$ 0.10–0.15 eV [179]. α-$RuCl_3$ is monoclinic at room temperature [27, 176] and undergoes a structural first order phase transition with a large hysteresis at around 150 K [15, 180]. The low-temperature structure is still subject of debates, but the magnetic response at low temperature shows approximate six-fold symmetry for in-plane fields due to the honeycomb arrangement of the Ru^{3+} ions, as shown by angle-dependent heat capacity measurements [62]. Neutron scattering in zero field reveals a continuum commonly interpreted as evidence for fractionalized excitations [181, 182]. Furthermore, signatures of Majorana fermions have been reported in the entropy [181, 183], and a broad continuum in THz spectroscopy persisting up to at least 100 K could be connected to fractionalized excitations, too [184, 185]. Altogether, α-$RuCl_3$ is concluded to be in proximity to a Kitaev spin liquid [186, 187]. Moderate in-plane magnetic fields of $\sim$ 7 T suppress the magnetic order, which might unveil underlying spin liquid physics. Excitingly, this exact field range beyond magnetic order features a half-integer quantized plateau in the thermal Hall conductivity κ_{xy} [13] expected for the Kitaev spin liquid and, thus, considered to evidence Majorana fermions in α-$RuCl_3$. Additionally, the peculiar sign structure of κ_{xy} under rotating the magnetic field in the honeycomb planes might further support the spin liquid scenario [60]. Especially the last discoveries attracted huge attention and put α-$RuCl_3$ forward as a prime candidate among other Kitaev materials.

Nevertheless, some inconsistencies are remaining because broad features in neutron scattering can also be explained by multi-magnon processes that do not require proximity to a spin liquid [58, 188–190]. Moreover, even the experimental observation of the sign structure in κ_{xy} upon rotating the in-plane field direction does not necessarily evidence a spin liquid. This behavior can appear in the partially-polarized phase as well [191]. Another study reported a pronounced temperature dependence of κ_{xy} betwen 3.5 K and 5.5 K rendering a constant half-quantized plateau questionable [192]. Furthermore, the plateau seems to be suppressed towards lower temperatures far below the half-quantized value [193], which is inconsistent with the Majorana fermion scenario [191]. Additionally, the field region of the thermal conductivity plateau varies between B = 7–9 T [13], B = 7–9 T [61], and B = 10–12 T [60], and strong sample dependence has been reported [61]. The latter might originate from disorder, which can suppress the half-integer plateau [194]. Interestingly, Tanaka *et al.* proposed the

formation of a gapless topological spin liquid phase for an in-plane field direction $\mathbf{B} \parallel \mathbf{b}$ as soon as magnetic order is suppressed [62]. This strongly suggests that another phase transition must occur upon leaving this gapless phase towards the gapped partially-polarized state. Several studies reported anomalies that might support this scenario, but they appear to be fairly weak [14, 15]. Very recently, strong quantum oscillations in the thermal conductivity κ_{xx} have been observed in the presumed field-induced spin liquid state interpreted as evidence for a spinon Fermi surface [192]. It remains unclear, though, why these oscillations are already visible deep in the ordered state. Moreover, the question arises how the anticipated gapless spinon Fermi surface can be reconciled with the gapped spectrum present for most in-plane field directions [62]. Altogether, the existence of a field-induced spin liquid phase in α-$RuCl_3$ is controversially discussed, and the measurements presented in the following try to shed light on the field evolution in α-$RuCl_3$.

In this work, the field-dependence of α-$RuCl_3$ has been investigated in detail by thermodynamic measurements of the specific heat and the magnetic Grüneisen parameter down to 200 mK in fields up to 14 T. The single crystals have been grown by Vladimir Tsurkan (EP V, University of Augsburg). The angle-dependence of in-plane fields has been carefully studied to thoroughly establish the field-temperature phase diagram for different field directions. Furthermore, the entropy evolution under magnetic field has been determined, and implications on the presumed spin liquid phase are discussed. Moreover, the entropy change between zero field and 14 T is compared to expected values. The chapter is concluded by a short comparison of zero-field specific heat of samples from different laboratories. Most results have been published in [94, 95].

It is well known that α-$RuCl_3$ is prone to stacking faults. The Ru^{3+} ions are arranged on 2D honeycomb layers, which are only weakly coupled by van-der-Waals forces. Therefore, the honeycomb planes are easily shifted by moderate shear force resulting in stacking faults. Several studies showed the influence of different stacking sequences. The ABC stacking results in a single transition at $T_N \sim 7$–8 K [176], which is nowadays considered to be the proof of high-quality crystals. As soon as ABAB stacking is introduced by cutting or uncareful handling of the sample, a second transition can be observed at $T_{N,2} \sim 14$ K [176, 195]. Sometimes, even more transitions or anomalies are found, for example, in the specific heat [178, 183, 195]. It is general consent that stacking faults have to be avoided in order to probe the intrinsic properties of α-$RuCl_3$. Therefore, each α-$RuCl_3$ crystal should be thoroughly characterized to confirm a single transition at around $T_N \sim 7$–8 K.

As a consequence, the sample for the dilution refrigerator was chosen carefully. Fig. 5.1(a) shows the magnetization of three different samples measured in the MPMS together with Anton Jesche and Yoshifumi Tokiwa (EP VI, University of Augsburg). A field of 1 T has been applied parallel to the honeycomb planes ($B \perp c^*$). Sample MK 4 (red data points) does not show any kinks except at $T_N \sim 7$ K. Most importantly, and in contrast to Sample A (green), no kink appears at around 14 K. Consequently, this sample has been used for all measurements in the MK 4. The absence of transitions above T_N has been additionally confirmed by a PPMS zero-field specific heat measurement [Fig. 5.1(b)] that has been repeated after the first runs in the dilution refrigerator. This result confirms that no stacking faults are induced by mounting or dismounting the sample.

Before discussing implications of the measurements on the presumed spin liquid state, several technical but important aspects have to be mentioned. The setup in the MK 4 is shown in [Fig. 5.1(c,d)]. The sample is fixed by N-Grease as described in Sec. 3.4. For each run, the cell is tilted by one or two brass wedges (10°, 15°, or 20°). This allows to adjust the in-plane field direction in ±5° steps for different combinations of the wedges.

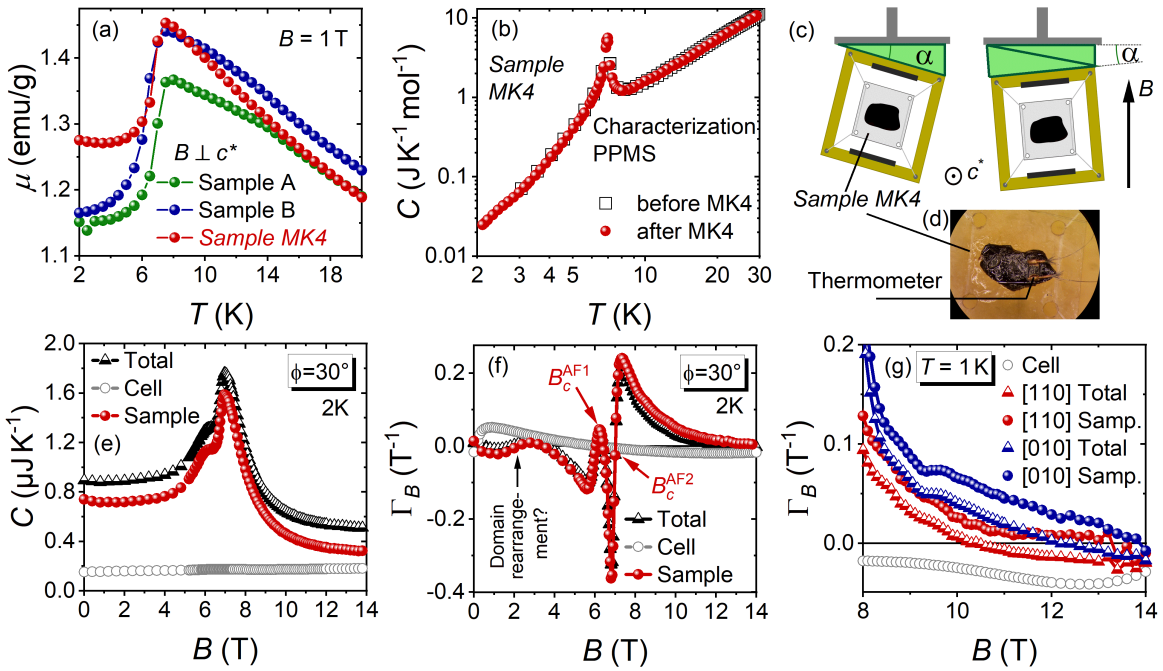

Figure 5.1. (a) Characterization via magnetization of three α-$RuCl_3$ samples. Sample MK 4 does not show any additional anomaly except of $T_N \sim 7$ K. The exact in-plane field direction has not been determined here. (b) Specific heat before and after the first measurements in the dilution refrigerator. (c,d) Setup in the MK 4. The rotation of the magnetic field in the honeycomb planes is controlled by using combinations of brass wedges. (e) Background subtraction for the field-dependent heat capacity $C(B)$ at 2 K. (f,g) Examples for background subtraction for the field-dependent magnetic Grüneisen parameter $\Gamma_{\mathrm{mag}}(B)$ that becomes increasingly important at low temperatures and high magnetic fields, where the sample signal becomes tiny. Graphs partially published in Refs. [94, 95], copyrighted by the American Physical Society.

The specific heat of α-$RuCl_3$ becomes rapidly suppressed in the ordered state below T_N. Therefore, careful background subtraction is crucially important. The addenda heat capacity of the cell including N-Grease and thermometer, C_{add}, has been measured in an additional run without the sample and is directly subtracted from the total heat capacity, $C_{\mathrm{Sa}} = C_{\mathrm{tot}} - C_{\mathrm{add}}$, as shown in Fig. 5.1(e), see also Sec. 3.4.3. Below 1 K, the addenda could not be determined due to 2τ behavior in the raw data [Sec. 3.4.1]. Thus, a background subtraction is not feasible anymore. The same holds true for the magnetic Grüneisen parameter below 1 K because the cell's heat capacity needs to be taken into account as well [Sec. 3.5]. It is important to note, however, that the main features in the field spectrum are independent of the background subtraction. The field-dependent magnetic Grüneisen parameter at 2 K in Fig. 5.1(f) exemplifies this very well. The most prominent anomalies at B_c^{AF1} and B_c^{AF2} at about 6–7 T, marked by red arrows, do not change their position by the addenda subtraction. Similar behavior can be seen for the broad sign change at ~ 2 T that might be related to domain rearrangements [178]. At high fields and low temperatures, though, the magnetic Grüneisen parameter turns out to be tiny, and the subtraction procedure becomes increasingly important [Fig. 5.1(g)]. The combined signal of sample and cell is negative at 1 K above $10 - 12$ T, depending on the field direction, but the sample alone clearly approaches zero while staying positive. It is noted in passing that the origin of the negative background signal remains unclear.

After these more technical remarks, the focus of the next paragraphs will be on the field- and angle-dependence of the magnetic Grüneisen parameter $\Gamma_{\mathrm{mag}}(B)$. First, the direction of the magnetic field in the honeycomb planes has to be carefully determined. For this purpose, several measurements at 2 K are shown in Fig. 5.2(a-d) with different in-plane field directions. The abrupt sign change from negative to positive at B_c^{AF2} is indicative of a 2$^{\mathrm{nd}}$ phase transition towards the disordered phase of α-$RuCl_3$. The maximum at B_c^{AF1} is interpreted as a 1$^{\mathrm{st}}$ order phase transition to an intermediate ordered phase, where interlayer couplings become relevant [196]. Both B_c^{AF1} and B_c^{AF2} depend strongly on the chosen field angle. The critical fields clearly decrease upon rotating the field from **B** ||[010] ($\Phi = 0°$) [Fig. 5.2(d)] towards **B** ||[110] ($\Phi = 30°$) [Fig. 5.2(a)]. This is equivalent to the field being parallel and perpendicular to Ru-Ru bonds, respectively, as indicated by the honeycomb sketches. Therefore, B_c^{AF1} and B_c^{AF2} can be used to determine the exact field direction of each measurement. The comparison to ac-susceptibility results [196] shows excellent agreement of the angle-dependence of the critical fields at 2 K [Inset of Fig. 5.2(c)]. The error of the angle Φ can be estimated by $\Gamma_{\mathrm{mag}}(B)$ at 0.5 K [Fig. 5.2(e)]. The curves for $\Phi = +5°$ and $\Phi = -5°$ do not overlap perfectly between 7 T and 7.5 T. Consequently, $\Phi = 0°$ might deviate by 1–2° from **B** ||[010]. Strictly speaking, the angle $\Phi = 20°$ corresponds to $\Phi = 100°$. This angle has been measured first [95], and the cell has been fixed in a different configuration rotated by 90° compared to the other angles. The perfect accordance in the inset of Fig. 5.2(c), however, corroborates the six-fold symmetry at low temperatures reported in Ref. [62]. It is noted in passing that the magnetic Grüneisen parameter for the field direction perpendicular to the honeycomb planes (Fig. 5.2(a), **B** || **c***) does not show any signal in the whole accessible field range. This is expectable due to the strongly anisotropic behavior in α-$RuCl_3$. During this last measurement, the sample was

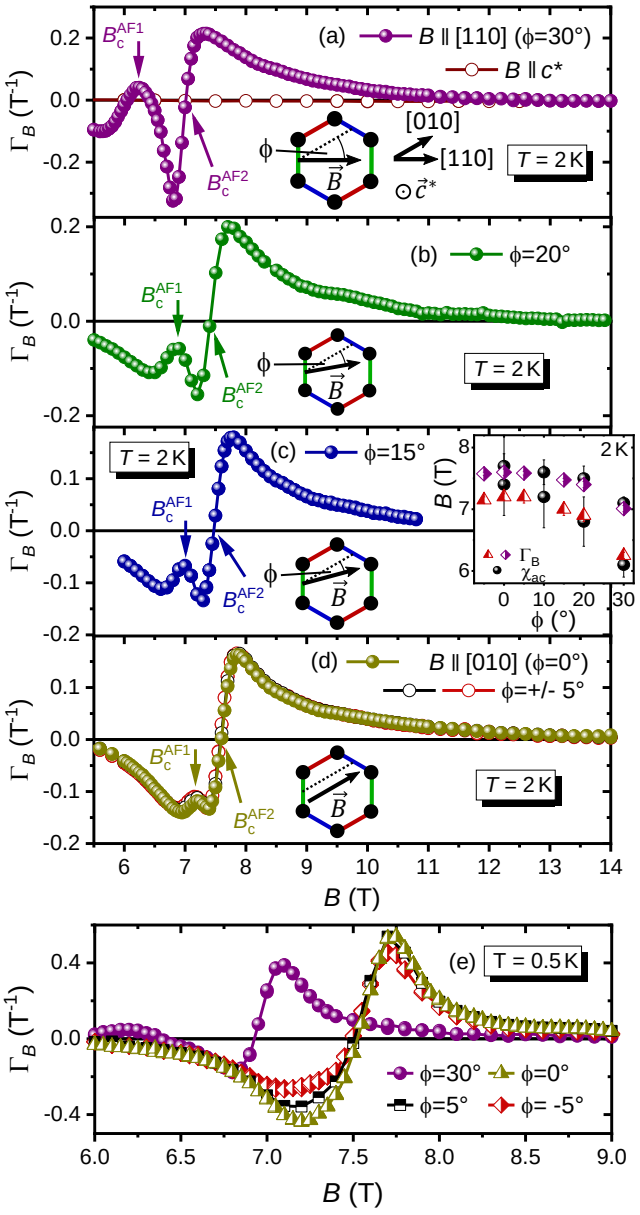

Figure 5.2. Magnetic Grüneisen parameter $\Gamma_{\mathrm{mag}}(B)$ of α-$RuCl_3$ for magnetic fields applied in the honeycomb plane. (a-d) Angle-dependence at 2 K. (e) Estimation of the deviation of $\Phi = 0°$ from **B** ||[010]. Graphs partially from Ref. [94], copyrighted by the American Physical Society.

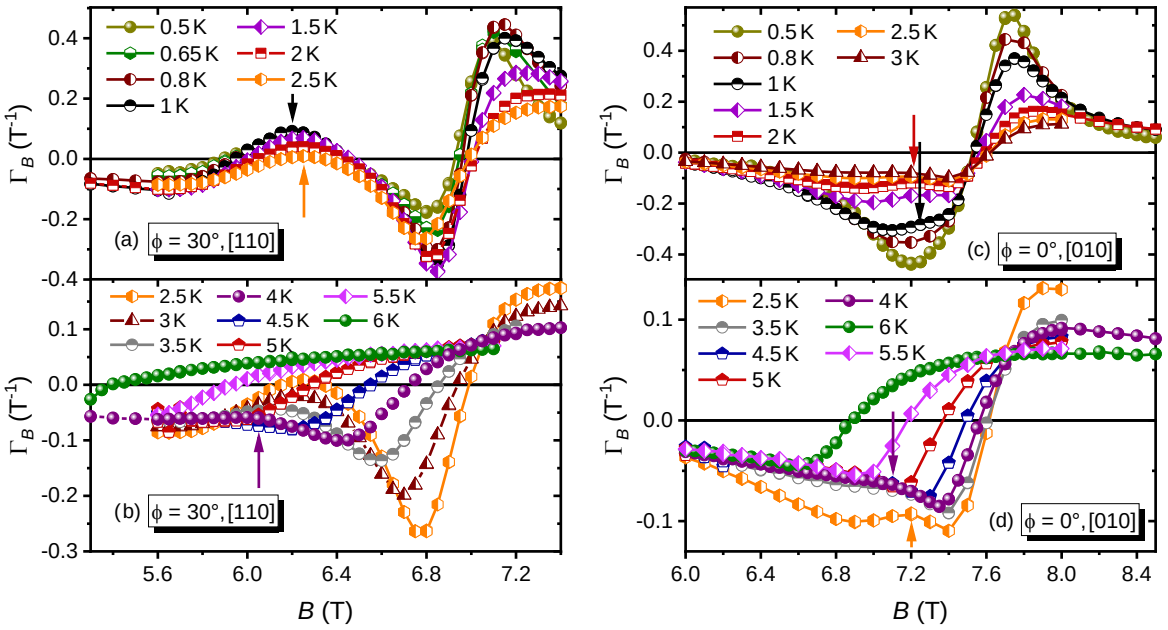

Figure 5.3. Detailed measurements on the magnetic Grüneisen parameter $\Gamma_{\mathrm{mag}}(B)$ for fields applied along the (a,b) [110] and (c,d) [010] directions, respectively. The temperature range is between 0.5 K and 5 K and allows to track the evolution of the field-induced phase transitions in α-$RuCl_3$. B_c^{AF2} can be easily identified by the abrupt sign change. The maximum at lower fields can be assigned to B_c^{AF1}, see the exemplary arrows. B_c^{AF1} is more pronounced for $\mathbf{B} \parallel [110]$. Graphs published in Ref. [94], copyrighted by the American Physical Society.

cleaved at around 13 T because the field applied along the hard axis induced a too strong torque effect.

Besides the calibration of the in-plane field angle, Fig. 5.2(a-d) provides first insights into the evolution of α-$RuCl_3$ beyond magnetic order. For all field directions, no indication of phase transitions above B_c^{AF2} can be found, which does not support the spin liquid scenario. The only anomaly is a weak change of the slope that is visible best in Fig. 5.2(b) for $\Phi = 20°$. Before having a look on this high-field analysis in detail, the evolution of B_c^{AF1} and B_c^{AF2} are discussed first. In Fig. 5.3, both phase transitions are investigated carefully using the magnetic Grüneisen parameter $\Gamma_{\mathrm{mag}}(B)$ at temperatures down to 0.5 K for the field applied along [110] ($\Phi = 30°$) and [010] ($\Phi = 0°$), respectively. The background is not subtracted here because the specific heat measurements $C(B)$ are much more time-consuming and, thus, are only available for selected temperatures. As mentioned above, this does not affect the position of the phase transitions.

First, the transition towards the disordered phase, B_c^{AF2}, is discussed, which is the dominating part of the measurement. For $\mathbf{B} \parallel [110]$ ($\Phi = 30°$), the sign change from negative to positive is shifted towards lower fields for increasing temperatures and $T > 2$ K [Fig. 5.3(b)]. This behavior is expectable because stronger thermal fluctuations destroy the magnetic order. Surprisingly, B_c^{AF2} shows the opposite trend below 2 K, where lowering the temperature results in a smaller critical field [Fig. 5.3(a)]. Very similar behavior can be found for the field applied along the [010] direction [Fig. 5.3(c,d)]. In other words, a small field range exists in the phase diagram where α-$RuCl_3$ becomes magnetically ordered upon cooling but enters the disordered phase again when the temperatures is further lowered. This is additionally confirmed by specific heat measurements that will be discussed later [Fig. 5.4]. Such a reen-

trant or inverse melting behavior has been proposed in some anisotropic spin models [197–199]. Thus, it might be interesting from theoretical side to look for this behavior in extended Kitaev models that are relevant for α-$RuCl_3$.

The second prominent anomaly is the transition B_c^{AF1} that occurs between two distinct zigzag-ordered states [196]. It is interpreted to be of 1$^{\mathrm{st}}$ order [196, 200] and, thus, characterized by a maximum in $\Gamma_{\mathrm{mag}}(B)$ that corresponds to a downward step in the field dependent entropy. In Fig. 5.3, it is indicated by arrows for selected temperatures. For $\mathbf{B} \parallel [110]$, B_c^{AF1} can be easily determined below 3 K. It is transformed into a kink at higher temperatures and cannot be identified anymore above 4 K [Fig. 5.3(a,b)]. The identification of B_c^{AF1} for $\mathbf{B} \parallel [010]$, however, is more challenging because it appears to be weaker. Additionally, it is located much closer to the dominating B_c^{AF2}. For temperatures of about 2.5 K, the maximum is clearly visible [Fig. 5.3(d)]. When the temperature is decreased, this maximum becomes broadened and cannot be determined unambiguosly anymore [Fig. 5.3(c)]. It is presumed that B_c^{AF1} is hidden by the B_c^{AF2} anomaly that becomes increasingly pronounced below 1 K. On the other hand, it cannot be excluded from that measurement whether B_c^{AF1} is completely suppressed at these temperatures and does not survive down to 0 K. For temperatures above 2.5 K, B_c^{AF1} evolves very similar to the field direction along [110] and vanishes above 4 K.

The specific heat $C(B)$ serves as a complementary thermodynamic measurement and offers an independent investigation of the phase diagram. Moreover, it allows the calculation of the field dependent entropy change via integration of $\partial S/\partial B = -\Gamma_{\mathrm{mag}} C$. Fig. 5.4(a,b) shows the specific heat and entropy change with fields along both [110] and [010] up to 14 T at 1 K and 2 K, respectively. For better comparison between those temperatures, both quantities have been scaled by T^2. The entropy has been shifted such that $\Delta S(14\,\mathrm{T}) = 0\,\mathrm{J\,mol^{-1}\,K^{-1}}$. In the specific heat, the phase transition B_c^{AF2} appears as a rather sharp peak and dominates the spectrum for both field configurations. In contrast, B_c^{AF1} is visible only for the field applied along the [110] direction. At 1 K, a second peak is present that is smeared out at higher temperatures. For $\mathbf{B} \parallel [010]$, B_c^{AF1} is most likely hidden in the steep increase of B_c^{AF2} for all temperatures. This coincides well with the results from the Grüneisen parameter $\Gamma_{\mathrm{mag}}(B)$. The field-dependent entropy change strongly resembles the specific heat evolution and shows very similar features. Above B_c^{AF2}, the specific heat and the entropy become rapidly suppressed without any further phase transition.

A direct comparison of the specific heat between different in-plane field angles is presented in Fig. 5.4(c-f) for several temperatures. As already reported in Ref. [62], the anisotropy for fields around the [010] direction is rather weak because the $\Phi = 5°$ data points cannot be distinguished from the measurement with $\Phi = 0°$ [Fig. 5.4(c-e)]. Increasing the angle further results in a shift of B_c^{AF2} towards lower fields and the development of a kink at B_c^{AF1} for $\Phi = 20°$, especially at 1 K [Fig. 5.4(c,d)]. This evolution coincides again very well with the Grüneisen parameter. It should be noted here that the absolute specific heat values of $\Phi = 20°$ at high fields differ from the other directions. Its data points are expected to be between the measurements of the [010] and [110] field orientations, and not below both. A natural explanation would be the background subtraction. The cell addenda has only been measured once, and the amount of N-Grease has been estimated. Consequently, deviations potentially occur between measurements with different amount of N-Grease. Indeed, all measurements on α-$RuCl_3$ used the same setup without removing the sample and, therefore, the same amount of N-Grease, except of $\Phi = 20°$. Thus, the subtracted background might be too large in the case of $\Phi = 20°$ or too small for the other angles. As a first approximation, an error of 0.1 µJ K^{-1} in the background measurement would be enough to reproduce the expected heat capacity for $\Phi = 20°$ at 2 K. That value could be realistic for N-Grease at

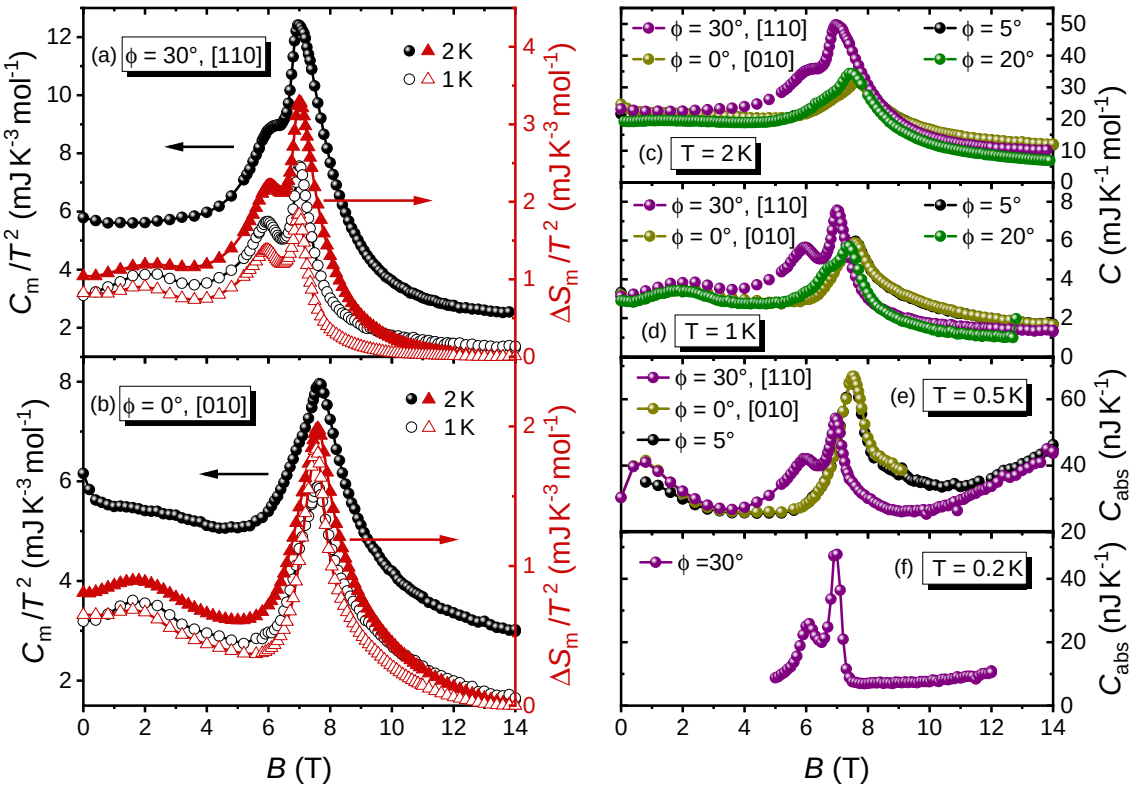

Figure 5.4. Field-dependent heat capacity $C(B)$ and relative entropy $\Delta S(B)$ of α-$RuCl_3$ at 1 K and 2 K for (a) **B** ||[110] and (b) **B** ||[010], respectively. No indication of a phase transition beyond B_c^{AF2} can be found (b-d) Additional results of $C(B)$ for more in-plane angles. At 0.5 K and 0.2 K, 2τ behavior appeared at high fields. Using the (inappropriate) single exponential function to analyse the raw data results in the unphysical increase of $C(B)$ above 10 T at $T \leq 0.5$ K. Graph partially from Ref. [94], copyrighted by the American Physical Society.

this temperature. Ideally, the addenda including N-Grease is independently determined in each run before mounting the sample. While this standard approach works well for PPMS measurements, it is usually not feasible in the dilution refrigerator due to severe time issues. However, this might be advisable for future measurements on samples with comparably small heat capacity. Nevertheless, this does not affect the statements based on the specific heat measurements because the addenda evolves rather smoothly [Fig. 5.1(e)].

The specific heat has also been measured at very low temperatures of 0.5 K [Fig. 5.4(e)]. The phase transition B_c^{AF2} is clearly resolved, and the same holds true for B_c^{AF1} for [110]. Above ∼10 T, however, the specific heat begins to grow again. This unphysical behavior in the partially-polarized phase is an artefact from the already mentioned 2τ behavior that impeded correct fitting of the raw data in this field range as well as a reasonable background subtraction. Details can be found in Sec. 3.4.1 or in [94]. Interestingly, the increase of the specific heat at high fields remains monotonic. A sharp phase transition comparable to B_c^{AF2} is clearly absent. This holds true even at 200 mK [Fig. 5.4(f)], which is more than one order of magnitude smaller than the reported temperature of the thermal conductivity plateau [13]. Altogether, the specific heat does not support the scenario of an additional phase above B_c^{AF2} before entering the partially-polarized state.

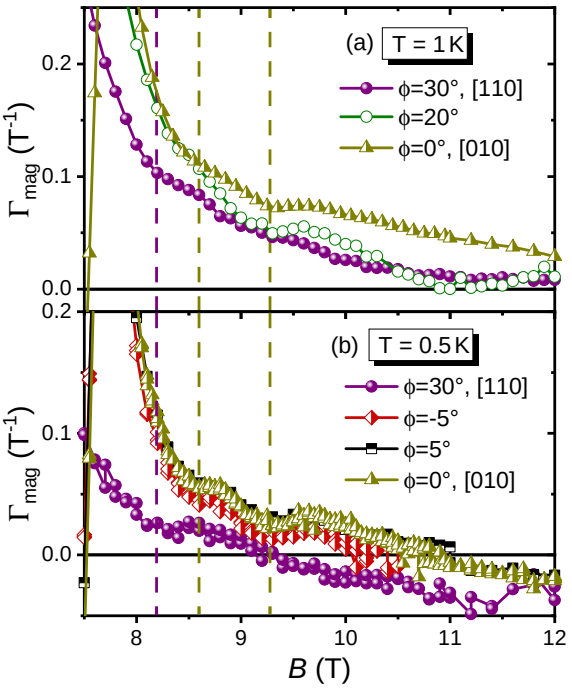

Figure 5.5. Evolution of $\Gamma_{\mathrm{mag}}(B)$ beyond B_c^{AF2} for various in-plane field angles at (a) 1 K and (b) 0.5 K, respectively. Additional phase transitions are absent. For 0.5 K, the background was not possible explaining the negative values. The dotted lines mark the position of the shoulder-like anomalies (see main text). Graph partially from Ref. [94], copyrighted by the American Physical Society.

In order to further evaluate the high-field evolution, a closer look onto the magnetic Grüneisen parameter is presented in Fig. 5.5. As already mentioned, $\Gamma_{\mathrm{mag}}(B)$ does not show any phase transition above B_c^{AF2}. Even at temperatures as low as 1 K, only weak anomalies appear in the form of a shoulder or a change of slope. Upon lowering the temperature down to 0.5 K, the anomalies become more pronounced as indicated by the dotted lines. For angles along or close to the [010] field direction, even two shoulders might be identified. In general, they seem to be located at higher fields for $\mathbf{B} \parallel [010]$ compared to $\mathbf{B} \parallel [110]$, in qualitative agreement with exact diagonalization (ED) results [94]. Such features can be interpreted using the generic expression of the Grüneisen ratio for gapped phases, $\Gamma_\lambda(T \to 0) = \Delta'/\Delta$. Here, λ is the tuning parameter, which is the magnetic field in the example of α-RuCl$_3$. When the gap closes, $\Delta \to 0$, then Δ' automatically changes sign from negative to positive. This results in divergent behavior in Γ at the critical tuning parameter λ_{crit}, which is characteristic for a QCP and can be seen in α-RuCl$_3$ at B_c^{AF2}. Clearly, this cannot be the origin of the high-field anomaly above B_c^{AF2}. An abrupt change in the excited states, however, creates a discontinuity in Δ' that results in a downward jump in Γ for $T \to 0$. At higher temperatures, this smears out to a shoulder anomaly as shown by ED calculations in [94, 95]. Consequently, the high-field feature(s) in α-RuCl$_3$ can be assigned to level crossing(s) of the first excited states and are not related to a transition from the suggested spin liquid towards the partially-polarized state.

Further evidence for the absence of a field-induced KSL phase can be found in the field-dependent entropy that decreases rapidly towards zero without any anomaly beyond B_c^{AF2} for both field directions [Fig. 5.4(a,b)]. This is not compatible with a KSL scenario, especially in the case of the [010] field direction. Here, a gapless spin liquid has been proposed [62], which should create a pronounced signature in the entropy upon entering the gapped partially-polarized state with a first order transition. Instead, the vanishing entropy clearly indicates a monotonically growing gap above B_c^{AF2} in accordance with a topologically trivial state beyond B_c^{AF2}.

The presented thermodynamic measurements can be condensed into the phase diagram of α-RuCl$_3$. It is shown in Fig. 5.6(a,b) for the field directions along [110] and [010], respectively. Most importantly, the results in this work do not support the existence of a KSL beyond B_c^{AF2}. The phase boundary of B_c^{AF2}, however, shows a non-monotonic, inverse melting behavior that can be followed for both field directions. The critical field B_c^{AF2} derived from the Grüneisen parameter is independently confirmed by the specific heat data below 2 K. The

discrepancy at higher temperatures in Fig. 5.6(a) might be a result of the broadened peak in the specific heat, see Fig. A.9 in the Appendix. This renders the determination of the critical field probably less precise than from the Grüneisen parameter with its sign change. It is worth mentioning that the phase boundary of B_c^{AF1} looks similar to B_c^{AF2} only for the field direction parallel to **B** ‖[110]. That observation is supported by the Clausius-Clapeyron equation for a first order transition, $\mathrm{d}B_c^{\mathrm{AF1}}/\mathrm{d}T = -\Delta S/\Delta M$ [201]. Here, ΔS and ΔM describe the evolution of the entropy and the magnetization across the phase transition, respectively. From experiments [27, 180] follows $\Delta M > 0$, which requires a negative contribution in the entropy, $\Delta S < 0$, at the phase transition if $\mathrm{d}B_c^{\mathrm{AF1}}/\mathrm{d}T > 0$. Indeed, $\Delta S < 0$ can be found for **B** ‖[110] around B_c^{AF1} [Fig. 5.4(a)], but not for **B** ‖[010] [Fig. 5.4(b)].

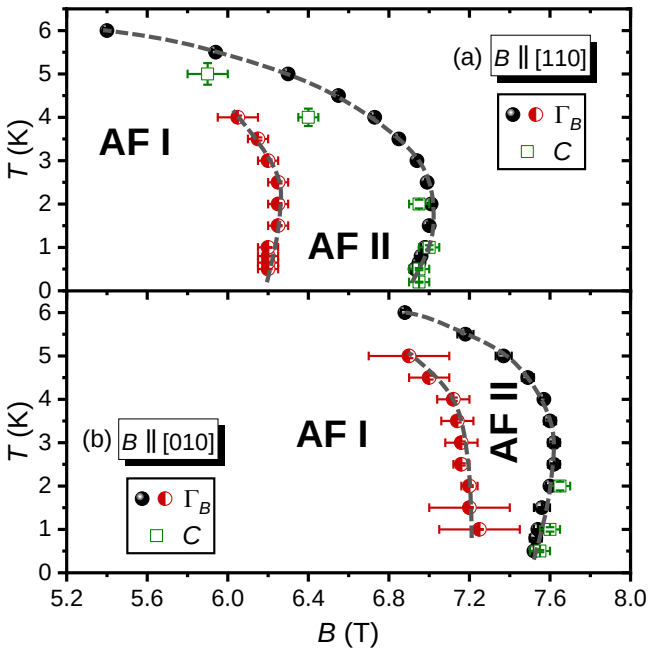

Figure 5.6. Phase diagram of α-$RuCl_3$ for in-plane magnetic fields along [110] and [010], respectively. B_c^{AF2} shows a non-monotonic evolution towards lowest temperatures and indicates anarrow region where inverse melting seems to occur. For B_c^{AF1}, this is only present for **B** ‖[110]. Graph from Ref. [94], copyrighted by the American Physical Society.

After establishing the phase diagram, the field-dependent entropy is revisited. Fig. 5.7(a) shows the direct comparison of the entropy evolution at 1 K for fields along the [110] and the [010] direction, respectively, with the normalization $\Delta S(0\,\mathrm{T}) = 0\,\mathrm{mJ\,mol^{-1}\,K^{-1}}$. Surprisingly, the change of the entropy $\Delta S(0\,\mathrm{T}) - \Delta S(14\,\mathrm{T})$ is as large as $0.8\,\mathrm{mJ\,mol^{-1}\,K^{-1}}$ and $0.65\,\mathrm{mJ\,mol^{-1}\,K^{-1}}$, respectively. The upper entropy limit expected from the magnon gap in α-$RuCl_3$ of $\Delta_{\mathrm{mag}} = 1.6\,\mathrm{meV}$ [202] can be approximated by a two-level system for $T \ll \Delta_{\mathrm{mag}}$. This provides an upper limit of $S_{\mathrm{mag}} = 0.0014\,\mathrm{mJ\,mol^{-1}\,K^{-1}}$ in zero field at 1 K. Applying magnetic fields further opens the gap and reduces the entropy of the system, but the calculated value is far below the actually measured entropy change.[1] Therefore, the unexpectedly huge entropy difference in α-$RuCl_3$ between zero field and 14 T must have a different origin. One possibility might be strong magnetoelastic effects in α-$RuCl_3$ that result in field-dependent phononic contribution. This could be interesting for future theoretical and experimental investigations, for example with magnetostriction or inelastic x-ray scattering measurements. On the other hand, if there were low-energy states in the gap that, for example, have been missed in the neutron scattering experiments due to the elastic line of 1 meV [202], this could naturally explain the entropy decrease in field. These additional states might be related to a minor fraction of free spins, which might be sample dependent.

To further elucidate the latter hypothesis, four different samples have been compared by means of zero-field heat capacity down to 500 mK [Fig. 5.7(b,c)]. One sample has been grown at the University of Toronto (UT) by Subin Kim from the group of Young-June Kim, two

[1] Even the lower limit from the error bar in [202], $\Delta_{\mathrm{mag}} = 1.4\,\mathrm{meV}$, with $S_{\mathrm{mag}} = 0.013\,\mathrm{mJ\,mol^{-1}\,K^{-1}}$ cannot explain the observed behavior.

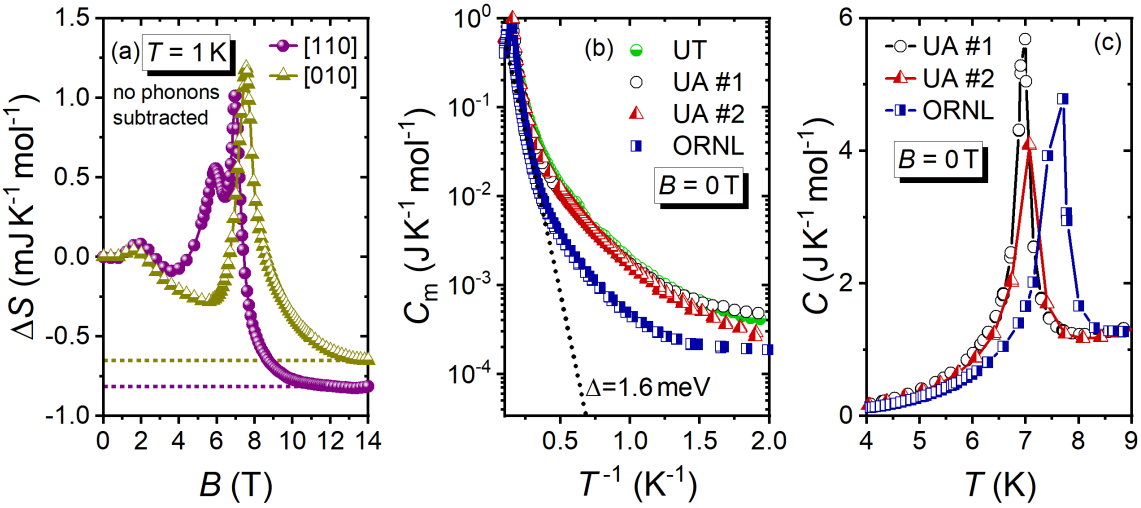

Figure 5.7. (a) Evolution of the field-dependent relative entropy $\Delta S(B)$ up to 14 T at 1 K for the field applied along [110] and [010], respectively. The entropy change between the partially-polarized state at 14 T and zero field is indicated by the dotted lines. It is much larger than expected for a 2D AF with a gap of 1.6 meV [202]. (b) Magnetic specific heat of four different samples at zero field. The data are presented on a log-scale over the inverse temperature. All samples deviate from the expected gapped behavior (compare dotted line, details in the main text). Moreover, the sample ORNL is distinct to the other samples. This can be also seen in panel (c), where two different transition temperatures are observed (7 K vs 8 K).

samples have been prepared at the University of Augsburg (UA#1, UA#2) by Vladimir Tsurkan (Experimental Physics V), and the last one has been synthesized at the Oak Ridge National Laboratory (ORNL) by Jiaqiang Yan. Before having a closer look onto the results, some technical details should be discussed. Several different measurement devices in different temperature ranges have been utilized for determining the heat capacity, as summarized in Table 5.1. Sample UT, for example, did not fit into the ^{3}He heat capacity puck and, thus, could not be measured in the PPMS or the DynaCool. Luckily, the setup of the dilution refrigerators has a bigger dimension that allowed mounting of the sample. Moreover, the MK 3 has been used for sample UT because the MK 4 was occupied at that time. It is noteworthy, too, that UA#1 is the sample, which has been extensively examined in the dilution refrigerator MK 4. All results in the context of this thesis presented so far are from this sample.

In Fig. 5.7(b), the zero-field magnetic specific heat is shown. For all samples, the phononic contribution $C_{\mathrm{lat}} = \beta T^3$ has been subtracted using $\beta = 1.0\,\mathrm{J\,mol^{-1}K^{-4}}$ [183]. The data are plotted as $\log(C_{\mathrm{m}})$ over T^{-1}. If the sample's specific heat follows an exponential behavior, it should appear as a straight line. For comparison, the dotted line shows the specific heat of a gapped 2D antiferromagnet, $C_{\mathrm{2D},\Delta} = AT(x^2 + 2x + 2)\exp(-x)$ with $x = \Delta/k_{\mathrm{B}}T$ and the prefactor A [72], using a gap of $\Delta = 1.6$ meV [202] and $A = 0.04\,\mathrm{J\,mol^{-1}\,K^{-2}}$. The latter has been adapted to roughly match the heat capacity below T_{N}. None of the α-$RuCl_3$ samples follows a straight line in Fig. 5.7(b) because they begin to bend around ~ 2 K. This is a clear indication for additional states in the gap of α-$RuCl_3$. They are present for all samples and do not depend on the presence or absence of additional transitions above T_{N} because UA#2 shows a second transition at 14 K, evidenced in Fig. A.9 in the Appendix. Furthermore, a pronounced difference is visible between sample ORNL and the other three samples. This

Table 5.1. Overview of the zero-field heat capacity measurements on different α-$RuCl_3$ samples. Measurements have been performed in Augsburg either in the dilution refrigerators MK 4 or MK 3, or with the ^{3}He-Option in the 0 T PPMS or the DynaCool. T_{max} denotes the highest measured temperature, respectively. Sample UT is too large to be mounted on the ^{3}He puck and, thus, would need to be cutted. Sample UA#1 has been destroyed during the last measurement when $\mathbf{B} \parallel \mathbf{c}^*$ was applied [Fig. 5.2(a)]. Sample UA#2 has been measured by Anton Jesche. For sample UT, Noah Winterhalter-Stocker strongly supported the measurement in the MK 3.

	MK 4	MK 3	^{3}He: 0T PPMS	^{3}He: DynaCool	T_{max}	Still ok?
UA#1	✓	–	✓	–	8 K, 30 K	no
UA#2	–	–	–	✓	20 K	no
UT	–	✓	✗	✗	7 K	yes
ORNL	–	–	✓	–	20 K	yes

cannot be attributed to problematic analysis of the background in the dilution refrigerator setup since Sample UA#2 has been measured independently with the ^{3}He option but matches UA#1 and UT very well. Consequently, the higher specific heat in the samples of Augsburg and Toronto seem to be the result of a higher concentration of in-gap states. This appears to be correlated to the position of the transition temperature T_N as presented in Fig. 5.7(c), where several PPMS/ DynaCool measurements are compared. The heat capacity peak of UA#1/2 is located at $T_N \sim 7$ K, whereas ORNL reveals $T_N \sim 8$ K. This discrepancy is consistent with several papers where, in most cases, either the former [15, 176, 177, 182, 200] or the latter [195] dominant transition temperature has been reported, but sometimes also in between [180, 202] or even below [178, 183]. It has been shown that inducing stacking faults with the $ABAB$ sequence can shift T_N towards 8 K, accompanied with the emergence of the second transition at 14 K [176]. This implies more stacking faults in crystals if $T_N \sim 8$ K, which definitely cannot be confirmed here. The ORNL sample does *not* obtain any sign of an additional transition at 14 K [Fig. A.9] and, additionally, seems to potentially feature less in-gap states that might be related to impurities, as explained below. Consequently, the puzzle of different Néel temperatures in α-$RuCl_3$ remains unresolved and certainly deserves further attention.

At this point, it can only be speculated about the origin of the additional in-gap states. A natural explanation would be free spins due to impurities that could also explain the entropy decrease in Fig. 5.7(a), which is much larger than expected. However, the samples UA#1, ORNL, and UT have all been characterized carefully without any signs of impurities or stacking faults. Therefore, they are considered to be of excellent quality, where only intrinsic properties should be releveant. Furthermore, the reproducibility of the zero-field specific heat and their connection to the Néel temperature speak against random impurities. Consequently, further systematic investigations are highly desirable. A direct comparison between the samples UA#1, UT, and ORNL would be very interesting regarding the field-evolution of $\Gamma_{mag}(B)$ and $C(B)$ in combination with $\Delta S(B)$. The latter is expected to show a smaller entropy reduction between 0 T and 14 T. It would also clarify if a different T_N influences, for example, the evolution of B_c^{AF1} and B_c^{AF2}. Moreover, neutron scattering experiments on various samples could be helpful, with the focus on the low-energy spectrum below 1.6 meV. Last but not least, these additional states pose the question how they may impact the half-integer plateau or the oscillations in the thermal conductivity.

In summary, extensive thermodynamic measurements on α-$RuCl_3$ have been presented using in-plane magnetic fields up to 14 T and temperatures down to at least 0.5 K. The in-plane field angle Φ has been varied in 5° steps by rotating the cell with brass wedges. The direct comparison to ac-susceptibility measurements allows the calibration of $\Phi(B)$. Interestingly, neither $\Gamma_{\mathrm{mag}}(B)$ nor $C(B)$ indicate a field-induced transition beyond B_c^{AF2}, which speaks against a spin liquid phase in α-$RuCl_3$. This observation is corroborated by the entropy change $\Delta S(B)$ that vanishes rapidly towards zero above B_c^{AF2}. Here, a pronounced signature would be expected upon leaving the putative spin liquid state, at least for the field applied along the [010] direction with the proposed gapless KSL from Ref. [62]. The shoulder-like anomalies in $\Gamma_{\mathrm{mag}}(B)$ at high fields can be attributed to crossings of the first excited states [94, 95]. Careful measurements of $\Gamma_{\mathrm{mag}}(B)$ reveal a non-monotonic behavior of the phase boundary B_c^{AF2} and suggest an inverse melting scenario. For $\mathbf{B} \parallel [110]$, this can also be seen for B_c^{AF1}. Here, further theoretical investigations are required to verify that possibility in realistic microscopic models of α-$RuCl_3$. Moreover, the comparison between different samples has shown that additional efforts should be undertaken to clarify the origin of the presumed states in the gap of α-$RuCl_3$.

6. Summary

The search for quantum spin liquids (QSL) has inspired physicists for decades. On the theoretical side, strong progress has been achieved by identifying an abundance of QSL on various lattice geometries. The experimental evidence of a clean QSL, however, remains a major challenge in solid state physics. Real materials usually exhibit additional, but undesired interactions, driving them away from more basic microscopic models. One main aspect of a QSL is its inherent quantum entanglement that can be investigated experimentally by neutron scattering. Another characteristic feature is the absence of magnetic ordering down to 0 K. Consequently, thermodynamic probes down to the lowest technically accessible temperatures are essential for classifying potential QSL candidates. This work focused on thermodynamic measurements of specific heat, magnetic Grüneisen parameter, and the magnetization in the millikelvin range in order to illuminate different aspects in several frustrated magnets. All samples were provided by various colleagues, who are listed explicitly at the beginning of each section, respectively.

Reliable thermometry was crucial for all experiments in this work. I fabricated several small-size thermometers ($0.5 \times 1\,\mathrm{mm}^2$ or $1 \times 1\,\mathrm{mm}^2$) by contacting polished RuO_2 chips with superconducting NbTi wires to minimize undesired heat flow to the chip. Subsequently, I carefully calibrated these thermometers down to 22 mK in fields up to 17.5 T to account for the magnetoresistance of RuO_2. The commercial thermometer Cernox X112017 and a CMN thermometer were used as reference. The latter contains a paramagnetic salt, which I calibrated by a Fixed Point Device with precisely known superconducting transition temperatures. The customized, field-calibrated RuO_2 thermometers are used for all heat capacity and magnetic Grüneisen parameter measurements. Additionally, the commercial thermometer ICE 2 was calibrated in the same temperature range for magnetization measurements, but also for diagnostic purposes on the temperature regulation plate (TRP).

I performed measurements on two different material classes. A large part was devoted to the investigation of several Yb^{3+} based triangular lattices [Ch. 4], on which the resonating valence bond (RVB) state was proposed - the prototype of a QSL. The second part comprised the field-dependent evolution of the Kitaev material α-$RuCl_3$. Here, the possible scenario of a field-induced Kitaev spin liquid (KSL) beyond magnetic order is discussed [Ch. 5]. Most of the results are already published in Refs. [68, 94, 95, 110, 121, 162] and will be briefly summarized in the following paragraphs.

$YbMgGaO_4$ was the first Yb^{3+} based QSL candidate, and strong efforts have been undertaken to understand its apparent disordered state down to the lowest temperature. My temperature-dependent measurements on $YbMgGaO_4$ provided valuable input to the vivid discussions about this material. I showed by comparison of field cooled and zero field cooled data that conventional spin freezing can be excluded, in contrast to the conclusions from ac-susceptibility results [12]. This could be seen as support of the quantum spin liquid (QSL) ground state in $YbMgGaO_4$.

On the other hand, several reports proposed the scenario of a spin liquid mimicry in $YbMgGaO_4$ due to the structural disorder from the Mg^{2+}/Ga^{3+} site mixing [10, 11]. My field-dependent magnetization measurements provided further arguments for the importance

of the structural randomness. Triangular lattices in antiferromagnets (TLAF) with Heisenberg interactions commonly show a 1/3-magnetization plateau due to the up-up-down (uud) phase, but $YbMgGaO_4$ is clearly distinct. MPMS measurements from Y. Li showed the absence of any plateau in $M(B)$ for in-plane and out-of-plane field directions $\mathbf{B} \perp \mathbf{c}$ and $\mathbf{B} \parallel \mathbf{c}$, respectively. The susceptibility as the field-derivative $\chi = \mathrm{d}M/\mathrm{d}H$, however, shows a plateau anomaly for both field directions, which might be regarded as the vestige of a strongly smeared magnetization plateau. I confirmed these results for $\mathbf{B} \parallel \mathbf{c}$ down to 40 mK, where thermal fluctuation are completely suppressed and cannot account for any broadening. Consequently, this unusual behavior must be intrinsic. I simulated the effect of structural randomness by developing an averaging procedure assuming random exchange couplings due to the locally different environment of each Yb^{3+} ion. This procedure was applied on Monte Carlo simulations of I. Iakovlev, who calculated $M(B)$ curves using various realistic parameter sets for $YbMgGaO_4$. His data suggest that $YbMgGaO_4$ without randomness should form the up-up-up-down (uuud) phase with a 1/2- instead of a 1/3-plateau. As soon as the randomness is taken into account by applying the averaging protocol, I reproduced the experimental behavior with the plateaus as well as their relative position in $\chi(B)$ for both field directions. This result corroborates the influence of structural randomness in $YbMgGaO_4$.

The $AYbX_2$ family attracted considerable interest because they realize a triangular lattice of Yb^{3+} ions without structural disorder. $KYbS_2$ belongs to this group and was suggested to be strongly frustrated [130]. I performed extensive temperature- and field-dependent thermodynamic measurements on a single crystal, which expands the temperature range down to 50 mK and investigates for the first time its field-evolution. The zero-field specific heat shows no sign of a phase transition down to the lowest temperatures, confirming the strongly frustrated ground state of $KYbS_2$. The only anomaly is a very weak kink at ∼200 mK. The interpretation of the zero-field specific heat is complicated by the contribution from a nuclear Schottky anomaly, that can be described as $C_{\mathrm{nuc}} = \alpha/T^2$ and becomes dominant below 100 mK. The fitting of the low-temperature part using $C = C_{\mathrm{nuc}} + C_{\mathrm{m}} = \alpha/T^2 + bT^p$ was most reasonable, but only in a small interval up to the anomaly around 200 mK. Nevertheless, it confirms gapless behavior of the magnetic specific heat, that might be close to quadratic behavior. This could point towards a Dirac QSL, but other scenarios such as spin glass behavior can account for this, too. Further investigations like neutron scattering, NMR, or μSR at lowest temperatures are highly desirable to probe the spin dynamics of the ground state.

$KYbS_2$ shows pronounced anisotropic behavior under magnetic fields. Out-of-plane fields ($\mathbf{B} \parallel \mathbf{c}$) only very weakly influence the specific heat even at 15 T. Applying an in-plane magnetic field ($\mathbf{B} \perp \mathbf{c}$), however, induces magnetic order in $KYbS_2$, which becomes suppressed again at higher fields. This indicates the formation of the plateau phase expected for TLAF. I also found a non-monotonic behavior of the nuclear contribution parameter $\alpha(B)$ and of the power law exponent $p(B)$ in the field region of the presumed plateau. I showed further evidence for an intermediate phase by the field-dependent magnetic Grüneisen parameter $\Gamma_{\mathrm{mag}}(B)$ as well as two more possible transitions at lowest temperatures. In combination with the specific heat $C(B)$, I calculated the entropy change $\Delta S(B)$ and established the temperature-field phase diagram of $KYbS_2$ for the first time. In order to confirm the possible uud state, magnetization measurements would be ideal to detect the anticipated 1/3-plateau.

$NaYbO_2$ is another $AYbX_2$ compound that was pushed forward as QSL candidate. I discussed the zero-field specific heat, where no magnetic order is detectable down to 70 mK evidencing strong magnetic frustration. Similar to $KYbS_2$, the low-temperature part including the nuclear contribution is difficult to analyse, and I discussed several possibilities to

quantify the nuclear contribution. Overall, a power law behavior seems to describe the data better than the exponential counterpart, which indicates gapless behavior in $NaYbO_2$. The power law exponent p depends on the chosen subtraction and might be close to 1 and, thus, be related to spinons. This interpretation could be validated by expanding the lowest measured temperatures down to below 50 mK in order to increase the fitting interval. Since $NaYbO_2$ is only available as polycrystalline sample, such a measurement is technically challenging due to the very small internal thermal conductivity of the powder pellet.

Applying magnetic fields induces magnetic order in $NaYbO_2$, in some sense comparable to $KYbS_2$. At higher fields, however, I found *two* phase transitions in $C(T)$, confirming previously reported results [132]. The origin of this second phase is not known yet, which certainly deserves further attention. My field-dependent measurements of the specific heat and the magnetic Grüneisen parameter were only performed up to 4 T. It would be interesting to expand this field range up to polarized state to investigate the field-dependent entropy change over the whole constructed phase diagram.

The Yb^{3+}-borate $KBaYb(BO_3)_2$ was also proposed as an alternative frustrated triangular lattice. The magnetic interaction in this material, however, is in the order of $J \ll 100$ mK, which is more than one order of magnitude smaller than in $YbMgGaO_4$ or in the $AYbX_2$ materials due to its larger Yb^{3+}-Yb^{3+} distance. Consequently, $KBaYb(BO_3)_2$ remains paramagnetic even at very low temperatures. I evidenced the absence of magnetic ordering by specific heat measurements down to 50 mK, in agreement with a previous report [163]. Applying a magnetic field opens a gap that results in a pronounced Schottky anomaly. Its maximum depends on the gap size and, thus, on the magnetic field, $T_{\max} \sim \Delta \sim B$. In other words, increasing the field shifts the entropy $S(T)$ towards higher temperatures. This makes $KBaYb(BO_3)_2$ an ideal candidate for adiabatic demagnetization refrigeration (ADR). I tested its performance using a pellet mixed of $KBaYb(BO_3)_2$ and silver powder for enhancing the internal thermal conductivity. Using the starting parameters of 2 K and 5 T under optimized conditions, the minimal end temperature is below 22 mK in zero field. In combination with its comparable entropy per volume ratio, $KBaYb(BO_3)_2$ is highly competitive compared to established materials such as the paramagnetic salts FAA or CPA. These salts, however, obtain severe disadvantages because of their delicate production in a metallic framework and their chemical instability in vacuum or upon heating due to their embedded crystal water. $KBaYb(BO_3)_2$ is free from these drawbacks. It is stable in vacuum and can be baked out up to 600 °C, which is crucial for UHV applications. Furthermore, $KBaYb(BO_3)_2$ can be simply mixed with silver powder for increasing the thermal conductivity and pressed into the desired form. Altogether, this renders $KBaYb(BO_3)_2$ an extremely promising candidate for ADR in the millikelvin range, which is for example needed for quantum computers.

Further performance improvements are possible by replacing Yb^{3+} by other rare-earth elements such as Gd^{3+} with higher spin to increase the available entropy per volume. Moreover, the distance between rare-earth ions and, thus, their magnetic interaction can be controlled by changing the non-magnetic ions, e.g. from K to Na or Ba to Sr. This way, fine tuning of the entropy curves might be possible. This would, in principle, allow exact tailoring of the cooling performance to the specific application making this material family extremely attractive for industrial purposes.

In Ch. 5, the focus switches towards the Kitaev candidate α-$RuCl_3$, where Ru^{3+} ions are arranged on a honeycomb lattice. Sizeable Kitaev interactions in this material raised the hope of a realization of the celebrated KSL, but it orders in zero-field in an antiferromagnetic zigzag pattern at the Néel temperature of $T_N \sim 7$ K. On the other hand, magnetic field can suppress the magnetic order, which might unveil the underlying spin liquid physics. Excitingly, a half-

quantized plateau in the thermal Hall conductivity was reported, exactly where magnetic order is suppressed. This is considered to be the ultimate proof of a field-induced KSL. As a consequence, another phase transition towards the partially polarized state should be visible, but several studies only found extremely weak anomalies. This motivated my field-dependent thermodynamic measurements on α-$RuCl_3$, where I applied in-plane magnetic fields along various directions in the honeycomb planes to account for the in-plane anisotropy.

The magnetic Grüneisen parameter $\Gamma_{\mathrm{mag}}(B)$ is highly sensitive to field-induced phase transitions and was measured at temperatures down to 500 mK. I observed two transitions at B_c^{AF1} and B_c^{AF2}, where the former is related to a change of the ordering vector inside the zigzag phase, and the latter to the suppression of the magnetic order. Both critical fields reveal nonmonotonic behavior below $T < 2\,\mathrm{K}$, where inverse melting may occur. This has been theoretically proposed in some anisotropic spin models, and it would be interesting, if it can be found as well in realistic microscopic models of α-$RuCl_3$. Beyond B_c^{AF2}, a very weak shoulder appears, becoming more pronounced at lower temperatures. In strong collaboration with D. Kaib, this anomaly could be identified as a level crossing of the first excited states, and not a phase transition due to a change of the ground state from the presumed KSL to the partially polarized phase.

My field-dependent specific heat measurements $C(B)$ provide further insights, and it can be used in combination with $\Gamma_{\mathrm{mag}}(B)$ to calculate the entropy change $\Delta S(B)$ up to 14 T. Both specific heat and entropy change show a clear maximum at B_c^{AF2}, but they are less sensitive for B_c^{AF1}, especially for fields parallel to Ru-Ru bonds ($\mathbf{B} \parallel [010]$). After the magnetic order is suppressed at B_c^{AF2}, both vanish rapidly without any further anomaly. This is clearly incompatible with the suggested gapless KSL phase for $\mathbf{B} \parallel [010]$ [62] because a strong signature in the entropy is expectable upon entering the gapped partially polarized phase. Altogether, my results speak against a field-induced spin liquid phase in α-$RuCl_3$ because of the missing transition to the partially polarized state.

Finally, I found that the field-induced entropy decrease between 0 T and 14 T is too large for the magnon gap in α-$RuCl_3$ with $\Delta = 1.6\,\mathrm{meV}$ [202]. The origin could be field-dependent phononic contributions, but additional states in the magnon gap could naturally account for this behavior, too. The latter interpretation is supported by my zero-field heat capacity measurements on several samples grown in different laboratories. All samples show a larger heat capacity at low temperature than expected for the anticipated gap. Moreover, the exact Néel temperature T_{N}, which varies between different reports, might be connected to the amount of in-gap states. Further investigations are highly desired to solve this surprising puzzle.

A. Additional Data and Measurements

A.1. Summary of Measured Samples

Table A.1. Overview of samples and measurements presented in this work. Single crystals and powder pellets denoted as SC and PP, respectively. For the $KBaYb(BO_3)_2$:Ag pellets, the mass ratio is given. For α-$RuCl_3$, the angle $\Phi = 0°$ and $\Phi = 30°$ are defined for a magnetic field applied in the honeycomb planes parallel to Ru-Ru bonds, $\mathbf{B} \parallel [010]$, and perpendicular to Ru-Ru bonds, $\mathbf{B} \parallel [110]$, respectively.

Formula	Sample	Mass (mg)	Run MK 4	Grown by	Measurement
$KBaYb(BO_3)_2$	PP	2.69	11, 13	K. Kavita	[1]
+Ag (1:1)	PP	?	PPMS	K. Kavita	[1]
+Ag (1:1)	PP	278.5	21	K. Kavita	Ad. Cooling
+Ag (1:1)	PP	4018	PPMS	K. Kavita	Ad. Cooling
$YbMgGaO_4$	SC	16.33	17 ($\mathbf{B} \parallel \mathbf{c}$)	Y. Li	[4,5]
	SC	10.48	18 ($\mathbf{B} \perp \mathbf{c}$)	Y. Li	[4]
$NaYbO_2$	PP	3.00	23	F. Grußler	[1,2,3]
	PP	?	PPMS	F. Grußler	[1]
$NaLuO_2$	PP	?	PPMS	F. Grußler	[1]
$KYbS_2$	SC	0.33	40 ($\mathbf{B} \parallel \mathbf{c}$)	F. Grußler	[1]
	SC	0.33	41 ($\mathbf{B} \perp \mathbf{c}$)	F. Grußler	[1,2,3]
α-$RuCl_3$	SC	6.63		V. Tsurkan	
$\Phi = 20°$			35, 36		[1,2,3]
$\Phi = 5°$			44		[3]
$\Phi = 15°$			45		[3]
$\Phi = -5°$			46		[3]
$\Phi = 0°$			47		[2,3]
$\Phi = 30°$			48		[2,3]
α-$RuCl_3$	SC	16.5	PPMS	V. Tsurkan	[1]
α-$RuCl_3$	SC	16.84	MK 3	S. Kim	[1]
α-$RuCl_3$	SC	11.45	DynaCool	J. Yan	[1]
					[1] $C(T)$
					[2] $C(B)$
					[3] $\Gamma_{\mathrm{mag}}(B)$
					[4] $M(T)$
					[5] $M(B)$

A.2. Calibration of the RuO_2 Thermometers

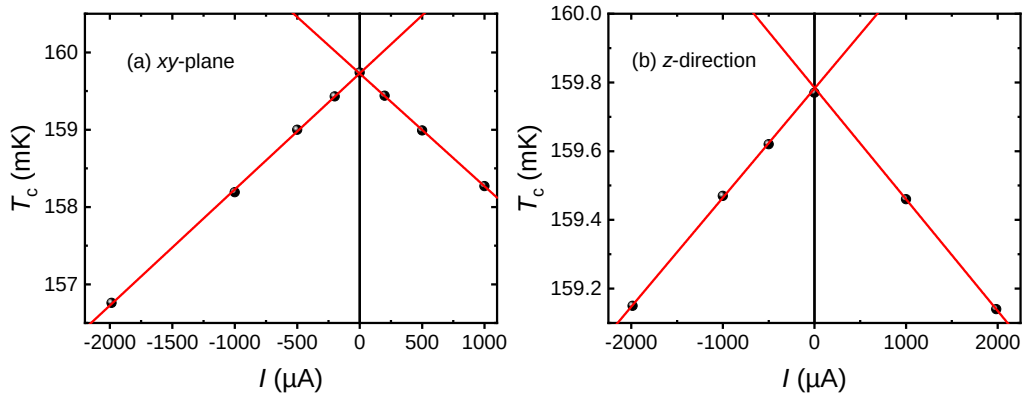

Figure A.1. Influence of the compensation coils on the Fixed Point Device (FPD). The superconducting transition temperature of $AuIn_2$ is suppressed by the compensation coils both in (a) the xy-plane and (b) the z-direction. The linear fits through the data points exactly match the transition temperature with zero current. Consequently, the compensation coils were not needed during the calibration.

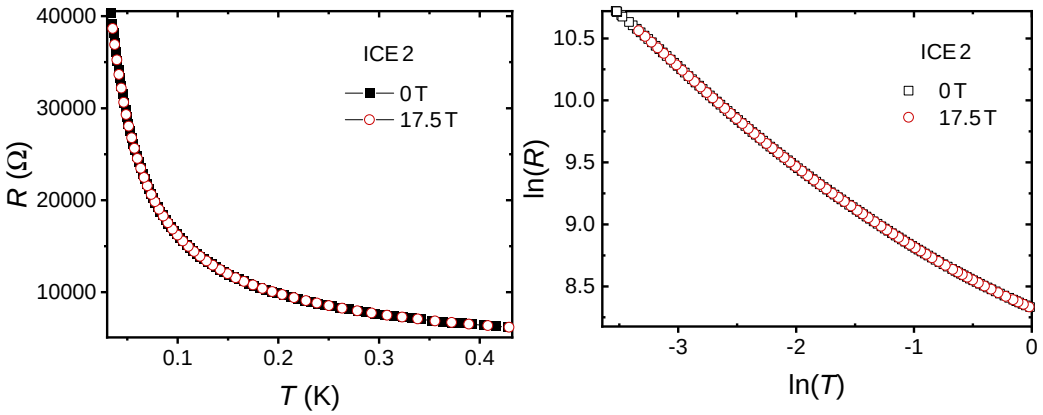

Figure A.2. Calibration of the thermometer ICE 2, which is located on the MC plate in the field-compensated zone of the MK 4 together with the CMN and the Cernox reference thermometers, respectively. Even the highest applied field of 17.5 T does not influence the calibration of the ICE 2. Consequently, the CMN thermometer provides a valid temperature determination independent of the magnetic field.

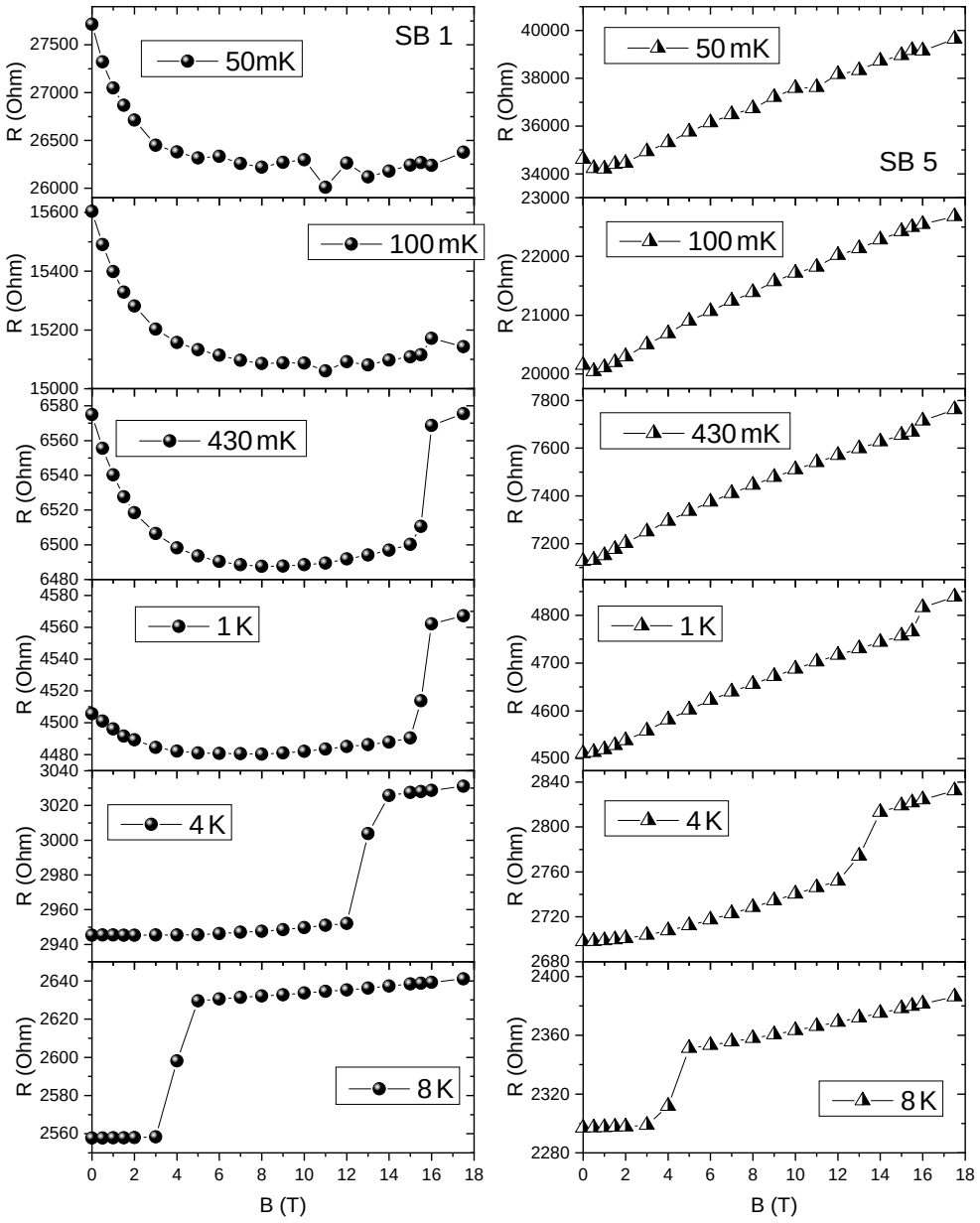

Figure A.3. Magnetoresistance up to 17.5 T of the thermometers SB1 and SB5 at several temperatures from 50 mK up to 8 K. Both thermometers are directly located in the field center and representative for their batch (details in main text, Sec. 3.3) and show opposite behavior (negative and positive magnetoresistance for SB1 and SB5, respectively). Furthermore, the resistance change is much stronger in the batch of SB5. The large positive jump at high fields, which is visible first in the data at 430 mK, results from the breakdown of the superconductivity in the NbTi wires. At higher temperatures, this transition becomes shifted towards much lower fields.

A.3. Information on Heat Capacity Fits in $KYbS_2$

Table A.2. Overview of fitting parameter for the nuclear and the magnetic contribution in $KYbS_2$ according to $C_m = \alpha/T^2 + bT^p$. The units of α and b are $10^{-4}\,\mathrm{J\,K\,mol^{-1}}$ and $\mathrm{Jmol^{-1}K^{-(p+1)}}$, respectively. The fit range is chosen from the lowest measured temperature up to 300 mK, whenever possible.

$B_\perp$	0 T	0.125 T	0.25 T	0.5 T	0.75 T	1 T	1.25 T	1.5 T	2 T	2.5 T	3 T
α	3.53	3.27	3.03	3.68	4.27	4.88	6.31	6.47	9.63	11.69	13.00
p	1.78	1.50	1.46	1.72	1.85	1.93	2.06	1.98	2.10	1.98	0.97
b	5.34	3.13	2.78	4.12	4.92	5.72	7.03	6.54	8.29	6.94	1.20

$B_\perp$	3.5 T	4 T	4.5 T	5 T	5.5 T	6 T	6.5 T	7 T	8 T	9 T	10 T	11 T
α	17.21	19.25	20.59	20.29	23.41	24.85	28.90	30.39	38.23	52.27	59.27	72.64
p	1.82	1.97	2.16	1.38	2.63	2.61	2.51	2.26	1.83	1.64	0.89	1.94
b	2.14	1.36	1.49	0.88	7.77	7.49	9.04	8.85	6.26	5.11	1.33	1.74

$B_\parallel$	0 T	0.125 T	0.25 T	0.375 T	0.5 T	0.75 T	1 T	1.25 T	1.5 T
α	3.80	3.36	3.03	3.02	3.22	3.41	3.83	4.14	4.61
p	1.91	1.46	1.50	1.57	1.63	1.71	1.78	1.82	1.86
b	6.86	2.90	3.09	3.35	3.59	3.78	4.00	4.14	4.30

$B_\parallel$	2 T	3 T	6 T	9 T	12 T	13.5 T	15 T
α	5.66	7.59	20.25	43.90	72.81	88.73	100.01
p	1.86	1.86	2.05	1.98	2.02	2.19	2.25
b	4.26	4.28	4.86	4.09	4.13	5.16	4.70

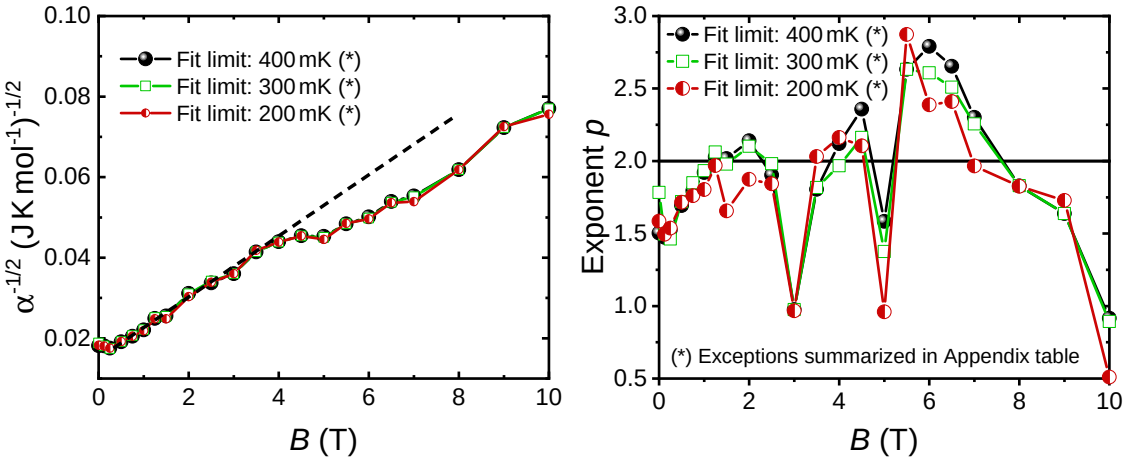

Figure A.4. Dependence of fitting parameters of the nuclear contribution α and the power law exponent p on different upper limits of the fitting interval (200 mK, 300 mK, 400 mK). Dotted line on the left side is guide to the eye to see change of slope more clearly indicating the onset of the plateau phase. For a few fields, the upper limit had to be chosen differently, which is summarized in detail in Table A.3.

Table A.3. Influence of fitted temperature range on fitting results. $B_\perp$, T_{end} and α are given in T, mK and $10^{-4}\,\mathrm{J\,K\,mol^{-1}}$, respectively. The upper limit of the temperature interval was chosen to 200 mK, 300 mK or 400 mK, whenever possible. For Fig. 4.7(d,e) in the main text, the upper limit of 300 mK is used as long as this was reasonable. Deviations from the upper limit are marked and explained below the table.

$B_\perp$	T_{end}	α	p	T_{end}	α	p	T_{end}	α	p
0	201	3.34	1.59	145[2]	3.53	1.78	401	3.29	1.50
0.125	202	3.26	1.49	153[2]	3.27	1.50	403	3.28	1.47
0.25	200	3.07	1.54	151[2]	3.03	1.46	399	3.07	1.53
0.5	201	3.68	1.72	305	3.68	1.72	402	3.65	1.69
0.75	202	4.20	1.76	305	4.27	1.85	403	4.21	1.80
1	206	4.79	1.80	298	4.88	1.93	358[2]	4.87	1.92
1.25	205	6.16	1.97	297	6.31	2.06	357[2]	6.22	2.03
1.5	204	6.15	1.66	296	6.47	1.98	356[2]	6.51	2.02
2	203	9.21	1.87	293	9.63	2.10	337[2]	9.71	2.14
2.5	199	11.47	1.84	301	11.69	1.98	398	11.39	1.90
3	197	12.98	0.97	298	13.00	0.97	298[2]	12.98	0.98
3.5	203	17.50	2.03	308	17.21	1.82	406	17.16	1.80
4	200	19.26	2.16	303	19.25	1.97	400	19.34	2.12
4.5	205	20.59	2.10	297	20.59	2.16	410	20.58	2.36
5	199[1]	19.84	0.96	301	20.29	1.38	397	20.51	1.58
5.5	203	23.52	2.87	256[2]	23.41	2.63	256[2]	23.44	2.63
6	201	24.61	2.39	305	24.85	2.61	403	25.12	2.79
6.5	205	28.80	2.41	307	28.90	2.51	369[2]	29.13	2.65
7	206	29.05	1.97	299	30.39	2.26	359[2]	30.64	2.30
8	196	38.26	1.83	298	38.23	1.83	298[2]	38.26	1.82
9	199	52.66	1.73	250[3]	52.27	1.64	250[3]	52.24	1.64
10	199[1]	57.18	0.51	302	59.27	0.89	398	59.36	0.92
11	-	-	-	510[4]	72.64	1.94	404	72.92	2.10

[1] Fitting range too small for reasonable fit.
[2] Smaller fitting range chosen to avoid problems with kinks/ humps/ ordering peak/ ...
[3] Bad fit quality if T_{end} is set to higher values.
[4] Higher fitting range more reasonable because of large C_{nuc}.

A.4. More Details on $NaYbO_2$

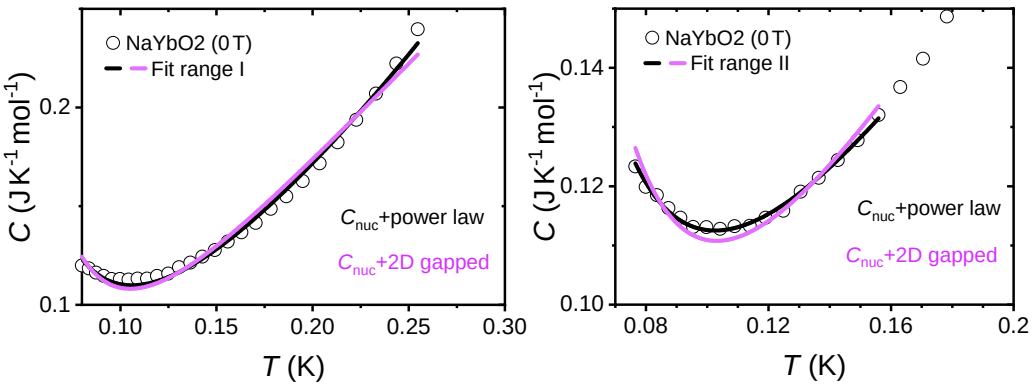

Figure A.5. Specific heat of $NaYbO_2$ including the nuclear contribution at lowest temperatures and zero field. Comparison between different presumed fit functions for the magnetic contribution $C_m(T)$. The fitting range is chosen up to 250 mK (left) and 150 mK (right). In both cases, the gapped function describes the data worse.

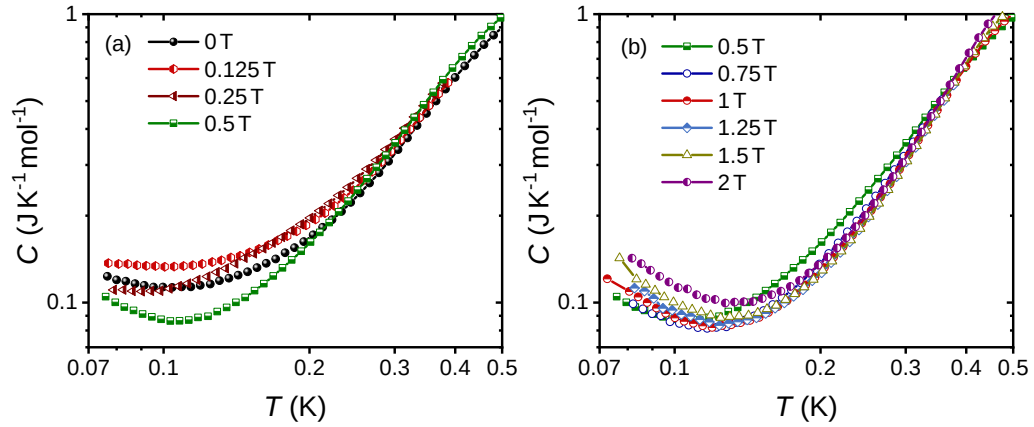

Figure A.6. Specific heat including nuclear contribution of $NaYbO_2$ below 500 mK at low fields. (a) The specific heat at very small fields of 0.125 T and 0.25 T seems to be enhanced at lowest temperatures compared to the zero-field measurement. This is in agreement with the $C(B)$ data in Fig. 4.17(b). In contrast, the specific heat at 0.5 T gets suppressed. (b) Evolution of the specific heat up to 2 T. The curves start to overlap above 0.5 T and ∼0.2 K. At lower temperatures, the nuclear contribution dominates with increasing fields.

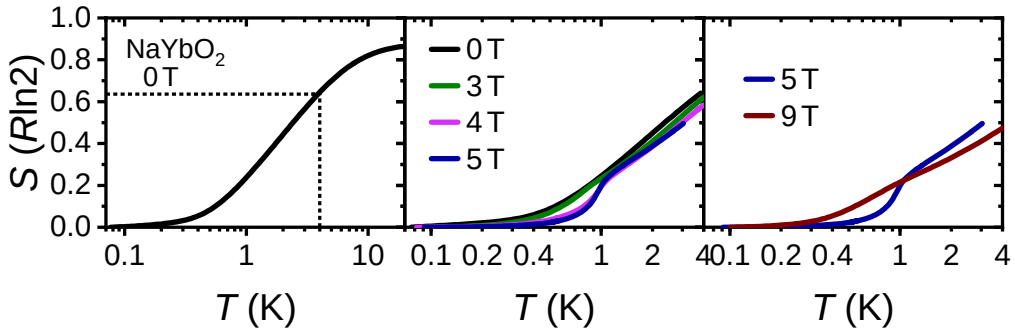

Figure A.7. Entropy evolution of $NaYbO_2$. All entropy curves are normalized to zero at the lowest measured temperature, respectively, which is around 70-90 mK. (a) Zero field up to 20 K (PPMS measurement for higher temperatures performed by Franziska Grußler). At $T \sim 4$ K, comparable to the exchange coupling in $NaYbO_2$ [68], approximately 65 % of $R \ln 2$ is reached, and the remaining entropy is released at higher temperatures. The zero-field entropy finally saturates at $0.9\,R \ln 2$ at 20 K close to the expected value of $R \ln 2$ of a spin-1/2 system. (b) Change of the entropy curves by applying magnetic fields up to 5 T. The field-induced order can be clearly seen in the steep increase near 1 K, where a lot of entropy is released. (c) Increasing the magnetic field to 9 T suppresses that sharp anomaly and restores the more continuos release of entropy. Unfortunately, other fields have only been measured down to 300 mK and could not be included here due to their unkown entropy evolution below 300 mK, resulting in problems with obtaining absolute values.

Table A.4. Overview of fitting parameter for the nuclear and the magnetic contribution in $NaYbO_2$ according to $C_m = \alpha/T^2 + bT^p$. The units for α and b are $10^{-4}\,\mathrm{J\,K\,mol^{-1}}$ and $\mathrm{Jmol^{-1}K^{-(p+1)}}$, respectively. The fit range is chosen from the lowest measured temperature up to 250 mK. For 0 T, the values of Fit I and Fit II are given, as explained in Fig. 4.14 and in the main text.

Field	0 T (I)	0 T (II)	0.125 T	0.25 T	0.5 T	0.75 T	1 T	1.25 T
α	5.14	4.09	5.36	3.75	4.90	5.66	6.45	6.86
p	1.43	1.06	1.24	1.37	1.99	2.17	2.21	2.21
b	1.59	0.81	1.33	1.72	3.64	4.09	4.08	3.86

Field	1.5 T	2 T	3 T	4 T	5 T	5.5 T	9 T
α	7.45	8.53	11.12	11.52	11.51	12.98	17.95
p	2.14	2.04	1.99	2.03	2.10	2.45	2.08
b	3.44	3.12	3.20	1.74	1.18	2.07	4.44

Table A.5. Entropy values from $KYbS_2$ at 4 T (partially interpolated) to shift $\Delta S(B)$ values of $NaYbO_2$ at 4 T assuming strong similarities in the entropy evolution in both compounds. These values are used to calculate the normalized entropy in the left phase diagram in Fig. A.8.

T (mK)	150	200	400	600	800	1.6	2
S ($\mathrm{J\,K^{-1}\,mol^{-1}}$)	0.080	0.094	0.104	0.225	0.483	1.691	1.748

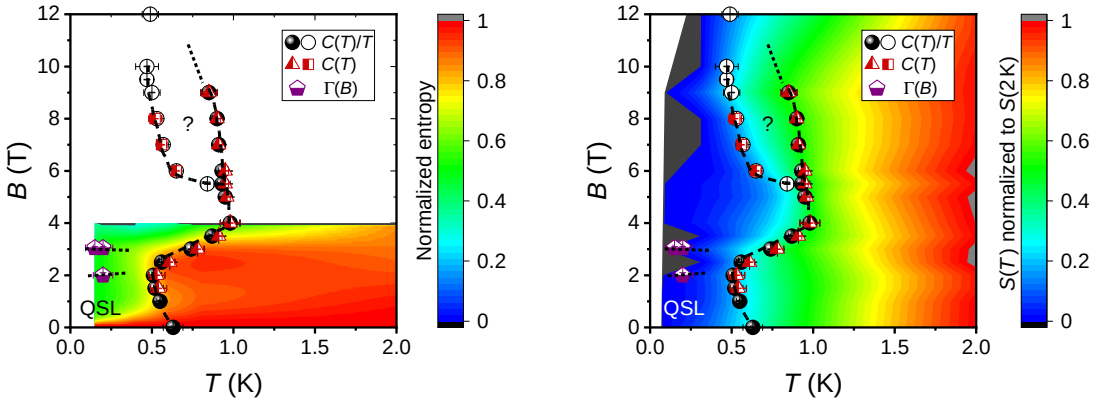

Figure A.8. Two different possibilities to present the entropy evolution in the phase diagram of $NaYbO_2$ [Fig. 4.18]. On the left side, $KYbS_2$ served as a reference to shift the entropy of $NaYbO_2$ at 4 T. The idea is here to use the similarities between $KYbS_2$ and $NaYbO_2$. First, all $NaYbO_2$ curves are shifted such that $\Delta S(T, 4\,\mathrm{T}) = 0\,\mathrm{J\,K^{-1}\,mol^{-1}}$. Subsequently, these values are shifted by the interpolated $KYbS_2$ values at 4 T summarized in Table A.5 and then normalized to the maximum value for each temperature, respectively. The resulting color plot roughly follows the evolution of the phase transitions/ crossover. The phase diagram on the right side uses the entropy calculated from $S(T) = \int \frac{C(T)}{T} \mathrm{d}T$. Several fields have only been measured down to 300 mK resulting in the black areas at low temperatures. The contour of the plateau phase is visible. The second transition line at higher fields and temperatures does not follow an obvious constant entropy line in this representation.

A.5. Additional Information on α-$RuCl_3$

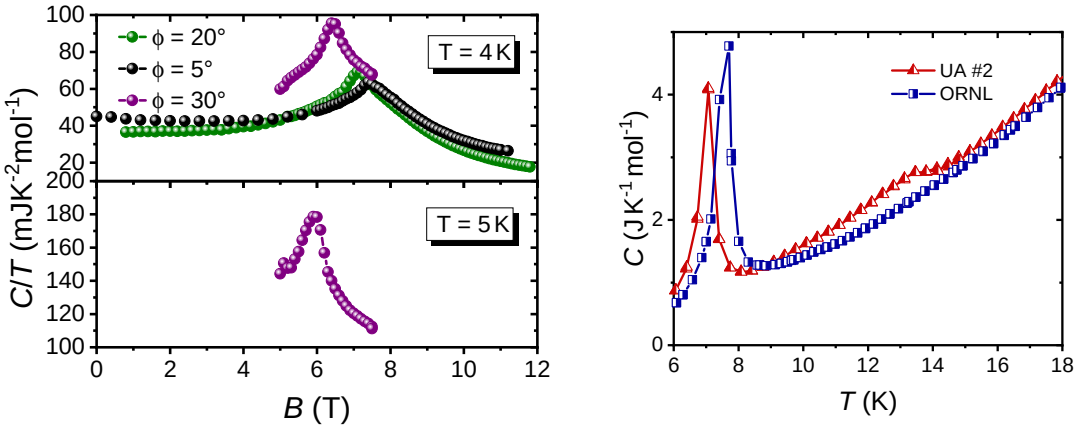

Figure A.9. Left side: Field-dependent specific heat of α-$RuCl_3$ at 4 K and 5 K partially used for the phase diagram in Fig. 5.6(a). Right side: Comparison of zero-field specific heat between sample UA#2 and ORNL. UA#2 shows an additional transition at $T = 14$ K induced by stacking faults, which does not influence the position of the lower transition at 7 K [see Fig. 5.7(c)]. This sample was *not* used for the magnetic Grüneisen parameter and specific heat measurements in the dilution refrigerator MK 4.

Bibliography

[1] Melitta Group. Geschäftsbericht 2020.

[2] P. Anderson. Resonating valence bonds: A new kind of insulator?. *Mater. Res. Bull.* **8**, 153–160 (1973).

[3] P. W. Anderson. The Resonating Valence Bond State in La2CuO4 and Superconductivity. *Science.* **235**, 1196–1198 (1987).

[4] P. A. Lee, N. Nagaosa, and X.-G. Wen. Doping a Mott insulator: Physics of high-temperature superconductivity. *Rev. Mod. Phys.* **78**, 17–85 (2006).

[5] D. A. Huse and V. Elser. Simple Variational Wave Functions for Two-Dimensional Heisenberg Spin-$\frac{1}{2}$ Antiferromagnets. *Phys. Rev. Lett.* **60**, 2531 (1988).

[6] T. Jolicoeur and J. C. Le Guillou. Spin-wave results for the triangular Heisenberg antiferromagnet. *Phys. Rev. B.* **40**, 2727 (1989).

[7] Y. Li, P. Gegenwart, and A. A. Tsirlin. Spin liquids in geometrically perfect triangular antiferromagnets. *J. Phys.: Condens. Matter.* **32**, 224004 (2020).

[8] A. Kitaev. Anyons in an exactly solved model and beyond. *Ann. Phys.* **321**, 2–111 (2006).

[9] A. Kitaev. Fault-tolerant quantum computation by anyons. *Ann. Phys.* **303**, 2–30 (2003).

[10] Z. Zhu, P. A. Maksimov, S. R. White, and A. L. Chernyshev. Disorder-Induced Mimicry of a Spin Liquid in $YbMgGaO_4$. *Phys. Rev. Lett.* **119**, 157201 (2017).

[11] S. Nakatsuji, Y. Nambu, H. Tonomura, O. Sakai, S. Jonas, C. Broholm, H. Tsunetsugu, Y. Qiu, and Y. Maeno. Spin Disorder on a Triangular Lattice. *Science.* **309**, 1697–1700 (2005).

[12] Z. Ma, J. Wang, Z.-Y. Dong, J. Zhang, S. Li, S.-H. Zheng, Y. Yu, W. Wang, L. Che, K. Ran, S. Bao, Z. Cai, P. Čermák, A. Schneidewind, S. Yano, J. S. Gardner, X. Lu, S.-L. Yu, J.-M. Liu, S. Li, J.-X. Li, and J. Wen. Spin-Glass Ground State in a Triangular-Lattice Compound $YbZnGaO_4$. *Phys. Rev. Lett.* **120**, 087201 (2018).

[13] Y. Kasahara, T. Ohnishi, Y. Mizukami, O. Tanaka, S. Ma, K. Sugii, N. Kurita, H. Tanaka, J. Nasu, Y. Motome, T. Shibauchi, and Y. Matsuda. Majorana quantization and half-integer thermal quantum Hall effect in a Kitaev spin liquid. *Nature.* **559**, 227–231 (2018).

[14] C. Balz, P. Lampen-Kelley, A. Banerjee, J. Yan, Z. Lu, X. Hu, S. M. Yadav, Y. Takano, Y. Liu, D. A. Tennant, M. D. Lumsden, D. Mandrus, and S. E. Nagler. Finite field regime for a quantum spin liquid in α-$RuCl_3$. *Phys. Rev. B.* **100**, 060405 (2019).

[15] S. Gass, P. M. Cônsoli, V. Kocsis, L. T. Corredor, P. Lampen-Kelley, D. G. Mandrus, S. E. Nagler, L. Janssen, M. Vojta, B. Büchner, and A. U. B. Wolter. Field-induced transitions in the Kitaev material α-$RuCl_3$ probed by thermal expansion and magnetostriction. *Phys. Rev. B.* **101**, 245158 (2020).

[16] S. Blundell. Magnetism in Condensed Matter. OUP Oxford, 2014.

[17] W. Nolting. Grundkurs Theoretische Physik 5/2, Quantenmechanik - Methoden und Anwendungen. Springer-Verlag, 2006.

[18] A. A. Tsirlin. Theorie des Magnetismus (University of Augsburg).

[19] C. Enss and S. Hunklinger. Low-Temperature Physics. Springer-Verlag, 2005.

[20] I. Levine. Quantum Chemistry. Pearson advanced chemistry series. Pearson, 2014.

[21] G. Jackeli and G. Khaliullin. Mott Insulators in the Strong Spin-Orbit Coupling Limit: From Heisenberg to a Quantum Compass and Kitaev Models. *Phys. Rev. Lett.* **102**, 017205 (2009).

[22] S. M. Winter, A. A. Tsirlin, M. Daghofer, J. van den Brink, Y. Singh, P. Gegenwart, and R. Valentí. Models and materials for generalized Kitaev magnetism. *J. Phys.: Condens. Matter.* **29**, 493002 (2017).

[23] K. W. Plumb, J. P. Clancy, L. J. Sandilands, V. V. Shankar, Y. F. Hu, K. S. Burch, H.-Y. Kee, and Y.-J. Kim. α-$RuCl_3$: A spin-orbit assisted Mott insulator on a honeycomb lattice. *Phys. Rev. B.* **90**, 041112 (2014).

[24] S. Hunklinger. Festkörperphysik. Oldenbourg Verlag, 2007.

[25] W. Nolting. Quantentheorie des Magnetismus - Band 1. B. G. Teubner Stuttgart, 1986.

[26] W. Nolting and A. Ramakanth. Quantum Theory of Magnetism. Springer Berlin Heidelberg, 2009.

[27] R. D. Johnson, S. C. Williams, A. A. Haghighirad, J. Singleton, V. Zapf, P. Manuel, I. I. Mazin, Y. Li, H. O. Jeschke, R. Valentí, and R. Coldea. Monoclinic crystal structure of α-$RuCl_3$ and the zigzag antiferromagnetic ground state. *Phys. Rev. B.* **92**, 235119 (2015).

[28] A. Sahasrabudhe, D. A. S. Kaib, S. Reschke, R. German, T. C. Koethe, J. Buhot, D. Kamenskyi, C. Hickey, P. Becker, V. Tsurkan, A. Loidl, S. H. Do, K. Y. Choi, M. Grüninger, S. M. Winter, Z. Wang, R. Valentí, and P. H. M. van Loosdrecht. High-field quantum disordered state in α-$RuCl_3$: Spin flips, bound states, and multiparticle continuum. *Phys. Rev. B.* **101**, 140410 (2020).

[29] P. Svendlindh and P. Nordblad. Spin Glasses and Random Fields. Ed. by A. Young. World Scientific, Singapore, 1998.

[30] C. G. Shull, W. A. Strauser, and E. O. Wollan. Neutron Diffraction by Paramagnetic and Antiferromagnetic Substances. *Phys. Rev.* **83**, 333 (1951).

[31] L. Balents. Spin liquids in frustrated magnets. *Nature.* **464**, 199 (2010).

[32] A. A. Tsirlin and P. Gegenwart. Frustration mit erstaunlicher Wirkung. *Phys. Unserer Zeit.* **50**, 71–77 (2019).

[33] A. P. Ramirez. Strongly Geometrically Frustrated Magnets. *Annual Review of Materials Science.* **24**, 453–480 (1994).

[34] G. H. Wannier. Antiferromagnetism. The Triangular Ising Net. *Phys. Rev.* **79**, 357 (1950).

[35] O. A. Starykh. Unusual ordered phases of highly frustrated magnets: a review. *Rep. Prog. Phys.* **78**, 052502 (2015).

[36] Y. Li, H. Liao, Z. Zhang, S. Li, F. Jin, L. Ling, L. Zhang, Y. Zou, L. Pi, Z. Yang, J. Wang, Z. Wu, and Q. Zhang. Gapless quantum spin liquid ground state in the two-dimensional spin-1/2 triangular antiferromagnet YbMgGaO4. *Sci. Rep.* **5**, 16419 (2015).

[37] T. Moriya. Anisotropic Superexchange Interaction and Weak Ferromagnetism. *Phys. Rev.* **120**, 91 (1960).

[38] P. A. Maksimov, Z. Zhu, S. R. White, and A. L. Chernyshev. Anisotropic-Exchange Magnets on a Triangular Lattice: Spin Waves, Accidental Degeneracies, and Dual Spin Liquids. *Phys. Rev. X.* **9**, 021017 (2019).

[39] Z. Zhu, P. A. Maksimov, S. R. White, and A. L. Chernyshev. Topography of Spin Liquids on a Triangular Lattice. *Phys. Rev. Lett.* **120**, 207203 (2018).

[40] Z. Zhu and S. R. White. Spin liquid phase of the $S = \frac{1}{2}$ $J_1 - J_2$ Heisenberg model on the triangular lattice. *Phys. Rev. B.* **92**, 041105 (2015).

[41] P. H. Y. Li, R. F. Bishop, and C. E. Campbell. Quasiclassical magnetic order and its loss in a spin-$\frac{1}{2}$ Heisenberg antiferromagnet on a triangular lattice with competing bonds. *Phys. Rev. B.* **91**, 014426 (2015).

[42] W.-J. Hu, S.-S. Gong, W. Zhu, and D. N. Sheng. Competing spin-liquid states in the spin-$\frac{1}{2}$ Heisenberg model on the triangular lattice. *Phys. Rev. B.* **92**, 140403 (2015).

[43] S. N. Saadatmand and I. P. McCulloch. Symmetry fractionalization in the topological phase of the spin-$\frac{1}{2}$ J_1-J_2 triangular Heisenberg model. *Phys. Rev. B.* **94**, 121111 (2016).

[44] R. Kaneko, S. Morita, and M. Imada. Gapless Spin-Liquid Phase in an Extended Spin 1/2 Triangular Heisenberg Model. *J. Phys. Soc. Jpn.* **83**, 093707 (2014).

[45] Y. Iqbal, W.-J. Hu, R. Thomale, D. Poilblanc, and F. Becca. Spin liquid nature in the Heisenberg $J_1 - J_2$ triangular antiferromagnet. *Phys. Rev. B.* **93**, 144411 (2016).

[46] S.-S. Gong, W. Zheng, M. Lee, Y.-M. Lu, and D. N. Sheng. Chiral spin liquid with spinon Fermi surfaces in the spin-$\frac{1}{2}$ triangular Heisenberg model. *Phys. Rev. B.* **100**, 241111 (2019).

[47] S. Hu, W. Zhu, S. Eggert, and Y.-C. He. Dirac Spin Liquid on the Spin-1/2 Triangular Heisenberg Antiferromagnet. *Phys. Rev. Lett.* **123**, 207203 (2019).

[48] J. Iaconis, C. Liu, G. B. Halász, and L. Balents. Spin Liquid versus Spin Orbit Coupling on the Triangular Lattice. *SciPost Phys.* **4**, 003 (2018).

[49] Z. Nussinov and J. van den Brink. Compass models: Theory and physical motivations. *Rev. Mod. Phys.* **87**, 1–59 (2015).

[50] H. Takagi, T. Takayama, G. Jackeli, G. Khaliullin, and S. E. Nagler. Concept and realization of Kitaev quantum spin liquids. *Nature Reviews Physics.* **1**, 264–280 (2019).

[51] S. Trebst. Kitaev Materials. arXiv: 1701.07056.

[52] C. Nayak, S. H. Simon, A. Stern, M. Freedman, and S. Das Sarma. Non-Abelian anyons and topological quantum computation. *Rev. Mod. Phys.* **80**, 1083–1159 (2008).

[53] Y. Singh and P. Gegenwart. Antiferromagnetic Mott insulating state in single crystals of the honeycomb lattice material Na_2IrO_3. *Phys. Rev. B.* **82**, 064412 (2010).

[54] F. Freund, S. C. Williams, R. D. Johnson, R. Coldea, P. Gegenwart, and A. Jesche. Single crystal growth from separated educts and its application to lithium transition-metal oxides. *Sci. Rep.* **6**, 35362 (2016).

[55] S. H. Chun, J.-W. Kim, J. Kim, H. Zheng, C. C. Stoumpos, C. D. Malliakas, J. F. Mitchell, K. Mehlawat, Y. Singh, Y. Choi, T. Gog, A. Al-Zein, M. M. Sala, M. Krisch, J. Chaloupka, G. Jackeli, G. Khaliullin, and B. J. Kim. Direct evidence for dominant bond-directional interactions in a honeycomb lattice iridate Na_2IrO_3. *Nat. Phys.* **11**, 462–466 (2015).

[56] S. C. Williams, R. D. Johnson, F. Freund, S. Choi, A. Jesche, I. Kimchi, S. Manni, A. Bombardi, P. Manuel, P. Gegenwart, and R. Coldea. Incommensurate counterrotating magnetic order stabilized by Kitaev interactions in the layered honeycomb α-Li_2IrO_3. *Phys. Rev. B.* **93**, 195158 (2016).

[57] S. Agrestini, C.-Y. Kuo, K.-T. Ko, Z. Hu, D. Kasinathan, H. B. Vasili, J. Herrero-Martin, S. M. Valvidares, E. Pellegrin, L.-Y. Jang, A. Henschel, M. Schmidt, A. Tanaka, and L. H. Tjeng. Electronically highly cubic conditions for Ru in α-$RuCl_3$. *Phys. Rev. B.* **96**, 161107 (2017).

[58] S. M. Winter, K. Riedl, P. A. Maksimov, A. L. Chernyshev, A. Honecker, and R. Valentí. Breakdown of magnons in a strongly spin-orbital coupled magnet. *Nat. Commun.* **8**, 1152 (2017).

[59] E. K.-H. Lee, J. G. Rau, and Y. B. Kim. Two iridates, two models, and two approaches: A comparative study on magnetism in three-dimensional honeycomb materials. *Phys. Rev. B.* **93**, 184420 (2016).

[60] T. Yokoi, S. Ma, Y. Kasahara, S. Kasahara, T. Shibauchi, N. Kurita, H. Tanaka, J. Nasu, Y. Motome, C. Hickey, S. Trebst, and Y. Matsuda. Half-integer quantized anomalous thermal Hall effect in the Kitaev material candidate α-$RuCl_3$. *Science.* **373**, 568–572 (2021).

[61] M. Yamashita, J. Gouchi, Y. Uwatoko, N. Kurita, and H. Tanaka. Sample dependence of half-integer quantized thermal Hall effect in the Kitaev spin-liquid candidate $\alpha-RuCl_3$. *Phys. Rev. B.* **102**, 220404 (2020).

[62] O. Tanaka, Y. Mizukami, R. Harasawa, K. Hashimoto, K. Hwang, N. Kurita, H. Tanaka, S. Fujimoto, Y. Matsuda, E.-G. Moon, and T. Shibauchi. Thermodynamic evidence for a field-angle-dependent Majorana gap in a Kitaev spin liquid. *Nature Physics* (. 2022).

[63] W. Nolting. Grundkurs Theoretische Physik 4, Spezielle Relativitätstheorie, Thermodynamik. Vol. 7. Springer-Verlag, 2010.

[64] H. B. Callen. Thermodynamics and an Introduction to Thermostatistics 2nd Edition. JohnWiley & sons, 1985.

[65] K. Stierstadt. Thermodynamik: von der Mikrophysik zur Makrophysik. Springer-Verlag, 2010.

[66] A. Tari. The specific heat of matter at low temperatures. Imperial Coll., 2003.

[67] S. Hunklinger. Festkörperphysik. Oldenbourg Verlag, 2018.

[68] L. Ding, P. Manuel, S. Bachus, F. Grußler, P. Gegenwart, J. Singleton, R. D. Johnson, H. C. Walker, D. T. Adroja, A. D. Hillier, and A. A. Tsirlin. Gapless spin-liquid state in the structurally disorder-free triangular antiferromagnet $NaYbO_2$. *Phys. Rev. B.* **100**, 144432 (2019).

[69] Y. Li, D. Adroja, R. I. Bewley, D. Voneshen, A. A. Tsirlin, P. Gegenwart, and Q. Zhang. Crystalline Electric-Field Randomness in the Triangular Lattice Spin-Liquid $YbMgGaO_4$. *Phys. Rev. Lett.* **118**, 107202 (2017).

[70] M. Takahashi. Modified spin-wave theory of a square-lattice antiferromagnet. *Phys. Rev. B.* **40**, 2494 (1989).

[71] A. Auerbach and D. P. Arovas. Spin Dynamics in the Square-Lattice Antiferromagnet. *Phys. Rev. Lett.* **61**, 617 (1988).

[72] K. E. Avers, P. A. Maksimov, P. F. S. Rosa, S. M. Thomas, J. D. Thompson, W. P. Halperin, R. Movshovich, and A. L. Chernyshev. Fingerprinting triangular-lattice antiferromagnet by excitation gaps. *Phys. Rev. B.* **103**, L180406 (2021).

[73] P. W. Anderson, G. Baskaran, Z. Zou, and T. Hsu. Resonating–valence-bond theory of phase transitions and superconductivity in La_2CuO_4-based compounds. *Phys. Rev. Lett.* **58**, 2790 (1987).

[74] S. Yamashita, Y. Nakazawa, M. Oguni, Y. Oshima, H. Nojiri, Y. Shimizu, K. Miyagawa, and K. Kanoda. Thermodynamic properties of a spin-1/2 spin-liquid state in a κ-type organic salt. *Nat. Phys.* **4**, 459– (2008).

[75] O. I. Motrunich. Variational study of triangular lattice spin-1/2 model with ring exchanges and spin liquid state in $\kappa-(ET)_2Cu_2(CN)_3$. *Phys. Rev. B.* **72**, 045105 (2005).

[76] S. Kundu, A. Shahee, A. Chakraborty, K. M. Ranjith, B. Koo, J. Sichelschmidt, M. T. F. Telling, P. K. Biswas, M. Baenitz, I. Dasgupta, S. Pujari, and A. V. Mahajan. Gapless Quantum Spin Liquid in the Triangular System $Sr_3CuSb_2O_9$. *Phys. Rev. Lett.* **125**, 267202 (2020).

[77] A. P. Ramirez, G. P. Espinosa, and A. S. Cooper. Strong frustration and dilution-enhanced order in a quasi-2D spin glass. *Phys. Rev. Lett.* **64**, 2070 (1990).

[78] A. P. Ramirez, G. P. Espinosa, and A. S. Cooper. Elementary excitations in a diluted antiferromagnetic Kagomé lattice. *Phys. Rev. B.* **45**, 2505 (1992).

[79] R. Küchler, N. Oeschler, P. Gegenwart, T. Cichorek, K. Neumaier, O. Tegus, C. Geibel, J. A. Mydosh, F. Steglich, L. Zhu, and Q. Si. Divergence of the Grüneisen Ratio at Quantum Critical Points in Heavy Fermion Metals. *Phys. Rev. Lett.* **91**, 066405 (2003).

[80] R. Küchler, P. Gegenwart, K. Heuser, E.-W. Scheidt, G. R. Stewart, and F. Steglich. Grüneisen Ratio Divergence at the Quantum Critical Point in $CeCu_{6-x}Ag_x$. *Phys. Rev. Lett.* **93**, 096402 (2004).

[81] Y. Tokiwa, T. Radu, C. Geibel, F. Steglich, and P. Gegenwart. Divergence of the Magnetic Grüneisen Ratio at the Field-Induced Quantum Critical Point in $YbRh_2Si_2$. *Phys. Rev. Lett.* **102**, 066401 (2009).

[82] L. Zhu, M. Garst, A. Rosch, and Q. Si. Universally Diverging Grüneisen Parameter and the Magnetocaloric Effect Close to Quantum Critical Points. *Phys. Rev. Lett.* **91**, 066404 (2003).

[83] Y. Tokiwa and P. Gegenwart. High-resolution alternating-field technique to determine the magnetocaloric effect of metals down to very low temperatures. *Rev. Sci. Instrum.* **82**, 013905 (2011).

[84] M. Garst and A. Rosch. Sign change of the Grüneisen parameter and magnetocaloric effect near quantum critical points. *Phys. Rev. B.* **72**, 205129 (2005).

[85] F. Schwabl. Statistische Mechanik. 3rd ed. Springer, 2006.

[86] Y. Shimura, T. Kitazawa, S. Tsuda, S. Bachus, Y. Tokiwa, P. Gegenwart, R. Yamamoto, Y. Yamane, I. Nishihara, K. Umeo, T. Onimaru, T. Takabatake, H. T. Hirose, N. Kikugawa, T. Terashima, and S. Uji. Fragile superheavy Fermi liquid in $YbCo_2Zn_{20}$. *Phys. Rev. B.* **101**, 241102 (2020).

[87] Quantum Design. Physical Property Measurement System - Heat Capacity Option User's Manual (26th edition).

[88] F. Pobell. Matter and Methods at Low Temperatures. Vol. 3. Springer, 2007.

[89] H. Ishimoto, N. Nishida, T. Furubayashi, M. Shinohara, Y. Takano, Y. Miura, and K. Ôno. Two-stage nuclear demagnetization refrigerator reaching 27 µK. *J. Low Temp. Phys.* **55**, 17–31 (1984).

[90] P. J. Shirron. Applications of the magnetocaloric effect in single-stage, multi-stage and continuous adiabatic demagnetization refrigerators. *Cryogenics.* **62**, 130–139 (2014).

[91] D. S. Greywall and P. A. Busch. Fast cerium magnesium nitrate (CMN) thermometer for the low millikelvin temperature range. *Review of Scientific Instruments.* **60**, 471–473 (1989).

[92] Lake Shore Cryotronics, Inc. *User's Manual: Model 372AC Resistance Bridge and Temperature Controller*. 2014.

[93] B. Andraka and Y. Takano. Simultaneous measurements of heat capacity and spin-lattice relaxation time in high magnetic field at low temperature. *Rev. Sci. Instrum.* **67**, 4256–4260 (1996).

[94] S. Bachus, D. A. S. Kaib, A. Jesche, V. Tsurkan, A. Loidl, S. M. Winter, A. A. Tsirlin, R. Valentí, and P. Gegenwart. Angle-dependent thermodynamics of α-$RuCl_3$. *Phys. Rev. B.* **103**, 054440 (2021).

[95] S. Bachus, D. A. S. Kaib, Y. Tokiwa, A. Jesche, V. Tsurkan, A. Loidl, S. M. Winter, A. A. Tsirlin, R. Valentí, and P. Gegenwart. Thermodynamic Perspective on Field-Induced Behavior of α-$RuCl_3$. *Phys. Rev. Lett.* **125**, 097203 (2020).

[96] J. Lasjaunias, B. Picot, A. Ravex, D. Thoulouze, and M. Vandorpe. Heat capacity and thermal conductivity measurements down to 25 mk on samples of poor thermal diffusivity and small specific heat. *Cryogenics.* **17**, 111–117 (1977).

[97] Oxford Instruments. Manual MK 4.

[98] T. Sakakibara, H. Mitamura, T. Tayama, and H. Amitsuka. Faraday Force Magnetometer for High-Sensitivity Magnetization Measurements at Very Low Temperatures and High Fields. *Japanese Journal of Applied Physics.* **33**, 5067 (1994).

[99] Y. Tokiwa, T. Radu, R. Coldea, H. Wilhelm, Z. Tylczynski, and F. Steglich. Magnetic phase transitions in the two-dimensional frustrated quantum antiferromagnet Cs_2CuCl_4. *Phys. Rev. B.* **73**, 134414 (2006).

[100] Y. Li, G. Chen, W. Tong, L. Pi, J. Liu, Z. Yang, X. Wang, and Q. Zhang. Rare-Earth Triangular Lattice Spin Liquid: A Single-Crystal Study of $YbMgGaO_4$. *Phys. Rev. Lett.* **115**, 167203 (2015).

[101] Y. Li. $YbMgGaO_4$: A Triangular-Lattice Quantum Spin Liquid Candidate. *Advanced Quantum Technologies.* **2**, 1900089 (2019).

[102] J. A. M. Paddison, M. Daum, Z. Dun, G. Ehlers, Y. Liu, M. B. Stone, H. Zhou, and M. Mourigal. Continuous excitations of the triangular-lattice quantum spin liquid $YbMgGaO_4$. *Nat. Phys.* **13**, 117–122 (2017).

[103] X. Zhang, F. Mahmood, M. Daum, Z. Dun, J. A. M. Paddison, N. J. Laurita, T. Hong, H. Zhou, N. P. Armitage, and M. Mourigal. Hierarchy of Exchange Interactions in the Triangular-Lattice Spin Liquid $YbMgGaO_4$. *Phys. Rev. X.* **8**, 031001 (2018).

[104] Y. Shen, Y.-D. Li, H. Wo, Y. Li, S. Shen, B. Pan, Q. Wang, H. C. Walker, P. Steffens, M. Boehm, Y. Hao, D. L. Quintero-Castro, L. W. Harriger, M. D. Frontzek, L. Hao, S. Meng, Q. Zhang, G. Chen, and J. Zhao. Evidence for a spinon Fermi surface in a triangular-lattice quantum-spin-liquid candidate. *Nature.* **540**, 559 (2016).

[105] Y.-D. Li, Y.-M. Lu, and G. Chen. Spinon Fermi surface $U(1)$ spin liquid in the spin-orbit-coupled triangular-lattice Mott insulator $YbMgGaO_4$. *Phys. Rev. B.* **96**, 054445 (2017).

[106] Y. Li, D. Adroja, D. Voneshen, R. I. Bewley, Q. Zhang, A. A. Tsirlin, and P. Gegenwart. Nearest-neighbour resonating valence bonds in $YbMgGaO_4$. *Nat. Commun.* **8**, 15814 (2017).

[107] S.-S. Lee and P. A. Lee. U(1) Gauge Theory of the Hubbard Model: Spin Liquid States and Possible Application to $\kappa-(BEDT-TTF)_2Cu_2(CN)_3$. *Phys. Rev. Lett.* **95**, 036403 (2005).

[108] Y. Li, D. Adroja, P. K. Biswas, P. J. Baker, Q. Zhang, J. Liu, A. A. Tsirlin, P. Gegenwart, and Q. Zhang. Muon Spin Relaxation Evidence for the U(1) Quantum Spin-Liquid Ground State in the Triangular Antiferromagnet $YbMgGaO_4$. *Phys. Rev. Lett.* **117**, 097201 (2016).

[109] Y. Xu, J. Zhang, Y. S. Li, Y. J. Yu, X. C. Hong, Q. M. Zhang, and S. Y. Li. Absence of Magnetic Thermal Conductivity in the Quantum Spin-Liquid Candidate $YbMgGaO_4$. *Phys. Rev. Lett.* **117**, 267202 (2016).

[110] Y. Li, S. Bachus, B. Liu, I. Radelytskyi, A. Bertin, A. Schneidewind, Y. Tokiwa, A. A. Tsirlin, and P. Gegenwart. Rearrangement of Uncorrelated Valence Bonds Evidenced by Low-Energy Spin Excitations in $YbMgGaO_4$. *Phys. Rev. Lett.* **122**, 137201 (2019).

[111] S. Nagata, P. H. Keesom, and H. R. Harrison. Low-dc-field susceptibility of CuMn spin glass. *Phys. Rev. B.* **19**, 1633–1638 (1979).

[112] T. Nishioka, Y. Tabata, T. Taniguchi, and Y. Miyako. Canonical Spin Glass Behavior in Ce_2AgIn_3. *J. Phys. Soc. Jpn.* **69**, 1012–1015 (2000).

[113] S. Süllow, G. J. Nieuwenhuys, A. A. Menovsky, J. A. Mydosh, S. A. M. Mentink, T. E. Mason, and W. J. L. Buyers. Spin Glass Behavior in URh_2Ge_2. *Phys. Rev. Lett.* **78**, 354 (1997).

[114] L. Yin, J. S. Xia, Y. Takano, N. S. Sullivan, Q. J. Li, and X. F. Sun. Low-Temperature Low-Field Phases of the Pyrochlore Quantum Magnet $Tb_2Ti_2O_7$. *Phys. Rev. Lett.* **110**, 137201 (2013).

[115] D. S. Fisher. Scaling and critical slowing down in random-field Ising systems. *Phys. Rev. Lett.* **56**, 416 (1986).

[116] T. Susuki, N. Kurita, T. Tanaka, H. Nojiri, A. Matsuo, K. Kindo, and H. Tanaka. Magnetization Process and Collective Excitations in the S=1/2 Triangular-Lattice Heisenberg Antiferromagnet $Ba_3CoSb_2O_9$. *Phys. Rev. Lett.* **110**, 267201 (2013).

[117] G. Koutroulakis, T. Zhou, Y. Kamiya, J. D. Thompson, H. D. Zhou, C. D. Batista, and S. E. Brown. Quantum phase diagram of the $S = \frac{1}{2}$ triangular-lattice antiferromagnet $Ba_3CoSb_2O_9$. *Phys. Rev. B.* **91**, 024410 (2015).

[118] G. Quirion, M. Lapointe-Major, M. Poirier, J. A. Quilliam, Z. L. Dun, and H. D. Zhou. Magnetic phase diagram of $Ba_3CoSb_2O_9$ as determined by ultrasound velocity measurements. *Phys. Rev. B.* **92**, 014414 (2015).

[119] K. M. Ranjith, S. Luther, T. Reimann, B. Schmidt, P. Schlender, J. Sichelschmidt, H. Yasuoka, A. M. Strydom, Y. Skourski, J. Wosnitza, H. Kühne, T. Doert, and M. Baenitz. Anisotropic field-induced ordering in the triangular-lattice quantum spin liquid $NaYbSe_2$. *Phys. Rev. B.* **100**, 224417 (2019).

[120] J. Xing, L. D. Sanjeewa, J. Kim, G. R. Stewart, A. Podlesnyak, and A. S. Sefat. Field-induced magnetic transition and spin fluctuations in the quantum spin-liquid candidate $CsYbSe_2$. *Phys. Rev. B.* **100**, 220407 (2019).

[121] S. Bachus, I. A. Iakovlev, Y. Li, A. Wörl, Y. Tokiwa, L. Ling, Q. Zhang, V. V. Mazurenko, P. Gegenwart, and A. A. Tsirlin. Field evolution of the spin-liquid candidate $YbMgGaO_4$. *Phys. Rev. B.* **102**, 104433 (2020).

[122] W. Steinhardt, Z. Shi, A. Samarakoon, S. Dissanayake, D. Graf, Y. Liu, W. Zhu, C. Marjerrison, C. D. Batista, and S. Haravifard. Constraining the parameter space of a quantum spin liquid candidate in applied field with iterative optimization. *Phys. Rev. Research.* **3**, 033050 (2021).

[123] Y. Shen, Y.-D. Li, H. C. Walker, P. Steffens, M. Boehm, X. Zhang, S. Shen, H. Wo, G. Chen, and J. Zhao. Fractionalized excitations in the partially magnetized spin liquid candidate $YbMgGaO_4$. *Nat. Commun.* **9**, 4138 (2018).

[124] C. Griset, S. Head, J. Alicea, and O. A. Starykh. Deformed triangular lattice antiferromagnets in a magnetic field: Role of spatial anisotropy and Dzyaloshinskii-Moriya interactions. *Phys. Rev. B.* **84**, 245108 (2011).

[125] M. Ye and A. V. Chubukov. Half-magnetization plateau in a Heisenberg antiferromagnet on a triangular lattice. *Phys. Rev. B.* **96**, 140406 (2017).

[126] J. G. Rau and M. J. P. Gingras. Frustration and anisotropic exchange in ytterbium magnets with edge-shared octahedra. *Phys. Rev. B.* **98**, 054408 (2018).

[127] P. Thalmeier, M. E. Zhitomirsky, B. Schmidt, and N. Shannon. Quantum effects in magnetization of J_1-J_2 square lattice antiferromagnet. *Phys. Rev. B.* **77**, 104441 (2008).

[128] A. V. Chubokov and D. I. Golosov. Quantum theory of an antiferromagnet on a triangular lattice in a magnetic field. *J. Phys.: Condens. Matter.* **3**, 69–82 (1991).

[129] W. Liu, Z. Zhang, J. Ji, Y. Liu, J. Li, X. Wang, H. Lei, G. Chen, and Q. Zhang. Rare-Earth Chalcogenides: A Large Family of Triangular Lattice Spin Liquid Candidates. *Chin. Phys. Lett.* **35**, 117501 (2018).

[130] R. Iizuka, S. Michimura, R. Numakura, Y. Uwatoko, and M. Kosaka. Single Crystal Growth and Physical Properties of Ytterbium Sulfide $KYbS_2$ with Triangular Lattice. In: *Proceedings of the International Conference on Strongly Correlated Electron Systems (SCES2019)*. eprint: https://journals.jps.jp/doi/pdf/10.7566/JPSCP.30.011097.

[131] M. Baenitz, P. Schlender, J. Sichelschmidt, Y. A. Onykiienko, Z. Zangeneh, K. M. Ranjith, R. Sarkar, L. Hozoi, H. C. Walker, J.-C. Orain, H. Yasuoka, J. van den Brink, H. H. Klauss, D. S. Inosov, and T. Doert. $NaYbS_2$: A planar spin-$\frac{1}{2}$ triangular-lattice magnet and putative spin liquid. *Phys. Rev. B.* **98**, 220409 (2018).

[132] K. M. Ranjith, D. Dmytriieva, S. Khim, J. Sichelschmidt, S. Luther, D. Ehlers, H. Yasuoka, J. Wosnitza, A. A. Tsirlin, H. Kühne, and M. Baenitz. Field-induced instability of the quantum spin liquid ground state in the $J_{\text{eff}} = \frac{1}{2}$ triangular-lattice compound $NaYbO_2$. *Phys. Rev. B.* **99**, 180401 (2019).

[133] M. M. Bordelon, E. Kenney, C. Liu, T. Hogan, L. Posthuma, M. Kavand, Y. Lyu, M. Sherwin, N. P. Butch, C. Brown, M. J. Graf, L. Balents, and S. D. Wilson. Field-tunable quantum disordered ground state in the triangular-lattice antiferromagnet $NaYbO_2$. *Nat. Phys.* **15**, 1058–1064 (2019).

[134] J. Ma, J. Li, Y. H. Gao, C. Liu, y Qingyong Ren, Z. Zhang, Z. Wang, R. Chen, J. Embs, E. Feng, F. Zhu, Q. Huang, Z. Xiang, L. Chen, E. S. Choi, Z. Qu, L. Li, J. Wang, H. Zhou, Y. Su, X. Wang, Q. Zhang, and G. Chen. Spin-orbit-coupled triangular-lattice spin liquid in rare-earth chalcogenides. arXiv: 2002.09224.

[135] Z. Zhang, J. Li, W. Liu, Z. Zhang, J. Ji, F. Jin, R. Chen, J. Wang, X. Wang, J. Ma, and Q. Zhang. Effective magnetic Hamiltonian at finite temperatures for rare-earth chalcogenides. *Phys. Rev. B.* **103**, 184419 (2021).

[136] J. Xing, L. D. Sanjeewa, J. Kim, G. R. Stewart, M.-H. Du, F. A. Reboredo, R. Custelcean, and A. S. Sefat. Crystal Synthesis and Frustrated Magnetism in Triangular Lattice $CsRESe_2$ (RE = La–Lu): Quantum Spin Liquid Candidates $CsCeSe_2$ and $CsYbSe_2$. *ACS Materials Letters*, 71–75 (2019).

[137] P.-L. Dai, G. Zhang, Y. Xie, C. Duan, Y. Gao, Z. Zhu, E. Feng, Z. Tao, C.-L. Huang, H. Cao, A. Podlesnyak, G. E. Granroth, M. S. Everett, J. C. Neuefeind, D. Voneshen, S. Wang, G. Tan, E. Morosan, X. Wang, H.-Q. Lin, L. Shu, G. Chen, Y. Guo, X. Lu, and P. Dai. Spinon Fermi Surface Spin Liquid in a Triangular Lattice Antiferromagnet $NaYbSe_2$. *Phys. Rev. X.* **11**, 021044 (2021).

[138] T. Dey, M. Majumder, J. C. Orain, A. Senyshyn, M. Prinz-Zwick, S. Bachus, Y. Tokiwa, F. Bert, P. Khuntia, N. Büttgen, A. A. Tsirlin, and P. Gegenwart. Persistent low-temperature spin dynamics in the mixed-valence iridate $Ba_3InIr_2O_9$. *Phys. Rev. B.* **96**, 174411 (2017).

[139] J. S. Helton, K. Matan, M. P. Shores, E. A. Nytko, B. M. Bartlett, Y. Yoshida, Y. Takano, A. Suslov, Y. Qiu, J.-H. Chung, D. G. Nocera, and Y. S. Lee. Spin Dynamics of the Spin-1/2 Kagome Lattice Antiferromagnet $ZnCu_3(OH)_6Cl_2$. *Phys. Rev. Lett.* **98**, 107204 (2007).

[140] S. Yamashita, T. Yamamoto, Y. Nakazawa, M. Tamura, and R. Kato. Gapless spin liquid of an organic triangular compound evidenced by thermodynamic measurements. *Nat. Commun.* **2**, 275 (2011).

[141] J. G. Cheng, G. Li, L. Balicas, J. S. Zhou, J. B. Goodenough, C. Xu, and H. D. Zhou. High-Pressure Sequence of $Ba_3NiSb_2O_9$ Structural Phases: New $S = 1$ Quantum Spin Liquids Based on Ni^{2+}. *Phys. Rev. Lett.* **107**, 197204 (2011).

[142] Y. Okamoto, M. Nohara, H. Aruga-Katori, and H. Takagi. Spin-Liquid State in the $S = 1/2$ Hyperkagome Antiferromagnet $Na_4Ir_3O_8$. *Phys. Rev. Lett.* **99**, 137207 (2007).

[143] H. D. Zhou, E. S. Choi, G. Li, L. Balicas, C. R. Wiebe, Y. Qiu, J. R. D. Copley, and J. S. Gardner. Spin Liquid State in the $S = 1/2$ Triangular Lattice $Ba_3CuSb_2O_9$. *Phys. Rev. Lett.* **106**, 147204 (2011).

[144] S. Bhattacharjee, V. B. Shenoy, and T. Senthil. Possible ferro-spin nematic order in $NiGa_2S_4$. *Phys. Rev. B.* **74**, 092406 (2006).

[145] E. M. Stoudenmire, S. Trebst, and L. Balents. Quadrupolar correlations and spin freezing in $S = 1$ triangular lattice antiferromagnets. *Phys. Rev. B.* **79**, 214436 (2009).

[146] J. Xing, L. D. Sanjeewa, J. Kim, W. R. Meier, A. F. May, Q. Zheng, R. Custelcean, G. R. Stewart, and A. S. Sefat. Synthesis, magnetization, and heat capacity of triangular lattice materials $NaErSe_2$ and $KErSe_2$. *Phys. Rev. Materials.* **3**, 114413 (2019).

[147] Y. Li, S. Bachus, Y. Tokiwa, A. A. Tsirlin, and P. Gegenwart. Gapped ground state in the zigzag pseudospin-1/2 quantum antiferromagnetic chain compound $PrTiNbO_6$. *Phys. Rev. B.* **97**, 184434 (2018).

[148] Y. Tokiwa, C. Stingl, M.-S. Kim, T. Takabatake, and P. Gegenwart. Characteristic signatures of quantum criticality driven by geometrical frustration. *Sci. Adv.* **1**, e1500001 (2015).

[149] Y. Tokiwa, M. Mchalwat, R. S. Perry, and P. Gegenwart. Multiple Metamagnetic Quantum Criticality in $Sr_3Ru_2O_7$. *Phys. Rev. Lett.* **116**, 226402 (2016).

[150] L. Seabra, T. Momoi, P. Sindzingre, and N. Shannon. Phase diagram of the classical Heisenberg antiferromagnet on a triangular lattice in an applied magnetic field. *Phys. Rev. B.* **84**, 214418 (2011).

[151] N. A. Fortune, Q. Huang, T. Hong, J. Ma, E. S. Choi, S. T. Hannahs, Z. Y. Zhao, X. F. Sun, Y. Takano, and H. D. Zhou. Evolution of magnetic field induced ordering in the layered quantum Heisenberg triangular-lattice antiferromagnet $Ba_3CoSb_2O_9$. *Phys. Rev. B.* **103**, 184425 (2021).

[152] M. Kenzelmann, G. Lawes, A. B. Harris, G. Gasparovic, C. Broholm, A. P. Ramirez, G. A. Jorge, M. Jaime, S. Park, Q. Huang, A. Y. Shapiro, and L. A. Demianets. Direct Transition from a Disordered to a Multiferroic Phase on a Triangular Lattice. *Phys. Rev. Lett.* **98**, 267205 (2007).

[153] M. M. Bordelon, C. Liu, L. Posthuma, P. M. Sarte, N. P. Butch, D. M. Pajerowski, A. Banerjee, L. Balents, and S. D. Wilson. Spin excitations in the frustrated triangular lattice antiferromagnet $NaYbO_2$. *Phys. Rev. B.* **101**, 224427 (2020).

[154] M. B. Sanders, F. A. Cevallos, and R. J. Cava. Magnetism in the $KBaRE(BO_3)_2$ (RE = Sm, Eu, Gd, Tb, Dy, Ho, Er, Tm, Yb, Lu) series: materials with a triangular rare earth lattice. *Mater. Res. Express.* **4**, 036102 (2017).

[155] S. Guo, T. Kong, F. A. Cevallos, K. Stolze, and R. Cava. Crystal growth, crystal structure and anisotropic magnetic properties of $KBaR(BO_3)_2$ (R=Y, Gd, Tb, Dy, Ho, Tm, Yb and Lu) triangular lattice materials. *J. Magn. Magn. Mater.* **472**, 104–110 (2019).

[156] S. Guo, A. Ghasemi, C. L. Broholm, and R. J. Cava. Magnetism on ideal triangular lattices in $NaBaYb(BO_3)_2$. *Phys. Rev. Materials.* **3**, 094404 (2019).

[157] S. Guo, T. Kong, W. Xie, L. Nguyen, K. Stolze, F. A. Cevallos, and R. J. Cava. Triangular Rare-Earth Lattice Materials $RbBaR(BO_3)_2$ (R = Y, Gd-Yb) and Comparison to the $KBaR(BO_3)_2$ Analogs. *Inorg. Chem.* **58**, 3308–3315 (2019).

[158] S. Guo, T. Kong, and R. J. Cava. $NaBaR(BO_3)_2$ (R = Dy, Ho, Er and Tm): structurally perfect triangular lattice materials with two rare earth layers. *Mater. Res. Express.* **6**, 106110 (2019).

[159] Y. Gao, L. Xu, Z. Tian, and S. Yuan. Synthesis and magnetism of $RE(BaBO_3)_3$ (RE=Dy,Ho,Er,Tm,Yb) series with rare earth ions on a two dimensional triangle-lattice. *J. Alloys Compd.* **745**, 396–400 (2018).

[160] K. Y. Zeng, L. Ma, Y. X. Gao, Z. M. Tian, L. S. Ling, and L. Pi. NMR study of the spin excitations in the frustrated antiferromagnet $YbBa(BO_3)_3$ with a triangular lattice. *Phys. Rev. B.* **102**, 045149 (2020).

[161] H. Cho, S. J. Blundell, T. Shiroka, K. MacFarquharson, D. Prabhakaran, and R. Coldea. Studies on Novel Yb-based Candidate Triangular Quantum Antiferromagnets: $Ba_3YbB_3O_9$ and $Ba_3YbB_9O_{18}$. arXiv: 2104.01005.

[162] Y. Tokiwa, S. Bachus, K. Kavita, A. Jesche, A. A. Tsirlin, and P. Gegenwart. Frustrated magnet for adiabatic demagnetization cooling to milli-Kelvin temperatures. *Communications Materials.* **2**, 42 (2021).

[163] B. L. Pan, J. M. Ni, L. P. He, Y. J. Yu, Y. Xu, and S. Y. Li. Specific heat and thermal conductivity of the triangular-lattice rare-earth material $KBaYb(BO_3)_2$ at ultralow temperature. *Phys. Rev. B.* **103**, 104412 (2021).

[164] B. Schmidt and P. Thalmeier. Frustrated two dimensional quantum magnets. *Phys. Rep.* **703**, 1–59 (2017).

[165] D. Jang, T. Gruner, A. Steppke, K. Mitsumoto, C. Geibel, and M. Brando. Large magnetocaloric effect and adiabatic demagnetization refrigeration with $YbPt_2Sn$. *Nat. Commun.* **6**, 8680 (2015).

[166] T. Gruner, D. Jang, A. Steppke, M. Brando, F. Ritter, C. Krellner, and C. Geibel. Unusual weak magnetic exchange in two different structure types: $YbPt_2Sn$ and $YbPt_2In$. *J. Phys.: Condens. Matter.* **26**, 485002 (2014).

[167] Quantum Design. Adiabatic Demagnetization Refrigerator (ADR) for DynaCool (D810) / PPMS (P810).

[168] O. E. Vilches and J. C. Wheatley. Measurements of the Specific Heats of Three Magnetic Salts at Low Temperatures. *Phys. Rev.* **148**, 509 (1966).

[169] J. M. Daniels, N. Kurti, and F. E. Simon. The thermal and magnetic properties of chromium potassium alum below 0.1°K. *Proceedings of the Royal Society of London. Series A. Mathematical and Physical Sciences.* **221**, 243–256 (1954).

[170] R. A. Fisher, E. W. Hornung, G. E. Brodale, and W. F. Giauque. Magnetothermodynamics of $Ce_2Mg_3(NO_3)_{12}\cdot 24H_2O$. II. The evaluation of absolute temperature and other thermodynamic properties of CMN to 0.6 m°K. *The Journal of Chemical Physics.* **58**, 5584–5604 (1973).

[171] D. A. Paixao Brasiliano, J.-M. Duval, C. Marin, E. Bichaud, J.-P. Brison, M. Zhitomirsky, and N. Luchier. YbGG material for Adiabatic Demagnetization in the 100 mK – 3 K range. *Cryogenics.* **105**, 103002 (2020).

[172] M. E. Zhitomirsky. Enhanced magnetocaloric effect in frustrated magnets. *Phys. Rev. B.* **67**, 104421 (2003).

[173] T. Esat, P. Borgens, X. Yang, P. Coenen, V. Cherepanov, A. Raccanelli, F. S. Tautz, and R. Temirov. A millikelvin scanning tunneling microscope in ultra-high vacuum with adiabatic demagnetization refrigeration. *Rev. Sci. Instrum.* **92**, 063701 (2021).

[174] M. Songvilay, J. Robert, S. Petit, J. A. Rodriguez-Rivera, W. D. Ratcliff, F. Damay, V. Balédent, M. Jiménez-Ruiz, P. Lejay, E. Pachoud, A. Hadj-Azzem, V. Simonet, and C. Stock. Kitaev interactions in the Co honeycomb antiferromagnets $Na_3Co_2SbO_6$ and $Na_2Co_2TeO_6$. *Phys. Rev. B.* **102**, 224429 (2020).

[175] X. Zhang, Y. Xu, R. Zhong, R. J. Cava, N. Drichko, and N. P. Armitage. In- and out-of-plane field induced quantum spin-liquid states in a more ideal Kitaev material: $BaCo_2(AsO_4)_2$. arXiv: 2106.13418.

[176] H. B. Cao, A. Banerjee, J.-Q. Yan, C. A. Bridges, M. D. Lumsden, D. G. Mandrus, D. A. Tennant, B. C. Chakoumakos, and S. E. Nagler. Low-temperature crystal and magnetic structure of α-$RuCl_3$. *Phys. Rev. B.* **93**, 134423 (2016).

[177] J. A. Sears, M. Songvilay, K. W. Plumb, J. P. Clancy, Y. Qiu, Y. Zhao, D. Parshall, and Y.-J. Kim. Magnetic order in α-$RuCl_3$: A honeycomb-lattice quantum magnet with strong spin-orbit coupling. *Phys. Rev. B.* **91**, 144420 (2015).

[178] J. A. Sears, Y. Zhao, Z. Xu, J. W. Lynn, and Y.-J. Kim. Phase diagram of α-$RuCl_3$ in an in-plane magnetic field. *Phys. Rev. B.* **95**, 180411 (2017).

[179] L. J. Sandilands, Y. Tian, A. A. Reijnders, H.-S. Kim, K. W. Plumb, Y.-J. Kim, H.-Y. Kee, and K. S. Burch. Spin-orbit excitations and electronic structure of the putative Kitaev magnet α-$RuCl_3$. *Phys. Rev. B.* **93**, 075144 (2016).

[180] Y. Kubota, H. Tanaka, T. Ono, Y. Narumi, and K. Kindo. Successive magnetic phase transitions in α-$RuCl_3$: XY-like frustrated magnet on the honeycomb lattice. *Phys. Rev. B.* **91**, 094422 (2015).

[181] S.-H. Do, S.-Y. Park, J. Yoshitake, J. Nasu, Y. Motome, Y. S. Kwon, D. T. Adroja, D. J. Voneshen, K. Kim, T.-H. Jang, J.-H. Park, K.-Y. Choi, and S. Ji. Majorana fermions in the Kitaev quantum spin system α-RuCl3. *Nat. Phys.* **13**, 1079–1084 (2017).

[182] A. Banerjee, J. Yan, J. Knolle, C. A. Bridges, M. B. Stone, M. D. Lumsden, D. G. Mandrus, D. A. Tennant, R. Moessner, and S. E. Nagler. Neutron scattering in the proximate quantum spin liquid α-RuCl3. *Science.* **356**, 1055–1059 (2017).

[183] S. Widmann, V. Tsurkan, D. A. Prishchenko, V. G. Mazurenko, A. A. Tsirlin, and A. Loidl. Thermodynamic evidence of fractionalized excitations in α-$RuCl_3$. *Phys. Rev. B.* **99**, 094415 (2019).

[184] S. Reschke, V. Tsurkan, S.-H. Do, K.-Y. Choi, P. Lunkenheimer, Z. Wang, and A. Loidl. Terahertz excitations in α-$RuCl_3$: Majorana fermions and rigid-plane shear and compression modes. *Phys. Rev. B.* **100**, 100403 (2019).

[185] A. Loidl, P. Lunkenheimer, and V. Tsurkan. On the proximate Kitaev quantum-spin liquid α-$RuCl_3$: thermodynamics, excitations and continua. *Journal of Physics: Condensed Matter.* **33**, 443004 (2021).

[186] A. Banerjee, C. A. Bridges, J.-Q. Yan, A. A. Aczel, L. Li, M. B. Stone, G. E. Granroth, M. D. Lumsden, Y. Yiu, J. Knolle, S. Bhattacharjee, D. L. Kovrizhin, R. Moessner, D. A. Tennant, D. G. Mandrus, and S. E. Nagler. Proximate Kitaev quantum spin liquid behaviour in a honeycomb magnet. *Nat. Mater.* **15**, 733–740 (2016).

[187] L. J. Sandilands, Y. Tian, K. W. Plumb, Y.-J. Kim, and K. S. Burch. Scattering Continuum and Possible Fractionalized Excitations in α-$RuCl_3$. *Phys. Rev. Lett.* **114**, 147201 (2015).

[188] S. M. Winter, K. Riedl, D. Kaib, R. Coldea, and R. Valentí. Probing α-$RuCl_3$ Beyond Magnetic Order: Effects of Temperature and Magnetic Field. *Phys. Rev. Lett.* **120**, 077203 (2018).

[189] R. L. Smit, S. Keupert, O. Tsyplyatyev, P. A. Maksimov, A. L. Chernyshev, and P. Kopietz. Magnon damping in the zigzag phase of the Kitaev-Heisenberg-Γ model on a honeycomb lattice. *Phys. Rev. B.* **101**, 054424 (2020).

[190] P. A. Maksimov and A. L. Chernyshev. Rethinking α-$RuCl_3$. *Phys. Rev. Research.* **2**, 033011 (2020).

[191] L. E. Chern, E. Z. Zhang, and Y. B. Kim. Sign Structure of Thermal Hall Conductivity and Topological Magnons for In-Plane Field Polarized Kitaev Magnets. *Phys. Rev. Lett.* **126**, 147201 (2021).

[192] P. Czajka, T. Gao, M. Hirschberger, P. Lampen-Kelley, A. Banerjee, J. Yan, D. G. Mandrus, S. E. Nagler, and N. P. Ong. Oscillations of the thermal conductivity in the spin-liquid state of α-$RuCl_3$. *Nat. Phys.* **17**, 915–919 (2021).

[193] J. A. N. Bruin, R. R. Claus, Y. Matsumoto, N. Kurita, H. Tanaka, and H. Takagi. Robustness of the thermal Hall effect close to half-quantization in a field-induced spin liquid state. arXiv: `2104.12184 [cond-mat.str-el]`.

[194] J. Nasu and Y. Motome. Thermodynamic and transport properties in disordered Kitaev models. *Phys. Rev. B.* **102**, 054437 (2020).

[195] M. Majumder, M. Schmidt, H. Rosner, A. A. Tsirlin, H. Yasuoka, and M. Baenitz. Anisotropic $Ru^{3+}4d^5$ magnetism in the α-$RuCl_3$ honeycomb system: Susceptibility, specific heat, and zero-field NMR. *Phys. Rev. B.* **91**, 180401 (2015).

[196] C. Balz, L. Janssen, P. Lampen-Kelley, A. Banerjee, Y. H. Liu, J.-Q. Yan, D. G. Mandrus, M. Vojta, and S. E. Nagler. Field-induced intermediate ordered phase and anisotropic interlayer interactions in α-$RuCl_3$. *Phys. Rev. B.* **103**, 174417 (2021).

[197] K. Hui. Reentrant behavior of an in-plane antiferromagnet in a magnetic field. *Phys. Rev. B.* **38**, 802 (1988).

[198] N. Schupper and N. M. Shnerb. Inverse melting and inverse freezing: A spin model. *Phys. Rev. E.* **72**, 046107 (2005).

[199] W. E. Parente, J. Pacobahyba, I. G. Araújo, M. A. Neto, J. Ricardo de Sousa, and Ü. Akinci. Critical and reentrant behavior of the spin quantum 1/2 anisotropic Heisenberg antiferromagnet model with Dzyaloshinskii–Moriya interaction in a longitudinal magnetic field. *J. Magn. Magn. Mater.* **355**, 235–239 (2014).

[200] R. Schönemann, S. Imajo, F. Weickert, J. Yan, D. G. Mandrus, Y. Takano, E. L. Brosha, P. F. S. Rosa, S. E. Nagler, K. Kindo, and M. Jaime. Thermal and magnetoelastic properties of α-$RuCl_3$ in the field-induced low-temperature states. *Phys. Rev. B.* **102**, 214432 (2020).

[201] E. Palacios, J. Bartolomé, G. Wang, R. Burriel, K. Skokov, S. Taskaev, and V. Khovaylo. Analysis of the Magnetocaloric Effect in Heusler Alloys: Study of $Ni_{50}CoMn_{36}Sn_{13}$ by Calorimetric Techniques. *Entropy.* **17**, 1236–1252 (2015).

[202] A. Banerjee, P. Lampen-Kelley, J. Knolle, C. Balz, A. A. Aczel, B. Winn, Y. Liu, D. Pajerowski, J. Yan, C. A. Bridges, A. T. Savici, B. C. Chakoumakos, M. D. Lumsden, D. A. Tennant, R. Moessner, D. G. Mandrus, and S. E. Nagler. Excitations in the field-induced quantum spin liquid state of α-$RuCl_3$. *npj Quantum Materials.* **3**, 8 (2018).

Acknowledgments

An dieser Stelle möchte ich allen Personen meinen Dank aussprechen, die mich während meiner Promotion unterstützt haben.

Prof. Dr. Philipp Gegenwart danke ich für die Aufnahme am Lehrstuhl Experimentalphysik VI, die hervorragende Betreuung meiner Arbeit sowie die Übernahme des Erstgutachtens. Mir wurde von Anfang an vollstes Vertrauen entgegen gebracht und die Aufsicht über den neuen Mischkühler MK 4 übertragen, obwohl ich keine Erfahrung in der Tieftemperaturphysik vorweisen konnte. Gerade im ersten Jahr mit viel Einarbeitung, Erdungsproblemen sowie einer äußerst zeitintensiven Thermometerkalibrierung erfuhr ich stets große Unterstützung, genau wie in den folgenden Jahren. Die Diskussionen meiner Ergebnisse waren äußerst hilf- und lehrreich, genau wie die praktischen Tipps für laufende Messungen. Ein besonders spannendes Thema war für mich persönlich die Anwendungsmöglichkeit von $KBaYb(BO_3)_2$, dessen Potential du bereits von Anfang an gesehen hast. Ich durfte diesen Prozess aktiv begleiten und meine Ideen einbringen, wofür ich sehr dankbar bin. Ich werde meine Promotionszeit in sehr guter Erinnerung halten!

Prof. Dr. Alois Loidl möchte ich für die Übernahme des Zweitgutachtens danken sowie für die gute Zusammenarbeit in Bezug auf α-$RuCl_3$. Ohne die bereitgestellten Proben von Vladimir Tsurkan (Experimentalphysik V) wäre ein wesentlicher Teil meiner Arbeit nicht möglich gewesen.

Einen ganz besonderen Dank möchte ich Dr. Yoshifumi Tokiwa aussprechen, der mehrere Jahre unsere kleine, aber feine Tieftemperaturgruppe leitete. Deine unschätzbare Erfahrung mit dem Mischkühler sowie einer Vielzahl an Messaufbauten half mir in verschiedensten Situationen. Du hattest stets ein offenes Ohr für alle Probleme und immer eine Lösungsidee. Durch unsere Zusammenarbeit konnte ich extrem viel lernen. Yoshi, ich wünsche dir und deiner Familie alles Gute in Japan!

Ein ebenso großer Dank geht an Dr. Alexander Tsirlin. Unsere Diskussionen über meine Ergebnisse waren unglaublich wertvoll, ebenso wie deine Tipps zur Auswertung oder beim Schreiben wissenschaftlicher Publikationen. Ohne deine Anregung und Motivation wäre vermutlich nie die Publikation über die feldabhängigen Messungen in $YbMgGaO_4$ enstanden. Zudem bin ich sehr dankbar, dass ich deine knappe Zeit immer wieder in Anspruch nehmen durfte und schätze deine Art sehr, komplexe Zusammenhänge in anschaulichen Worten zu erklären ("quantum soup") – egal ob in einer Vorlesung oder bei Meerrettich und Haselnuss im Söllerhaus. Ich hoffe sehr, dass wir auch in Zukunft immer wieder das edle Schachbrett in der Weihnachtsedition nutzen werden!

Many thanks to Ilia Iakovlev, who visited Augsburg twice. During your first stay, we worked a lot together to reproduce the field-dependent behavior of $YbMgGaO_4$. Your Monte Carlo calculations were the basis for the averaging procedure, which I applied to explain the unusual behavior in $YbMgGaO_4$. Unfortunately, your second stay started and ended at the same time as the long Covid-19 lockdown in Germany. What a bad luck! Nevertheless, I enjoyed our Zoom meetings very much, talking about this and that - let's keep this tradition!

Außerdem möchte ich mich sehr herzlich bei David Kaib bedanken, der zusammen mit Dr. Steve Winter und Prof. Dr. Roser Valentí eine sehr große Unterstützung in Bezug auf meine

Messungen an α-$RuCl_3$ war. Deine theoretischen Berechnungen sowie unsere Diskussionen waren extrem hilfreich, um die Vorgänge in α-$RuCl_3$ besser zu verstehen. Außerdem hast du geduldig alle meine "Experimentalphysiker-Fragen" beantwortet.

Dr. Yuesheng Li strongly supported my work in Augsburg by providing various samples. He was always very interested in getting into contact with new techniques and we discussed a lot about the dilution refrigerator. He motivated a bunch of measurements, and his efficient way of working was inspiring. To use your own words: Yuesheng, thanks for your hard work!

Eine Promotion am Mischkühler kann nur erfolgreich sein, wenn man Proben zum Messen hat. Da ich selbst keine Synthesen durchgeführt habe, möchte ich mich ganz herzlich bei allen bedanken, die mir Proben zur Verfügung gestellt haben. Sie alle namentlich zu nennen, würde diese Danksagung sprengen, da nur ein (kleiner) Teil davon in dieser Arbeit diskutiert wurde. Deswegen geht mein Dank an dieser Stelle an Dr. Yuesheng Li, Franziska Grußler, Kavita, Dr. Vladimir Tsurkan, Subin Kim sowie Dr. Jiaqiang Yan. Ebenfalls bedanke ich mich sehr herzlich bei PD Dr. Veronika Fritsch, die u.a. durch ihre betreuten Bachelor- und Masterarbeiten stets einen reichen Vorrat an Proben zur Verfügung stellen konnte.

Mit PD Dr. Anton Jesche sowie Alexander Bellon arbeitete ich eng zusammen, um die Herstellung von $KBaYb(BO_3)_2$ zu größeren Mengen zu skalieren, was äußerst spannend war. Außerdem unterstütze mich Anton bei diversen kleineren Messprojekten bezüglich α-$RuCl_3$.

Ganz herzlichen Dank auch an Sebastian Heitzer, der mir beim Lösen des gekoppelten DGL Systems für die Relaxationsmethode einige wertvolle Tipps gegeben hat.

Ein riesiges Dankeschön möchte ich hier an diejenigen aussprechen, die oft vergessen werden. Christine Schäfer, Birgitta Eisenschmid und Chenh Dung Lai standen bei allen Fragen zur Verfügung und sorgten dafür, dass es am Lehrstuhl reibungslos läuft - und das Ganze immer mit einem Lächeln. Über eure extrem große Unterstützung und die tolle Zusammenarbeit war ich sehr froh! Dasselbe gilt auch für Klaus Wiedenmann und Alex Herrnberger, die jederzeit alles stehen und liegen ließen, wenn es im Labor mal wieder gebrannt hat. Zudem möchte ich mich bei German Hammerl bedanken für seine extrem wertvolle Unterstützung gerade im Bezug auf die TRR80-Homepage, aber auch generell für sein stets offenes Ohr. Auch bei den Mitarbeitern aus der Feinmechanischen Werkstatt möchte ich mich herzlich bedanken. Bei allen Projekten wurde mir stets kompetent und unkompliziert weitergeholfen.

Ohne die Jungs aus dem Büro wäre meine Zeit am Lehrstuhl um einiges langweiliger gewesen. Danke an Andi, Andi, Max und Sven für die unzähligen Momente, in denen man den Stress aus dem Labor vergessen konnte! Dasselbe gilt natürlich auch für Fritz, Ina, Manu, Noah, Vera, Alex, Robert, Georg, Franzi, Franzi, Elias, Stefan und viele mehr: Egal ob Söllerhaus, Plärrer, Grillsessions, Pubquiz oder im überragenden Fußballteam (schade, Fritz, dass es nie beim Turnier geklappt hat!) – mit euch konnte ich meine Zeit in Augsburg genießen. Dasselbe gilt auch für die Spielerunde Nerd III: sensationell, dass wir das trotz aller Lockdowns bewahren konnten.

Zu guter Letzt möchte ich mich bei meiner gesamten Familie bzw. Sippschaft bedanken. Ich bin stolz, ein Teil von euch zu sein – ihr seid zu jeder Zeit ein enormer Rückhalt. Das gilt natürlich ganz besonders für dich, Caeci. Es hat wirklich Spaß gemacht, gemeinsam unsere Wege am Physikinstitut zu gehen. Nun geht es Richtung unentdecktes Land, aber zunächst... freue ich mich schon auf unser Abschiedsessen in der Mensa. Den Kartoffelsalat genießt man eben am besten im klingonischen Original!